

RETURNING MATERIALS:
Place in book drop to remove this checkout from your record. FINES will be charged if book is returned after the date stamped below.

# CORRELATIONS BETWEEN MOLECULAR STRUCTURE AND ELECTROCHEMICAL REACTIVITY

Ву

Joseph Thomas Hupp

#### A DISSERTATION

Submitted to
Michigan State University
in partial fulfillment of the requirements
for the degree of

DOCTOR OF PHILOSOPHY

Department of Chemistry

1983

#### ABSTRACT

# CORRELATIONS BETWEEN MOLECULAR STRUCTURE AND ELECTROCHEMICAL REACTIVITY

Ву

#### Joseph Thomas Hupp

Differential capacitance measurements indicate that several simple anions are adsorbed extensively at the silver-aqueous interface.

Electrochemical roughening which is required in order to observe Surface Enhanced Raman Scattering (SERS) from adsorbed ions was found to yield only small changes in the average surface concentrations of such ions.

Correlations were established between the intensities of SERS signals and the surface concentrations of the Raman scatterers.

Modification of the silver-aqueous interface via underpotential deposition (UPD) of a single atomic layer of lead or thallium alters the interfacial properties such that adsorption is inhibited and the solvent inner-layer is restructured.

Electron-transfer reactivity for several chromium complexes at silver is markedly decreased following UPD of lead or thallium. The decrease in reactivity was traced to a change of reaction mechanism from inner- to outer-sphere. Reactions following outer-sphere mechanisms at mercury, UPD lead/silver and UPD thallium/silver exhibit similar rates

at each surface (after correcting for diffuse double-layer effects), but markedly different activation parameters. The differences for the latter are speculatively attributed to solvent-related work terms.

An encounter preequilibrium treatment of electrochemical kinetics is proposed. It is utilized to examine the nonadiabaticy question for outer-sphere electrochemical reductions. The treatment is also employed to correlate homogeneous and heterogeneous electron-transfer reactivity, particularly for aquo complexes of transition metals. It is concluded from such correlations that the  $Fe(H_20)_6^{3+/2+}$  homogeneous self-exchange follows an anomalous, possibly inner-sphere, reaction pathway.

Correlations of reaction entropies with molecular parameters suggest that a molecular rather than a continuum treatment of the solvent is required in order to describe ionic solvation adequately.

Absolute calculations of electron-transfer rate constants for homogeneous cross reactions and electrochemical reactions show tolerable agreement with experiment. The residual differences are attributed to ligand-specific work terms as well as specific reactant-solvent interactions. A method for incorporating the entropic component of such interactions into theoretical treatments of electron transfer is proposed.

All glory to the Father of Lights and to his son Christ Jesus.

#### ACKNOWLEDGMENTS

I wish to thank several people who helped me along the road to the Ph.D. degree. From the beginning Professor Michael Weaver shared his enthusiasm for research, encouraged genuine collaboration and sought to develop the scientific interests and abilities of this student.

Each of these factors made research in his group an enjoyable experience and for this I sincerely thank him.

Dr. George Leroi is gratefully acknowledged for filling in as the major professor at Michigan State.

The assistance and interest of the members of the Weaver group both at Michigan State and Purdue is appreciated. Special mention must be made of Dr. Ned Larkin who imparted to the author the secrets of solid electrodes and who helped initiate the studies of UPD metal surfaces. Thanks are due also to H.Y. Liu who tenaciously pursued parallel experimental work and willingly shared his findings and insights. Thanks also to Dr. Tomi Li for producing some ruthenium compounds on short notice.

The Postal Service is expressly acknowledged for attempting to deliver the degree several weeks late. I am grateful to Liz, Mike and Janet Sarault for their special efforts in helping to overcome this obstacle.

My appreciation is expressed to my family - especially my wife

Liz, my parents, and Mary and Madolyn - for supporting and encouraging

my efforts.

### TABLE OF CONTENTS

		Page
LIST OF	TABLES	ix
LIST OF	FIGURES	xiii
CHAPTER	I - INTRODUCTION	1
Α.	Overview	1
	1. Electrode Chemistry	1
в.	Structure of Electrochemical Interfaces	7
	1. Thermodynamics	7 13
C.	Electrochemical Kinetics	19
D.	Electron Transfer Theory	26
CHAPTER	II - EXPERIMENTAL	34
A.	Materials	34
	1. Solvents	34 35 36 37
В.	Apparatus	39
C.	Electrochemical Measurements	42
	1. Differential Capacitance	42 43 45

	III - DOUBLE-LAYER STRUCTURE AND IONIC ADSORPTION SOLID METAL ELECTRODE-AQUEOUS INTERFACES	46
AI	SOLID REIAL ELECTRODE-AQUEOUS INTERFACES	40
A.	Specific Adsorption of Halide and Pseudohalide Ions at Electrochemically Roughened Versus Smooth Silver-	
	Aqueous Interfaces	46
	1. Introduction	46
	2. Results and Discussion	48
	a. Determination of Roughness Factors for	
	Silver Surfacesb. Determination of Anion Specific Adsorption	48 54
	b. Determination of Anion Specific Adsorption	74
	3. Surface Crystallographic Changes Induced by	
	Electrochemical Roughening	81
	4. Implications for Surface-Enhanced Raman	0.0
	Scattering	86
В.	Specific Adsorption of Transition-Metal Complexes at	
	Silver	92
C.	The Influence of Lead Underpotential Deposition on the	
	Capacitance of the Silver-Aqueous Interface	97
	1. Introduction	97
	2. Electrode Preparation	99
	3. Results	
	4. Discussion	106
D.	The Influence of Lead Underpotential Deposition on	
	Anion Adsorption at the Silver-Aqueous Interface	111
	1. Introduction	111
	2. Results	
	3. Discussion	131
E.	The Influence of Thallium Underpotential Deposition on	
	Anion Adsorption and the Double Layer Structure at the	
	Silver-Aqueous Interface	136
		136
	2. Electrode Preparation	
	3. Results	138
	a. Capacitance Measurements in Single	100
	Electrolytesb. Capacitance Measurements and Anion Specific	138
	Adsorption in Mixed Electrolytes	140
		140
	4. Discussion	154
	5. Conclusions	155

F.	The Role of the Surface Metal Composition in Deter-	
	mining Anion Adsorption	155
	1. Introduction	
	2. Results and Discussion	
	3. Conclusions	162
_		
G.	A Method for Evaluating the Surface Concentrations of	
	Two Like-Charged Ions Simultaneously Adsorbed at an	
	Electrode-Solution Interface	163
CHA DTTD	IV - ELECTROCHEMICAL KINETICS	171
ORAL IBA	17 - BLECTROCHEMICAL RINGITOS	1/1
A.	The Frequency Factor for Electrochemical Reactions	171
	• • . • . •	
	1. Introduction	
	2. The Collisional Model	
	3. The Encounter Preequilibrium Model	
	4. Comparisons of Models	182
	5. Relation Between Electrochemical and Homogeneous	
	Rate Constants	185
	6. Comparison Between the Kinetics of Corresponding	
	Inner- and Outer-Sphere Pathways	188
	7. The Apparent Frequency Factor from the Temper-	
	ature Dependence of Electrochemical Kinetics	190
	8. More Sophisticated Treatments	
	9. Conclusions	194
	The Circlinance of Dischards about 1 Activation Days	
ь.	The Significance of Electrochemical Activation Para-	105
	meters for Surface-Attached Reactants	195
	1. Introduction	195
	2. Relationship between Activation Parameters for	177
	Surface-Attached and Bulk Solution Reactants	197
	3. Significance of the Frequency Factor for	17/
	Attached Reactants	206
	vergones Mesocants	200
C.	An Experimental Estimate of the Electron-Tunneling Dis-	
- •	tance for Some Outer-Sphere Electrochemical Reactions	211
	1. Introduction	211
	2. Discussion	
	3. Conclusions	
D.	The Influence of the Electrode Surface Composition on	
	Redox Reaction Pathways and Electrochemical Kinetics	230
	1. Introduction	
	2. Results and Discussion	231
	a. Rate Formulations	231
	b. Reduction Kinetics of Complexes Containing	
	Potential Bridging Ligands	232

c. Reduction Kinetics for Complexes Lacking	
Bridging Ligands	248
d. Activation Parameters for Outer-Sphere	
Reductions at UPD Lead/Silver	250
3. Conclusions	
J. 0011C1G1CH9	250
CHAPTER V - INFLUENCES OF SPECIFIC REACTANT-SOLVENT INTER-	
ACTIONS ON ELECTRON-TRANSFER KINETICS AND THERMODYNAMICS	050
ACTIONS ON ELECTRON-TRANSFER KINETICS AND INERMODINAMICS	200
A Min Tailing of Garatila Barahan Galama Tahan Atlan	
A. The Influence of Specific Reactant-Solvent Interactions	
on Intrinsic Activation Entropies for Outer-Sphere	
Electron Transfer Reactions	258
1. Introduction	
2. Origin of the Intrinsic Activation Entropy	261
3. Real Chemical Environments. Incorporating Spe-	
cific Reactant-Solvent Interactions in Activation	
Entropy Calculations	267
4. Comparisons with Experiment	
B. Utility of Surface Reaction Entropies for Examining	
Reactant-Solvent Interactions at Electrochemical Inter-	
faces. Ferricinium-Ferrocene Attached to Platinum	
Electrodes	276
Precrodes	2/0
1 Parkers described as	
1. Introduction	
2. Measurement of Surface Reaction Entropies	279
3. Interpretation of Surface Reaction Entropy	
Values	283
C. Size, Charge, Solvent and Ligand Effects on Reaction	
Entropies	289
1. Introduction	289
2. Results	290
3. Discussion	294
4. Conclusions	
CHAPTER VI - APPLICATIONS OF THE RELATIVE ELECTRON-TRANSFER	
THEORY	304
	J 0 7
A. Electrochemical and Homogeneous Exchange Kinetics for	
Transition-metal Aquo Couples: Anomalous Behavior	205
iransition-metal wino conbies: Anomalous benavior	305
1 The section 1	
1. Introduction	
2. Rate Constants for Electrochemical Exchange	309
3. Rate Constants for Electron Exchange from Homo-	
geneous Cross-Reaction Kinetics	313
4. Comparison Between Electrochemical and Homo-	
geneous Exchange Kinetics	327
5. Correlation of Intrinsic Barriers with Reactant	
Structure	329
6. Conclusions and Mechanistic Implications	334

B. Some Comparisons between the Energetics of Electro-	
chemical and Homogeneous Electron-Transfer Reactions	337
<ol> <li>Introduction</li></ol>	338 341 345 346
C. Entropic Driving Force Effects Upon Preexponential Factors for Intramolecular Electron Transfer: Implications for the Assessment of Nonadiabaticity	360
CHAPTER VII - COMPARISONS BETWEEN EXPERIMENTAL KINETICS PARA- METERS AND THE ABSOLUTE PREDICTIONS OF ELECTRON-TRANSFER THEORY	373
A. Introduction	373
B. Calculation of Kinetics Parameters	375
<ol> <li>Pre-exponential Terms</li></ol>	380
C. Results	392
D. Discussion	414
E. Conclusions	424
CHAPTER VIII - CONCLUSIONS AND SUGGESTIONS FOR FURTHER WORK	425
A. Conclusions	425
B. Suggestions for Further Work	428
APPENDIX I - REACTION ENTROPIES FOR TRANSIT ION-METAL REDOX COUPLES IN VARIOUS SOLVENTS	431
APPENDIX II - NEGATIVE ACTIVATION ENTHALPIES	434
REFERENCES	437

## LIST OF TABLES

<u>Table</u>	Pag	<u>e</u>
3.1	Coverage of Roughened Silver (RF=1.9) by Bromide Ions at the Capacitance Peak Potential in Mixed Electrolytes 6	8
3.2	Standard Free Energies of Adsorption $\triangle G_a^0(kJ \text{ mole}^{-1})$ for Anions at Various Silver Surfaces	2
3.3	Standard Free Energies of Adsorption $\Delta G_a^0(kJ \text{ mol}^{-1})$ and Interaction Parameters g for Anions at UPD Lead/Silver	2
3.4	Standard Free Energies of Adsorption $\Delta G_a^0(kJ \text{ mol}^{-1})$ of Anions at a Polycrystalline Lead Electrode	3
3.5	Standard Free Energies of Adsorption $\Delta G_a^0(kJ \text{ mol}^{-1})$ and Interaction Parameters g for Anions at Several Surfaces	6
3.6	Rnthalpies of Desolvation for Anions in Water a	8
3.7	Heats of Formation of Metal Oxides a	1

4.1	Kinetic and Thermodynamic Data for the One-Electron Reduction of Cr(III) Complexes at the Mercury-Aqueous Interface at 25°C	217
4.2	Apparent Rate Constants for the Reduction of Complexes  Containing Potential Bridging Ligands. E = -700 mV	234
4.3	Effects of Iodide Addition on Rate Constants at UPD Lead/	238
4.4	Formal Equilibrium Constants for Anion Adsorption at Solid Electrode/Aqueous Interfaces	241
4.5	Estimated Values of Rate Constants for the Elementary  Electron-Transfer Step of Several Reactions. E = -700 mV	243
4.6	Ratios of Estimated k Values for Reactions at UPD Thallium/	247
4.7	Rate Constants for Outer-Sphere Reactions. E = -1000 mV	249
4.8	Ideal Activation Enthalpies (kJ mol <sup>-1</sup> ) for Reductions of Metal Complexes at UPD Lead/Silver, Mercury and Lead Surfaces	254
4.9	Ideal Activation Entropies (J deg <sup>-1</sup> mol <sup>-1</sup> ) for Reductions of Metal Complexes at UPD Lead/Silver, Mercury and Lead Surfaces	255

2.1	intrinsic Activation Entropies for Selected Homogeneous Self-
	Exchange Reactions, $\Delta S_{int}^*$ (J deg <sup>-1</sup> mol <sup>-1</sup> ), calculated without
	(Equation 5.12) and with (Equation 5.13) Consideration of
	Specific Reactant-Solvent Interactions, and Comparison with
	Experiment
5.2	Formal Potentials (mV) and Reaction Entropies (J deg mol 1)
	for Surface-Attached and Bulk-Solution Ferricinium-Ferrocene
	Couples 284
6.1	Kinetics and Related Thermodynamics Parameters for the Elec-
	trochemical Exchange of some M(III)/(II) Aquo Redox Couples
	at the Mercury-Aqueous Interface at 25°C
6.2	Estimation of Work-Corrected Rate Constants $k_{ex}^{h}(\underline{M}^{-1} \text{ sec}^{-1})$ at
	25°C for Fe <sup>3+/2+</sup> , $V_{aq}^{3+/2+}$ , $Eu_{aq}^{3+/2+}$ , and $Cr_{aq}^{3+/2+}$ Self-Exchange
	from Selected Cross-Reaction Data
6.3	Summary of Rate Constants for Electron Exchange at 25°C, and
	Comparison with Theoretical Predictions 325
6.4	Reaction Entropies, $\triangle S_{rc}^{0}$ (J deg mol 1) for Various Redox
	Couples in Aqueous Solution. a
7.1	Thermodynamic and Structural Parameters for Redox Couples 378

7.2	Observed and Calculated Rate Constants (M <sup>-1</sup> s <sup>-1</sup> ) for Homo-
	geneous Electron-Transfer Reactions
7.3	Observed and Calculated Rate Constants for Electrochemical
	Electron-Transfer Reactions
7.4	Observed and Calculated Electron Transfer Parameters 397
7.5	Observed and Calculated Activation Entropies and Entropy
	Driving Forces (J deg mol for Homogeneous Electron
	Transfer 406
7.6	Observed and Calculated Activation Entropies and Thermo-
	dynamic Driving Forces for Electrochemical Electron-Transfer
	Reactions 408
7.7	· · · · · · · · · · · · · · · · · · ·
	mic Enthalpy Driving Forces (kJ mol <sup>-1</sup> ) for Homogeneous
	Electron-Transfer Reactions 409
7.8	Observed and Calculated Activation Enthalpies and Thermodyna-
	mic Enthalpy Driving Forces (kJ mol-1) for Electrochemical
	Electron-Transfer Reactions 412
A.1	Reaction Entropies (J deg 1 mol 1) for Transition-Metal
	Redox Couples in Various Solvents

### LIST OF FIGURES

<u>Figure</u>		<u>Page</u>
1.1	Model of the interface between an electrode and an	
	electrolyte solution showing the decay of potential	
	from the metal surface $(\phi_m)$ to the outer Helmholtz	
	plane $(\phi_2)$ to the bulk electrolyte solution $(\phi_8)$	16
1.2	Schematic representation of overlapping vibrational	
	states superimposed on classical potential energy sur-	
	faces. The magnitude of the splitting of potential	
	energy curves in the intersection region corresponds	
	to twice the value of the electronic coupling matrix	
	element HAB	28
3.1	Differential capacitance of polycrystalline silver in	
	0.5 M NaClO4 plotted against electrode potential for	
	various roughness factors (RF)indicated	49
3.2	Differential capacitance for polycrystalline silver at	
	-550 mV versus roughness factor as determined using UPD	
	method (see text)	52

3.3A	Differential capacitance versus electrode potential for	
	electropolished polycrystalline silver (RF 1.2) in NaClO4-	
	NaCl mixtures at ionic strength 0.5. Keys to chloride	
	concentrations: 1, 0 mm; 2, 1 mm; 3, 2.5 mm; 4, 6 mm;	
	5, 15 m <u>M;</u> 7, 100 m <u>M;</u> 8, 200 m <u>M</u>	58
3.3B	As in Figure 3.3A, but for electrochemically roughened	
	silver (RF 1.9)	59
3.4	Surface concentration of specifically adsorbed chloride	
	(per cm <sup>2</sup> real area) at electropolished (solid curves) and	
	roughened silver (dashed curves) versus electrode potential	
	for bulk chloride concentrations of 0.015 $\underline{M}$ and 0.10 $\underline{M}$ ,	
	analyzed from Figures 3A and B as outlined in text	60
3.5A	Differential capacitance vesus electrode potential for	
	electropolished polycrystalline silver in NaClO4-NaBr mix-	
	tures of ionic strength 0.5. Key to bromide concentration	
	(solid curves): 1, 0 mM; 2, 0.6 mM; 3, 2 mM; 4, 5 mM;	
	5, 15 mm; 6, 40 mm; 7, 100 mm. The dashed curve is the	
	cell resistance for 100 $m\underline{M}$ bromide plotted on the same	
	potential scale	61
3.5B	As in Figure 3.5A, but for roughened silver (RF=1.9)	62
3.5C	As in Figure 3.5A, but for roughened silver (RF=4.2)	63

3.6A	Surface concentration of specifically adsorbed bromide (per
	cm <sup>2</sup> real area) at electropolished (solid curve) and rough-
	ened silver (dashed, dotted-dashed curves) for bulk concen-
	tration x at 15 mm obtained from Figures 3.5A and B 64
3.6B	As in Figure 3.6A but for x=100 mM
3.7A	Differential capacitance versus electrode potential for
	electropolished silver in NaClO4-NaI mixtures of ionic
	strength 0.5. Key to iodide concentrations: 1,0 mm; 2,
	0.2 mM; 3, 0.5 mM; 4, 1.2 mM; 5, 2.2 mM; 6, 5 mM; 7, 10 mM. 70
3.7B	As in Figure 3.7A but for roughened silver (RF 4.6) 71
3.8A	Differential capacitance versus electrode potential for
	electropolished silver in NaClO <sub>4</sub> -NaNCS mixtures of ionic
	strength 0.5. Key to thiocyanate concentrations: 1, 0 mm;
	2, 0.3 mm; 3, 1 mm; 4, 3 mm; 5, 10 mm; 6, 30 mm; 7, 100 mm. 72
3.8B	As in Figure 3.8A but for roughened silver (RF=2.1) 73
3.9	Differential capacitance versus electrode potential for
	roughened silver in KC1-KSCN mixtures of ionic strength
	0.1. Key to thiocyanate concentrations: 1, 0 mm; 2, 5 mm;
	3, 10 m <u>M;</u> 4, 23 m <u>M;</u> 5, 50 m <u>M</u>

J.IVA	principal cabacitance Acress propriets for capital tot
	electropolished silver in NaClO4-NaN3 mixtures of ionic
	strength 0.5. Key to azide concentrations: 1, 0 mM; 2,
	1 m <u>M</u> ; 3, 3 m <u>M</u> ; 4, 10 m <u>M</u> ; 5, 30 m <u>M</u> ; 6, 100 m <u>M</u>
3.10B	As in Figure 3.10A, but for roughened silver (RF=2.3) 78
3.11	Surface concentration of specifically adsorbed azide
	(per cm <sup>2</sup> real area) at electropolished (solid curves) and
	roughened silver (dashed curves) versus electrode potential
	for bulk azide concentrations of 0.01 M and 0.1 M analyzed
	from Figures 3.10A, 3.10B as outlined in the text 79
3.12	Atomic positions of the (100), (110), and (111) faces in
	the fcc structure (after Hamelin, et al., reference 1) 85
3.13	Fractional coverage, 0, of chloride anions (solid curve)
	and normalized Raman peak intensity (dashed curve) for
	Ag-Cl stretching mode, both plotted against electrode
	potential. Electrolyte is 0.4 M NaClO <sub>4</sub> + 0.1 M NaCl. Raman
	data from reference 102 89
3.14	Fractional coverage, $\theta$ , of bromide anions (solid curve) and
	normalized Raman peak intensity (dashed curve) for Ag-Br

stretching mode,	both plo	tted again	st electr	ode pot	tential.	
Electrolyte is 0	.45 <u>M</u> NaC	104 + 0.05	M NaBr.	Raman d	iata from	l
reference 102						90

- 3.17 Linear sweep current-potential curves for anodic removal of lead layer deposited on silver. Sweep rate was 5 mV sec<sup>-1</sup>, electrode rotated at 600 r.p.m. Electrolyte was 0.5 M/L NaClO<sub>4</sub> adjusted to pH 3.5 with HClO<sub>4</sub>, containing 0.6 μM/L Pb<sup>2+</sup>. Lead deposits corresponding to anodic stripping curves (a)-(c) formed as follows: (a) Electrode rotated at

600 r.p.m., held at -0.585 V for 10 mins. (b) As (a), but	
held at $-1.20~\text{V}_{2}$ for additional 20 mins. with no rotation. (	(c)
Electrode rotated at 600 r.p.m., held at -0.65 v for 10	
minutes 101	)1

- 3.20 Differential electrode capacitance C versus electrode potential E for UPD lead layer on polycrystalline silver having various coverages of lead. Electrolyte was 0.5 M

	NaClO <sub>4</sub> , pH 3.5, with 0.6 µM Pb <sup>2+</sup> . Lead coverages
	(percentage of monolayer): (a) 0%; (b) 22%; (c) 35%;
	(d) 61%; (e) 93%; (f) 100%107
3.21	Differential capacitance vs. electrode potential for UPD
	lead/silver in NaCl + NaF mixed electrolytes at an ionic
	strength of 0.5 M. Key to chloride concentrations: (O)
	0 m <u>M;</u> (●) 8 m <u>M;</u> (▼) 20 m <u>M;</u> (▲) 60 m <u>M;</u> (■) 200 m <u>M</u> 113
3.22	Differential capacitance vs. electrode potential for UPD
	lead/silver in NaBr + NaF mixed electrolytes at an ionic
	strength of 0.5 M. Key to bromide concentrations: (O)
	0 m <u>M;</u> (♠) 3 m <u>M;</u> (♠) 10 m <u>M;</u> (♥) 30 m <u>M</u>
3.23	Differential capacitance vs. electrode potential for UPD
	lead/silver in NaI + NaF mixed electrolytes at an ionic
	strength of 0.5 M. Key to iodide concentrations: (●) 0 mM;
	(O) 0.3 m <u>H;</u> (▼) 1 m <u>H;</u> (△) 3 m <u>M;</u> (▲) 10 m <u>H;</u> (□) 30 m <u>M;</u>
	(■) 100 m <u>M</u>
3.24	Surface concentration of chloride vs. electrode potential
	for UPD lead/silver. Conditions as in Figure 3.21116
3.25	Surface concentration of bromide vs. electrode potential
	for UPD lead/silver. Conditions as in Figure 3.22117

3.26	Surface concentration of iodide vs. electrode potential for
	UPD lead/silver. Solid line: NaI + NaF. Dashed line:
	NaI + NaClO <sub>4</sub> . Concentrations as in Figure 3.23118
3.27	Surface concentration of chloride vs. electrode charge
	density for UPD lead/silver. Conditions as in Figure
	3.21119
3.28	Surface concentration of bromide vs. electrode charge
	density for UPD lead/silver. Conditions as in Figure
	3.22122
3.29	Surface concentration of iodide vs. electrode charge
	density for UPD lead/silver. Conditions as in Figure
	3.26121
3.30	Differential capacitance vs. electrode potential for UPD
	lead/silver in NaBr + NaClO <sub>4</sub> mixed electrolytes at an
	ionic strength of 0.5 M. Key to bromide concentrations:
	(O) $0 \ \underline{\text{mM}}$ , ( $\bullet$ ) $1 \ \underline{\text{mM}}$ , ( $\bullet$ ) $3 \ \underline{\text{mM}}$ , ( $\blacktriangle$ ) $10 \ \underline{\text{mM}}$ , ( $\blacktriangledown$ ) $30 \ \underline{\text{mM}}$ , ( $\square$ ) $100$
	m <u>M</u> 120
3.31	Surface concentration of thiocyanate vs. electrode potential
	for UPD lead/silver in NaNCS + NaF mixed electrolytes at an
	ionic strength of 0.5 $\underline{M}$ . Key to thiocyanate concentrations:
	(△) 1 mM, (●) 3 mM, (○) 10 mM, (■) 30 mM, (□) 100 mM124

3.32	Surface concentration of azide vs. electrode potential for
	UPD lead/silver in NaN3 + NaF mixed electrolytes at an ionic
	strength of 0.5 M. Key to azide concentrations: (0) 3 mM,
	(■) 10 mM, (△) 30 mM, (△) 121 mM
3.33	Surface concentration of perchlorate vs. electrode potential
	for UPD lead/silver in NaClO <sub>4</sub> + NaF at an ionic strength of
	0.5 M. Key to perchlorate concentrations: (■) 10 mM, (O)
	30 mM, (●) 80 mM, (△) 200 mM, (▲) 500 mM (data at 500 mM
	were extrapolated)126
3.34	Surface concentration of thiocyanate vs. electrode charge
	density for UPD lead/silver. Conditions as in Figure 3.31127
3.35	Surface concentration of azide vs. electrode charge density
	for UPD lead/silver. Conditions as in Figure 3.32128
3.36	Surface concentration of perchlorate vs. electrode charge
	density for UPD lead/silver. Conditions as in Figure 3.33129
3.37	Linear sweep current-potential curves for anodic of thallium
	layer deposited on silver. Sweep rate was 20 mV/s. Electro-
	lyte was 0.5 $\underline{M}$ NaF, containing 0.8 $\mu\underline{M}$ TlCl0 <sub>4</sub> . Curve (a):

	600 RPM; (b) electrode held at -960 mV for 12 minutes at
	600 RPM and then held for 15 minutes at -1300 mV without
	rotation137
3.38	Differential capacitance versus electrode potential for: (a)
	a monolayer of underpotentially deposited thallium on poly-
	crystalline silver in 0.05 M NaClO4; (b) the equivalent of
	circa. 3 monolayers of thallium on polycrystalline silver in
	0.05 <u>M</u> NaClO <sub>4</sub> ; (c) as in (a), except in 0.2 <u>M</u> NaClO <sub>4</sub> 139
3.39	Differential capacitance vs. electrode potential for UPD
	thallium/silver in NaCl+NaF mixed electrolytes at an ionic
	strength of 0.5 M. Key to chloride concentrations:
	(●) 0 mM; (O) 1 mM; (▲) 10 mM; (▽) 50 mM (■) 100 mM; (◇) 200
	<u>■</u> 141
3.40	Differential capacitance vs. electrode potential for UPD
	thallium/silver in NaBr + NaF mixed electrolytes at an ionic
	strength of 0.5 M. Key to bromide concentrations: ( 0 0 mM;
	(■) 20 m <u>M</u> ; (▲) 50 m <u>M</u> ; (▼) 100 m <u>M</u> ; (♠) 200 m <u>M</u>
3.41	Differential capacitance vs. electrode potential for UPD
	thallium/silver in NaI + NaF mixed electrolytes at an ionic
	strength of 0.5 M. Key to iodide concentrations: (△) 0 mM;
	(●) 1 mM; (O) 5 mM; (■) 10 mM; (□) 20 mM (◆) 50 mM143

electrode held at -960 mV for 12 minutes while rotating at

3.42	Surface concentration of chloride vs. electrode potential for
	UPD thallium/silver. Conditions as in Figure 3.38144
3.43	Surface concentration of bromide vs. electrode potential for UPD thallium/silver. Conditions as in Figure 3.39145
3.44	Surface concentration of iodide vs. electrode potential for
	UPD thallium/silver. Conditions as in Figure 3.40146
3.45	Surface concentration of chloride vs. electrode charge density for UPD thallium/silver. Conditions as in Figure 3.38147
3.46	Surface concentration of bromide vs. electrode charge density for UPD thallium/silver. Conditions as in Figure 3.39148
3.47	Surface concentration of iodide vs. electrode charge density
	for UPD thallium/silver. Conditions as in Figure 3.40149
3.48	Surface concentration of perchlorate vs. electrode potential for UPD thallium/silver in NaClO <sub>4</sub> + NaF mixed electrolytes at
	an ionic strength of 0.5 M. Key to perchlorate concentrations: (O) 10 mM; (△) 60 mM; (□) 200 mM
3.49	Surface concentration of thiocyanate vs. electrode potential for UPD thallium/silver in NaNCS + NaF mixed electrolytes at
	an ionic strength of 0.5 M. Key to thiocyanate concentrations: (○) 1 mM, (■) 5 mM, (△) 20 mM, (●) 50 mM, (□) 100 mM151

3.50	Surface concentration of perchlorate vs. electrode charge	
	density for UPD thallium/silver. Conditions as in	
	Figure 3.8152	
3.51	Surface concentration of thiocyanate vs. electrode charge	
	density for UPD thallium at silver. Conditions as in	
	Figure 3.9153	
4.1	Schematic potential-energy surfaces for a single step elec-	
	trode reaction, illustrating the distinction between "real"	
	and "ideal" activation enthalpies for attached reactants (see	
	text for details)205	
4.2	Schematic plot of electronic transmission coefficient Kel for	
4.2	Schematic plot of electronic transmission coefficient $\kappa_{el}$ for an outer-sphere electrochemical reaction against the	
4.2	<b>61</b>	
4.2	an outer-sphere electrochemical reaction against the	
4.2	an outer-sphere electrochemical reaction against the reactant-electrode separation distance r. A'A" and B'B"	
4.2	an outer-sphere electrochemical reaction against the reactant-electrode separation distance r. A'A" and B'B" represent anticipated planes of closest approach for Cr(III)	
4.2	an outer-sphere electrochemical reaction against the reactant-electrode separation distance r. A'A" and B'B" represent anticipated planes of closest approach for Cr(III) ammine and aquo, reactants, respectively. The shaded and	
4.2	an outer-sphere electrochemical reaction against the reactant-electrode separation distance r. A'A" and B'B" represent anticipated planes of closest approach for Cr(III) ammine and aquo, reactants, respectively. The shaded and cross-hatched areas represent the corresponding values of the	
4.2	an outer-sphere electrochemical reaction against the reactant-electrode separation distance r. A'A" and B'B" represent anticipated planes of closest approach for Cr(III) ammine and aquo, reactants, respectively. The shaded and cross-hatched areas represent the corresponding values of the "effective reaction zone thickness" $\kappa_{el}^{0}$ or for these	

4.4	Log of apparent rate constant at UPD lead/silver or UPD
	thallium/silver versus log of apparent rate constant at
	silver. Key to reactants: (1) Cr(NH <sub>3</sub> ) <sub>5</sub> NCS <sup>2+</sup> ; (2)
	$Cr(H_2O)_5NCS^{2+};$ (3) $Cr(NH_3)_5N_3^{2+};$ (4) $Cr(H_2O)_5N_3^{2+};$ (5)
	$Cr(NH_3)_5C1^{2+}$ ; (6) $Cr(H_2^0)_5C1^{2+}$ ; (7) $Cr(NH_3)_5Br^{2+}$
4.5	Diffuse layer potential $\phi_2$ versus electrode potential at UPD
	lead/silver. Electrolytes: (a) 0.5 M NaF; (b) 0.5 M
	NaClO <sub>4</sub> ; (c) 0.47 <u>M</u> NaClO <sub>4</sub> + 0.03 <u>M</u> NaI
4.6	Estimated value (outer-sphere assumption) for log k at UPD
	lead/silver versus log k at silver. Reactants as in Figure
	4.4
5.1	Schematic representation of the ionic entropy of an individual
	redox center as a function of its effective ionic charge
	during the electron transfer step. See text for details266
5.2	Plot of relative ionic entropy of Ru(bpy) <sup>n</sup> <sub>3</sub> (bpy=2,2'
	-bipyridine) in acetonitrile as a function of the square of
	the ionic charge n. The solid line is the best fit line
	through the experimental points; the dashed line is the
	slope of this plot predicted by the Born model275
5.3	Mode of attachment of ferrocene to platinum surface281

5.4	Ferrocene derivative (n-ferrocenemethylene-p-toluidine) used
	as as solution analog of surface-attached ferrocene in Figure
	5.3281
5.5	Representative plot of formal potential for surface-attached
	ferricinium-ferrocene couple, Ea, versus temperature in
	aqueous 0.1 M TEAP. Potentials versus saturated calomel
	electrode at 24 C, using nonisothermal cell arrangement282
5.6	Plot of reaction entropies for surface-attached and solution-
	phase ferricinium-ferrocene couples in various solvents
	versus solvent Acceptor Number, taken from reference 277.
	Filled triangles: surface-attached ferrocene (Figure 5.3);
	open triangles: bulk-solution derivatized ferrocene (Figure
	5.4); open circles: bulk-solution ferrocene. Key to
	solvents: 1, acetone; 2, dimethylformamide; 3, propylene
	carbonate; 4, acetonitrile; 5, dimethylsulfoxide; 6,
	nitromethane; 7, N-methylformamide; 8, formamide; 9,
	methano1; 10, water287
5.7	Reaction entropy versus effective radius of reactant. Key
	to solvents: (O) water; (△) dimethylsulfoxide; (□)
	acetonitrile. Key to reactants:(1) Cr(bpy) <sub>3</sub> <sup>3+</sup> ; (2) Fe(bpy) <sub>3</sub> <sup>3+</sup> ;
	(3) $Ru(bpy)_3^{3+}$ ; (4) $c-Ru(NH_3)_2(bpy)_2^{3+}$ ; (5) $c-Ru(H_20)_2bpy^{3+}$ ;
	(6) $t-Ru(H_2O)_2(bpy)_2^{3+}$ ; (7) $Ru(NH_3)_4bpy^{3+}$ ; (8) $Ru(NH_3)_4phen^{3+}$ ;
	(9) Ru(en) <sub>3</sub> <sup>3+</sup> ; (10) Ru(NH <sub>3</sub> ) <sub>5</sub> py <sup>3+</sup> ; (11) Ru(NH <sub>3</sub> ) <sub>6</sub> <sup>3+</sup> ;

	(12) $0s(NH_3)_6^{3+}$ ; (13) $Ru(NH_3)_5H_2^{3+}$ ; (14) $Ru(NH_3)_4(H_2^{0})_2^{3+}$ ;
	(15) Ru(H <sub>2</sub> 0) <sub>6</sub> <sup>3+</sup> 291
5.8	Reaction entropy versus 1/r. Keys to solvents and reactants
	as in Figure 5.7292
5.9	Reaction entropy for ruthenium tris bipyridine couples in
	acetonitrile versus the difference in the squares of the
	charges on the oxidized and reduced states293
5.10	Reaction entropy versus solvent acceptor number. Key to
	reactants: ( <b>m</b> ) $Cr(bpy)_3^{3+}$ , (O) $Ru(en)_3^{3+}$ , (D) $Ru(NH_3)_6^{3+}$ ,
	(●) Co(en) <sub>3</sub> <sup>3+</sup> , (▲) Co(sepulchrate) <sup>3+</sup> . Solvents (and
	acceptor numbers): water (55), formamide (40),
	N-methylformamide (31), nitromethane (20.5), acetonitrile
	(19), dimethylsulfoxide (19), propylenecarbonate (18),
	dimethylformamide (16), acetone(12.5)295
5.11	Reaction entropy versus solvent acceptor number. Key to
	reactants: (◊) ferricinium, (Ο) Co(EFME-oxosar-H) <sup>2+</sup> , (Δ)
	Ru(NH <sub>3</sub> ) <sub>5</sub> NCS <sup>2+</sup> . Solvents as in Figure 5.10, plus methanol
	(41)296
5.12	Structure of Co(EFME-oxosar-H) <sup>2+</sup> 297

- Reaction entropy in water versus  $(z_{ox}^2-z_{red}^2)/radius$ . Key to reactants: (1)  $Fe(CN)_6^{3-}$ ; (2)  $Fe(CN)_4 bpy^{2-}$ ;
  - (3) ferricinium; (4) Cr(bpy)<sub>3</sub><sup>3+</sup>; (5) Ru(NH<sub>3</sub>)<sub>5</sub>C1<sup>2+</sup>;
- Plot of (2 log  $k_{12}^h$  log  $k_{22}^h$ ) vs.  $[\log K_{12} + (\log K_{12})^2/4]$ 6.1  $\log (k_{11}^h k_{22}^h / z_h^2)$ ] for homogeneous cross reactions involving  $Fe_{aq}^{3+/2+}$ , calculated as  $Fe_{aq}^{2+}$  oxidations.  $k_{ex}^{h}$  for low spin M(III)/(II) polypyridines taken as 1 x 10<sup>9</sup>  $M^{-1}$  sec<sup>-1</sup> (see text).  $k_{11}^h$  refers to  $Fe_{aq}^{3+/2+}$  self exchange;  $k_{22}^h$  to self exchange for coreactant couples. Zh assumed to equal  $1 \times 10^{12} \, \underline{\text{M}}^{-1} \, \text{sec}^{-1}$ ; value of  $k_{11}^{h}$  required for plot obtained by iteration:  $k_{11}^{h} = 10^{-3} \, \underline{\text{M}}^{-1} \, \text{sec}^{-1}$ . Data sources given in Table 6.2 or reference 311 unless othewise stated. points refer to cross reactions; open point to "observed"  $Fe_{ac}^{3+/2+}$  self exchange. Key to oxidants: 1.  $Ru_{ac}^{3+}$ ; 2.  $\text{Eu}_{\text{ag}}^{3+}$ ; 3.  $\text{Cr}_{\text{ag}}^{3+}$ ; 4.  $\text{U}_{\text{ag}}^{4+}$ ; 5.  $\text{V}_{\text{ag}}^{3+}$  6.  $\text{Ru}(\text{NH}_3)_{6}^{3+}$ ; 7.  $\text{Ru}(\text{en})_{3}^{3+}$ ; 8.  $Ru(NH_3)_{5}py^{3+}$ ; 9.  $Ru(bpy)_{3}^{3+}$ ; 10.  $Ru(NH_3)_{5}nic^{3+}$ , reference 320; 11. Ru(NH<sub>3</sub>)<sub>5</sub>isn<sup>3+</sup>; 12. Ru(NH<sub>3</sub>)<sub>4</sub>bpy<sup>3+</sup>, reference 310; 13.  $Os(bpy)_3^{3+}$ , reference 334; 14.  $Fe(bpy)_3^{3+}$ , reference 335; 15. Fe(phen) $_{3}^{3+}$ , reference 336; 16. Co(phen) $_{3}^{3+}$ , reference 337; [17-19 from reference 330]; 17. Ru(terpy) $_{2}^{3+}$ ; 18.  $Ru(phen)_3^{3+}$ ; 19.  $Ru(bpy)_2(py)_2^{3+}$ ; [20-23 from reference 338] 20.  $0s[5,5'-(CH_3)_2bpy]_3^{3+}$ ; 21.  $0s(phen)_2^{3+}$ ; 22.  $0s(5-C1-phen)_3^{3+}$ ; 23.  $Ru[5,5'-(CH_3)_2 bpy]_3^{3+}$ ; [24-31] from reference 339]; 24. Ru[3,4,7,8-(CH<sub>3</sub>)<sub>4</sub> phen]<sub>3</sub><sup>3+</sup>; 25.

- 6.4 Schematic illustration of general relationship between electrochemical and homogeneous redox reaction energetics. Curves 11' and 22' are plots of activation free energy  $\Delta G_e^*$  versus thermodynamic driving force -FE for an electro-

- The electrochemical free energy of activation,  $\Delta G_e^*$ , for  $Cr(H_20)_6^{3+/2+}$  at the mercury-aqueous interface, plotted against the electrode potential for both anodic and cathodic overpotentials. Solid lines are obtained from the experimental rate constant-overpotential plot in reference 313, by using Equation 6.15. Dashed lines are the predictions from Equation 6.24.
- 6.6 Plot of  $\triangle G_{12}^*/\triangle G_{1,12}^*$  against  $-\triangle G_{12}^0/\triangle G_{1,12}^*$  for homogeneous cross rections involving oxidation of aquo cations.

  Reductants: (①) Eu2+ (△) Cr2+ (▽) V2+ (△) Ru2+ (△) Ru2+ (△) Cr2+ (△) V2+ (△) Ru3+ (△) Ru2+ (△) Ru3+ (△)

- Plot as for Figure 6.6, but involving reactants other than aquo complexes. Key to reactants and data sources: (●)

  Co(III)/(II) macrocycle oxidants (data are given in Figures

  2, 5 and 6 of reference 351); (O) other nonaquo oxidants; 1,

  Ru(NH<sub>3</sub>)<sub>5</sub>py<sup>3+</sup> + Ru(NH<sub>3</sub>)<sub>6</sub><sup>2+</sup>; 2, Ru<sup>3+</sup><sub>aq</sub> + Ru(NH<sub>3</sub>)<sub>6</sub><sup>2+</sup>; 3, Co(phen)<sub>3</sub><sup>3+</sup> +

  Ru(NH<sub>3</sub>)<sub>6</sub><sup>2+</sup>; 4, Co(bpy)<sub>3</sub><sup>3+</sup> + Ru(NH<sub>3</sub>)<sub>6</sub><sup>2+</sup>; 5, Co(phen)<sub>3</sub><sup>3+</sup> +

  Ru(NH<sub>3</sub>)<sub>5</sub>py<sup>2+</sup> (data sources for 1-5 are listed in reference

  311); 6, horse heart ferricytochrome c + Ru(NH<sub>3</sub>)<sub>6</sub><sup>2+</sup> (reference

  389); 7, Co(phen)<sub>3</sub><sup>3+</sup> + horse heart ferrocytochrome c (reference

  390); 8, Ru(NH<sub>3</sub>)<sub>6</sub>bpy<sup>3+</sup> + Ru(NH<sub>3</sub>)<sub>5</sub>py<sup>2+</sup> (reference 310)......355
- Plot of  $(^{\Delta}G_{12}^{*} ^{\Delta}G_{1,12}^{*})$  for homogeneous cross reactions involving oxidation of aquo complexes given in Figure 6.5, against the thermodynamic driving force function—  $[0.5\Delta G_{12}^{0} + (^{\Delta}G_{12}^{0})^{2}/16\Delta G_{1,12}^{*}]$ . Closed symbols are obtained from homogeneous data; key to points as in Figure 6.5. Open symbols are corresponding points obtained from electrochemical kinetic data for oxidation of aquo cations (see text for details)....356

Plot of the experimental activation entropy,  $\Delta S_{exp}^*$ , against 6.9 the activation entropy,  $\Delta S_{FC}^{\star}$ , calculated from Equation 6.32 for bimolecular reactions involving 3+/2+ redox couples. Data sources quoted reference 311 unless otherwise noted (aq = OH2, en = enthylenediamine, bpy = 2,2'-bipyridine, phen = 1, 10'-phenanthroline, terpy = 2,2',2"-terpyridine, py = pyridine). Reactions: 1.  $Co_{ac}^{3+} + Fe_{ac}^{2+}$ ; 2.  $Co_{ac}^{3+} + Fe_{ac}^{3+}$  $\operatorname{Cr}_{aq}^{2+}$ ; 3.  $\operatorname{Fe}_{aq}^{3+} + \operatorname{Ru}_{aq}^{2+}$ ; 4.  $\operatorname{Fe}_{aq}^{3+} + \operatorname{V}_{aq}^{2+}$ ; 5.  $\operatorname{Fe}_{aq}^{3+} + \operatorname{Fe}_{aq}^{2+}$ ; 6.  $V_{aq}^{3+} + V_{aq}^{2+}$ ; 7.  $Fe_{aq}^{3+} + Ru(NH_3)_6^{2+}$ ; 8.  $Fe_{aq}^{3+} +$  $Ru(NH_3)_{5}py^{2+}$ ; 9.  $Fe_{aq}^{3+} + Ru(en)_{3}^{2+}$ ; 10.  $Ru(bpy)_{3}^{3+} + Fe_{aq}^{2+}$ ; 11.  $Ru(phen)_3^{3+} + Ru_{aq}^{2+}$ ; 329 12.  $Fe(bpy)_3^{3+} + Fe_{aq}^{2+}$ ; 359 13.  $Fe(phen)_3^{3+} + Fe_{aq}^{2+}; ^{335}$  14.  $Ru(terpy)_2^{3+} + Fe_{aq}^{2+}; ^{329};$  15.  $\text{Ru(bpy)}_{2}(\text{py)}_{2}^{3+} + \text{Fe}_{a\sigma}^{2+};$  16.  $\text{Ru(NH}_{3})_{6}^{3+} + \text{V}_{a\sigma}^{2+};$  17.  $Ru(NH_3)_{5}py^{3+} + V_{ad}^{2+};$  18.  $Co(en)_3^{3+} + V_{ad}^{2+}$  19.  $Co(bpy)_3^{3+} + V_{ad}^{2+}$  $V_{aq}^{2+}$ ; 310 20. Co(phen)<sub>3</sub><sup>3+</sup> +  $V_{aq}^{2+}$ ; 310 21. Ru(NH<sub>3</sub>)<sub>5</sub>py<sup>3+</sup> +  $\operatorname{Cr}_{ag}^{2+}$ ; 360 22.  $\operatorname{Ru}(\operatorname{NH}_3)_4 \operatorname{bpy}^{3+} + \operatorname{Ru}(\operatorname{NH}_3)_4 \operatorname{phen}^{2+}$ ; 28 23.  $Ru(NH_3)_6^{3+} + Ru(NH_3)_6^{2+};$  24.  $Ru(en)_3^{3+} + Ru(NH_3)_6^{2+};$  25.  $Co(en)_{3}^{3+} + Co(en)_{3}^{2+}; 26. Co(bpy)_{3}^{3+} + Co(bpy)_{3}^{2+}; 27.$  $Co(phen)_3^{3+} + Co(phen)_3^{2+} = 28. Co(en)_3^{3+} + Cr(bpy)_3^{2+};$  361 29.  $Co(phen)_3^{3+} + Ru(NH_3)_6^{2+}; 30. Co(phen)_3^{3+} +$ 

7.1	Schematic representation of the relationships between the
	nuclear reaction coordinate, forward and reverse reorgan-
	ization energies, and the classical free energy barrier to
	electron transfer

- 7.2 The log of the work-corrected experimental rate parameter k<sub>corr</sub> plotted against the log of the corresponding theoretical parameter k(T) for electron transfer between reactants possessing identical ligand compositions. Key:

  (O) aquo complexes; (△) polypyridine complexes; (●) ammine complexes. Reactions and rate constants listed in Table
  7.2
- 7.4 Experimental activation entropies versus theoretical activation entropies. Key to reaction type: ( electrochemical; others as in Figures 7.2 and 7.3. Results listed in Table 7.4.....

7.5	Work-corrected experimental activation enthalpies versus theore-
	tical activation enthalpies. Key to reaction type as in Figures
	7.2 and 7.3. Results listed in Table 7.5 405
7.6	Log [k(T)/k corr] for reactions involving aquo complexes plotted
	against the reduced driving force $\Delta G^{0}/(\lambda_{f}^{2}+\lambda_{r}^{2})$ . Key to reaction
	type as in Figures 7.3 and 7.4 415
7.7	Log [k(T)/k corr] for reactions between polypyridine and aquo
	complexes plotted against the reduced driving force
	$\Delta G^{O}/(\lambda_{f}^{O}+\lambda_{r}^{O})$ . Key: (4) low-spin polypyridines with aquos;
	high-spin polypyridines with aquos
A.1	Variation of calculated activation parameters with free energy
	driving force, $G^{\circ}$ , for a reaction for which $G_{\text{int}}^{*} = 44 \text{ kJ mol}^{-1}$
	$S_{int}^* = 0 \text{ J deg}^{-1} \text{ mol}^{-1} \text{ and } S_{int}^0 = -180 \text{ J deg}^{-1} \text{ mol}^{-1} \dots 436$

### CHAPTER I

#### INTRODUCTION

The first section of this chapter provides an overview of the dissertation research, while the sections that follow present background information.

# A. <u>Overview</u>

The research described herein was directed towards understanding several fundamental problems in electrochemistry. Each portion relates in one way or another to the overall question of the relationship between molecular structure - of the interfacial region, the electrode surface, the solvent, and the reactant - and electrochemical, as well as homogeneous, electron-transfer reactivity. The first few chapters might be termed studies in "electrode chemistry", while the latter chapters are concerned with "electron-transfer chemistry". The section on the influence of the electrode material on electron-transfer kinetics provides a connection between the two.

# 1. Electrode Chemistry

A central area of interest in electrochemistry concerns the role of electrode composition in determining the thermodynamic and

electrocatalytic properties of the metal-solution interface. Historically, research on interfacial electrochemistry, particularly the thermodynamic aspects, has focused on the mercury-aqueous interface. However, in the last decade the behavior of various solid electrodes in contact with aqueous solutions has been described in an increasing, albeit a limited number of studies. Although comparisons between the results for different metal electrodes are instructive, several problems remain. First, the data are not as extensive as one would like (are they ever?). Second, the substitution of one metallic element for another represents a fairly drastic change of electrode material. Finally, with the exceptions of mercury, silver, and to a lesser extent gold, it has yet to be proven that clean, smooth, oxide-free electrode surfaces can be prepared in a reproducible manner.

To circumvent these problems, experiments designed to examine anion adsorption, double-layer properties and heterogeneous electron-transfer kinetics were carried out first with carefully prepared polycrystalline silver surfaces and then with silver electrodes which had been modified via underpotential deposition of a single atomic layer or less of lead<sup>2</sup> or thallium.<sup>3,4</sup> This represents a convenient and exact method of altering the metallic composition of the surface. Although underpotentially deposited (UPD) layers have been widely examined as possible catalysts for complicated electrochemical reactions,<sup>5</sup> applications to fundamental studies of interfacial properties have thus far been few. The effect itself is well established<sup>6</sup> and has been thoroughly investigated from the point of view of understanding metal deposition reactions. Basically,

underpotential deposition involves the deposition of one to two monolayers of one metal onto a second, less electronegative metal at potentials positive of the thermodynamic potential for bulk deposition. It is observed when the energetics of forming a heteronuclear metal-surface bond (e.g. lead-silver) are appreciably more favorable than for homonuclear metal-surface bond formation (e.g. lead-lead).

Another aspect of electrode composition is the atomic morphology of the surface. This is especially important in Surface Enhanced Raman Spectroscopy (SERS). Generally SERS signals can be observed only with electrochemically roughened surfaces. The first section of Chapter III describes a comparative thermodynamic study of anion adsorption at smooth and roughened silver electrodes, with particular emphasis on the relevance to related SERS studies. Chapter III also describes the surface redox reactivity of Raman-active transition metal complexes at roughened ("SERS-active") silver.

# 2. <u>Electron-transfer</u> Chemistry

The underlying premise of the electrochemical kinetics research is that it would be desirable to examine electron transfer energetics at metal surfaces in a parallel fashion and with a similar degree of sophistication as that employed for homogeneous rate processes. The latter area has been characterized by a renaissance of interest and a remarkable degree of progress over the last few years. This renewal might be traced to two or three key developments. First, the acquisition of structural data for a number of simple inorganic redox couples 10-12 has been accompanied most recently by a realization that

the interplay between theory and experiment is no longer limited to testing the Marcus cross relations 13 but instead can be pursued essentially at an absolute level. 10 Secondly, ab initio calculations 14,15 and the influx of ideas from areas such as energy transfer kinetics 16 have drawn attention to the quantum mechanical aspects of the problem, in particular nuclear and electron tunneling. Consideration of the latter has led to more realistic models of the frequency factor. 17,18 Thirdly, some of the most difficult aspects of the physics of electron transfer 19-22 have been repackaged and essentially translated 9,23,24 so as to be understandable to researchers trained as chemists. This has caused a rethinking of electron transfer in terms of the theory of radiationless transitions 25 rather than transition state theory, 13 leading to fresh insights and also a redirection of research efforts to different aspects of the problem. 26

The most ambitious portion of the dissertation research in this regard is that contained in Chapter VII where theoretical calculations of rate parameters are undertaken for about fifty homogeneous cross reactions and electrochemical reactions. These calculations rely heavily on recently published EXAFS 10 and x-ray data 11,12 and are carried out along the lines of Brunschwig and Sutin's work on self-exchange processes. Thus, inner-shell components of the Franck-Condon barrier to electron transfer are calculated from changes in metal-ligand bond distances. Together with the results obtained from new models for solvent reorganization and precursor formation 8,9,17 these calculations yield absolute theoretical estimates of kinetics parameters that an be compared directly with the corresponding

experimental data. Significant discrepancies are uncovered between theory and experiment and are used to evaluate particular features of contemporary theories.

Several other segments of the research build on a simple yet important concept advanced by Sutin. 27,28 He proposed that an "encounter pre-equilibrium" formalism be employed in place of the Marcus reactive collision model 13 in describing bimolecular electron transfer reactions in solution. Thus, the overall experimental rate constant is taken to be the product of an equilibrium constant for the formation of a reactive binuclear complex and a first-order rate constant for the elementary electron transfer step. (Interestingly, a similar proposal was put forth by North in 1964 for solution-phase reactions in general, 29 but failed to attract attention). In parallel with Sutin's work, a heterogeneous "encounter pre-equilibrium" model has recently been advocated. 30,31 This pre-equilibrium treatment of electrochemical kinetics has been refined and further developed as outlined in Chapter IV. The molecular basis of the approach is examined and compared with the underlying assumptions of the usual "collisional" model. 13 The pre-equilibrium treatment is found to provide a more satisfactory description under most conditions. The implications of this approach for the interpretation of experimental observables such as frequency factors and rate constants are explored.

The formulation of the pre-equilibrium treatment for heterogeneous electron transfer was one of the key developments of the dissertation research since it provided a means of comparing outer- and inner-sphere electrode reactions on a common basis, thereby enabling the findings concerning differences in electron-transfer reactivity at different metal surfaces to be interpreted quantitatively. This approach also forms the basis of the experimental probe of nonadiabatic effects reported in Chapter IV.

Another useful concept, which stems in part from the preequilibrium models, is the representation of the electrode surface as a "coreactant" which requires no activation and possesses a continuously variable "formal potential". (The latter is simply the applied electrode potential). This approach enables comparative reactivities of complex ions in homogeneous versus heterogeneous environments to be evaluated objectively. The concept is applied to a small extent in Chapter VII, but is deserving of further utilization.

A second major premise of the electron-transfer studies is that homogeneous redox reactions can be viewed as coupled electrochemical "half reactions". This gives rise to the intriguing notion that various features of homogeneous reactions can be probed experimentally and conceptually by examining related electrochemical reactions. In particular, the energetics of each half of a "whole" bimolecular reaction can be separately examined as unimolecular electrode processes. Some of the questions of interest with regard to electron transfer are the importance of nonadiabaticity (i.e. electron tunneling as a rate-determining factor), the influence of thermodynamic driving forces on reactivity, the reasons for the "anomalous" behavior of certain redox couples and the role of specific reactant-solvent interactions in determining reactivity. The results summarized in

Chapters VI and VII and parts of Chapter IV represent attempts to utilize electrochemistry to answer these questions.

The remainder of the research (Chapter V) reports some empirical observations concerning ionic solvation and attempts to establish the connections between the thermodynamics of ionic solvation and the energetics of the nonequilibrium solvent polarization process which precedes electron transfer. <sup>13</sup> In particular, a molecular rather than continuum picture of the solvent is advocated in order to rationalize some of the experimental data.

# B. Structure of Electrochemical Interfaces

Most of the experimental studies of interfacial structure outlined in Chapter III are based on well-established thermodynamic approaches. However, surface thermodynamics is hardly an area of general knowledge in chemistry. In view of this, and in particular since an extension of the conventional adsorption analysis is proposed in the last section of Chapter III, the relevant aspects of surface thermodynamics are described here.

Following this, a model of the electrical double layer is decribed. Since the bulk of the dissertation research centers on interfacial phenomena, such a review is considered to be desirable.

### 1. Thermodynamics

An interface is defined for thermodynamic purposes as the boundary region between two pure phases, in the present case the

electrolyte solution and the metal electrode. 32 In this "interphasial" region we may expect to find excesses or deficiencies of ions, electrons, solvent molecules or other components of the pure phases. In fact the interphasial region may be defined as the region within which such excesses and deficiencies exist.

In order to gain information about the interface it is useful to conceive of a dividing surface which separates the two pure phases.

The surface can be located anywhere within the interphasial region. At constant temperature and pressure the Gibbs adsorption isotherm describing the thermodynamic state of the surface is:

$$-\mathbf{d} \gamma = \sum_{i} \Gamma^{0} \mathbf{d} \mu_{i}$$
 (1.1)

where  $\Upsilon$  is the surface tension (or interfacial tension),  $\Gamma_{i}^{0}$  is the surface excess concentration of component i (i.e., the excess amount of i in the interphasial zone, divided by the surface area), and i is the electrochemical potential of i. The significance of the quantity can be understood by noting that the excess free energy of a stable surface is minimized by minimizing the surface area. (If a surface instead maximized its area it would not remain a surface for very long!) The surface tension is defined as the partial derivative of the excess free energy with respect to area.

From the Gibbs adsorption isotherm, which describes interfaces in general, the electrocapillary equation can be derived. (See reference 33 for a fairly simple, clear derivation of this equation as well as the Gibbs adsorption isotherm.) General expressions of the

electrocapillary equation are cumbersome.<sup>32</sup> However, an example will serve to illustrate the form of the equation. For an aqueous NaBr solution in contact with a metal electrode the equation can be written as:

$$-d \gamma = {^{m}_{\sigma}}dE^{+} + \Gamma_{Br} d\mu_{NaBr}$$
 (1.2)

where  $\sigma^m$  is the charge on the electrode surface.

The quantity  $B^+$  is the electrode potential versus a reference electrode that is reversible with respect to the sodium cation. (Experimentally,  $E^+$  can be obtained by using an actual reversible reference such as a sodium ion selective electrode, or it can be calculated from estimates of the cation activity together with potentials measured against a fixed reference electrode). The quantity  $\Gamma_{Br}$  is the surface excess concentration of bromide ions relative to the surface excess concentration of water and therefore differs slightly from the absolute surface excess concentration  $\Gamma_{Br}^{\circ}$  which would appear in the Gibbs equation. The symbol  $\mu_{NaBr}$  represents the chemical potential of NaBr. Since the NaBr "molecule" is neutral there is no electrical contribution to its activity and

 $\mu_{\mbox{NaBr}}$  -  $\mu_{\mbox{NaBr}}$  . An equivalent formulation of the electrocapillary equation is

$$-\mathbf{d} = \mathbf{m} \mathbf{d} \mathbf{E} + \mathbf{r}_{\mathbf{N} \mathbf{a}} \mathbf{d} \mathbf{\mu}_{\mathbf{N} \mathbf{a} \mathbf{B} \mathbf{r}}$$
 (1.3)

where  $E^-$  is the electrode potential versus a reference which responds reversibly to the activity of  $B^-$ .

Equations 1.2 and 1.3 suggest that the charge on an electrode can be determined from the variation of the surface tension with electrode potential.

Thus,

$$-(\partial Y/\partial E^{-}) = -(\partial Y/\partial E^{+}) = \sigma^{m}$$
 (1.4)

Equation 1.4 is known as the Lippmann equation. Also, since  $d\mu_{\mbox{NaBr}} = -\mbox{RT} \ d \mbox{ln} \ a_{\mbox{NaBr}}, \ \mbox{where} \ a_{\mbox{NaBr}} \ \ \mbox{is the activity of the salt, we can}$  write

$$-(1/RT)(\partial Y/\partial \ln a_{NaBr})_{E+} = \Gamma_{Br}$$
 (1.5)

and

$$-(1/RT)(\partial Y/\partial \ln a_{NaBr})_{E-} = \Gamma_{Na}$$
 (1.6)

Additional equations analogous to 1.5 and 1.6 can be written if there are more components of the interphasial system. A curious aspect of the electrocapillary equation and related expressions is that they yield directly surface excess concentrations rather than activities. (Indeed, it could be argued that the concept of "surface activity" has no meaning).

Evidently a complete description of an electrochemical interface can be gained by evaluating the electrocapillary equation. Nevertheless, there are some restrictions and complications. First, Equations 1.1 through 1.6 are derived by assuming ideal polarizability of the interface. In other words it is assumed that no material or charge is transported across the interface when the potential is changed. Clearly this condition is not met if, for example, the electrode is dissolving or if it is exchanging electrons with some reactive substance dissolved in the solution.

Another problem is that the spatial distribution of each solute component at the interface cannot be specified thermodynamically. Often, however, one wishes to know how much material is actually contacting the metal surface, i.e. is specifically adsorbed. measured surface excess of a substance can be partitioned between the metal surface and the rest of the interphasial zone only by making modelistic assumptions concerning the structure of the interphasial or "double-layer" region. This is done, for example, in the Grahame-Soderberg analysis of electrocapillary or differential capacitance data. 34 (A description of the structure of the electrical double layer is outlined in the next subsection.) A very clever analysis scheme which nonetheless manages to avoid all but a few modelistic assumptions in extracting specifically adsorbed surface excesses from electrocapillary data has been formulated independently by Hurwitz<sup>35</sup> and by Parsons and Dutkiewicz.<sup>36</sup> The Hurwitz-Parsons method forms the basis for most of the adsorption studies reported in Chapter III.

A final problem is that directly measured values of the interfacial tension are largely inaccessible at solid electrodes.

(However, see reference 37). A thermodynamic parameter which is readily measurable at a solid electrode-solution interface is the differential capacitance C. The interfacial tension is related to the differential capacitance via Equation 1.7:

$$\gamma = \iint cd^2E + K_1 + K_2$$
 (1.7)

where  $K_1$  and  $K_2$  are integration constants. These constants are the absolute electrode charge and the absolute surface tension at a known potential. Another important equation is

$$\sigma^{m} = \int CdE + K_{1}$$
 (1.8)

The difficulty in using Equations 1.1 through 1.8 to study adsorption and double-layer properties at solid electrodes is that the integration constants needed to evaluate Equation 1.7 are in many circumstances unavailable from experiments. This problem can be circumvented in certain cases by using analyses which require only relative values of surface tension. One of the main virtues of the Hurwitz-Parsons method is that arbitrary values of K<sub>1</sub> and K<sub>2</sub> can be used in carrying out an analysis. Basically this is a consequence of fixing certain aspects of the diffuse double-layer structure by maintaining a constant solution ionic strength. This is explained further in Chapter III.

Once surface concentration or excess data have been gathered these are generally fitted to an adsorption isotherm. The ultimate goal is to find an "equation of state" which interrelates the electrical variable, the surface concentration  $\Gamma$  of a given substance and its bulk solution activity. From a more practical point of view adsorption isotherms are useful for systematizing and comparing large amounts of data. One of the best known is the Frumkin isotherm:

$$(C_b/C_o)\exp(-\Delta G_a^O/RT)=(\Gamma_g/\Gamma_o)[\theta/(1-\theta)]\exp(-g\theta)$$
 (1.9)

where  $\Delta G_a^0$  is the standard free energy of adsorption,  $C_b$  is the bulk concentration of the adsorbing substance,  $\Gamma_g$  is the surface concentration at saturation,  $\theta$  is the fractional surface coverage which equals  $\Gamma^{'}/\Gamma_g$ , g is the interaction parameter and  $C_0$  and  $\Gamma_0$  are the standard states in bulk solution and at the surface. The standard states are usually taken to be 1 mole liter<sup>-1</sup> and 1 molecule cm<sup>-2</sup>, respectively. The so-called Langmuir term  $[\theta/(1-\theta)]$  takes account of the progressive loss of adsorption sites as the coverage increases, while the Frumkin g parameter supposedly reflects lateral interactions between adsorbed molecules. The value of  $\Delta G_a$  in the limit of zero coverage can be found from the intercept of a plot of  $\{\ln C_b - \ln[\theta/(1-\theta)]\}$  against  $\theta$ . The slope of this plot yields g.

### 2. A Model of the Double Layer

A description of the structure of the electrical double layer which is generally regarded as being approximately correct is the

Gouy-Chapman-Stern (GCS) model as modified by Grahame. This description is accepted largely on the basis of Grahame's experimental work which showed that the model can rationalize a sizable amount of capacitance and surface-tension data in a manner consistent with thermodynamic requirements.

The basic premise of the GCS model is that the solution side of the double layer consists of two regions: an inner layer of solvent molecules in contact with the metal electrode and a diffuse layer of ions under the influence of the electrical field generated by a certain charge density on the electrode surface. The electrode is taken to be a perfectly conducting metal such that all of its excess charge resides exactly at the surface. (The possible shortcomings of this last approximation have been examined recently by Goodisman, et al. 39) A sketch of a GCS-type double layer is shown in Figure 1.1. The dividing line between the inner and diffuse layers is the so-called outer Helmholtz plane (o.H.p.) which corresponds to the plane of closest approach of nonspecifically adsorbed ions. Grahame's modification was to allow for penetration of the inner layer by adsorbing ions, i.e. specific ionic adsorption.

One consequence of the GCS description is that the double layer can be represented as a pair of capacitors. Thus, differential capacitance measurements may be expected to supply qualitative information concerning the structure of the double layer. Since the structure of the inner layer is unaffected by changes in the bulk electrolyte concentration (provided that specific adsorption is absent) its capacitance is taken to be independent of ionic strength. To a

first approximation it also is expected to be independent of electrode potential and charge. (Commonly, however, significant variations of the inner-layer capacitance with E and om are observed). On the other hand, the diffuse-layer capacitance varies systematically with both the electrolyte concentration and the electrode charge. The smallest values are expected in dilute solutions under conditions of little or Since the diffuse-layer and inner-layer no electrode charge. capacitances are arranged in series the total (measured) interfacial capacitance is given by their reciprocal sum, with the smaller of the two providing the dominant contribution. As a consequence, in dilute solutions a distinct minimum attributable to the diffuse-layer component is generally observed in the capacitance-potential curve. The minimum appears in the vicinity of the potential of zero charge. (pzc). Capacitance measurements therefore provide a convenient route to the absolute charge on the electrode surface. This information enables equations 1.1 through 1.8 to be used to the fullest extent since one now has the integration constant K, of Equations 7 and 8.

This method is unambiguous when applied to homogeneous electrode surfaces (e.g., liquids or single crystals) in contact with nonspecifically adsorbing electrolytes. The situation is more complicated ("hopeless" with the polycrystalline surfaces employed here. Such surfaces are comprised of arrays of different crystallites, each with its own inner- and diffuse-layer properties. Here the potential of the capacitance minimum corresponds fairly closely to the potential of zero charge of the least densely packed single crystal facet, rather than to the overall zero charge potential of the polycrystalline

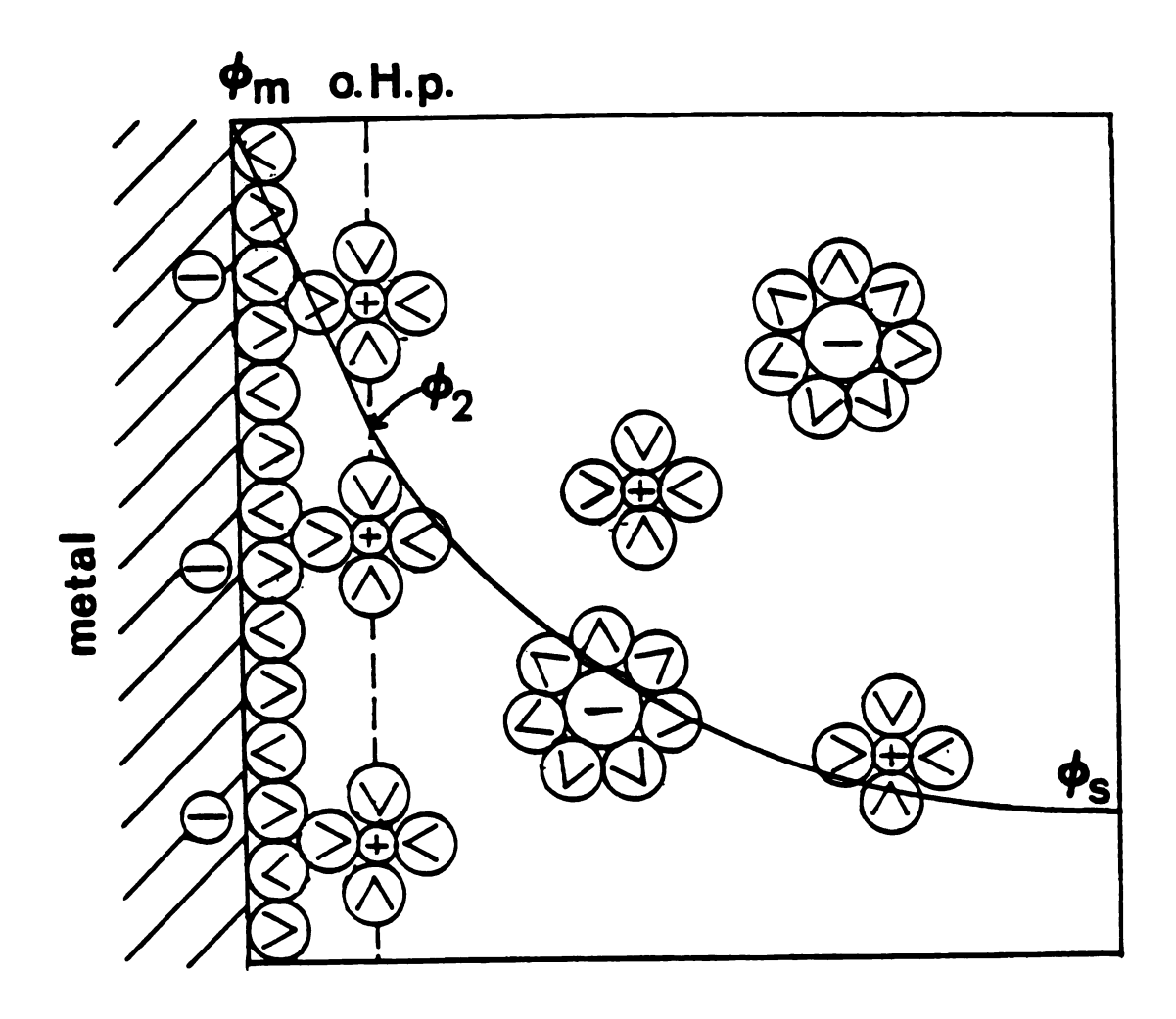


Figure 1.1 Model of the interface between an electrode and an electrolyte solution showing the decay of potential from the metal surface  $(\phi_m)$  to the outer Helmholtz plane  $(\phi_2)$  to the bulk electrolyte solution  $(\phi_s)$ .

surface. 44 (The latter in fact no longer possesses a unique value, being instead a complex function of the solution ionic strength). 42

At silver the crystallographic anisotropy of the potential of zero charge is sufficiently large (circa 300 mV)<sup>44</sup> that capacitance measurements are of limited value in establishing overall zero charge potentials. On the other hand, for "white metals" such as lead, the potential of the capacitance minimum may well correspond to within 50 mV of the true overall pzc. 1

The mathematical formulation of the GCS theory is of interest since it allows the average potential difference between the bulk solution and the outer Helmholtz plane (and all points in between) to be estimated. These estimates in turn are valuable for electrode kinetics studies, since they can be used to calculate the electrostatic work of transporting a reactant from the bulk solution to a reaction site in the diffuse layer. A detailed description of such work corrections is given later. Suffice to say that an accurate knowledge of the magnitude of electrostatic work terms is essential for interpreting electrochemical kinetics measurements (Sections IV D).

The dependence of the potential drop,  $\phi_2$ , from the o.H.p. to the bulk solution upon the electrolyte concentration  $C_b$  and the electrode charge is given by:  $^{33}$ 

$$\phi_2 = \frac{2kT}{Ze} \sinh^{-1} \left[\sigma^{m}/(8RT \epsilon \epsilon_0 C_b)^{1/2}\right]$$
 (1.10)

where Z is the charge number of the ions in a charge symmetric electrolyte, e is the electronic charge, k is Boltzmann's constant, R is the gas law constant,  $\epsilon$  is the dielectric constant of the medium and  $\epsilon_0$  is the permittivity of free space. Evidently the absolute magnitude of  $\phi_2$  is smallest when  $\sigma^m$  is small and the electrolyte concentration is large. In order to minimize work corrections such conditions are often intentionally chosen in electrode kinetics studies. (Note the parallel between  $\phi_2$  values and diffuse-layer capacitances with regard to the influences of  $C_b$  and  $\sigma^m$  on the magnitude of each).

A modification to Equation 1.10 is needed if specific adsorption occurs. Since additional charge F  $\Gamma$  will be accumulated on the electrode side of the interface in the form of adsorbed ions, we must rewrite Equation 1.10 as:

$$\phi_2 = \frac{2kT}{Ze} \sinh^{-1}[(\sigma^m + F\Gamma)]/(8RT \varepsilon \varepsilon_0 C_b)^{1/2}] \qquad (1.11)$$

In calculating  $\phi_2$  values from interfacial compositional data via Equation 1.11 one must be fairly careful since the presence of adsorbed ionic charge generally will produce compensating changes in the electrode metal charge. An important implication of Equation 1.11 is that specific adsorption, by inducing variations in  $\phi_2$ , can be expected to influence the kinetics of electrode processes.

In contrast to the diffuse layer potential, the potential drop across the inner layer is not easily calculable. Nor is it amenable to experimental investigation. What can be said is that it likely does

not change with alterations in electrode charge at a fixed electrode potential or with changes in electrolyte concentration.<sup>38</sup>

# C. <u>Electrochemical Kinetics</u>

In Chapter IV the kinetics of several reactions of the type

$$ox + e^{-}$$
 (electrode) + red (1.12)

are discussed. The intent here is to outline a largely phenomenological view of electrochemical kinetics. 46 A description of the microscopic quantum representation of reactions such as Equation 1.12 is delayed until the next section.

The rates of electrochemical reactions are most often determined, as might be expected, by measuring currents. (All of the kinetics data reported in this dissertation were determined by measuring currents). The current which flows as a consequence of a reaction such as 1.12 is governed by two factors: the kinetics of electron transfer and the rate of transport of the reactant from the bulk solution to the surface. As long as the electron transfer rate is comparable to or slower than the mass transport rate we can separate the two, since the latter is independently calculable. Many electrochemical analysis techniques are specifically designed to maximize the rate of mass transport in order to facilitate the rate separation and allow fast electron-transfer reactions to be studied. Once a "mass transport corrected" rate (i.e. current) is obtained it can be directly translated into a rate constant, provided that the

reaction follows kinetics which are first order with respect to the reactant in solution. This is the case for the reactions studied here.

The relation between the current i and the electron-transfer rate constant k is:

$$k = i/nFC_{bA}$$
 (1.13)

where n is the number of electrons transferred, F is the Faraday, C<sub>b</sub> is the bulk concentration of the reactant in mole cm<sup>-3</sup> and A is the electrode area in cm<sup>2</sup>. The rate constant obtained from Equation 1.13 has the unusual units of cm s<sup>-1</sup>, reflecting the fact that a solute in a three-dimensional solution is reacting at a two-dimensional surface.

One factor that can complicate rate measurements is the occurrence of a significant back reaction (red going to ox). In this case the result from Equation 1.13 must be adjusted in order to obtain the rate constant for the forward (reduction) reaction alone. In the present study this problem was avoided in two ways. First, some reactions were monitored under conditions sufficiently removed from equilibrium that the reverse reaction occurred to a negligible extent in comparison to the forward process. For other reactions, notably reductions of chromium(III) ammine complexes, electron transfer is followed by a very rapid aquation of the product, rendering a direct back reaction impossible. Reactions of this type are said to be chemically irreversible. (Of course, one must check that the aquation product itself is not readily oxidizable, lest errors result from this process).

An essentially universal feature of rate constants for simple electrochemical reactions is that they respond to the electrode potential E in the manner indicated by Equations 1.14 and 1.15:

$$k_f = k^8 \exp[-\alpha F(E-E^f)/RT] \qquad (1.14)$$

$$k_h = k^8 \exp[(1-\alpha)(F)(E-E^f)/RT]$$
 (1.15)

The parameters in the equations are the forward (reduction) and backward (oxidation) rate constants  $k_f$  and  $k_b$ , respectively, the transfer coefficient , the electrode potential E, and the standard rate constant  $k_g$  which is defined as the value of k at the formal potential  $E^f$ . The transfer coefficient can be viewed as an electrochemical analog of the Bronstead coefficient and similar parameters which relate reactivity to thermodynamic driving force. <sup>46</sup> The value of  $\alpha$  is typically close to 0.5.

For chemically irreversible reactions, measurements of formal potentials, and necessarily k<sup>8</sup> values, are often precluded.

Nevertheless, the rate-potential relationship can still be expressed by noting how the value of k is related to the rate constant at some arbitrary fixed potential E', as in Equation 1.16:

$$k = k^{E'} \exp[-\alpha F(E-E')/RT]$$
 (1.16)

All of the rate constants discussed thus far can be termed "apparent rate constants." What is meant by this is that the measured

k values reflect not only the intrinsic reactivity of the reactant, the thermodynamic driving force, and the degree of coupling between the reactant and the electrode, but also the work required to bring the reactant to a reaction site close to the electrode surface and to transport the product back into the bulk solution. It is desirable to separate out these last factors in order to gain some idea of the "true" reactivity of a molecule at an electrode.

While there are numerous factors that might contribute to work terms for electrode reactions, electrostatic interactions between a charged electrode surface and charged reactant and product molecules definitely are known to be important. For outer-sphere reactions, defined here as reactions taking place in the diffuse double layer rather than in the inner layer, the Frumkin equation can be used to estimate the magnitude of nonspecific electrostatic effects on rate constants. According to Frumkin 47

$$\ln k = \ln k_{corr} - (1/RT)[(2-n\alpha_{corr}) F\phi_r] \qquad (1.16)$$

where

$$\alpha_{corr} = [-Z(d\phi_r/dE)]/[1-(d\phi_r/dE)]$$
 (1.17)

The parameters in Equations 1.16 and 1.17 are the apparent rate constant k, the work-corrected rate constant  $k_{\rm corr}$ , the work-corrected transfer coefficient  $\alpha_{\rm corr}$ , the reactant charge Z, the diffuse-layer

potential  $\phi_{\mathbf{r}}$  at the reaction site, and the number of electrons, n, which are transferred. In the absence of detailed information  $\phi_{\mathbf{r}}$  is often assumed to equal  $\phi_{\mathbf{2}}$ . Additional terms are sometimes added to Equation 1.16 to take into account supposed specific electrostatic interactions ("discreteness-of-charge effects").  $^{48,49}$ 

Equation 1.16 represents a special case of a more widely applicable formulation describing the general influence of work terms on electrode reactions. 31 This expression can be written as

$$\ln k = \ln k_{corr} - (1/RT)[n\alpha_{corr}(W_s - W_p) + W_p]$$
 (1.18)

where  $\alpha_{\rm corr}$  is specified by the potential dependence of the work terms. In Equation 1.18,  $W_{\rm p}$  is the work required to bring the reactant from the bulk solution to a reaction site, while  $W_{\rm g}$  is the work expended in bringing the product from the bulk solution to the same reaction site. The subscripts p and s stand for "precursor" and "successor" which are the labels given to the reactant and product, respectively, when they are located at the interfacial reaction site. The chief virtue of Equation 1.18 is that it provides a formalism for treating not only outer-sphere reactions but also reactions proceeding through a specifically adsorbed precursor or successor state.  $^{31}$ 

In addition to obtaining rate constants it is sometimes desirable to measure their temperature dependence (cf. Chapter IV D). Although the significance and validity of such measurements for homogeneous chemical reactions are well established, doubts have been expressed concerning the corresponding electrochemical measurements, 50 and

confusion persists even in the current literature. 51 One reason for such problems is that there are essentially an infinite number of ways of controlling the electrical variable as the temperature is varied. Interestingly, Randles pointed out over thirty years ago that there is at least one approach which yields activation parameters of clear significance. 52 This approach is to measure the temperature dependence of the rate constant at the formal potential (or at a fixed overpotential, E-E<sup>f</sup>) at each temperature. The kinetics parameters obtained in this way have been labeled "real" activation parameters. 53,54 Clearly this approach is limited to chemically reversible reactions and to chemically irreversible reactions for which the temperature coefficient of the formal potential can be reliably estimated. The significance of real activation parameters has been eruditely discussed by Weaver who concluded that these correspond to the enthalpic and entropic reaction barriers which would be observed under conditions of zero (or constant, if  $E-E^{f}\neq 0$ ) enthalpy and entropy driving forces, respectively. 53,54 In the context of Marcus' treatment of electron transfer, real activation parameters correspond to "intrinsic" activation enthalpies and entropies. 13

A second approach is to measure rate constants at a fixed metal-solution Galvani potential  $\phi^m$  as the temperature is varied. 54 The obvious difficulty with this approach is that the potential difference across a single electrochemical interface is a thermodynamically inaccessible quantity. Furthermore, as noted in Section B it is not amenable to calculation. Nevertheless, this approach turns out to be feasible because the quantity  $\phi^m/dT$  in all likelihood can be

arranged to be essentially zero by using a nonisothermal cell configuration involving minimal thermal liquid junction potentials. 55

In the nonisothermal cell the temperature of the reference comparent is held constant while the temperature of the working compartment is varied. 55

The temperature coefficients derived from rate measurements at constant Galvani potential have been labeled "ideal" activation parameters. 53,54

The significance of ideal activation enthalpies and entropies is discussed in reference 54 where it is shown that these represent, for redox reactions, the actual enthalpic and entropic barriers to charge transfer for a single reacting ion.

In most cases the ideal parameters differ from the corresponding real parameters since the reacting ion experiences net thermodynamic entropy and enthalpy driving forces even when the free energy driving force (E-E<sup>f</sup>) is zero.<sup>53</sup> The origin of such thermodynamic asymmetry can be traced to the inherent chemical asymmetry of electrode reactions. The connections between the two types of activation parameters<sup>53</sup> are summarized in Equations 1.19 and 1.20:

$$\Delta H_{ideal}^* = \Delta H_{real}^* + \alpha T S_{rc}^0$$
 (1.19)

$$\Delta S_{ideal}^{*} = \Delta S_{real}^{*} + \alpha \Delta S_{rc}^{0}$$
 (1.20)

where  $\Delta S_{rc}^{o}$  is the thermodynamic reaction entropy and is given by  $^{55}$ 

$$\Delta S_{rc}^{o} = (dE_f/dT)_{\phi m}$$
 (1.21)

# D. Electron Transfer Theory

Most of the theoretical work on electron-transfer kinetics has been directed towards understanding homogeneous, bimolecular reactions. 56-60 The key ideas however, can be transposed to electrochemical processes by formally treating the electrode as one of the reactants. The chief differences between homogeneous and electrochemical reactions are that the electrode, unlike solution reactants, need not be activated and the thermodynamic driving force can be continuously varied by altering the applied electrode potential.

Before considering the theories of outer-sphere electron transfer it may be useful to digress briefly in order to clarify some potentially confusing terminology. The terms "outer sphere" and "inner sphere" commonly refer to types of reaction mechanisms. 61 The former mechanism involves electron transfer between reactants which retain their coordination shells intact throughout the process. The analog of the coordination shell for an electrode surface is the solvent inner Therefore, an inner-sphere mechanism is one involving layer. penetration of the coordination layer of one reactant by the other, in other words "ligand bridging". Specific adsorption of the precursor complex is the equivalent of ligand bridging in an electrochemical environment. 73 On the other hand, the terms "inner shell" and "outer shell" refer to components of the Franck-Condon barrier to electron transfer. 13 These are metal-ligand bond adjustments (inner shell) and solvent reorganization (outer shell). Although the expressions "innersphere" and "outer-sphere" have also been used in this context, we prefer to employ the above terms to avoid confusion.

Outer-sphere electron transfer reactions are thought to proceed by the following sequence of steps: 9,17

$$M(L)_{x}^{m} + M(L)_{y}^{n} + M(L)_{x}^{m} \cdots M(L)_{y}^{n} + M(L)_{x}^{*m} \cdots M(L)_{y}^{*n} \xrightarrow{3}$$

$$M(L)_{x}^{*m+1} \cdots M(L)_{y}^{*n-1} \stackrel{4}{\rightarrow} M(L)_{x}^{m+1} \cdots M(L)_{y}^{n-1} \stackrel{5}{\rightarrow}$$

$$M(L)_{x}^{m+1} + M(L')_{y}^{n-1}$$
 (1.22)

The first step is the formation of a precursor state consisting of a pair of weakly interacting reactants in a bimolecular complex. Except in the case of diffusion-controlled reactions, precursor formation can be viewed as an equilibrium step. Step 5 is essentially the reverse of step 1, and exerts (via the work term W<sub>8</sub>) only a minor influence on the overall energetics. The crux of the electron transfer problem is contained in steps 2 through 4.

Although early in the development of electron-transfer theory Marcus demonstrated that the central problem could be treated fairly successfully via statistical mechanics, <sup>13,62</sup> it has since become evident that the detailed dynamics can best be understood in terms of the quantum mechanics of radiationless transitions. <sup>21,25</sup> In particular, the latter approach is able to rationalize various peculiarities associated with extreme exothermicity, <sup>63</sup> low

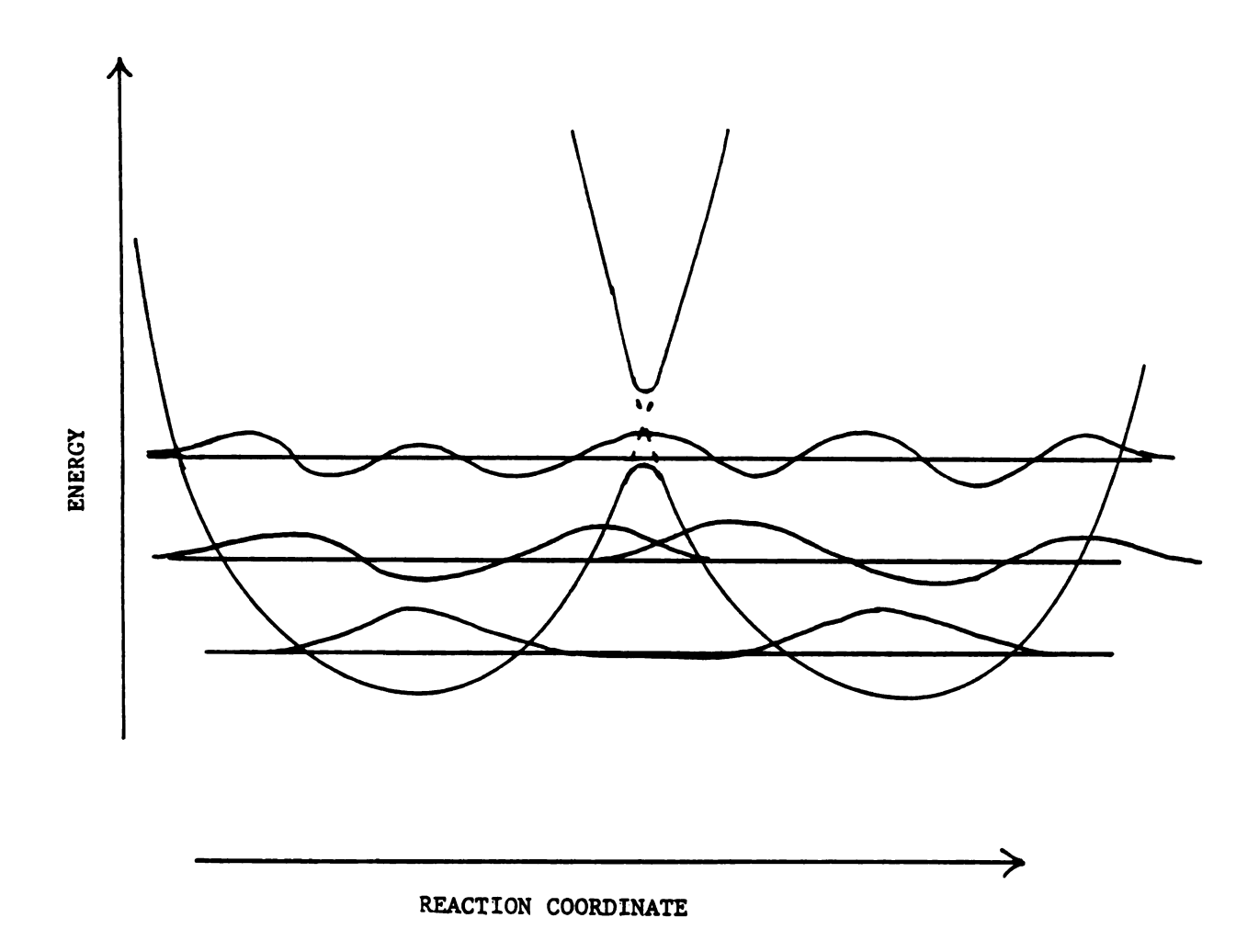


Figure 1.2. Schematic representation of overlapping vibrational states superimposed on classical potential energy surfaces. The magnitude of the splitting of potential energy curves in the intersection region corresponds to twice the value of the electronic coupling matrix element  $\mathbf{H}_{AB}$ .

temperatures<sup>58,64</sup> and isotopic substitution,<sup>65,66</sup> as well as account for rate behavior under more normal conditions.

The basic idea of the quantum mechanical treatment is that charge transfer constitutes a radiationless transition between weakly coupled electronic states, namely, the oxidized and reduced states of each reactant. In the parlance of theoretical chemistry the precursor states of reaction 1.22 are said to be "vibronically coupled." What is meant is that the actual radiationless transition (electron transfer, step 3) is greatly facilitated by prior vibrational excitation of the metal-ligand and intra-ligand bonds of the reactants together with solvent repolarization. [Strictly speaking, solvent repolarization evidently involves librational (restricted rotational) rather than vibrational motion]. 56b

Figure 1.2 is a schematic representation of selected vibrational states superimposed on classical reactant and product potential energy surfaces. According to the Franck-Condon principle, 67 "the probability of an electronically allowed transition is proportional to the absolute square of the overlap integral of the vibrational wavefunctions of the initial and final states." 68 The square of the overlap integral or "Franck-Condon factor" will be maximized in the intersection region of the classical potential energy surfaces. In this region the positions of the nuclei in a classical sense are identical in the initial and final excited vibrational states. Nevertheless, electronic transitions can also take place outside of the intersection region, albeit with less probability since the overlap of vibrational wavefunctions is diminished. 68 This yields the peculiar result that the "positions" of

the nuclei, as specified by the maxima in the vibrational wavefunctions, change in the course of the electron transfer. In the semi-classical theory of electron transfer (popularized by Sutin) this is referred to as "nuclear tunneling." An illuminating discussion of the Franck-Condon principle in connection with electronic transitions can be found in reference 68.

An additional requirement for a radiationless transition is that the initial and final vibronic states be isoenergetic, at least to the extent specified by the uncertainty principle. However, energy conservation for the inner-shell and solvent modes separately is not required. Evidently energy sharing between modes can occur, although as yet a thoroughly consistent theoretical description of this process is lacking. 96

The Franck-Condon principle indicates that electronic transitions will occur from a range of excited initial vibronic states centered around the classical intersection region. However, the transition probabilities are weighted not only by the vibrational overlap integrals but also by the Boltzmann factors describing the relative population of each vibrational level (both initial and final). 21,23 Typically, the Boltzmann factors will tend to favor transitions from vibrational states lying below the intersection region, and increasingly so as the temperature is lowered. In consequence, such "nuclear tunneling" becomes more important at lower temperatures. 23

If the actual electronic transition (step 3, Equation 1.22) is the slow process in the overall reaction scheme, the reaction is termed nonadiabatic and the rate constant is given by:

$$k = \int K_{p}(r) v_{el}(r) \Sigma F.C.(r) dr \qquad (1.23)$$

where  $K_p$  is the precursor formation constant and incorporates work terms, steric factors, etc.,  $v_{e1}$  is the frequency of passage between activated reactant and product states, and  $\Sigma$  F.C. is the Boltzmann and Franck-Condon weighted sum of the transition probabilities between the initial and final states. Each of these factors depends on the reactant separation distance r. The frequency  $v_{e1}$  is determined chiefly by the square of the matrix element  $H_{AB}$  describing the degree of coupling between donor and acceptor electronic orbitals. In terms of classical potential energy surfaces  $2H_{AB}$  is represented as a "resonance splitting" of the diabatic reactant and product surfaces into upper and lower adiabatic surfaces (Figure 1.2). 15,57a

In the case of strong coupling of electronic orbitals,  $v_{\rm el}$  may become sufficiently large that vibrational activation becomes the slow step. In this circumstance the electron transfer reaction is described as "adiabatic". (The term evidently originates from the idea that the reaction system when strongly coupled will follow the lower adiabatic potential energy surface rather than one of the diabatic surfaces of Figure 1.2). Quantum-mechanical treatments of electron-transfer have tended to emphasize nonadiabatic rather than adiabatic reaction mechanisms because of calculational difficulties with the latter. One of these centers on the applicability of Boltzmann statistics given that the populations of the higher energy vibrational states will be rapidly and continuously depleted by rapid electron transfer. 17,24,60

Nevertheless, the rate constant for adiabatic electron transfer can be formulated to a good approximation as in Equation 1.23, except with a nuclear activation frequency  $v_n$  in place of  $v_{el}$ .

Although Equation 1.23 represents an adequate description of the overall rate process it is often convenient for computational purposes to formulate rate expressions somewhat differently. It is useful to imagine that reactions proceed by a classical transition state mechanism. 13,23 The pre-equilibrium formulation is retained. However, the reactants are assumed to surmount a fixed activation barrier and to decay to products at a frequency  $v_{\perp}$ . The activated state is defined as the unique nonequilibrium solvent and bond configuration for which reactant and product free energy curves intersect. This is equivalent to assuming a Franck-Condon factor of unity in the intersection region and zero elsewhere. Forbidden transitions are taken into account by introducing a nuclear tunneling correction  $\Gamma_n$ . 19,20,23 In essence this lowers the barrier from its classical value to a value representing the best compromise between the Boltzmann distribution terms and Franck-Condon factors. Additionally, an electron tunneling term  $\kappa_{el}$  is introduced to reflect the possibility that electron transfer may not occur every time a transition-state configuration is reached. If  $H_{AR}$  is known,  $\kappa_{el}$  evidently can be estimated with tolerable accuracy from the Landau-Zener theory. (An enlightening "mechanical" derivation of this theory in terms of timescales for traversing different portions of the classical potential energy surfaces is given by Kauzmann<sup>69</sup>).

According to the classical theory with quantum corrections, 23 the overall electron transfer rate constant is given by:

$$k = K_p \vee_n \Gamma_n \kappa_{el} \exp(-\Delta G^*/RT)$$
 (1.24)

where  $\Delta G^*$  is the activation free energy corresponding to the height of the classical Franck-Condon barrier. The primary virtue of the classical approach is that the most significant element, namely the Franck-Condon barrier, can be calculated in a straightforward manner.

According to Marcus,  $^{13}\Delta G^*$  is usefully divided into intrinsic and thermodynamic elements. The latter is determined largely by the energy gap between the wells of the reactant and product free energy curves. The former is calculated from the changes in metal-ligand and intraligand bond distances accompanying electron transfer and also from solvent dielectric properties. The detailed aspects of such calculations for reactions of transition metal complexes are described in Chapter VII.

Although Equation 1.24 is a somewhat artificial formulation which may well misrepresent the detailed dynamics of electron transfer reactions, nonetheless it provides a surprisingly accurate numerical description of the (theoretical) rate constant formulated in Equation 1.23.<sup>23</sup> Therefore the use of this semi-classical approach<sup>23</sup> (i.e. transition state theory plus quantum corrections) to calculate rate constants for comparison with experiment appears to be justified.

#### CHAPTER II

#### EXPERIMENTAL

### A. Materials

#### 1. Solvents

Formamide was purchased from Eastman. Sulfolane (tetramethylene sulfone) and N-methylformamide, both 99% pure, were purchased from Aldrich. The remaining nonaqueous solvents were either Aldrich "Gold Label" grade or Burdick and Jackson doubly-distilled materials. Containers of each solvent were opened and subsequently stored inside an inert atmosphere box. Each solvent was dried over activated 4% molecular seives. Although electrochemical experiments were performed outside of the box, the nonaqueous solutions were prepared and added to sealed electrochemical cells under inert atmosphere conditions.

Solvent preparation and purification efforts were considerably more involved for aqueous experiments. The chief reason for this is the sensitivity of surface electrochemistry work, e.g. electrode kinetics and double-layer capacitance measurements, to small amounts of both organic and inorganic impurities. In the laboratory at Michigan State, water was distilled twice from alkaline permanganate  $(0.01\underline{\text{M}}\text{ KOH}, 0.01\ \underline{\text{M}}\text{ KMnO}_{\Delta})$  to oxidize organic impurities and eliminate other nonvolatile

organic and inorganic contaminents. Remaining ionic impurities were eliminated by distillation through a quartz nonboiling still (Dida Sciences). At Purdue it was discovered, largely through the efforts of David Milner, that sufficiently pure water could not be obtained from the available feed water using these methods. However, it was found that water of surprisingly high purity could be obtained by circulating house distilled water through a Milli-Q Reagent Grade Water System (Millipore Corp.) equipped with a Twin-90 output particulate filter. A key to obtaining pure water is to avoid contact with Tygon or other plastic tubing. Water purity was monitored chiefly through capacitance and stripping voltammetry experiments at a hanging mercury drop electrode, the former being sensitive to organic impurities and the latter to heavy metals.

## 2. Electrolytes

Where possible, salts of reagent grade or better were used.

Otherwise, these were recrystallized two or three times from water and dried in a vacuum oven before use. Doubly distilled 70% HClO4 from G.F. Smith Chemical Co. was used without further purification.

Lanthanum perchlorate solutions were prepared by dissolving high purity La203 in HClO4. In nonaqueous experiments similar results were obtained with and without drying the supporting electrolyte in a vacuum oven immediately prior to solution preparation.

Certain experiments involved controlled formation of an underpotentially deposited monolayer of lead or thallium. This was achieved by rotating a disk electrode for several minutes in solutions that were submicromolar in lead or thallium ions (see Chapter III D). As such, it was absolutely essential that the concentrations of other reducible metal ions be maintained orders of magnitude below  $10^{-6} \text{M}$  in order to avoid also depositing these on the electrode surface. The presence of unwanted metal ions was signaled by extraneous peaks on stripping voltammograms. Satisfactory results were obtained only by using rigorously purified electrolytes, namely, triply recrystallized reagent grade NaClO<sub>4</sub> from G.F. Smith Chemical Co. or "ultra pure" NaF from Alfa Products. To avoid contamination, carefully cleaned glass (rather than metal) spatulas were used for transferring chemicals for solution preparation. Since silver readily adsorbs common impurities such as Cl<sup>-</sup>, Br<sup>-</sup> and I<sup>-</sup> to a much greater extent than either F<sup>-</sup> or ClO<sub>4</sub><sup>-</sup>, the same precautions were taken before attempting capacitance measurements at this surface in NaClO<sub>4</sub> or NaF solutions.

## 3. Metal Complexes

Samples of Os(NH<sub>3</sub>)<sub>5</sub>pyrazine·Cl<sub>3</sub>, Os(NH<sub>3</sub>)<sub>5</sub>pyridine·Cl<sub>3</sub>,
Os(NH<sub>3</sub>)<sub>5</sub>4,4'-bipyridine-H·(CF<sub>3</sub>SO<sub>3</sub>)<sub>4</sub>, Ru(NH<sub>3</sub>)<sub>5</sub>pyridine·(PF<sub>6</sub>)<sub>3</sub>,
Ru(NH<sub>3</sub>)<sub>5</sub>pyrazine·(PF<sub>6</sub>)<sub>3</sub> and Ru(NH<sub>3</sub>)<sub>6</sub>·(CF<sub>3</sub>COO)<sub>3</sub> were kindly supplied by
Dr. Peter Lay and Dr. Roy Magnuson. Samples of Ru(en)<sub>3</sub>·Br<sub>3</sub> and
Ru(NH<sub>3</sub>)<sub>2</sub>(bpy)<sub>2</sub>·(ClO<sub>4</sub>)<sub>2</sub> were provided by Dr. Gilbert Brown, while
Ru(NH<sub>3</sub>)<sub>4</sub> phen·(CF<sub>3</sub>COO)<sub>2</sub>·3H<sub>2</sub>O was supplied by Professor Larry Bennett
(phen=1,10-0-phenanthroline). Samples of Ru(bpy)<sub>3</sub>·Cl<sub>3</sub> and Ru(NH<sub>3</sub>)<sub>6</sub>·Cl<sub>3</sub>
were purchased from G.F. Smith Chemical Co. and Matthey-Bishop,
respectively. Ferrocene was purchased from Aldrich and
N-ferrocenemethylene-para-toluidine from the Alfred Bader Library of

Rare Chemicals. A surface-attached ferrocene derivative was prepared from ferrocene carboxaldehyde (Aldrich) as outlined in reference 70. Solutions of  $\operatorname{Eu}(\operatorname{H}_20)_3^{3+}$ ,  $\operatorname{Cr}(\operatorname{H}_20)_6^{3+}$ ,  $\operatorname{Cr}(\operatorname{H}_20)_5\operatorname{Cl}^{2+}$ ,  $\operatorname{Cr}(\operatorname{H}_20)_5\operatorname{Cl}^{2+}$ ,  $\operatorname{Cr}(\operatorname{H}_20)_5\operatorname{Cl}^{2+}$ ,  $\operatorname{Cr}(\operatorname{H}_20)_5\operatorname{Cl}^{2+}$ ,  $\operatorname{Cr}(\operatorname{H}_20)_5\operatorname{NCS}^{2+}$ ,  $\operatorname{Cr}(\operatorname{NH}_3)_5\operatorname{H}_2$ ,  $\operatorname{Cr}(\operatorname{NH}_3)_5\operatorname{H}_2$ ,  $\operatorname{Cr}(\operatorname{NH}_3)_5\operatorname{NCS}^{2+}$ 

## 4. Electrodes

Platinum flag, gold flag, glassy carbon disk and hanging mercury drop electrodes were all used in measuring formal potentials and reaction entropies. The choice of electrode was dictated by the formal potential of the complex and the region of ideal polarizability of the electrode material.

High purity silver disk electrodes (4 mm or 2.5 mm diameter) encased in teflon were used for most surface electrochemistry experiments. A specially designed silver disk electrode exhibiting minimal thermal conduction between the electrode surface and the stainless steel lead was employed in variable temperature kinetics experiments.

Careful attention was given to surface preparation in kinetics and capacitance experiments. The object was to insure that each

experiment was begun with a clean, smooth metal surface. To achieve this a silver electrode was first mechanically polished with 1.0 micron and then 0.3 micron alumina (Beuhler, Ltd.) on Beuhler Microcloth. A two-speed polishing wheel (Buehler 44-1502-160) was employed. After thorough rinsing with water the electrode was immersed in an electropolishing solution of 41 g  $1^{-1}$  NaCN, 44 g  $1^{-1}$  AgNO<sub>3</sub> and 38 g  $1^{-1}$  K<sub>2</sub>CO<sub>3</sub> and held at +0.2 V versus an SCE reference for two minutes.44 electropolishing step exerts a smoothing and cleaning effect by continuously dissolving and redepositing the cold-worked layer of silver which is formed by mechanical polishing. Electrochemical surface area measurements indicated that the true area of the electropolished silver typically was only about 1.2 times greater than the geometric area. 86 Although most contaminants are removed by electropolishing, some cyanide, possibly in the form of silver complexes, remains. 87 This was removed by rinsing the electrode, followed by soaking in  $2\underline{M}$  HC10<sub>4</sub> for fifteen minutes, further rinsing, and immersion under potentiostatic control (-0.7 V versus SCE) in 0.1M Naf. Once immersed the potential was switched to -1.7 V where hydrogen evolved on the silver surface. After one minute the potential was returned to -0.7 V. Hydrogen bubbles on the silver disk were removed by bubbling the solution with purified nitrogen. The hydrogen evolution and nitrogen bubbling steps were then repeated.

The importance of the overall electrochemical pretreatment is evident in comparative differential capacitance experiments. Electropolished surfaces yield capacitance-potential curves which are unchanged in repeated scans and exhibit sharp features in adsorbing

electrolytes. Capacitance-potential curves obtained with electrodes which are subjected to mechanical polishing and rinsing only, although resembling those for electropolished surfaces, lack detailed features. Also, the capacitance increases slightly with each successive potential scan, with a significant hysteresis between forward and reverse potential scans. The differences in behavior between the mechanically polished and electropolished electrodes can be attributed to the presence of surface contaminants at the former which apparently are gradually removed by repeated adsorption and desorption of the electrolyte.

For SERS-related work, electrodes were roughened by immersing in 0.1 M KCl at -140 mV, switching the potential to +210 mV until 20-40 mC cm<sup>-2</sup> of anodic charge had passed, and then stepping the potential back to -140 mV until an essentially equal amount of cathodic charge had passed. For the experiments reported in Section III A (anion adsorption) the roughened electrodes were soaked in 2 M HClO<sub>4</sub> for fifteen minutes to remove adsorbed chloride. Interestingly, electrochemical roughening alone was insufficient to clean mechanically polished electrodes as evidenced again by comparative capacitance studies with electrodes which had been electropolished prior to roughening.

The preparation of underpotentially deposited metal surfaces is described in Section III C.

## B. Apparatus

Two-compartment cells of various designs were used. The compartment in which the reference electrode was immersed was separated from the section containing the working and counter electrodes by two "fine" or "very fine" porosity glass frits (Corning, Inc.). For activation parameter and reaction entropy measurements a nonisothermal cell was employed in which the temperature of the working compartment was adjusted by circulating water through a surrounding jacket. A Braun Melsungen circulating thermostat was used for this purpose. Cells for rotating disk voltammetry held approximately 10 ml and were constructed such that the working compartment diameter was roughly three times greater than the diameter of the working electrode. A teflon collar was fitted to the top of each cell so that the solution could be isolated, at least partially, from the outside atmosphere. Cells for capacitance experiments held 30 to 50 ml and were equipped with a port for adding solutions during an experiment. The cells were constructed such that contact with the external atmosphere was possible only through an opening of circa 1/8" diameter in the top of each cell.

A platinum wire was used as a counter electrode in all experiments. In capacitance experiments the counter electrode was at least one hundred times larger in area than the working electrode, and at least three hundred times larger than the geometric area of roughened electrodes. This insures that the measured cell capacitance is essentially that of the working electrode alone.

Saturated calomel electrodes were employed as reference electrodes. In perchlorate electrolytes an SCE filled with NaCl rather KCl was used in order to avoid spurious liquid junction potentials which might arise from precipitation of KClO<sub>4</sub> in the reference electrode frit. The potential of each reference electrode was routinely checked against the potential of a master SCE filled with KCl. Due to the

differing mobilities of Na<sup>+</sup> and Cl<sup>-</sup> in water a liquid junction potential which varies significantly with the ionic strength of the experimental solution is introduced between this solution and the reference electrode. Therefore, potentials measured against the NaSCE were corrected to equal those which would be obtained versus the KSCE, since the KCl filled reference more nearly maintains a constant electrode-solution potential difference as the electrolyte composition is varied.

In nonaqueous work the reference compartment was filled with an aqueous solution. The thermal junction between the working and reference compartments was filled with the nonaqueous solvent in order to minimize contamination of the working compartment by water. In reference 55, arguments were outlined which supported the notion that thermal liquid junction potentials are negligible in non-isothermal cells when the reference compartment and thermal junction are filled with 3 M KCl. Although there are no reasons a priori to expect negligible thermal liquid junction potentials when low ionic strength nonaqueous solvents are used in place of aqueous 3 M KCl, Saeed Sahami has verified that this is indeed the case for a number of solvents.

Since oxygen is potentially electroactive, all solutions were deoxygenated by bubbling with nitrogen or argon and then maintained under a stream of either gas. Argon was preferred when ruthenium complexes were examined since ruthenium (II) is capable of binding dinitrogen. Before being introduced into a cell, nitrogen or argon was passed through a column packed with BASF R3-11 catalyst (Chemical Dynamics Corp., Plainfield, NJ) heated to 140°C in order to remove

residual traces of oxygen and then saturated by bubbling through the appropriate solvent.

# C. Electrochemical Measurements

## 1. Differential Capacitance

Initially double layer capacitance measurements were made by using a null-balance method. A small amplitude 1000 Hz AC signal was applied to the cell. The output was then matched against an external resistance and capacitance through a Wein bridge configuration. The measured cell resistance and capacitance were assumed to correspond to the resistance of the solution and the double layer capacitance of the working electrode. This method is sufficiently tedious and time consuming that only a limited number of data could be gathered in each set of measurements. (Typically, one capacitance measurement was made over each 50 mV interval of electrode potential). Very low signal-to-noise ratios were encountered in dilute solutions, thereby limiting the applicability of the technique to solutions which were 10 mm or greater in electrolyte concentration. Due to instability of the oscillator, measurements below 500 Hz were not feasible.

In later experiments a phase-detection technique was employed. 90 An AC signal (typically 4 mV peak-to-peak, 100 Hz) from a signal generator contained in a PAR 5204 lock-in analyzer was applied to the cell. At the same time the electrode potential was slowly varied using a PAR 175 Universal Programmer and a PAR 173 potentiostat. The output current from the cell was then resolved into quadrature and in-phase

currents,  $i_Q$  and  $i_I$ , respectively. These were simultaneously recorded versus the electrode potential by using a pair of Houston 2000 Omnigraphic X-Y recorders. The cell capacitance C was calculated from

$$1/\omega = (i_1^2 + i_0^2)/i_0$$
 (2.1)

where  $\omega$  is the AC frequency (radian s<sup>-1</sup>) and V is the root-mean-square potential of the AC signal. The cell resistance R was calculated from

$$R = Vi_{1}/(i_{1}^{2} + i_{0}^{2})$$
 (2.2)

At very low frequencies C is essentially proportional to  $i_Q$  thus simplifying the analysis.

For adsorption studies at silver, scan rates of 5 -10 mV s<sup>-1</sup> were sufficient to insure that identical capacitance-potential curves were obtained in forward and reverse scans in most electrolytes. However, in thiocyanate solutions scan rates of 2 mV s<sup>-1</sup> or less were required.

# 2. Electrode Kinetics

A major goal of the electrode kinetics studies at underpotentially deposited electrodes was to obtain electron-transfer rate data at surfaces having a fixed metal composition over a range of potentials beyond the UPD region. Conventional kinetics measurement techniques such as rotating disk voltammetry yield changes in surface composition as the electrode potential is changed, with significant bulk deposition of metal atoms occurring during excursions to potentials

negative of the UPD region. However this problem can be avoided by employing normal pulse polarography. By selecting an initial potential just positive of the bulk deposition potential for lead or thallium, changes in surface composition due to additional metal deposition can occur only during the 50 msec pulses to more negative potentials. In dilute solutions of  ${\bf PbF_2}$  or  ${\bf T1Cl0_4}$ , metal deposition during the pulses proved to be negligible. The pulse polarography technique produced satisfactory results provided that the electrode was rotated at a rate between 600 and 1500 RPM. Moderate rotation replenishes the reactant in the diffusion layer during the 2 or 5 second interval between pulses. 91 In comparative kinetics studies with other solid electrodes for which cyclic voltammetry, rotating disk voltammetry, and pulse polarography could all be used, rate constants for electron-transfer reactions determined by the three methods agreed within experimental error. 92 Current-potential curves were obtained using a PAR 174A polarographic analyzer (Princeton applied Research Corp.), a Hewlett-Packard 7045A X-Y recorder and a Pine Instrument ASR2 electrode rotator. Rate constant-potential data were extracted from the curves by using the Oldham-Parry analysis. 93

In a few cases rate constants were determined from irreversible cyclic voltammetry waves by using the analysis devised by Galus.<sup>94</sup>

Potential sweeps at rates of 50 to 500 mV s<sup>-1</sup> were generated with a PAR 174 or 174A polarographic analyzer.

## 3. Formal Potentials

Formal potentials were estimated by averaging the oxidation and reduction peak potentials of reversible or quasi-reversible (peak separations of 60 to 100 mV) cyclic voltammograms. Typically, scan rates of 100 mVs<sup>-1</sup> were used. Strictly speaking, the half-wave potential obtained from a reversible cyclic voltammogram will differ slightly from the formal potential if the diffusion coefficients of the oxidized and reduced halves of the redox couple are inequivalent. Since this complication yields errors of perhaps 2 or 3 mV the distinction between half-wave and formal potentials was ignored.

Surface formal potentials  $E_a^f$  for adsorbed osmium redox couples were obtained from fast cyclic voltammetry measurements in dilute solutions (circa 50  $\underline{M}$ ) of the reactant of interest. The strategy here was to "outrun" the diffusion of the osmium complex to the surface. Current due to a solution species increases with the square root of the potential scan rate, while current due to an adsorbed reactant increases linearly. Scan rates of 10 to 200 V s<sup>-1</sup> were sufficient to generate cyclic voltammograms which reflected the electrochemistry of the adsorbed, rather than solution, reactant. Measurements were performed using a PAR 175 potentiostat and a PAR 173 potential programmer capable of providing sweep rates of 1000 V s<sup>-1</sup>. At high scan rates voltammograms are distorted by the iR drop associated with the solution resistance. Complications due to iR drop can be fairly well eliminated by using an adjustable feedback circuit built into the PAR 173. Voltammograms were recorded on a Nicolet Explorer digital storage oscilloscope. stored data were then transmitted to a conventional X-Y recorder.

#### CHAPTER III

# DOUBLE-LAYER STRUCTURE AND IONIC ADSORPTION AT SOLID METAL ELECTRODE-AQUEOUS INTERFACES

A. Specific Adsorption of Halide and Pseudohalide Ions at

Electrochemically Roughened Versus Smooth Silver-Aqueous

Interfaces

[Originally published in Surface Science, 125, 429 (1983)]

## 1. Introduction

The discovery of Surface-Enhanced Raman Scattering (SERS) from adsorbates at silver electrodes that have been roughened by means of a prior "oxidation-reduction cycle" (ORC)<sup>8</sup> has generated intense interest in characterizing the nature of the physical phenomena involved. The effect shows promise of providing a valuable in situ spectroscopic tool for elucidating the microscopic structure of metal-electrolyte interfaces. A central question to be addressed for this purpose is the relationship between the nature and intensity of the SERS signals and the structure and composition of the metal-electrolyte interfaces, especially the surface concentration of the adsorbate acting as the Raman scatterer. However, little progress on this matter has been made to date; the required studies of the interfacial composition under conditions where SERS are observed have largely been absent.

Halide and pseudohalide anions form an especially interesting series of model adsorbates for fundamental SERS studies in view of their simple structure and tendency to adsorb strongly at a number of solid metals, including the silver-aqueous interface which has been utilized in most Raman investigations so far. Most importantly, the anionic surface concentrations can be determined quantitatively from measurements of the differential double-layer capacitance  $C_{d}$  against the electrode potential E for varying bulk concentrations of the adsorbing anions, 86,95 using the so-called "Hurwitz-Parsons" analysis. 35,36 Silver is an especially tractable metal for this purpose since surprisingly reproducible values of Cd that are largely independent of the applied a.c. frequency can be obtained at smooth electropolished surfaces. 44,86,95 Nevertheless, this simple vet powerful method for extracting the surface compositional data needed for the quantitative interpretation of SERS has received scant attention by practitioners in this area.

We have recently obtained specific adsorption data for chloride, bromide, iodide, azide, and thiocyanate at a polycrystalline silver-aqueous interface from C<sub>d</sub>-E data and also using a "kinetic probe" technique. Although these anions are very strongly adsorbed, especially at more positive potentials, these surfaces exhibit no detectable Raman scattering. However, mild ORC roughening, corresponding to the redeposition of only a few silver layers, can yield surfaces displaying measurable Raman scattering for these and other inorganic adsorbates. 96,97 It is therefore of interest to explore the influence of electrochemical roughening on the double-layer structure

of the silver-aqueous interface, in particular on the surface concentration of such structurally simple adsorbates. Fleischmann et al. have recently noted the effect of extensive electrochemical roughening upon the capacitance of a silver electrode in chloride media, although no thermodynamic analysis of the data was undertaken.<sup>98</sup>

We report here specific adsorption measurements for chloride, bromide, iodide, azide, and thiocyanate obtained from C<sub>d</sub>-E data at electrochemically roughened silver electrodes. These are compared with corresponding data gathered at a smooth polycrystalline surface. The results indicate that the surface roughening procedure that is crucial to SERS has a relatively small influence on the average surface concentration of these anions, although noticeable changes occur in the morphology of the capacitance-potential curves. The data enable quantitative comparisons to be made between the appearance of SERS and the average surface concentration of the Raman scatters.

## 2. Results and Discussion

## a. Determination of Roughness Factors for Silver Surfaces

Figure 3.1 shows three representative  $C_d$ -E curves obtained for polycrystalline silver in contact with 0.5  $\underline{M}$  NaClO<sub>4</sub>. This medium was chosen as the "inert" background electrolyte for the present studies in view of the relatively weak adsorption of perchlorate. Although we previously used 0.5  $\underline{M}$  NaF for this purpose, <sup>86</sup> fluoride anions appear to be more strongly adsorbed than perchlorate on silver, <sup>99</sup> so that 0.5  $\underline{M}$  NaClO<sub>4</sub> is preferred here. The lowest curve in Figure 3.1 was obtained

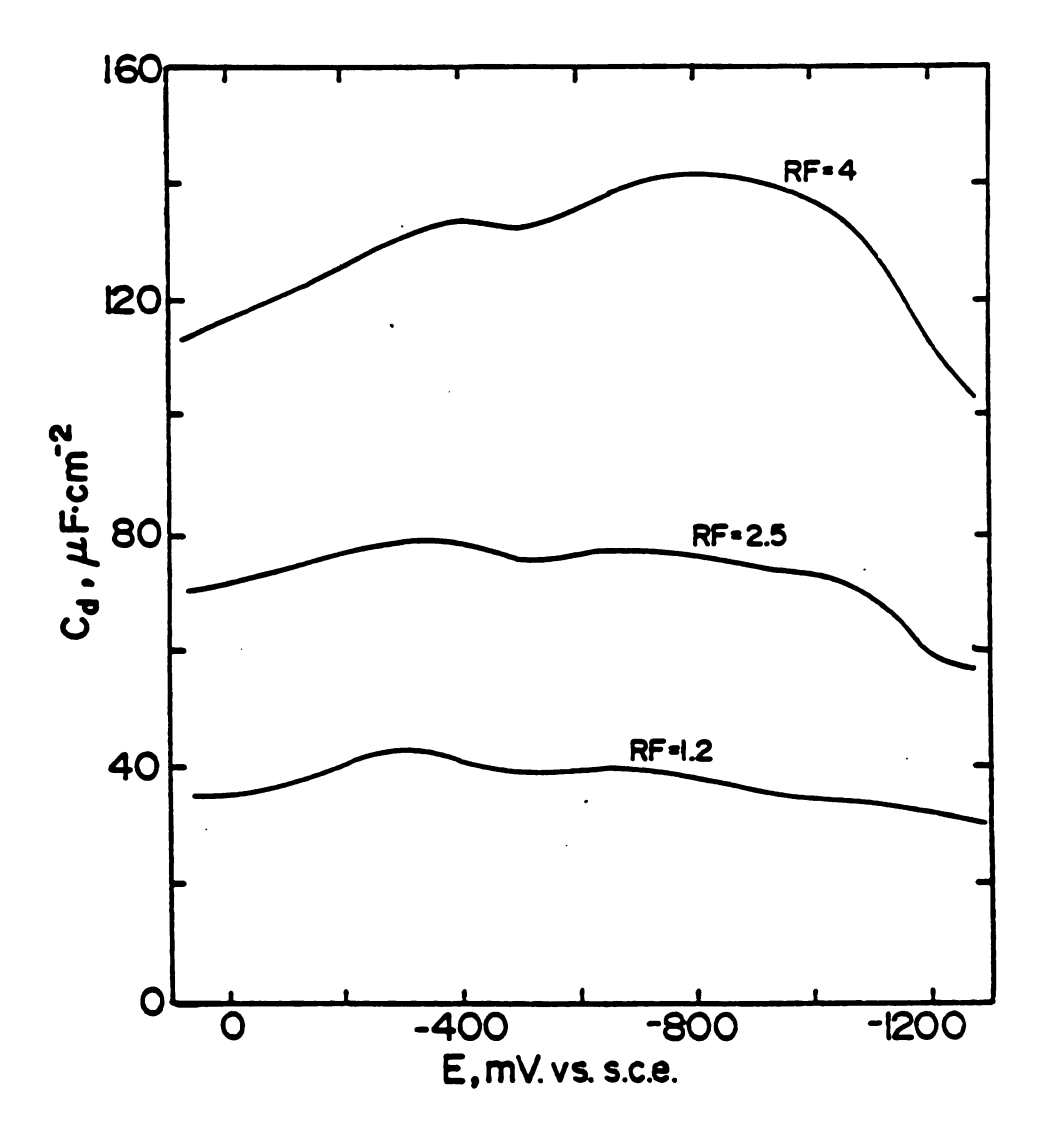


Figure 3.1. Differential capacitance of polycrystalline silver in  $0.5~\underline{\text{M}}~\text{NaClO}_4$  plotted against electrode potential for various roughness factors (RF) indicated.

after electropolishing the electrode in a cyanide medium,  $^{86}$  whereas the upper two curves were measured following oxidation-reduction cycles in 0.1 M KCl as described above. Both these ORCs involved passing greater amounts of anodic charge, (ca. 50 and 120 mC cm<sup>-2</sup> for the middle and upper curves, respectively), than are normally required in order to induce SERS for adsorbed anions such as chloride. Nevertheless, no marked changes in the shape of the  $C_d$ -E curves are seen, the capacitance increasing monotonically with increasing roughness brought about by passing larger quantities of anodic charge,  $\sigma_{ORC}$ , during the ORC. This suggests that approximate estimates of the roughness factor RF (i.e., the ratio of the actual to geometric surface area) can be obtained simply from the ratio of measured capacitances at a given electrode potential with respect to that for a smooth surface.

This method for determining RF was checked against an alternative approach which involved measuring the faradaic charge consumed for the deposition or redissolution of a monolayer of underpotential deposited (UPD) lead.  $^{3}$ ,  $^{100}$ ,  $^{101}$  The procedure entailed measuring the charge under the cathodic-anodic cyclic voltammetric peaks obtained in the potential region -300 to -400 mV for a solution containing 5 mM Pb<sup>2+</sup>. Essentially symmetrical cyclic voltammograms were obtained using slow sweep rates (ca. 5 mV s<sup>-1</sup>. The roughness factor was calculated by assuming that the charge required for deposition (or redissolution) of a monolayer of lead atoms on a perfectly smooth silver surface equals 310  $\mu$ C cm<sup>-2</sup>. (In performing this calculation the contribution due to double layer charging was neglected. Since the capacitance of a smooth silver electrode is about 35  $\mu$ F cm<sup>-2</sup> over the 250 mV interval where

underpotential deposition occurs, double layer charging would require about 9  $\mu$ C cm<sup>-2</sup>. This yields an error of perhaps 3% in the estimates of electrode area). Three voltammetric peaks could be resolved, at about -300, -320, and -350 mV. Roughening the electrode produced little change in the appearance of the cyclic voltammograms besides enhancing the current. This together with the similar form of the C<sub>d</sub>-E curves seen in Figure 3.1, indicates that no major changes are occurring in the average microscopic properties of the silver surface beyond an increase in the overall surface area.

Generally, the values of the RF obtained from the double-layer capacitances agree quite well (within ca. 10-20%) with those found using the lead UPD method (Figure 3.2). Electrodes roughened sufficiently to yield intense SERS signals, say  $\sigma_{\rm ORC} = 10~{\rm mC~cm}^{-2}$ , exhibited only moderate roughness factors; thus typically RF=1.5-2 for  $\sigma_{\rm ORC} = 20$  mC cm<sup>-2</sup>. For electropolished silver it was found that RF 1.2 from the lead UPD method. The values of RF for the roughened electrodes were somewhat irreproducible, depending upon the exact manner of the washing and soaking steps following the ORC. An examination of these factors was made by recording  $C_d$ -E curves in the 0.1  $\underline{M}$  KC1 electrolyte used for the ORC. A Cd-E curve obtained immediately after an ORC by scanning the potential from -100 mV to and from various more negative potentials out to -1200 mV exhibited negligible hysteresis even after several potential scans over 15-20 minutes. Interestingly, this reversibility is in complete contrast to the behavior of the SERS 240 cm<sup>-1</sup> mode (silver-chloride stretching) for adsorbed chloride which is almost entirely and irreversibly quenched upon scanning more

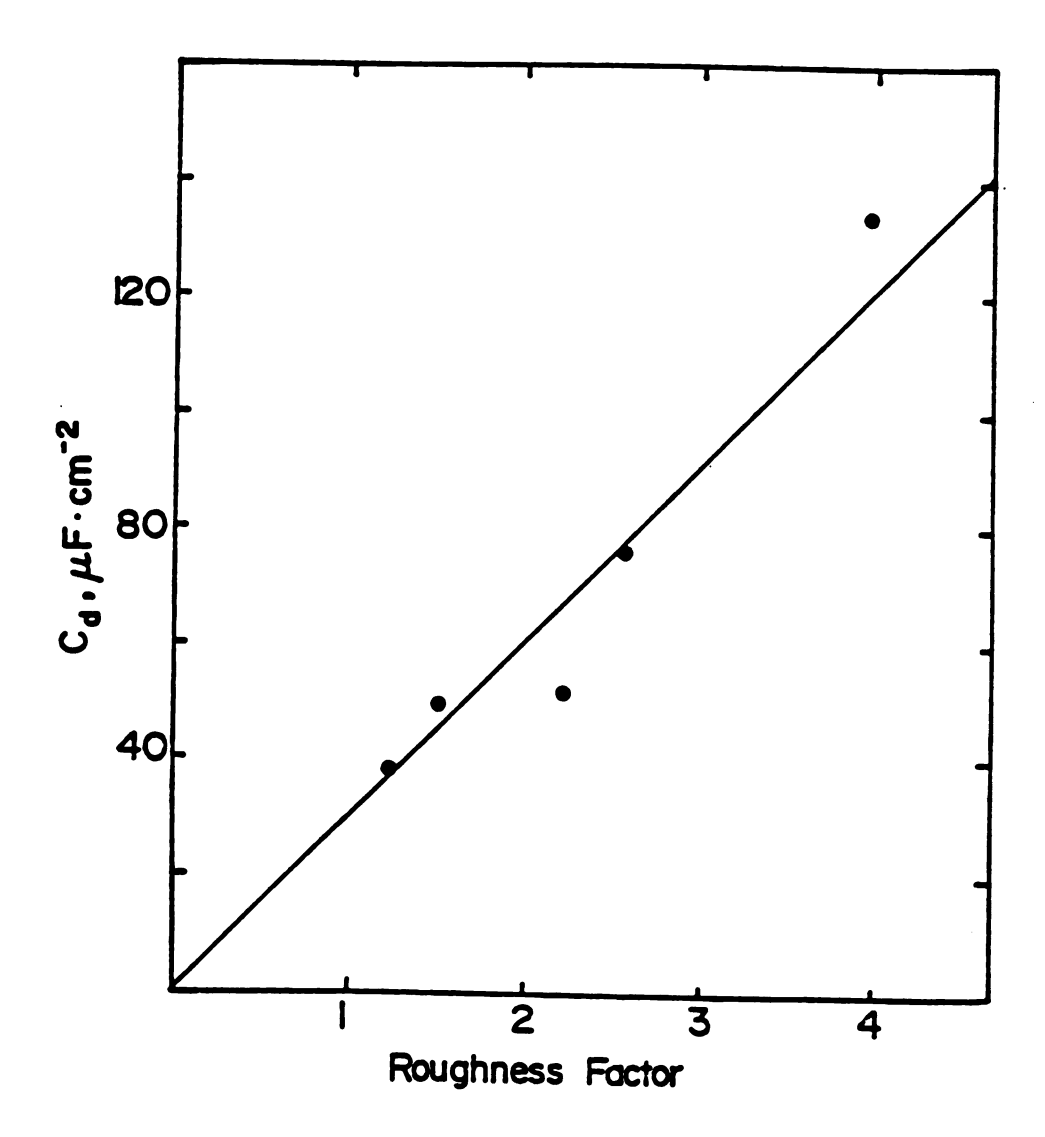


Figure 3.2. Differential capacitance for polycrystalline silver at -550 mV versus roughness factor as determined using lead UPD method (see text).

negative than ca. -500 mV under these conditions.  $^{102}$  Washing and soaking the roughened electrode in perchloric acid yielded significant decreases in the capacitance in 0.1 M KCl, corresponding to RF decreases of up to ca. 30%, depending on the vigor of the washing procedure and the soaking time (up to ca. 30 minutes). Nevertheless, the individual  $C_d$ -E curves obtained after returning the electrode to the cell consistently exhibited little or no hysteresis.

Although most capacitance data were obtained using an a.c. frequency of 100 Hz, the frequency dependence of C, was also examined. Over the frequency range 20-1500 Hz in 0.5  $\underline{M}$  NaClO,, the apparent values of Cd generally increased with decreasing frequency, although only of the order of ca. 10% for every 10-fold frequency change. The extent of this frequency dispersion was similar on roughened and electropolished surfaces, and largely independent of the electrode potential. This behavior is somewhat more ideal than found for electropolished silver in 0.5 M NaF, where noticeably greater frequency dispersions were found at potentials positive of ca. -700 mV.86 However, in solutions containing small amounts (<10 mM) of strongly adsorbing anions such as chloride or bromide the frequency dispersion problem may well be more serious, judging from the differences in capacitance values obtained at 1000 Hz in 0.5 M NaF and at 100 Hz in 0.5  $\underline{\text{M}}$  NaClO<sub>4</sub>. The results of our earlier study <sup>86</sup> quite possibly are somewhat in error, the reported surface concentrations being smaller than the true surface concentrations.

### b. Determination of Anion Specific Adsorption

These results indicate that the electrochemically roughened silver surfaces exhibit sufficiently well-behaved and reproducible behavior to allow quantitative estimates of specific anion adsorption to be obtained from  $C_d$ -E data using the Hurwitz-Parsons approach. Following our earlier measurements,  $^{86}$   $C_d$ -E curves were recorded in a series of mixed electrolytes having the general composition (0.5-x)M NaClO<sub>4</sub> + xM NaX, where X is the adsorbing anion, either Cl<sup>-</sup>, Br<sup>-</sup>, I<sup>-</sup>, NCS<sup>-</sup>, or N<sub>3</sub>. The general procedure was to record a  $C_d$ -E curve for a previously roughened or electropolished silver electrode in 0.5 M NaClO<sub>4</sub>, and then obtain  $C_d$ -E curves following successive additions of NaX using the same electrode.

The surface concentrations of specifically adsorbed anions were calculated from each family of  $\mathbf{C_d}$ -E curves using two variants of the Hurwitz-Parsons analysis, as follows. The electrocapillary equation for the mixed electrolytes employed here can be written as  $^{36}$ 

$$-d \Upsilon = \sigma^{m} dE + [\Gamma_{X} - \{x/(0.5-x)\}\Gamma_{C10_{L}}]RTd1nx$$
 (3.1)

where  $\Gamma$  is the surface tension,  $\sigma^{\mathbf{m}}$  is the excess electronic charge density on the metal surface, E is the electrode potential, and  $\Gamma_{\mathbf{X}}$  and  $\Gamma_{\mathbf{C10}_{\downarrow}}$  are the surface excesses of the added anion X and the perchlorate anion. Provided that the components of  $\Gamma_{\mathbf{X}}$  and  $\Gamma_{\mathbf{C10}_{\downarrow}}$  in the diffuse layer,  $\Gamma_{\mathbf{X}}^{\mathbf{d}}$  and  $\Gamma_{\mathbf{C10}_{\downarrow}}^{\mathbf{d}}$  respectively, are present in the same ratio as the anion mole fractions, i.e.  $\Gamma_{\mathbf{X}}^{\mathbf{d}}/\Gamma_{\mathbf{C10}_{\downarrow}}^{\mathbf{d}} = \mathbf{x}/(0.5-\mathbf{x})$ , as expected,  $^{36}$  then Equation (3.1) can be rewritten as

$$-d Y = \sigma^{m} dE + [\Gamma_{X} - \{x/(0.5-x)\}\Gamma_{C10_{ij}}]RTd1nx$$
 (3.2)

where  $\Gamma_{X}$  and  $\Gamma_{C10_{4}}$  is small (vide infra), we can write

$$-d\gamma = \sigma^{m}dE - \Gamma_{x}^{n}RTdlnx$$
 (3.3)

Equation (3.3) suggests that the desired values of  $\Gamma_{X}$  can be obtained simply from

$$\Gamma_{X} = -(1/RT)(\partial Y/\partial \ln x)_{E} = -(1/RT)(\partial \Delta Y/\partial \ln x)_{E}$$
 (3.4)

The required coefficients  $(3 \text{ Y/} 3 \text{lnx})_{\text{E}}$  were obtained from the  $\text{C}_{\text{d}}$ -E curves by noting that the observed coincidence of these curves at negative potentials will also be associated with values of  $\sigma^{\text{m}}$  and that are both independent of x. Therefore the  $\text{C}_{\text{d}}$ -E curves can be integrated twice to yield a corresponding set of  $\Delta Y$ -E curves, where  $\Delta Y$  is the surface tension with respect to the (unknown) value at some suitably negative potential. [Since the  $\text{C}_{\text{d}}$ -E curves were often not quite coincident at the most negative potentials (ca. -1300 to -1400 mV) at which  $\text{C}_{\text{d}}$  could be accurately evaluated due to the onset of hydrogen evolution, a short extrapolation of these curves to more negative potentials was required]. The required values of  $\left(\frac{1}{2}Y\right)$  were obtained for various values of x and E from the family of  $\Delta Y$ -E curves, yielding plots of  $\left(\frac{1}{2}Y\right)$  against E for various values of x. We shall denote this approach as Method I. It has been recently employed, for example, to determine chloride specific adsorption at single-crystal silver surfaces.

We have previously used a related approach, denoted here as Method II, <sup>86</sup>, <sup>103</sup>, <sup>104</sup> based on the following "cross-differential" relation which can be obtained from Equation (3.3): <sup>103</sup>

$$(\partial_{\sigma}^{\mathbf{m}}/\nabla_{\mathbf{X}})_{\mathbf{E}} = \partial_{\sigma} - \mathbf{R} \mathbf{T} (\mathbf{1} \mathbf{n} \mathbf{x} / \partial_{\sigma} \mathbf{E})_{\Gamma},$$
 (3.5)

Provided that the coefficient  $(\partial \sigma^m/\partial \Gamma_X)_E$  is essentially independent of coverage,  $\Gamma_X$  can be found from

$$\Gamma = -(\Delta \sigma^{\mathbf{m}})_{\mathbf{E}} / \mathbf{R} \mathbf{T} (\partial \mathbf{l} \mathbf{n} \mathbf{x} / \partial \mathbf{E})_{\Gamma}, \qquad (3.6)$$

where  $(\Delta \sigma^m)_E$  is the change in electrode charge density at a given electrode potential brought about by the addition of the adsorbing anion X. This quantity can easily be found by back-integrating the  $C_d$ -E curves as before, but only once to yield a family of relative  $\sigma^m$ -E curves. The required coefficient  $(\partial \ln x/\partial E)_\Gamma$ , can be evaluated from the relative shape of these  $\sigma^m$ -E curves as described in reference 103. [Note that Methods I and II require only information on the changes in  $\sigma^m$  (or Y) brought about by altering the anion concentration, x, so that a knowledge of the potential of zero charge or absolute values of  $\sigma^m$  is not required].

Although Method II provides a particularly direct route to  $\Gamma_X$ , its use, at least as outlined above, proved impossible with the present systems. The chief difficulty is that the coefficient  $(\partial \ln x/\partial E)_{\Gamma}$ , in each case varied with both the surface anion concentration and electrode potential, and therefore could not be assessed from the

relative shapes of  $\sigma^m$ -E curves. When such variations are minor the coefficient can still be evaluated via an iterative analysis. However, the iterative approach, when tried here, yielded divergent results.

Figure 3.3A shows a typical set of  $C_d$ -E curves for electropolished silver (RF $^{2}$ 1.2) in a series of mixed NaClO $_4$ -NaCl electrolytes with x = 0 to 0.2 M. Figure 3.3B gives a corresponding set gathered for a roughened silver electrode ( $\sigma_{ORC}$  = 40 mC cm $^{-2}$ , RF = 1.9). Comparisons of Figures 3.3A and 3.3B shows that the general features of the  $C_d$ -E curves are similar on the smooth and roughened electrodes (vide supra). The latter curves have values of  $C_d$  that are about 50% higher in accordance with the measured roughness factor. [Here and elsewhere  $C_d$  is reported in terms of the geometrical (apparent) surface area.] At potentials more negative than ca. -1300 mV, the capacitance is almost independent of the bulk chloride concentration, indicating that here chloride specific adsorption is negligible. As the potential becomes less negative, progressive increases in  $C_d$  are seen for the chloride-containing solutions which become larger with increasing bulk concentration as a consequence of greater chloride specific adsorption.

The resulting values of  $\Gamma_{C1}$  as a function of potential for two chloride concentrations, 0.015 and 0.1 M are shown in Figure 3.4 for both electropolished (solid curves) and roughened surfaces (dashed curves). (The surface concentrations here and below are reported in terms of the actual surface area, i.e. by taking into account the measured roughness factors RF 1.2 and 1.9 for the electropolished and roughened surfaces, respectively). It is seen that the corresponding  $\Gamma_{C1}$  values are somewhat smaller on the roughened compared to the

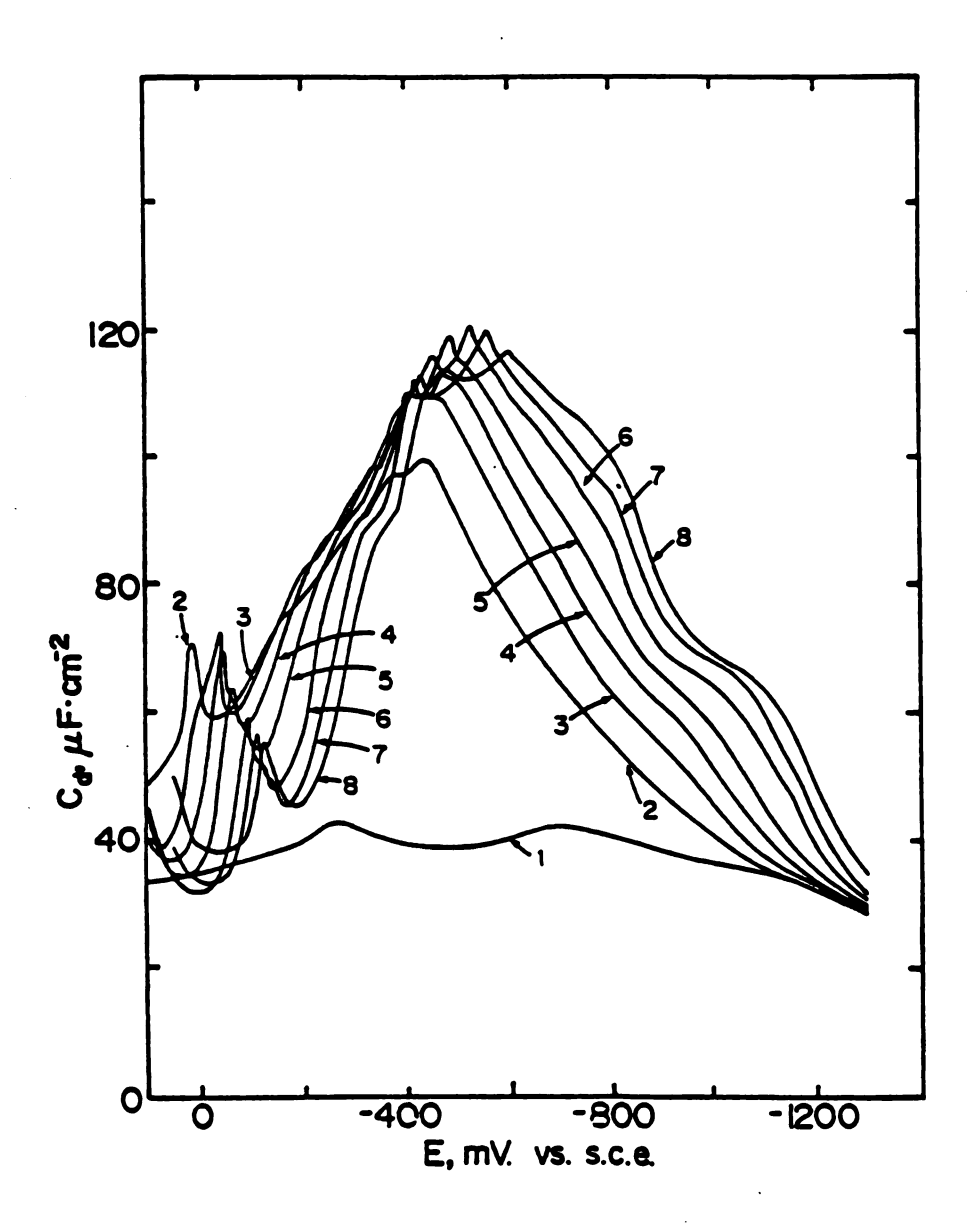


Figure 3.3A. Differential capacitance versus electrode potential for electropolished polycrystalline silver (RF = 1.2) in NaClO<sub>4</sub>-NaCl mixtures at ionic strength 0.5. Keys to chloride concentrations: 1, 0m<u>M</u>; 2, 1 m<u>M</u>; 3, 2.5 m<u>M</u>; 4, 6 m<u>M</u>; 5, 15 m<u>M</u>; 6, 40m<u>M</u>; 7, 100 m<u>M</u>; 8, 200 m<u>M</u>.

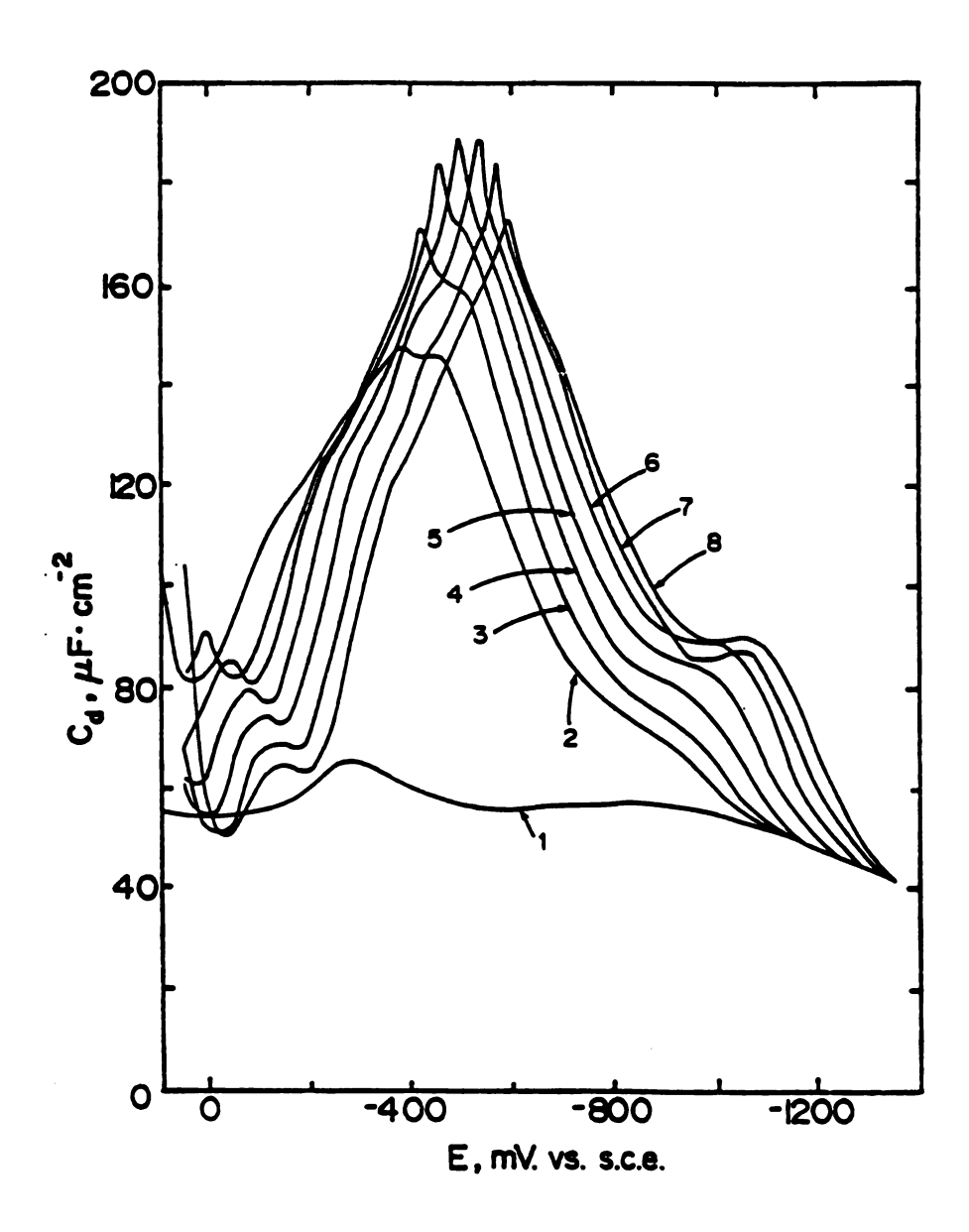


Figure 3.3B. As in Figure 3.3A, but for electrochemically roughened silver (RF  $\approx$  1.9).

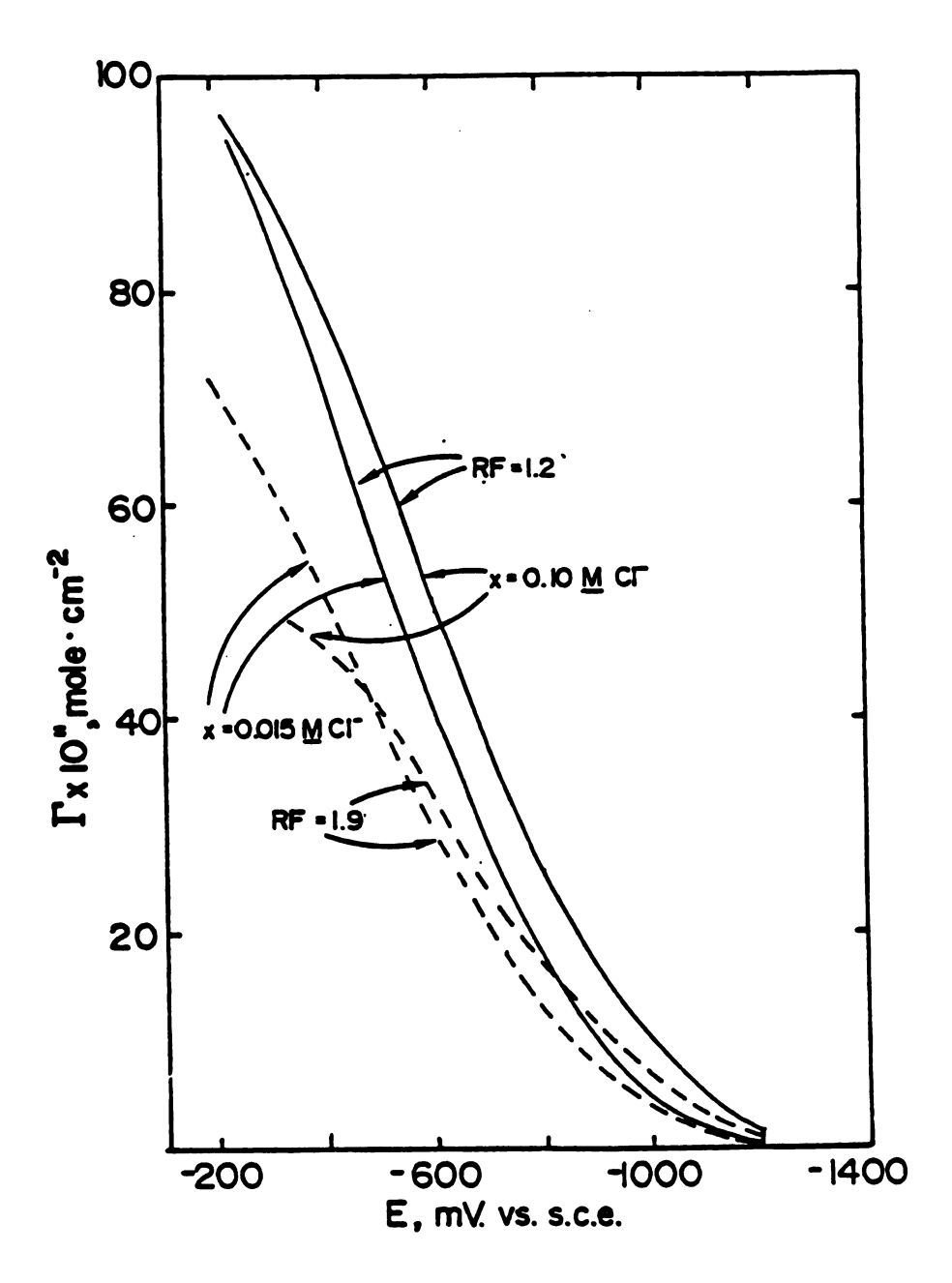


Figure 3.4. Surface concentration of specifically adsorbed chloride (per cm<sup>2</sup> real area) at electropolished (solid curves) and roughened silver (dashed curves) versus electrode potential for bulk chloride concentrations of 0.015  $\underline{M}$  and 0.10  $\underline{M}$ , analyzed from Figures 3.3A and 3.3B as outlined in text.

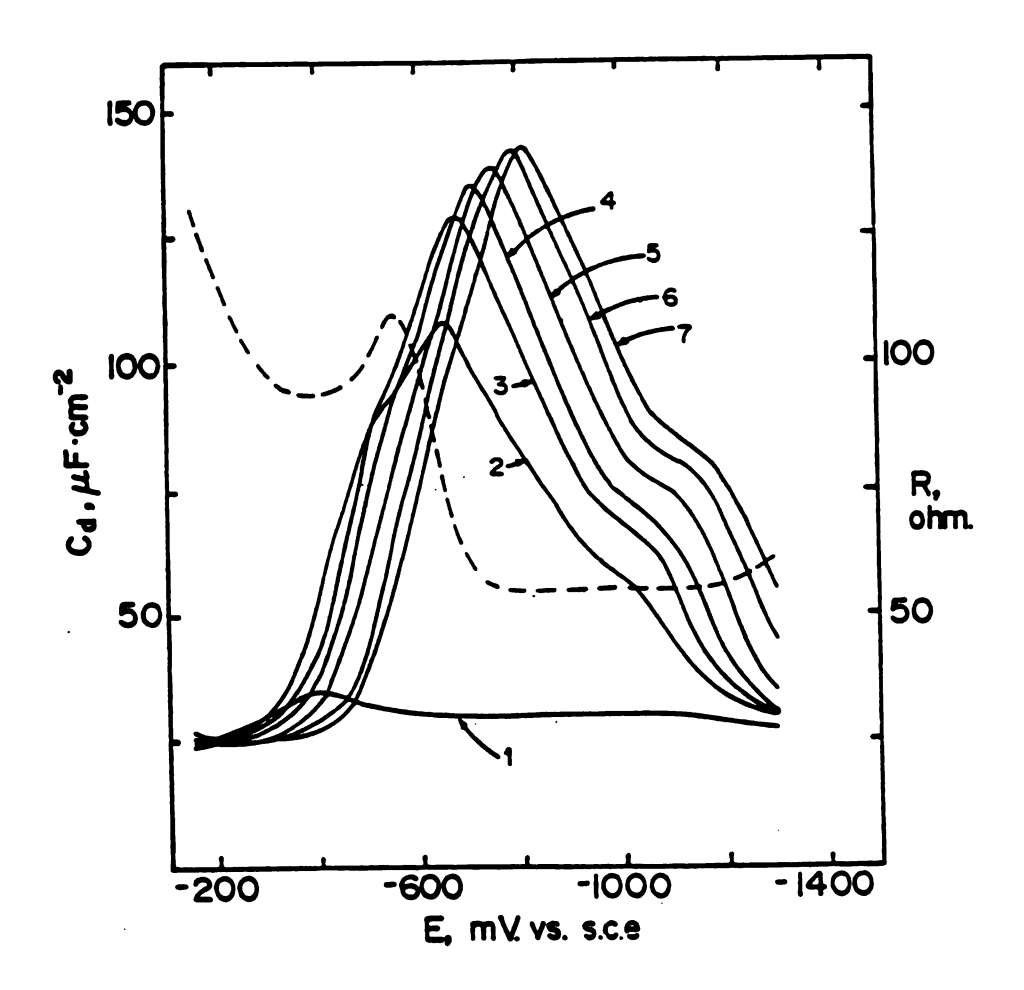


Figure 3.5A. Differential capacitance versus electrode potential for electropolished polycrystalline silver in NaClO<sub>4</sub>-NaBr mixtures of ionic strength 0.5. Key to bromide concentration (solid curves): 1, 0 mM; 2, 0.6 mM; 3, 2 mM; 4, 5 mM; 5, 15 mM; 6, 40 mM; 7, 100 mM. The dashed curve is the cell resistance for 100 mM bromide plotted on the same potential scale.

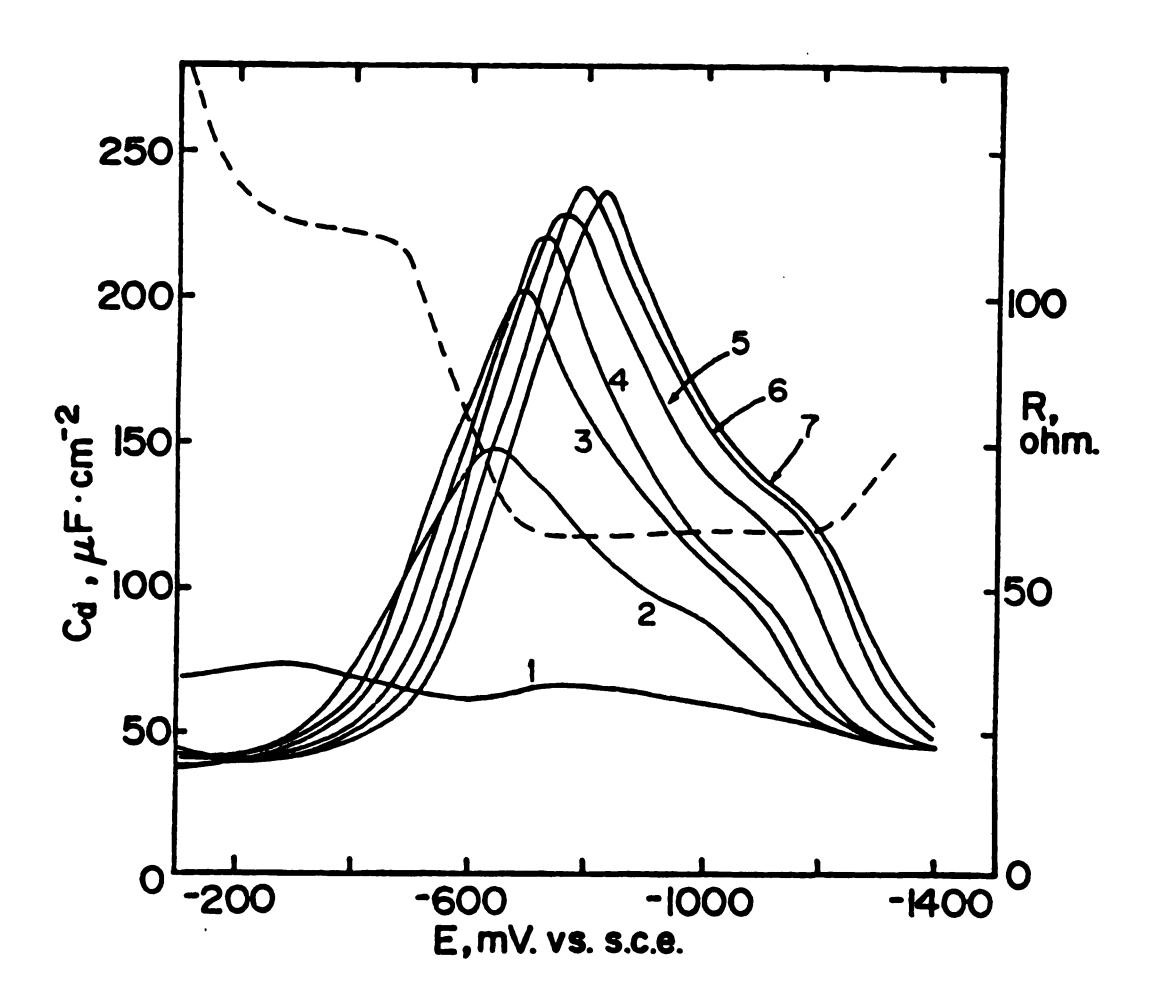


Figure 3.5B. As in Figure 3.5A, but for roughened silver (RF=1.9).

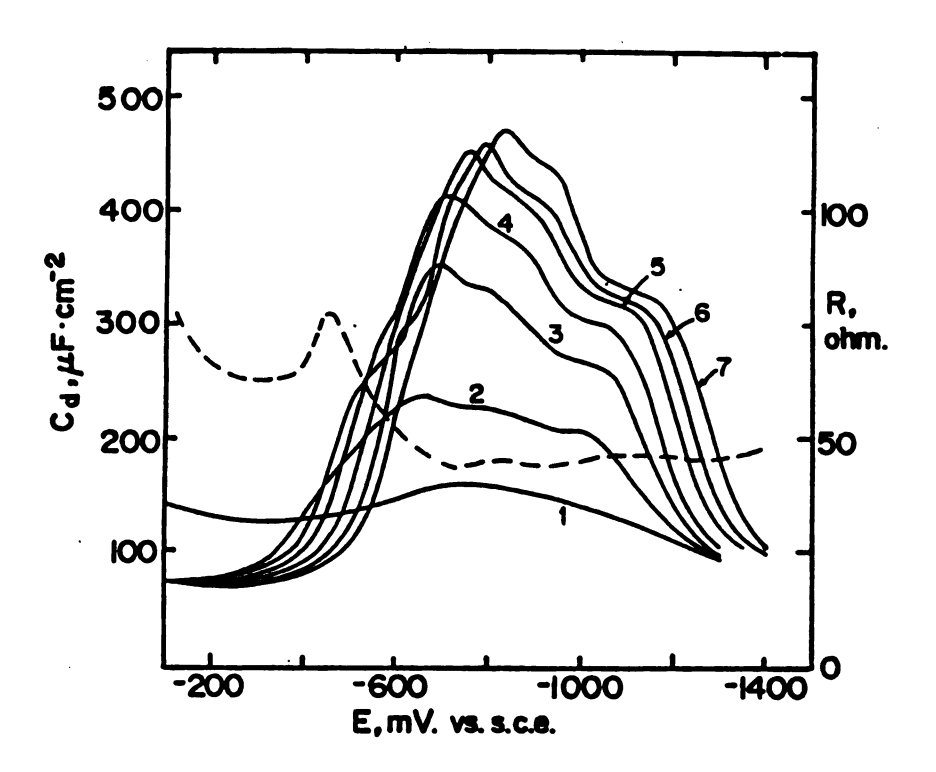


Figure 3.5C. As in Figure 3.5A, but for roughened silver (RF=4.2).

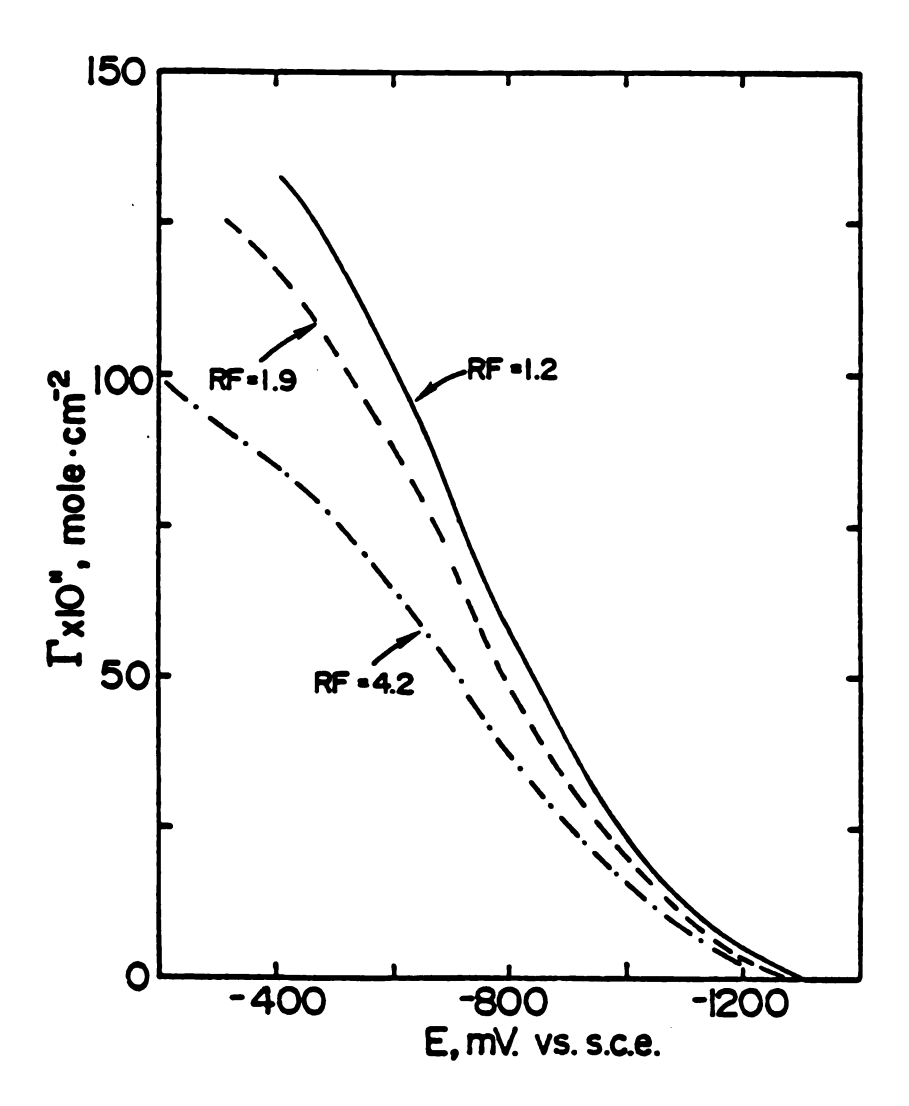


Figure 3.6A. Surface concentration of specifically adsorbed bromide (per cm $^2$  real area) as electropolished (solid curve) and roughened silver (dashed, dotted curves) for bulk concentration x at 15 mM obtained from Figures 3.5A and B.

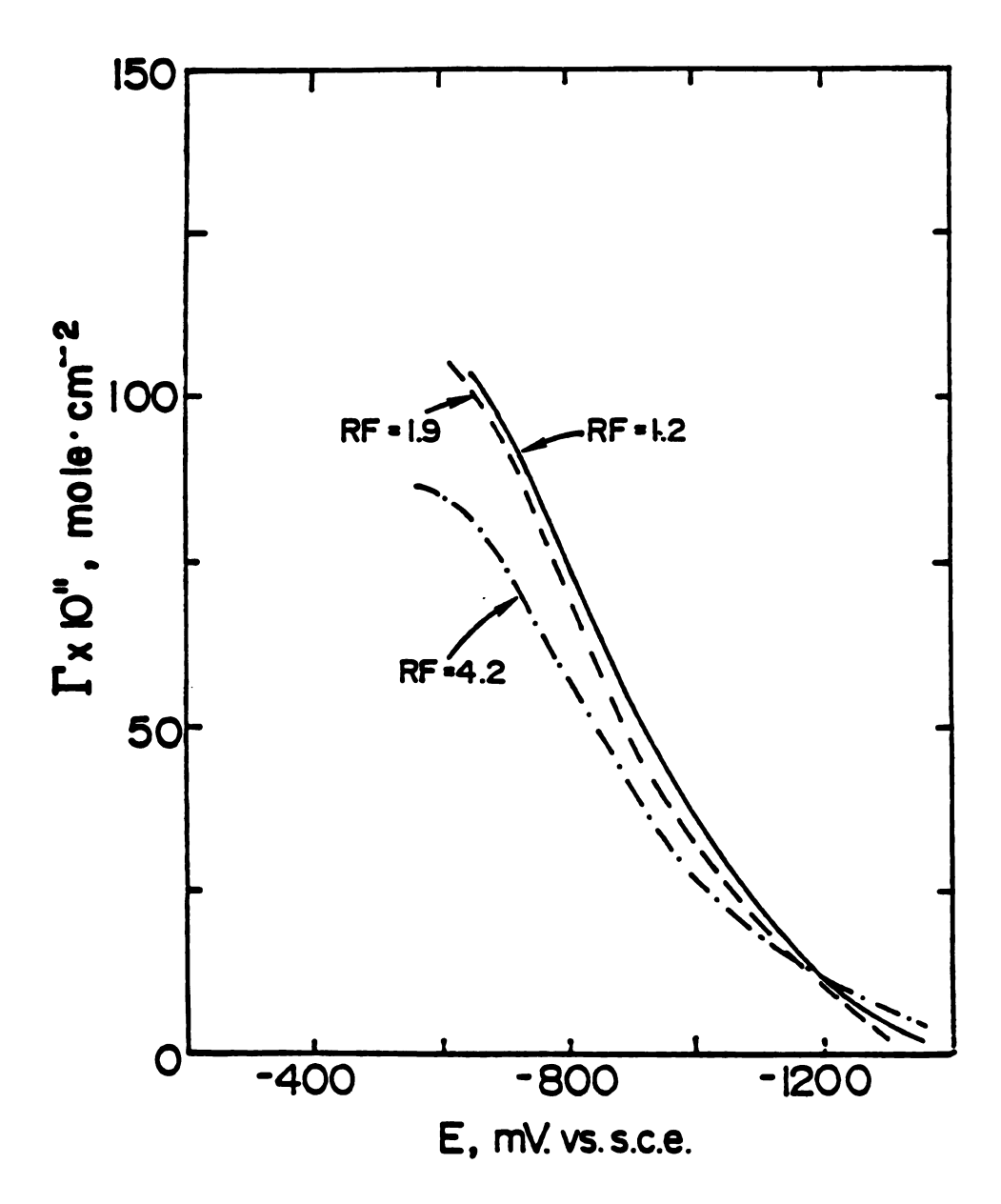


Figure 3.6B. As in Figure 3.6A, but for x = 100 mM.

electropolished surface, and only increase marginally with increasing bulk chloride concentration. Although the decrease in  $\Gamma_{C1}$  upon surface roughening is relatively mild (up to ca. 30%) it is considered to be greater than the experimental uncertainty in  $\chi$ , which under favorable conditions is estimated to be no larger than 10-15%.

Figures 3.5A-C show representative  $C_d$ -E curves gathered for bromide electrolytes,  $(0.5\ \underline{M}\ \text{NaClO}_4 + \underline{x}\underline{M}\ \text{NaBr}\ \text{with x=0}$  to  $0.1\ \underline{M})$ , using electropolished (Figure 3.5A) and roughened silver having RF values of 1.9 (Figure 3.5B) and 4.2 (Figure 3.5C). Again, the shapes of the  $C_d$ -E curves on the roughened surfaces largely resemble those at the smooth electrode, the values of  $C_d$  being greater on the former to an extent that is approximately in accordance with the measured roughness factor. Figure 6A shows the resulting plots of  $\Gamma_{Br}$  against electrode potential for 0.015  $\underline{M}$  bromide at these three surfaces, and Figure 3.6B shows the corresponding plot for 0.1  $\underline{M}$  bromide. As for chloride, the values of  $\Gamma_{Br}$  are marginally smaller on the roughened compared to the electropolished surface, and to an extent which increases with increasing roughness.

Figures 3.5A-C also show representative plots of the resistive component R of the measured impedance against potential for 0.1 M bromide, shown as dashed curves. Although R is approximately constant beyond -700 mV, it exhibits sharp variations at potentials positive of the major C<sub>d</sub> peak where high coverages of bromide are obtained. Similar behavior was observed for the other adsorbates studied here (cf. reference 86). Such variations are inconsistent with the usual representation of the interface as a pure "RC" circuit. The reason for

this behavior is unclear, but may be associated with a sluggish restructuring of the adsorbate layer at high coverages. In any event, the derived  $\Gamma_{\overline{X}}$  values are clearly less trustworthy under these conditions.

Nevertheless, the shape of the Cd-E curves in the high coverage region can still yield useful information. The measured capacitance can be considered to consist of two components, one reflecting the dielectric properties of the particular interfacial composition ("constant coverage" capacitance) and an additional part arising from the variation in the adsorbate concentration with electrode potential. 105 This latter component will be greatest when the fractional surface coverage  $\theta$  is about 0.5 because  $(\partial \Gamma_{\mathbf{X}}^{2}/\partial \mathbf{E})_{\mathbf{x}}$  and hence  $(\partial \sigma^{\mathbf{m}}/\partial \mathbf{E})_{\mathbf{x}}$ are anticipated to reach maximum values at this point and will vanish in the limits of low and saturation coverage since then  $(\partial \Gamma_{X}^{\prime}/\partial E)_{Y} \rightarrow 0$ . Therefore the major capacitance peak will occur at a surface coverage around 0.5. This is borne out in Table 3.1 for Br adsorption at roughened silver. The onset of concentration-independent and relatively potential-independent capacitances at more negative and positive potentials signals that the anion coverages approach zero and unity, respectively. For chloride, the Cd-E curves converge only at positive potentials close to the onset of surface oxidation, ca. 0 mV. Bromide adsorption is sufficiently stronger so that the major capacitance peak occurs at more negative potentials and the  $\mathbf{C}_{\mathbf{d}}$ -E curves converge to a plateau at potentials positive of ca. -300 mV, indicating that a monolayer of adsorbed bromide is formed in this region. The surface

Table 3.1

Coverage of Roughened Silver (RF=1.9) by Bromide Ions at the Capacitance Peak Potential in Mixed Electrolytes

[Br]	Coverage
0.002 <u>M</u>	0.45
0.005	0.40
0.015	0.47
0.040	0.53
0.100	0.52

concentration corresponding to a close-packed monolayer is estimated to be 1.6  $\times$  10<sup>-9</sup> and 1.35  $\times$  10<sup>-9</sup> moles cm<sup>-2</sup> for chloride and bromide, respectively.<sup>86</sup>

Figures 3.7A and 3.7B show C<sub>d</sub>-E curves for iodide-containing electrolytes obtained on electropolished and roughened electrodes. respectively, and Figures 3.8A and 3.8B show the same for thiocyanate. Both these anions are sufficiently strongly adsorbed to yield large increases in C, upon their addition to 0.5 M NaClO, even at the most negative potential (ca. -1300 mV) at which measurements could be made without interference from hydrogen evolution. precludes a quantitative adsorption analysis since sizeable extrapolations to more negative potentials are required to a value where anion adsorption is negligible from which the Cd-E curves can be integrated. Nevertheless, once again the shapes of the C<sub>d</sub>-E curves on the electropolished and roughened electrodes are similar, the latter merely exhibiting larger C, values to an extent consistent with the roughness factor determined in 0.5  $\underline{M}$  NaClO<sub>A</sub>. Both iodide and thiocyanate are tenaciously adsorbed, apparently saturating the surface at potentials positive of ca. -900 mV for bulk anion concentrations of a few millimolar and above on the basis of the plateaus observed in the  $C_A$ -E curves under these conditions (Figures 3.7, 3.8). However, the  $C_d$ -E curves for thiocyanate exhibit a pronounced structure in the more positive potential region, most notably yielding a large capacitance peak at ca. -250 mV which grows sharply as the bulk thiocyanate concentration is increased above 1 mM. The magnitude of this peak is noticeably dependent on the a.c. frequency, being markedly smaller at

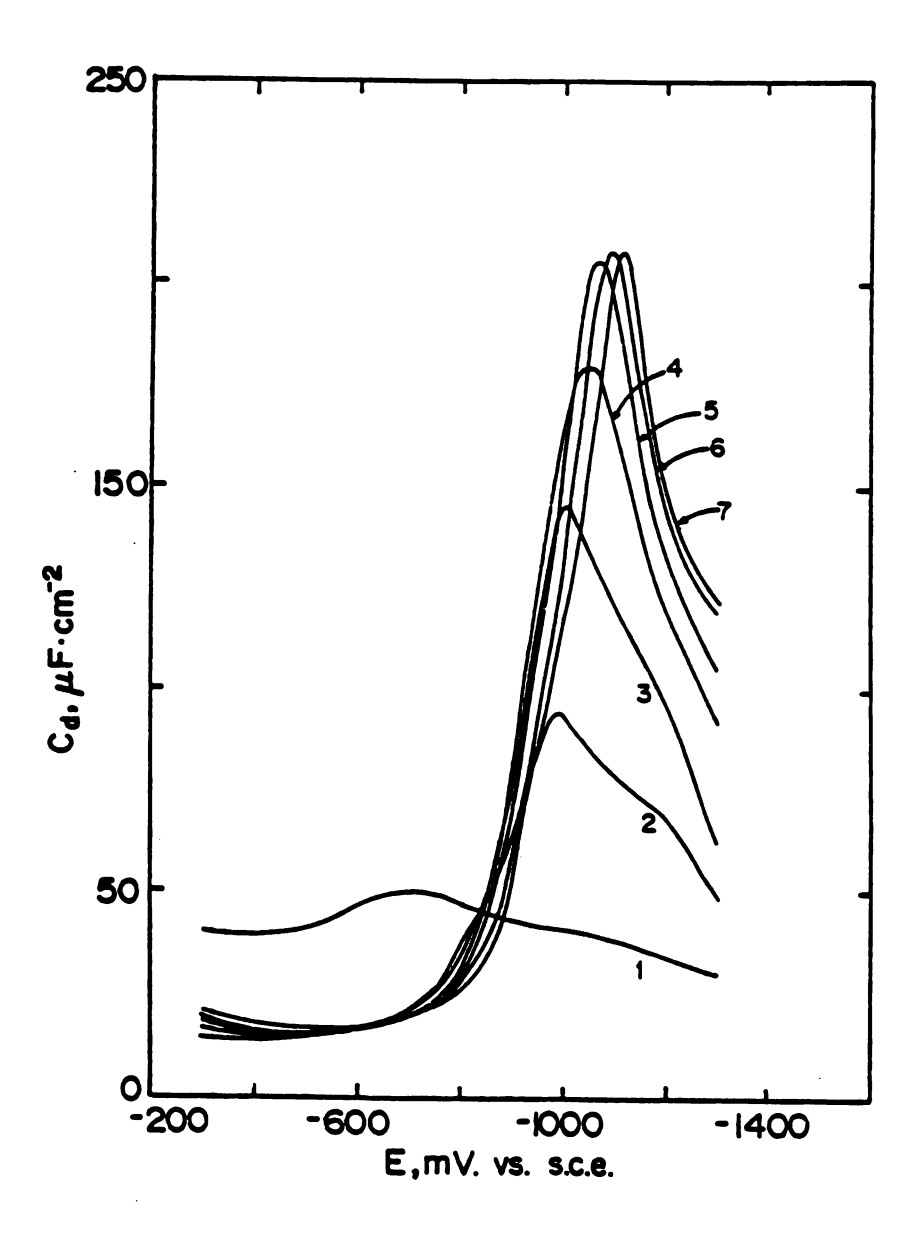


Figure 3.7A. Differential capacitance versus electrode potential for electropolished silver in NaClO<sub>4</sub>-NaI mixtures of ionic strength 0.5.

Key to iodide concentrations: 1, 0 mM; 2, 0.2 mM; 3, 0.5 mM; 4, 1.2 mM; 5, 2.2 mM; 6, 5 mM; 7, 10 mM.

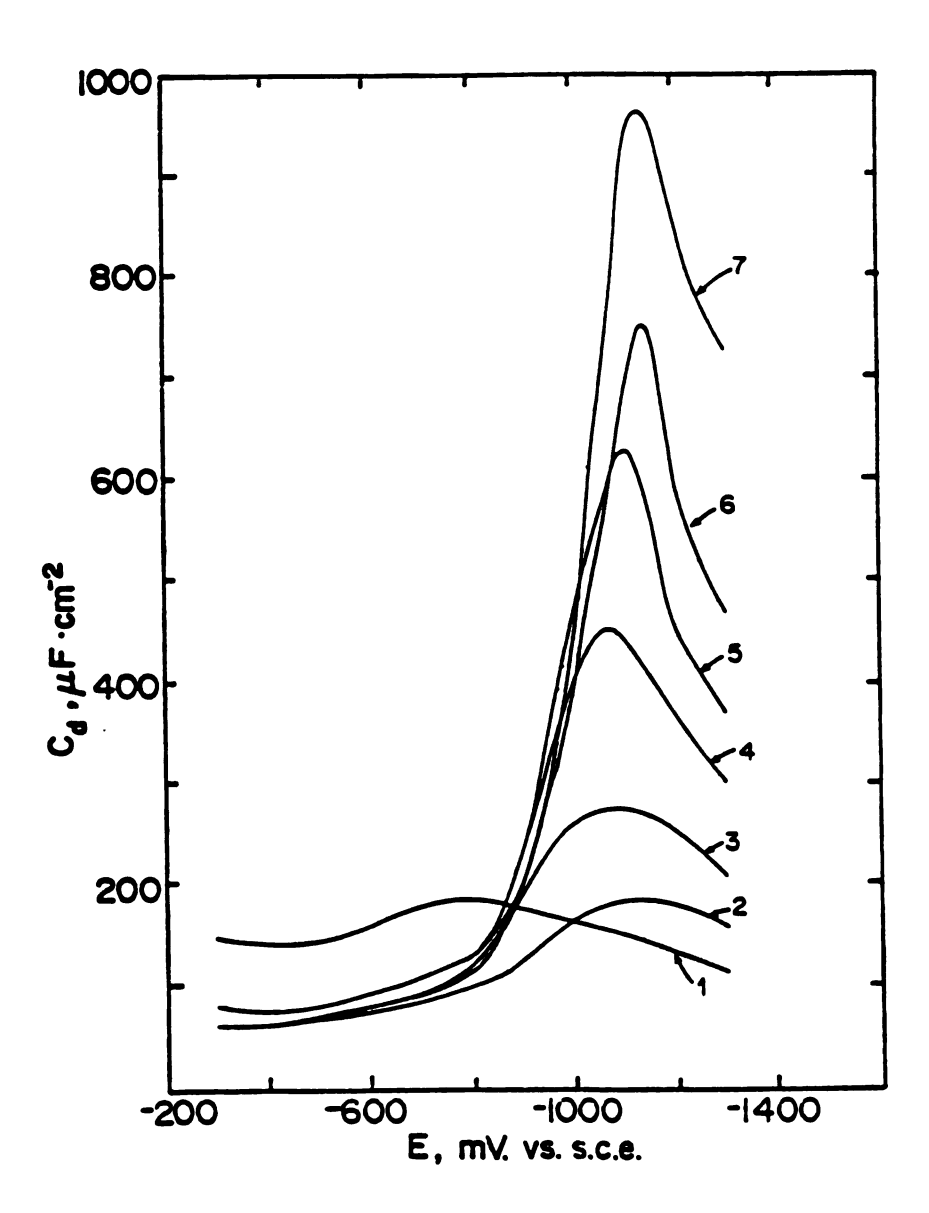


Figure 3.7B. As in Figure 3.7A, but for roughened silver (RF  $\simeq$  4.6).

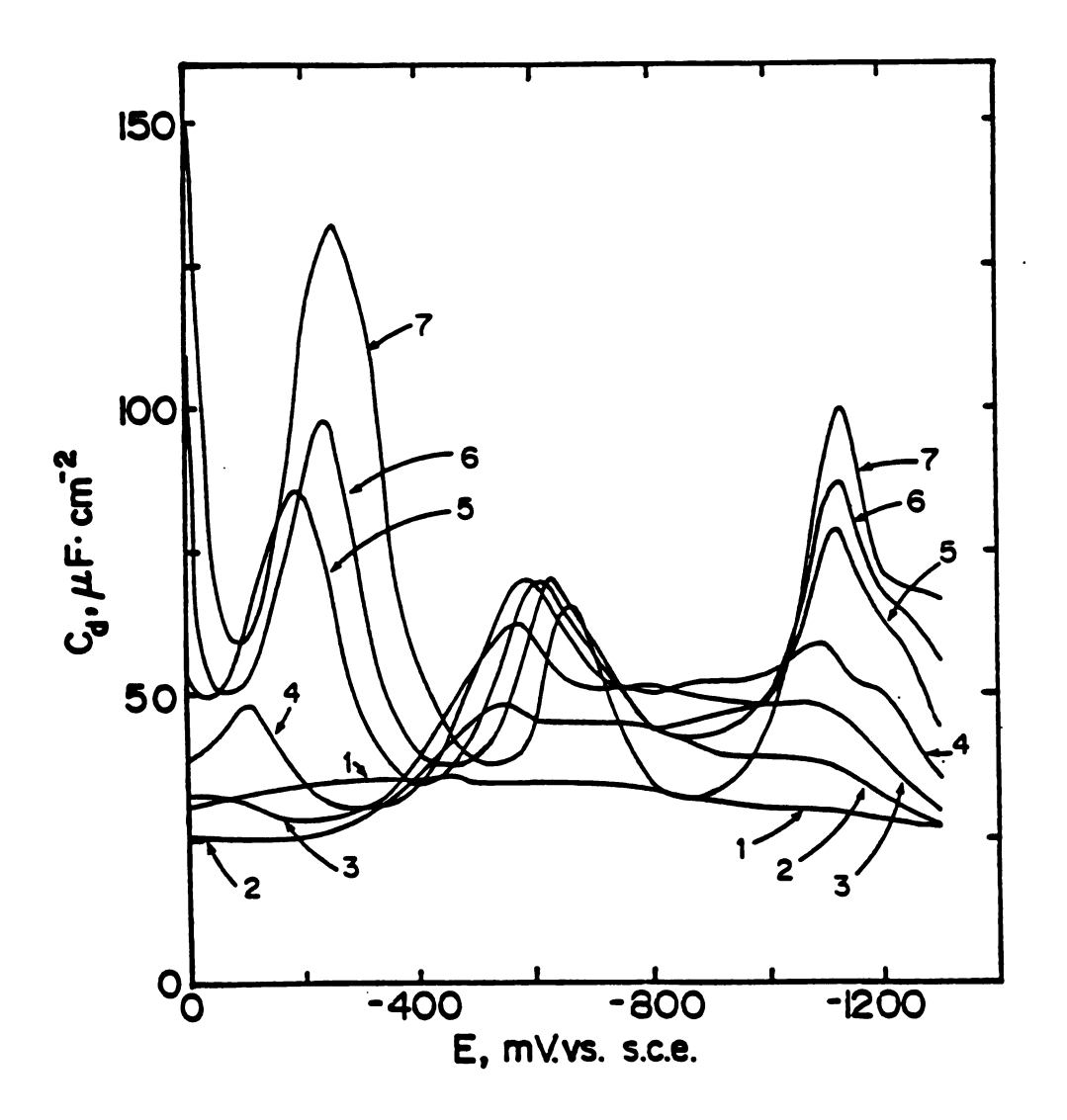


Figure 3.8A. Differential capacitance versus electrode potential for electropolished silver in NaClO<sub>4</sub>-NaSCN mixtures of ionic strength 0.5.

Key to thiocyanate concentrations: 1, 0 mM; 2, 0.3 mM; 3, 1 mM; 4, 3 mM; 5, 10 mM; 6, 30 mM; 7, 100 mM.

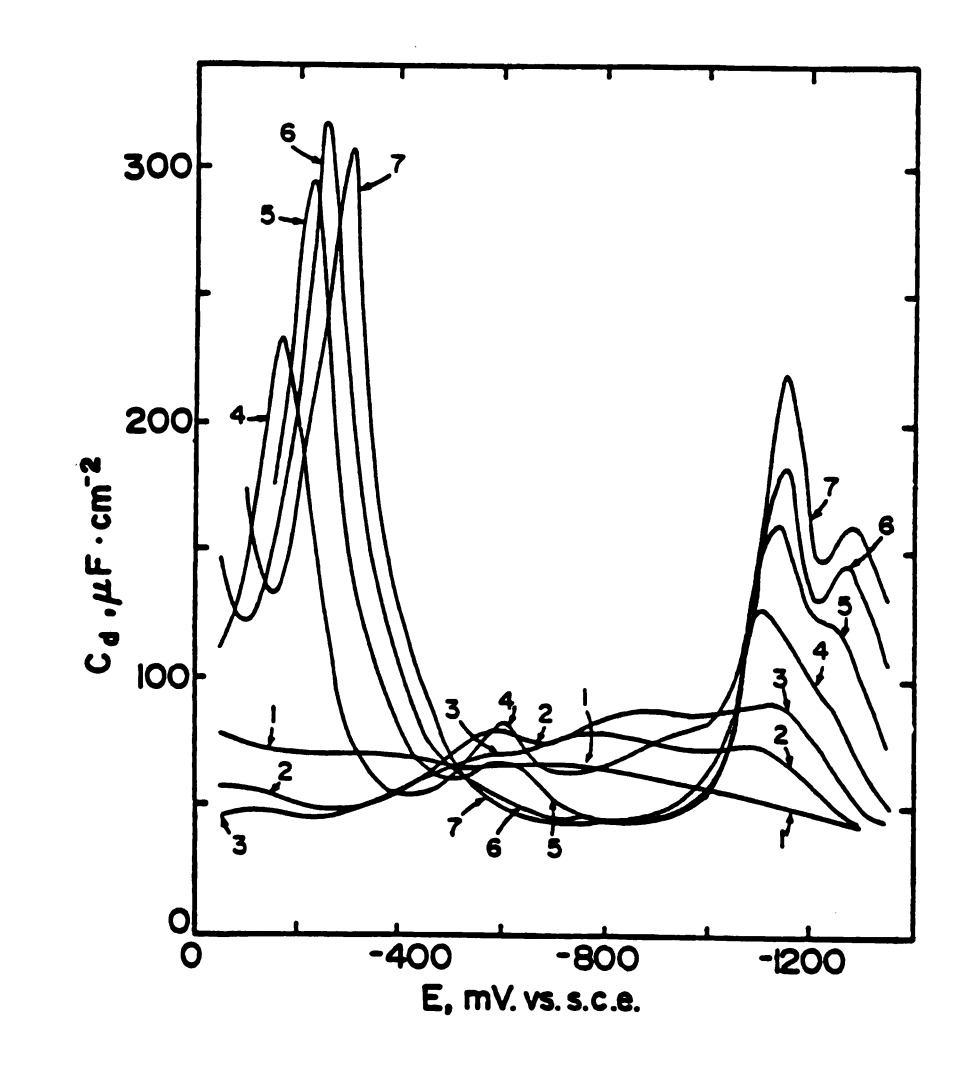


Figure 3.8B. As in Figure 3.8A, but for roughened silver (RF = 2.1).

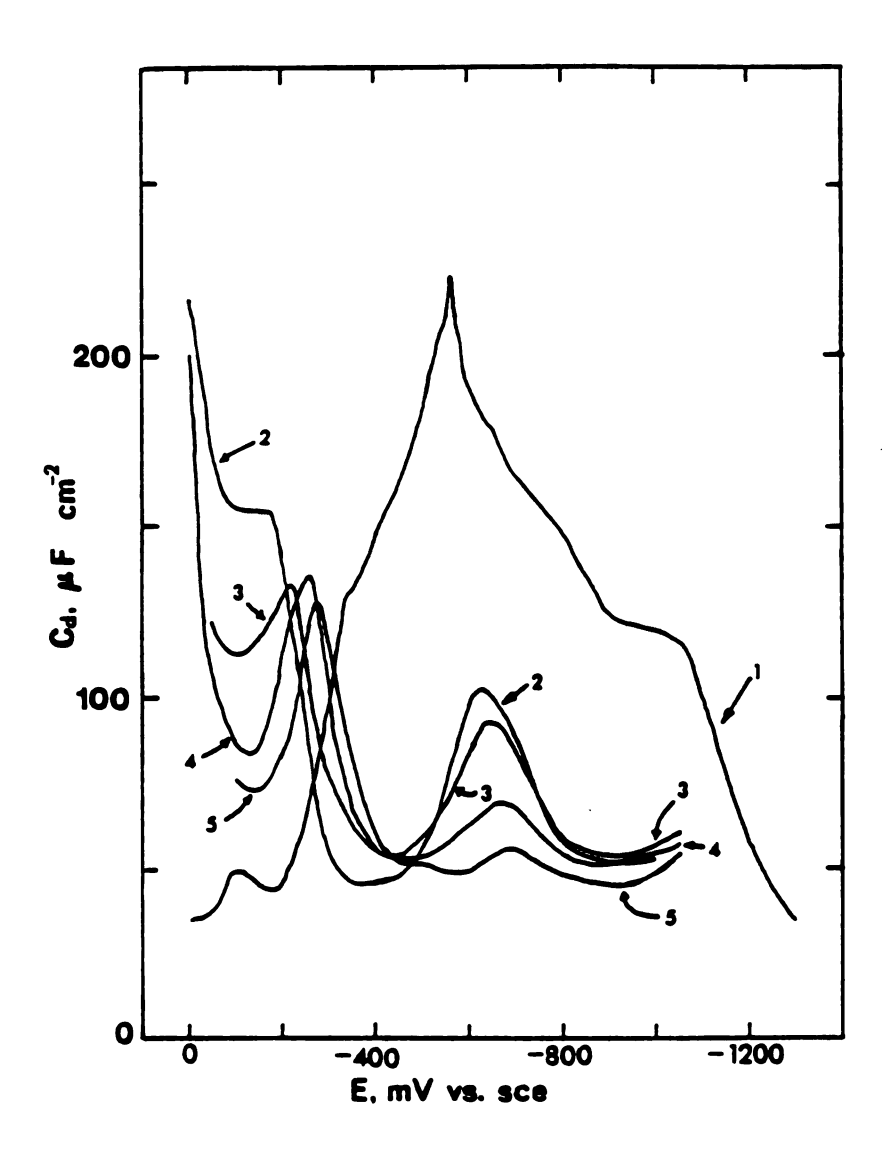


Figure 3.9. Differential capacitance versus electrode potential for roughened silver in KCl-KSCN mixtures of ionic strength 0.1. Key to thiocyanate concentrations: 1, 0 mM; 2, 5 mM; 3, 10 mM; 4, 23 mM; 5, 50 mM.

1000 Hz than at 100 Hz; the latter was used to obtain the data in Figure 3.8. (No faradaic current was detected at these potentials.) In contrast, the  $C_d$ -E curves for iodide are featureless and essentially independent of the bulk iodide concentration in this region.

It seems feasible that these additional features observed for thiocyanate are due to potential-dependent rearrangements of the adsorbate layer associated with alterations in the surface bonding geometry. Although thiocyanate very likely binds to metal surfaces preferentially via the sulfur atom, <sup>97</sup> the nitrogen atom should also have some affinity for the silver surface which could result in a relatively flat or bent orientation. At more positive potentials, the enhanced electrostatic field at the silver surface resulting from larger positive electronic charge densities <sup>95</sup> and greater packing densities may increasingly favor a more perpendicular orientation with the NCS ion bound only via the sulfur where most of the anionic charge is located.

Since the most comprehensive SERS study of thiocyanate employed chloride-thiocyanate mixtures, <sup>97</sup> it is of interest to examine thiocyanate adsorption at roughened silver under these conditions. Figure 3.9 shows C<sub>d</sub>-E curves for KCl-KSCN mixed electrolytes. Although a quantitative analysis is again precluded, it is evident that only small bulk concentrations of NCS are needed in order to produce curves which are characteristic of NCS adsorption and completely lacking the features associated with Cl adsorption. These data are most reasonably interpreted in terms of strong preferential adsorption of thiocyanate at the expense of chloride. This conclusion is consistent

with the finding in the SERS study that the usually intense Ag-Cl stretching mode at 240 cm<sup>-1</sup> is completely eliminated when millimolar amounts of NCS are added to the bulk solution.<sup>97</sup>

The Cd-E curves for azide at electropolished (Figure 3.10A) and roughened silver (Figure 3.10B) form an interesting comparison with the behavior of thiocyanate in view of the structural similarities of the two anions. Azide is sufficiently weakly adsorbed at the most negative potentials to allow values of  $\Gamma_{\chi}$  to be determined. The resulting plots of  $\Gamma_{N_3}$  vs. E for azide concentrations of 0.01 and 0.1  $\underline{M}$ at electropolished and roughened silver are shown in Figure 3.11. In contrast to chloride and bromide, azide yields significantly larger values of  $\Gamma_{\overline{X}}$  on the roughened compared to the electropolished surfaces. Although the extent of azide adsorption is comparable to that of bromide at relatively negative potentials, ca. -900 to -1200 mV, the increases in  $\Gamma_{N_-}$  as the potential becomes less negative are less pronounced than those for bromide (Figure 3.6). Therefore values of  $\Gamma_{N_0}$ close to that expected for a monolayer of azide adsorbed "end on", ca. 1.6  $\times$  10<sup>-9</sup> mole cm<sup>-2</sup>, are barely attained even at the most positive potentials (ca. 0 mV), and at x = 0.1 M (Figure 3.11). This feature can also be deduced from the shape of the Cd-E plots for azide (Figure 3.10); instead of the single major capacitance peak and a decrease to much smaller values at more positive potentials as seen for the halides, the azide curves exhibit two relatively shallow peaks. One possible reason for this more complicated behavior is that there is a change in orientation of the adsorbed azide with increasing coverage. A relatively flat orientation of the linear N<sub>3</sub> ion which may be

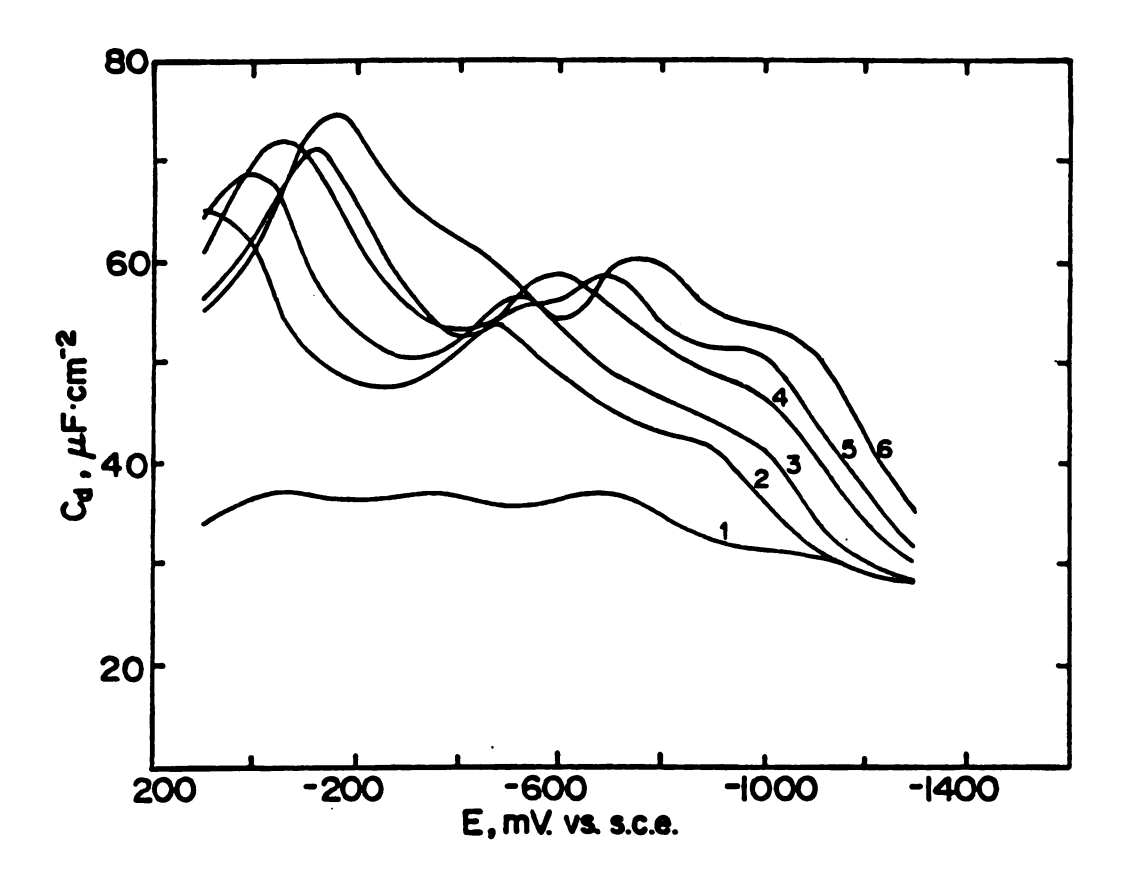


Figure 3.10A. Differential capacitance versus electrode potential for electropolished silver in NaClO<sub>4</sub>-NaN<sub>3</sub> mixtures of ionic strength 0.5. Key to azide concentrations: 1, 0 mM; 2, 1 mM; 3, 3 mM; 4, 10 mM; 5, 30 mM.

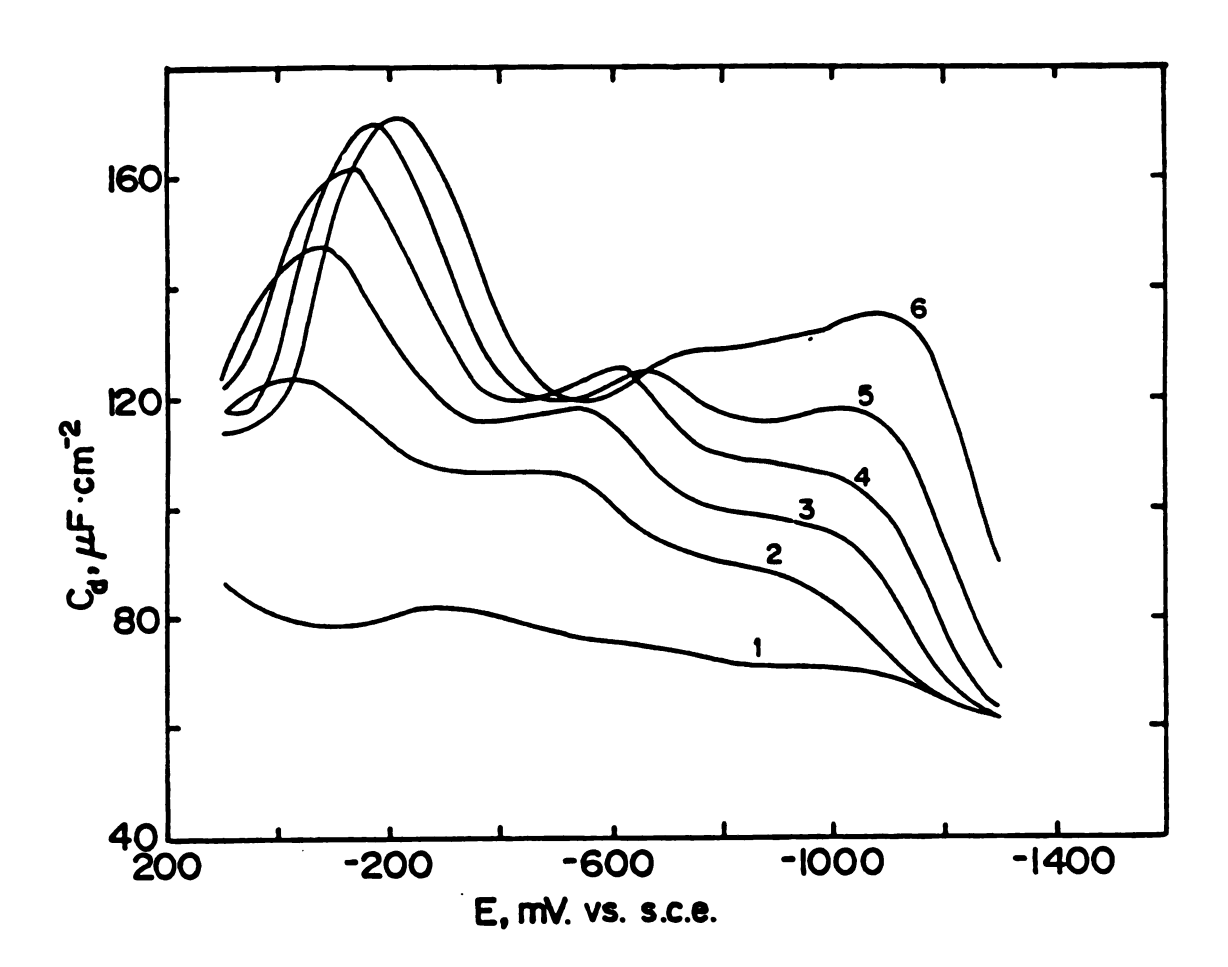


Figure 3.10B. As in Figure 3.10A, but for roughened silver (RF = 2.3).

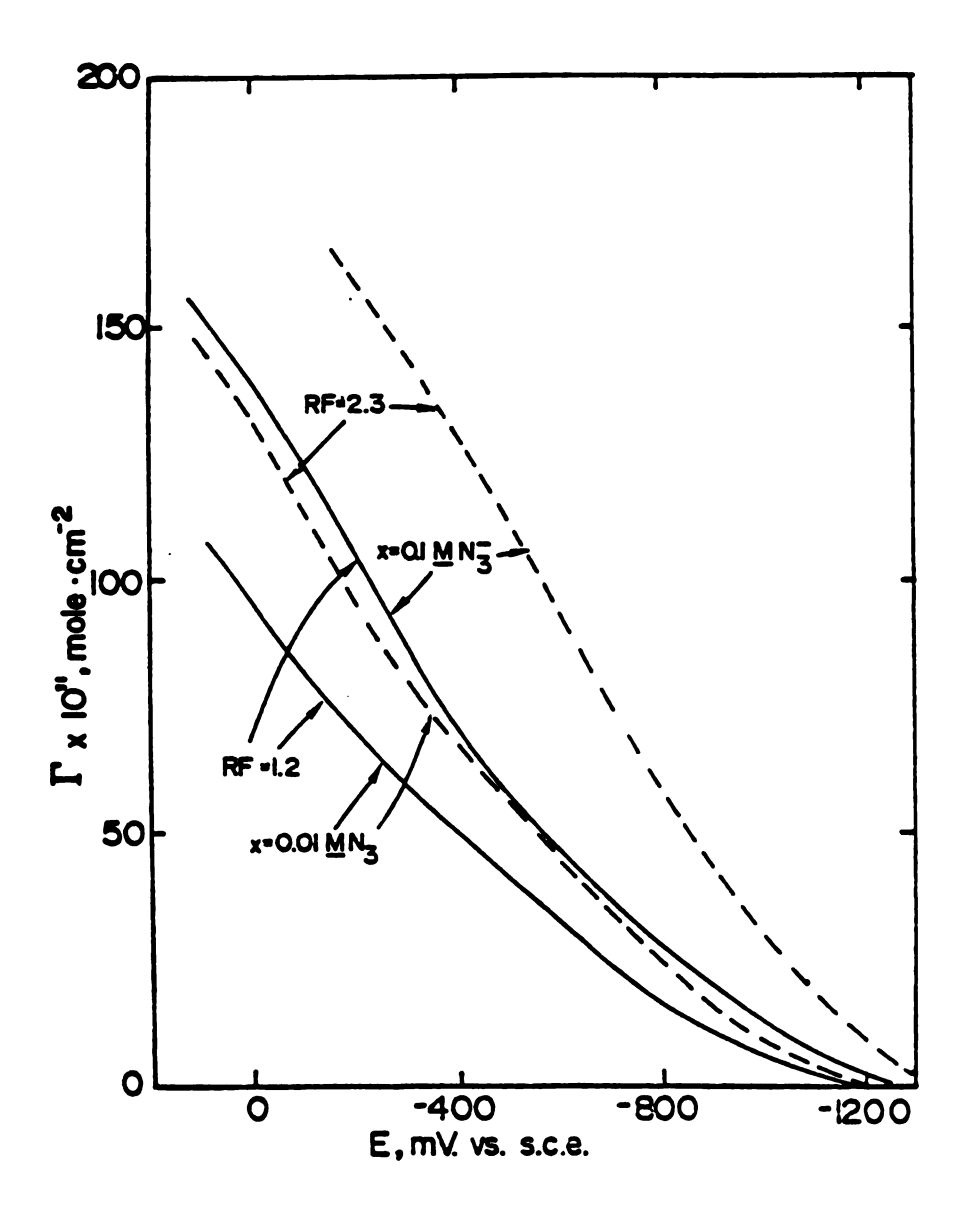


Figure 3.11. Surface concentration of specifically adsorbed azide (per cm $^2$  real area) at electropolished (solid curves) and roughened silver (dashed curves) versus electrode potential for bulk azide concentrations of 0.01  $\underline{\text{M}}$  and 0.1  $\underline{\text{M}}$ , analyzed from Figures 3.10A and B as outlined in the text.

preferred at low coverages as a result of ligand-metal overlap would need to give way to a more compact "end on" orientation in order to achieve surface concentrations above ca.  $7 \times 10^{-10}$  moles cm<sup>-2</sup>.

Support for this interpretation is also obtained from the related observation that the so-called "electrosorption valency",  $-(RT/F)(\partial \ln x/\partial E)_{\Gamma_X}$ , 106 for azide depends markedly on the adsorbate coverage and electrode potential, changing from about 0.3 at the most negative potentials to about 0.15 in the potential region positive of the major  $C_d$  peak at ca. -900 mV. This is nicely consistent with a change in azide orientation from flat to vertical in that this transformation would place the anionic charge further from the electrode. The latter orientation would yield a smaller value of EV since this quantity depends in part on the fraction of the double-layer potential drop traversed by the anionic charge upon adsorption. 106,107

Since the surface concentration data in Figures 3.4, 3.6 and 3.11 were obtained by using Equation 3.3, significant errors in  $\Gamma_X$  may arise from perchlorate coadsorption. 108 Approximate estimates of their magnitude can be estimated by inspecting Equation 3.2 which takes this factor into account. In general Equation 3.3 will tend to underestimate  $\Gamma_X$  since the second term in brackets in Equation 3.2, which is neglected in Equation 3.3, will always be positive. The error is most likely to be significant for the least strongly adsorbing anion, chloride, for which the largest bulk anion concentrations, and hence x/(0.5-x), are required in order to induce a given value of  $\chi$ . Although  $\Gamma_{C10_4}$  is not known quantitatively, kinetic probe measurements indicate that in pure perchlorate media F  $\Gamma_{C10_4}$   $\approx \sigma^m$  over a range of

positive electrode charges,  $^{86}$ ,  $^{109}$ ,  $^{110}$ , yielding  $\Gamma_{\text{C10}_{\downarrow}}^{}$  = 2.5 to 3.5 x  $^{10^{-10}}$  mol cm<sup>-2</sup> in the potential region ca. -200 to -400 mV. For high chloride concentrations, say x = 0.1 so that [x/(0.5-x)] = 0.25, the apparent values of  $\Gamma_{X}^{'}$  from Equation 3.3 are about 8 to 10 x  $^{10^{-10}}$  mol cm<sup>-2</sup> in this potential region, so that the magnitude of the correction term  $[x/(0.5-x)]\Gamma_{\text{C10}_{\downarrow}}^{'}$ , ca. 1 x  $^{10^{-10}}$  mol cm<sup>-2</sup>, is small yet significant. However, the actual error in  $\Gamma_{X}^{'}$  is almost undoubtedly smaller than this since strong chloride adsorption will inevitably diminish  $\Gamma_{\text{C10}_{\downarrow}}^{'}$  substantially. The errors in  $\Gamma_{X}^{'}$  are likely to be negligible for smaller values of x and with the other adsorbing anions. Admittedly, the presence of the perchlorate may still influence the values of  $\Gamma_{X}^{'}$  from Equation 3.3 but the analysis errors themselves appear to be minor.

Interaction parameters and standard free energies of adsorption at  $\sigma^{m} = 0$  were calculated for each ion by fitting surface concentration data to the Frumkin isotherm (Equation 1.9) with standard states of 1 molecule cm<sup>-2</sup> for the adsorbate and 1 mole liter<sup>-1</sup> for the anion in bulk solution. The effective potential of zero charge in 0.5 M NaClO<sub>4</sub> was taken as -930 mV. The results for electropolished and roughened polycrystalline silver are listed in Table 3.2 together with Valette's findings for chloride<sup>95,111</sup> and bromide<sup>111,112</sup> at single crystals.

# C. <u>Surface Crystallographic Changes Induced by Electrochemical</u> Roughening

In addition to yielding quantitative information on the extent of specific ionic adsorption, the  $\mathbf{C_d}$ -E curves can also provide useful

Table 3.2 Standard Free Energies of Adsorption  $\triangle G_a^0(kJ \text{ mole}^{-1})$  for Anions at Various Silver Surfaces

<u>Electrode</u>	<u>Adsorbate</u> <sup>a</sup>	$G_{\mathbf{a}}^{\mathbf{O}}$	8
polycrystalline silver (smooth)	C1-(0.5 M NaC104)	-95	90
polycrystalline silver (smooth)	Br (0.5 <u>M</u> NaClO <sub>4</sub> )	~-101	50
polycrystalline silver (smooth)	N <sub>3</sub> (0.5 <u>M</u> NaClO <sub>4</sub> )	- 95	70
roughened silver (RF 2)	C1 (0.5 <u>M</u> NaC10 <sub>4</sub> )	- 92	90
roughened silver (RF 2)	Br (0.5 <u>M</u> NaClO <sub>4</sub> )	-100	40
roughened silver (RF 2)	N <sub>3</sub> (0.5 <u>M</u> NaClO <sub>4</sub> )	- 94	14
(111) silver	C1 (0.04 <u>M</u> NaF)	-100 <sup>b</sup>	
(110) silver	C1 (0.04 <u>M</u> NaF)	- 95 <sup>b</sup>	
(100) silver	C1 (0.04 <u>M</u> NaF)	- 93 <sup>b</sup>	
(110) silver	C1 (0.04 <u>M</u> KPF <sub>6</sub> )	- 93.5 <sup>c</sup>	160
(110) silver	Br (0.04 <u>M</u> NaF)	- 98 <sup>d</sup>	40
(110) silver	Br (0.04 <u>M</u> KPF <sub>6</sub> )	- 99 <sup>c</sup>	45

a. Base electrolyte listed in parentheses. b. From reference 95, based on a virial isotherm. c. Calculated from data given in reference 111. d. Calculated from data given in reference 112.

clues to the crystallographic nature of the metal surface. Thus the shapes of the  $C_d$ -E curves obtained at single-crystal silver electrodes can be diagnostic of the particular crystallographic orientation exposed at the surface. 44,95,98 Moreover, a number of well defined capacitance peaks are obtained in chloride and bromide electrolytes whose shape and potential are characteristic of the surface crystallographic orientation. 95,98 This suggests that comparisons of  $C_d$ -E curves obtained for polycrystalline and various single-crystal surfaces in a given electrolyte could provide information on the crystallographic components of the former surface, and shed light on the structural changes induced by electrochemical roughening.

The major featurs of the C<sub>d</sub>-E curves in, for example 0.1 M chloride at electropolished silver in Figure 3A, are a shoulder at -1000 mV (feature I), a major peak with a sharp summit at -550 mV (II), and a sharp peak at -100 mV (III). Upon roughening the electrode (Figure 3.3B), features I and II become more pronounced, and III is diminished. A C<sub>d</sub>-E curve with similar features to those in Figure 3.3B was also obtained by Fleischmann et al. for highly roughened silver (RF = 15) in 0.1 M NaCl. 98 Comparisons with the C<sub>d</sub>-E curves obtained for comparable chloride concentrations at silver surfaces having (111), (100), and (110) orientations 95,98 reveal that feature I closely resembles that found for (110) crystallites, feature III with (100), and feature III with (111) crystallites. Sketches of surfaces possessing (111), (100) and (110) orientations are shown in Figure 3.12. The Miller index notation for face centered cubic crystals is used. It appears that electrochemical roughening in chloride media results in an

increase in the proportion of facets resembling (100) and (110), and a decrease in those resembling (111) crystallites.

The C<sub>d</sub>-E curves for bromide electrolytes are consistent with this interpretation. The two main features at electropolished polycrystalline silver in 0.1 M bromide (Figure 3.5A) are a shoulder at ca. -1150 mV (I) and a major broad peak at -800 mV (II). Roughening the electrode (Figures 3.5B,C) results in little change in II but yields a significant increase in I. Comparison with corresponding single crystal data 95 suggests that feature II is probably formed from a composite of closely overlapping peaks from several low-index faces, whereas I is predominantly associated with the (110) and (100) faces. These and possibly other higher index planes therefore seem to be more prevalent on the roughened surfaces. This finding seems reasonable since metal oxidation and rapid redeposition would be expected to produce a relatively "loose" and somewhat disordered surface, with a smaller proportion of the most densely packed (111) plane.

Nevertheless it should be noted that the overall changes, both in the shapes of the C<sub>d</sub>-E curves themselves and in the surface anion concentrations induced by even quite extensive surface roughening are surprisingly mild, the major effect being simply to enhance the effective surface area. Thus, although the morphology of the surface at the 1 micron level that is probed by scanning electron microscopy is strikingly altered by electrochemical roughening 113 it appears that such large-scale surface reconstruction gives rise to only relatively minor alterations in the average crystallographic structure as well as in the average double-layer composition.

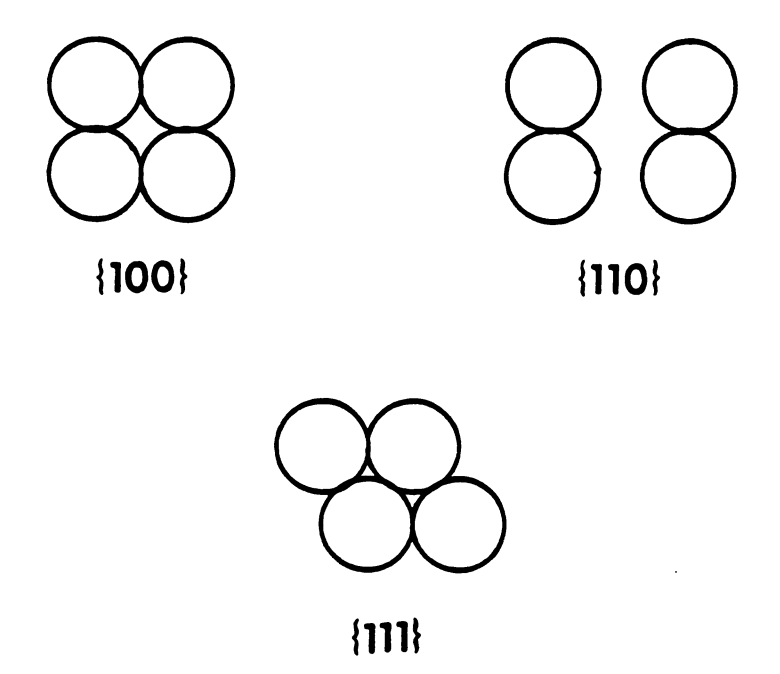


Figure 3.12. Atomic positions of the (100), (110) and (111) faces in the fcc structure (after Hamelin, et al., reference 1).

# d. Implications for Surface-Enhanced Raman Scattering

The enormous increases in the intensity of SERS brought about by electrochemical roughening of the type and magnitude employed here 114 stand in sharp contrast to the relatively moderate (1.5-to 4-fold) increases in the actual surface areas and the minor changes in the surface concentration of adsorbed anions. This implies that the role of surface roughness in promoting SERS is to enhance greatly the inelastic scattering efficiency of the adsorbate scattering centers, in harmony with commonly held views. 8,114 Nevertheless, it is of considerable interest to ascertain the functional relationships, if any, between the intensity and nature (frequency, bandshape) of the Raman scattering and the average surface concentration of the Raman-active adsorbate.

The adsorption data presented here show that substantial specific adsorption of a number of anions occurs even at strongly negative potentials. Thus in the range of adsorbate concentrations  $0.01\text{-}0.1\,\text{M}$ , bromide, iodide, and thiocyanate are adsorbed with coverages above half a monolayer at potentials positive of about -800, -1150, and -1100 mV, judging by the position of the major peaks in the  $C_d$ -E curves (Figures 3.5-3.8). Although stable SERS signals are observed for these anions at potentials close to the anodic limit, ca. 0 to -250 mV, the scattering intensity is found to diminish to small or even imperceptible levels upon shifting the potential to these more negative values.  $^{97,115-117}$  Moreover, as noted above for chloride, scanning the potential to such negative values and returning yields negligible hysteresis in the  $C_d$ -E curves and hence the  $\Gamma_y$ -E plots, yet the SERS

signals are almost entirely irreversibly quenched upon the return scan. 97,116,117 Further. comparisons between the present adsorption data and SERS spectra obtained under comparable conditions as a function of electrode potential for chloride, bromide. iodide. 115 thiocyanate. 95,117 and azide 118 indicate that in each case the Raman signals at a previously roughened silver electrode become markedly and irreversibly weaker as the potential is shifted negative only to the point where the anion coverage falls significantly below a monolayer. as signaled by an increase in C, towards the major C,-E peak. This result holds for Raman signals associated with both metal surfaceligand and internal vibrational modes. From Figures 3.3B, 3.5B and C. 3.7B, 3.8B, and 3.10B these potentials for x = 0.01 M are ca. -200, -500. -900. -900. and +100 mV for chloride, bromide, iodide, thiocyanate, and azide, respectively. For azide, a monolayer is only formed close to the onset of metal dissolution at ca. 150 mV; indeed stable SERS spectra for this anion are not seen at more negative potentials 117 even though extensive azide adsorption occurs as far negative as ca. -800 mV (Figure 3.11).

A likely explanation for this surprising behavior is that the most efficient Raman scattering occurs from specific surface sites associated with particular morphologies, probably small metal clusters which are metastable with respect to incorporation into the metal lattice. At adsorbate coverages close to a monolayer, anions will bind to these sites giving rise to SERS and will also occupy the large majority of nearby metal lattice sites. Although not contributing to the observed Raman signal, the latter adsorbate can stabilize the

Raman-active clusters by preventing their dissipation into the surrounding lattice. Altering the potential to sufficiently negative values so that a fraction of this adsorbate is desorbed will provide lattice positions into which the least stable clusters can rearrange, leading to an irreversible decrease in the Raman intensity. However, judging by the essentially reversible nature of the C<sub>d</sub>-E curves, this rearrangement process appears to involve only a small fraction of the metal surface.

These considerations provoke the desirability of examining the potential dependence of SERS on time scales that are sufficiently short that the irreversible decay of the Raman signal does not occur. Data gathered under such conditions, largely using a spectrograph optical multichannel analyzer arrangement for rapid time resolution, are starting to appear. 97,102,119 In Figure 3.13 electrochemically determined surface coverages (a value of 1.0 corresponds to a monolayer) and relative Raman scattering intensities for chloride at silver are plotted against electrode potential. The SERS data were gathered by Weaver, et al. at the IBM Research Laboratory in San Jose, CA. 102 The intensities are normalized such that a value of 1.0 is obtained at the most positive potentials. A similar plot for bromide at silver is shown in Figure 3.14. Both figures indicate that there is indeed an approximate proportionality between the surface concentration and the Raman intensity for chloride and bromide. However, thiocyanate exhibits somewhat different behavior inasmuch as marked (ca. 3-fold) decreases in Raman intensity for the C-N stretching mode ( $v_{\text{CN}}$ ) occur under reversible conditions when the potential is made more negative in

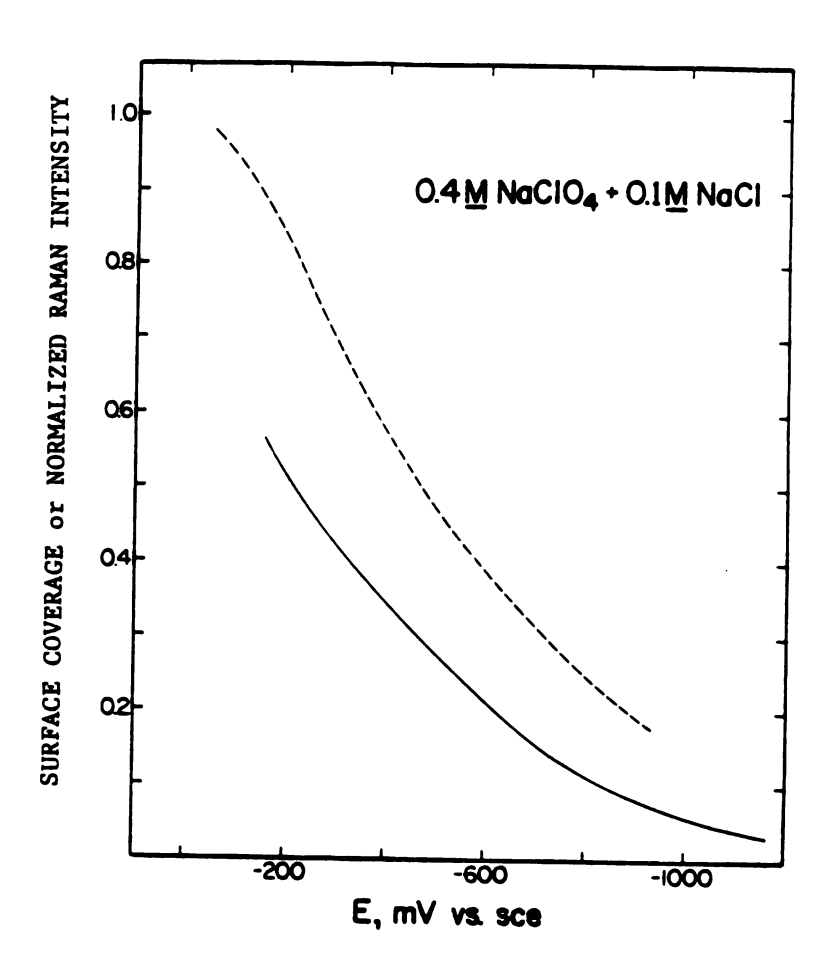


Figure 3.13. Fractional coverage,  $\theta$ , of chloride anions (solid curve) and normalized Raman peak intensity (dashed curve) for Ag-Cl stretching mode, both plotted against electrode potential. Electrolyte is 0.4  $\underline{\text{M}}$  NaClO<sub>4</sub> + 0.1  $\underline{\text{M}}$  NaCl. Raman data from reference 102.

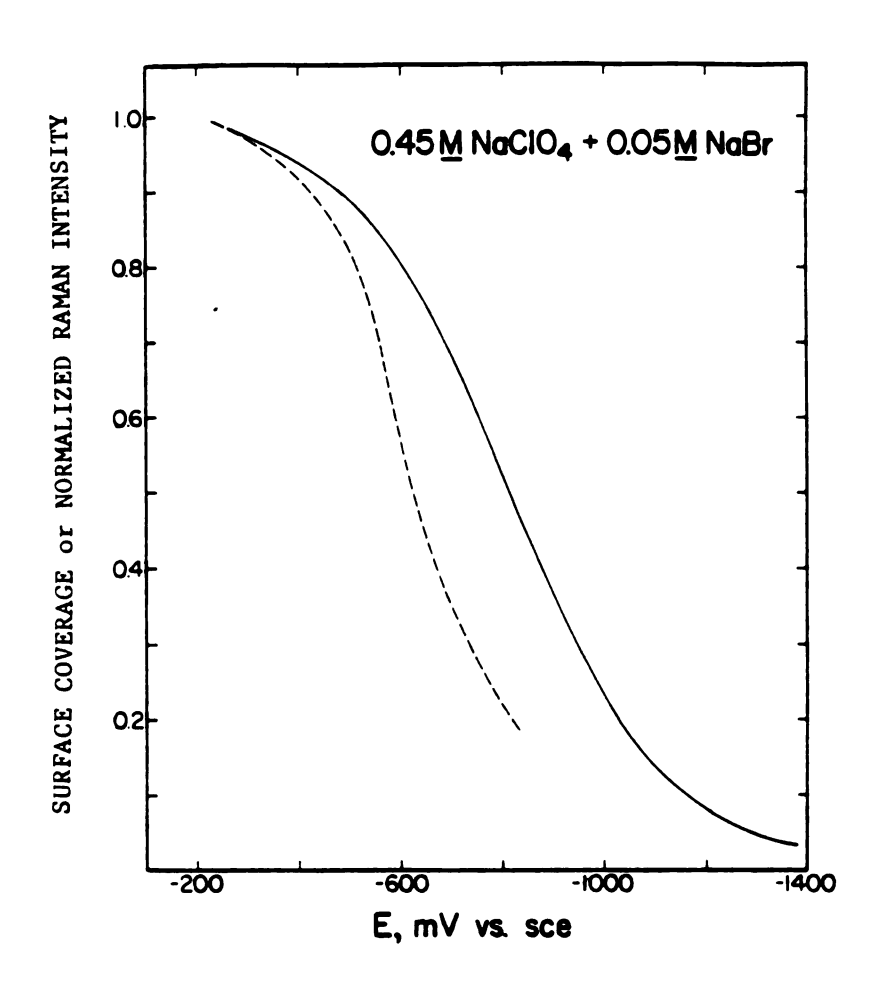


Figure 3.14. Fractional coverage,  $\theta$ , of bromide anions (solid curve) and normalized Raman peak intensity (dashed curve) for Ag-Br stretching mode, both plotted against electrode potential. Electrolyte is 0.45 M NaClO<sub> $\Lambda$ </sub> + 0.05 M NaBr. Raman data from reference 102.

the region ca. -150 to -750 mV<sup>120</sup> even though the thiocyanate coverage is maintained near a monolayer throughout.<sup>97</sup> This behavior may be associated with the potential dependence of thiocyanate orientation that was suggested above.<sup>97</sup> Thus a change in adsorbate surface bonding to a less perpendicular orientation as the potential is made more negative would be expected to yield a decrease in the Raman scattering efficiency of the v<sub>CN</sub> mode since the component of the polarization vector normal to the surface would thereby be diminished.<sup>121</sup>

Finally, it should be noted that considerably (ca. 10-fold) more intense Raman scattering can be obtained for several adsorbed anions such as chloride, bromide, and thiocyanate if the electrode surface is illuminated by the laser beam during the ORC.  $^{122,123}$  Nevertheless, preliminary measurements indicate that such laser illumination has only a small influence upon the  $\rm C_d$ -E curves recorded in the presence of such anions, indicating that only minor changes in both the effective surface area and the anion surface concentrations occur under these conditons.  $^{124}$ 

The observations reported here suggest that there are two main requirements for the observation of stable SERS signals for anions at silver. First, active sites must be generated. Dissolution and redeposition of silver in complexing media evidently accomplishes this. Second, the active sites must be stabilized, e.g. by anion adsorption to the extent of saturation as suggested above. The inability to meet one or both of these requirements may account for the absence of SERS from most other metal electrodes. Thus, lead 125, thallium 126 and other white metals may be SERS-inactive because only small coverages of

anionic adsorbates can be obtained even at the most positive available potentials. Mercury is another SERS-inactive metal exhibiting only weak tendencies to adsorb ions. 127 On the other hand, the difficulty of forming active sites may account for the lack of SERS at noble metals. Although anions are adsorbed extensively at platinum, for example, this material resists dissolution. At gold, SERS is observed only under extreme conditions 128 where metal dissolution (and active site formation?) become possible. In contrast, the SERS effect is well established at copper 129 which, like silver adsorbs anions readily and is easily dissolved and redeposited. Nevertheless, there are indications that other factors such as optical properties of surfaces may contribute to the electrode selectivity of the effect. 8

Although preliminary, the observations at silver point to the desirability of correlating the nature and intensity of SERS signals with the interfacial composition, both from the standpoint of understanding the nature of the SERS effect itself and its utilization as a microscopic probe of electrochemical surface structure. It will clearly be important to study structurally simple adsorbates having known surface concentrations and well-defined bonding geometries in order to unravel the importance of such basic factors as surface concentration, surface bonding and stereochemistry to SERS.

## B. Specific Adsorption of Transition-Metal Complexes at Silver

In addition to simple anions, the adsorption of some transitionmetal complexes at silver was examined. The study was undertaken within the context of the overall group effort to explore the physical phenomena associated with Surface-Enhanced Raman Scattering (SERS) and use the effect to examine electron transfer reactions at surfaces. Such electrochemical measurements provide independent information concerning the surface concentration and redox reactivity of SERS-active molecules. In particular, fast cyclic voltammetry in dilute solutions (50 to  $100~\mu \underline{\text{M}}$ ) of strongly adsorbing complexes represents a powerful and convenient electrochemical means of acquiring such information. 85,130

The molecules studied were Os(NH<sub>3</sub>)<sub>5</sub>pyridine<sup>3+</sup>, Os(NH<sub>3</sub>)<sub>5</sub>pyrazine<sup>3+</sup> and Os(NH<sub>3</sub>)<sub>5</sub>bipyridine<sup>3+</sup>. All three are substitutionally inert and undergo reversible electron transfer at convenient potentials. Shown in Figure 3.15 is a surface cyclic voltammogram (200 V s<sup>-1</sup>) for Os(NH<sub>2</sub>)<sub>5</sub> py<sup>3+</sup> reduction and reoxidation at roughened silver in 0.1 M NaBr + 0.08 M NaCl + 0.02 M HCl. The almost symmetrical shape and near coincidence of the anodic and cathodic peaks, together with the linear dependence of the peak current upon potential (not shown), indicate that the waves arise from adsorbed reactant. From the area underneath the current peaks the surface concentration of the complex is calculated to be about 3 x 10-11 mole cm<sup>-2</sup>. A monolayer would require about 15 to 20 x  $10^{-11}$  mole cm<sup>-2</sup> for a "vertical" orientation with adsorption via the pyridine ring. The peak width at half height is 125 mV. This is greater than the value of 90 mV expected for Langmuir adsorption and indicates that repulsive interactions exist between adsorbed molecules. 33

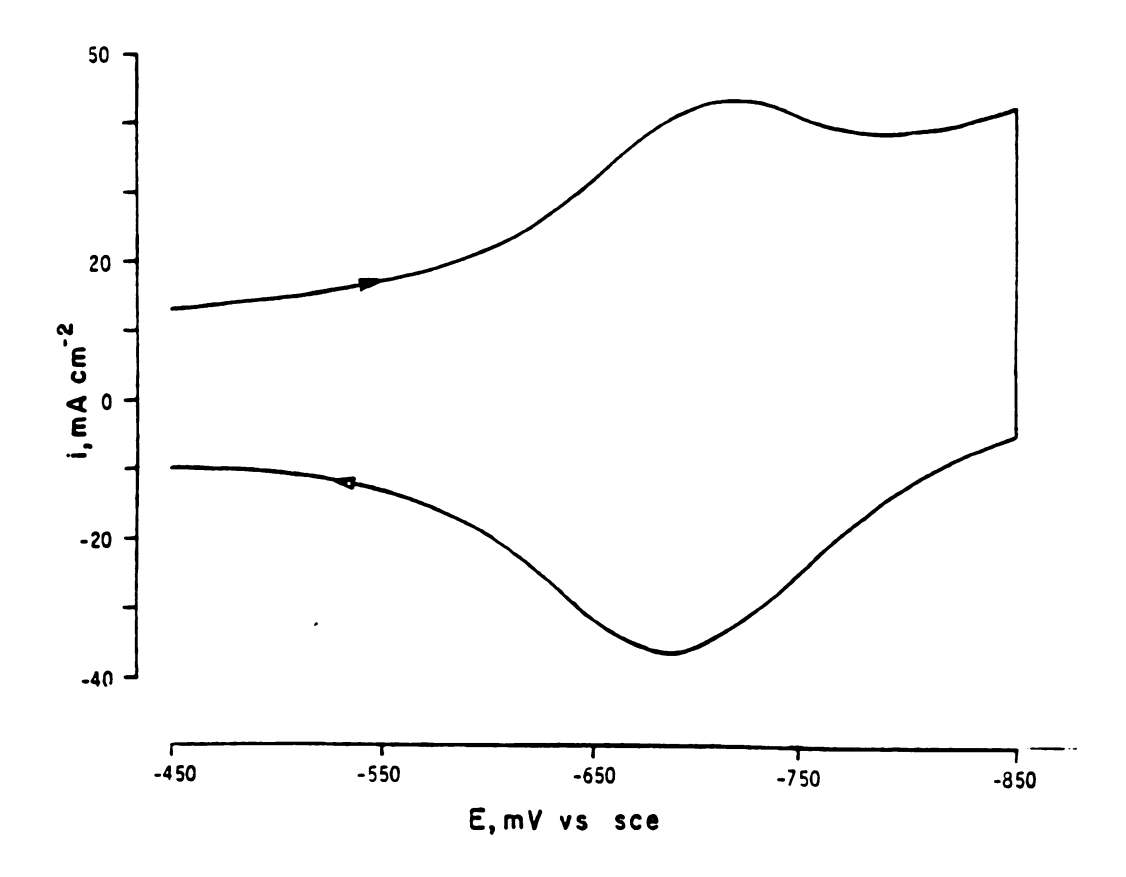


Figure 3.15. Cathodic-anodic voltammogram for adsorbed  $Os(NH_3)_5 py^{III/II}$  redox couple at roughened silver-aqueous interface in 0.1 M NaBr + 0.08 M NaCl + 0.02 M HCl. Electrode roughened by means of an oxidation-reduction cycle in this supporting electrolyte; (roughness factor ca. 1.8 on basis of capacitance measurements). Bulk  $Os^{III}(NH_3)_5 py$  concentration = 50  $\mu M$ ; sweep rate = 100 V sec<sup>-1</sup>.

From the average peak potential a surface formal potential, Ef, of -705 mV is inferred. This is significantly negative of the bulk solution formal potential of -650 mV 131 and indicates that the complex is bound more strongly in the Os(III) than in the Os(II) state. Interestingly, in 0.1 M NaCl + 0.1 M HCl the surface formal potential is shifted to -670 mV (Figure 3.16). The 35 mV difference in  $E_a^f$  values may well represent the influence of the double layer on the surface redox thermodynamics. Thus, the presence of the electrical double layer subjects the adsorbed reactant to an electrostatic interaction with the charge at the electrode surface. Addition of an electron to the reactant reduces its charge and therefore its interaction with the electrode charge. For a one-electron reduction of an adsorbed cationic complex the difference in electrostatic interactions for the oxidized versus the reduced state should yield a change in surface formal potential of  $\phi$ . Recall that  $\phi$  is determined to a first approximation by the total charge,  $\sigma^m + F\Gamma$ , at the surface (see Equation 1.11). In both chloride and bromide electrolytes the total charge, and therefore  $\boldsymbol{\varphi}_{_{\boldsymbol{T}}},$  should be negative (see Section III. A), but  $\boldsymbol{\varphi}_{_{\boldsymbol{T}}}$  should be more negative in the latter, thereby yielding a shift of  $\mathbf{E}_{a}^{f}$  in the observed direction.

The influence of electrode potential on the amount of adsorption of  $0s(NH_3)_5py^{3+}$  was investigated by selecting different initial potentials for the fast cyclic voltammetry measurements, as shown in Figure 3.16. (With dilute solutions of the reactant and fast sweeps the potential perturbation will "outrun" the adsorption-desorption equilibrium and provide a measure of the extent of adsorption at the

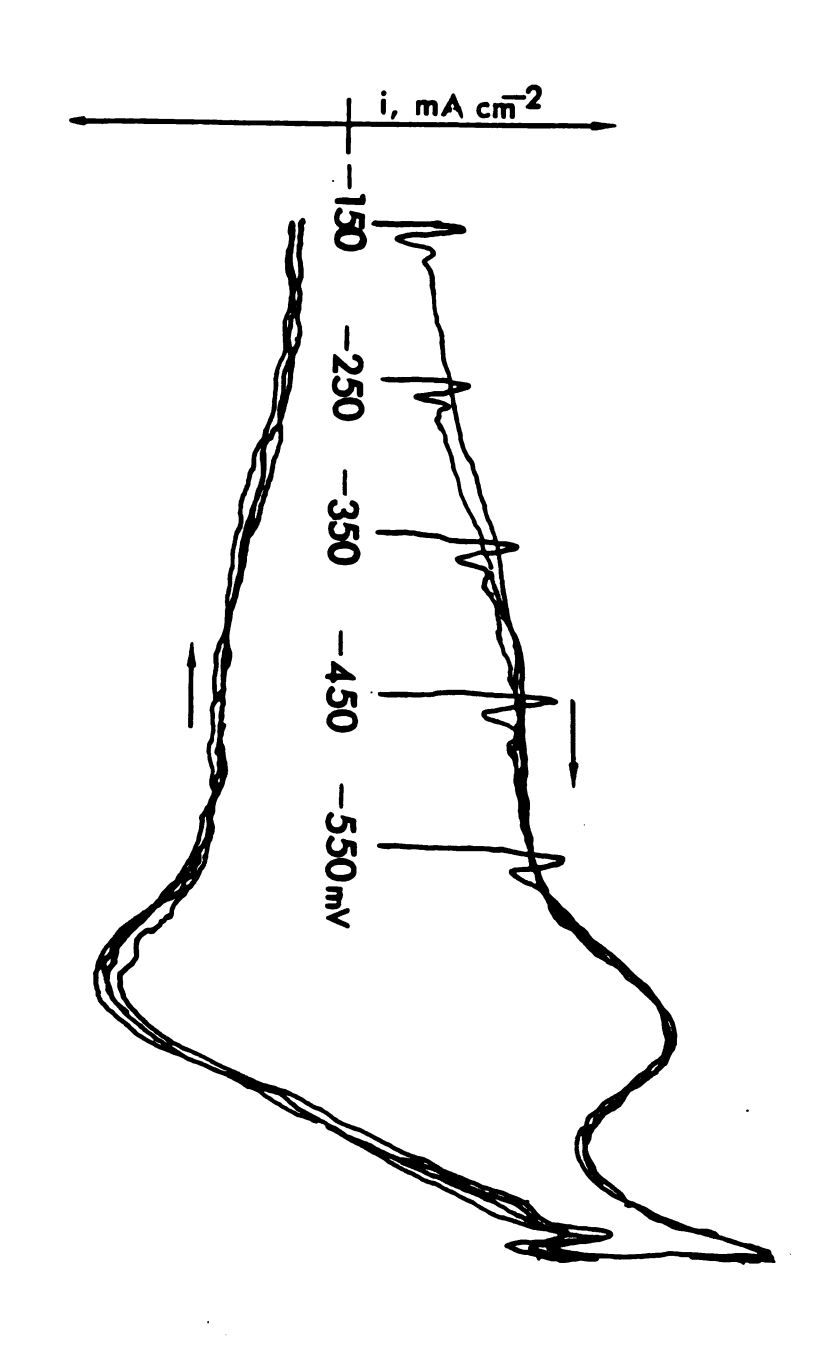


Figure 3.16. Cyclic voltammetry of surface bound Os(NH<sub>3</sub>)<sub>5</sub>py III/II in 80 mM NaCl + 20 mM HCl. each sweep are indicated. Sweep rate = 50 V sec<sup>-1</sup>. Bulk Os<sup>III</sup>(NH<sub>3</sub>)<sub>5</sub>py concentration = 50  $\mu$ M. Silver electrode was roughened by means of an oxidation-reduction cycle. Initial potentials for

initial potential, as demonstrated by Guyer<sup>85</sup>). Surprisingly, the adsorption of Os(NH<sub>3</sub>)<sub>5</sub>py<sup>3+</sup> shows little sensitivity to electrode potential.

Surprisingly,  $Os(NH_3)_5$  pyrazine<sup>3+</sup> adsorption was barely detectable despite the availability of an uncoordinated nitrogen which might be expected to bind to silver. One possibility is that the complex actually is adsorbed to a considerable extent via the nitrogen, but is electrochemically inactive due to a shift of  $E_a^f$  to a value positive of -100 mV. According to this interpretation, the  $E_a^f$  value of -330 mV in 0.1 M NaCl would correspond to a minor component adsorbed in a less favorable configuration. The solution formal potential  $E_b^f$  reportedly equals -240mV. 132

For  $0s(NH_3)_5bpy^{3+/2+}$  in 0.1 M NaCl,  $E_a^f$  equals -490 mV, while  $E_b^f$  is reported to be -465mV. <sup>132</sup> For a description of the corresponding SERS studies of osmium redox couples the reader is referred to the publications of Farquharson, Lay and Weaver. <sup>131,132</sup>

C. The Influence of Lead Underpotential Deposition on the

Capacitance of the Silver-Aqueous Interface

[Originally published in J. Electroanal. Chem., 131, 299 (1982)]

#### 1. Introduction

The chemical composition of the metal substrate is known to play an important role in determining the thermodynamic properties of metalelectrolyte interfaces, as evidenced by the large changes in doublelayer capacitance and the potential of zero charge (pzc) that are generally observed when the electrode material is altered. <sup>130</sup> At least under conditions where the extent of ionic specific adsorption is small, the variations have been attributed to a combination of the electronic properties of the metal (work function) together with differences in the orientation of solvent dipoles in the inner-layer region. <sup>133</sup> A difficulty in comparing the experimental data obtained to date is that the substitution of one pure metal substrate for another represents a fairly drastic change in system state.

A method of varying the metallic composition of an electrode surface is a more subtle manner is to deposit varying quantities of one metal on to a different metal substrate. A number of systems of this type involve "underpotential deposition" (UPD) of the metal in submonolayer amounts; <sup>134</sup> this facilitates the preparation of surfaces in situ whose composition can be varied in a systematic and controllable way from the pure substrate through to a monolayer of deposited metal and beyond. In particular, the comparison of the double layer properties of the pure substrate with those for surfaces having monolayer and multilayer quantities of the depositing metal should enable an assessment to be made of the relative structural influences of the surface atomic layer and the underlying bulk metal.

Nevertheless, to our knowledge, there are no previous reports of the determination of the double-layer capacitance at electrodes containing such UPD layers. (Since this work was published, a report has appeared by Bruckenstein describing capacitance measurements at UPD silver on gold). We have recently been investigating the kinetics of simple inorganic electrode reactions at various metal surfaces in

order to explore the possible influences of the electrode material upon the reaction energetics. In conjunction with these studies, we have obtained double-layer structural data at polycrystalline silver and lead electrodes in a variety of aqueous electrolytes, including adsorption data for a number of anions and transition-metal complexes. 86,136 It has been shown that lead forms stable UPD layers on a silver substrate. The conditions necessary for their formation and some properties of these layers are well established. 2,86,137,138 We have therefore chosen to study the double-layer capacitance of electrode surfaces formed by the deposition of varying amounts of lead on a silver substrate in aqueous sodium perchlorate and sodium fluoride media. These electrolytes were chosen since it was expected that fluoride and perchlorate ions would be only weakly adsorbed. Initially it was suspected that the insolubility of lead fluoride would preclude measurements in concentrated fluoride electrolytes, but no difficulties were encountered. Capacitance-potential plots were determined for lead layers with coverages both below and above monolayer levels. These results are presented in this section.

#### 2. Electrode Preparation

The UPD lead electrodes were prepared using the following novel procedure. The pretreated silver electrode was attached to a rotating disk electrode assembly (Model ASR2 rotator, Pine Instruments, Inc.), then introduced into the cell containing the appropriate electrolyte and the differential capacitance C determined as a function of electrode potential E. Sufficient acidic lead fluoride solution was

then added to bring the lead concentration in the cell to between 0.2 and 0.6  $\mu$  M. (In the initial experiments the solutions were made slightly acidic, pH 3.5, to minimize adsorption of lead onto the glass cell walls. 139 This was later found to be unnecessary.) The electrode potential was then set such that it was negative of the value required for UPD but positive of that required for bulk lead deposition. (The exact potentials used were of course dependent on the lead ion concentration in solution). The rotator was then turned on (a rotation speed of 600 rpm being used in all experiments) and the electrode held at the preset potential for a known time (ca 10 minutes). At the end of this period the deposited lead was stripped off using an anodic linear potential sweep and the current-potential profile recorded. procedure was repeated using gradually longer formation times until a UPD monolayer was deposited. This point was determined as that beyond which the size of the anodic stripping peak no longer increased with time. A typical stripping curve is shown in Figure 3.17 (curve a).

It was desired to determine the differential capacitance C of the UPD layer over as wide a range of electrode potential E as possible at a series of constant lead coverages. Therefore it was necessary for the layer once formed to be stable over the period of time (ca. 20 minutes) required to obtain a complete set of C versus E measurements for a particular electrode and solution composition. Initially, attempts were made to avoid further deposition of lead by transferring the electrode to another solution free of  $Pb^{2+}$ . This method was only partly successful. However, it was subsequently discovered that if only very small (<1  $\mu$  M) bulk concentrations of  $Pb^{2+}$  were employed

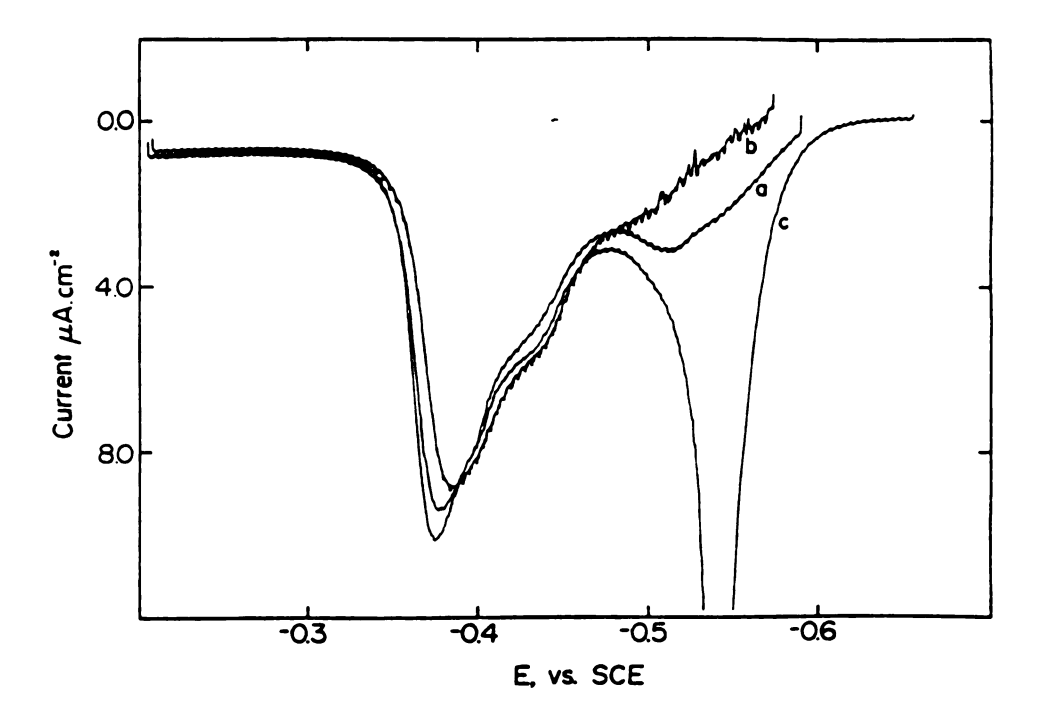


Figure 3.17. Linear sweep current-potential curves for anodic removal of lead layer deposited on silver. Sweep rate was 5 mV sec<sup>-1</sup>, electrode rotated at 600 r.p.m. Electrolyte was 0.5 M NaClO<sub>4</sub> adjusted to pH 3.5 with HClO<sub>4</sub>, containing 0.6 μM Pb<sup>2+</sup>. Lead deposits corresponding to anodic stripping curves (a)-(c) formed as follows: (a) Electrode rotated at 600 r.p.m., held at -0.585 V for 10 minutes. (b) As (a), but held at -1.20 V for additional 20 minutes with no rotation. (c) Electrode rotated at 600 r.p.m., held at -0.65 v for 10 minutes.

to form the UPD layers, no further significant lead deposition occurred during the time required to perform the capacitance measurements if the electrode rotator was turned off and the solution unstirred. This was true even at potentials sufficiently negative so that the deposition of "bulk" lead can occur. A typical result is shown in Figure 3.17 (curve b). It is seen that the stripping curves a and b are almost identical. even though the electrode was held at -1.2 V for an additional 20 minutes without rotation prior to recording the latter curve. In experiments where a monolayer or less of UPD lead was formed, the alteration in coverage during the time required to perform the capacitance measurements generally amounted to less than 2-3%. On the other hand, rotation of the electrode allowed the deposition of lead to occur at a controlled rate, even at potentials where bulk lead was deposited. The presence of bulk, in addition to UPD lead deposits were determined from the appearance of a second peak on the anodic stripping curve at potentials less positive than those required for the dissolution of UPD lead (curve c in Figure 3.17).

The extent of UPD and bulk lead deposition was determined individually from the coulombic charge under the stripping curves. The fractional coverage of UPD lead was determined from the ratio of the anodic charge required to strip the layer to the charge required to remove a monolayer. This method involves the assumption that the so-called "electrosorption valency" of the deposited lead is independent of the coverage  $\theta$ . Although this is unlikely to be entirely correct, the error so introduced is unlikely to be major; for UPD lead on silver the electrosorption valency has been found to be close to the value

(2.0) expected for the electrodeposition of ordinary lead. 137

## 3. Results

Figure 3.18 summarizes typical plots of the differential electrode capacitance C against the electrode potential E for polycrystalline silver (curve a), a monolayer of UPD lead on silver (curve b), UPD lead with additional (ca two monolayers) bulk lead deposit (curve c), and polycrystalline bulk lead (curve d), each immersed in aqueous 0.5 M sodium perchlorate. This large ionic strength was chosen so to minimize the influence of the diffuse layer. The dashed part of curve b represents the potential region where the UPD layer coverage falls progressively below unity as the potential becomes less negative, eventually (at about -0.3 V) being removed entirely. Anodic removal of the lead deposits gave silver surfaces that exhibited C-E curves that were very similar (C within ca 10%) to those for the original silver surface, indicating that lead deposition did not produce any noticeable irreversible changes in the surface structure.

The dependence of C upon the ionic strength is shown in Figure 3.19 for UPD lead (curves a-d) and bulk lead (curves a', d'). In each case, there are close similarities between the corresponding C-E curves for UPD and bulk lead, 136 the capacitance generally being substantially smaller than for bulk silver. Also, as expected, the deposition of lead beyond a monolayer (i.e. forming "bulk" rather than UPD lead layers) yielded C-E curves that are very similar to those for polycrystalline bulk lead (Figure 3.17).

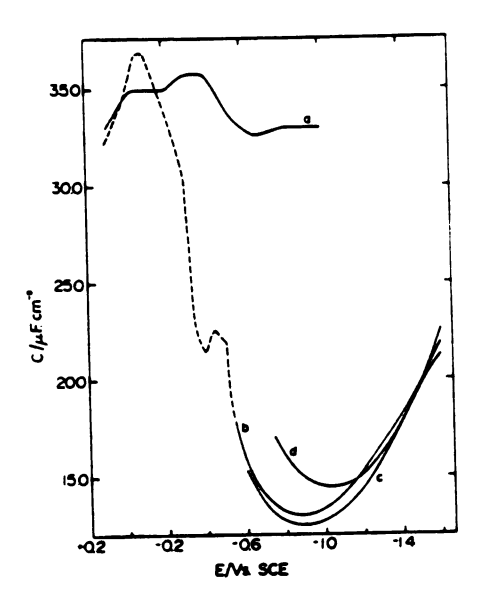


Figure 3.18. Differential electrode capacitance C versus electrode potential E for: (a) polycrystalline silver; (b) silver containing a monolayer of UPD lead; (c) as in (b) but with additional ca. 2 monolayers of bulk lead deposit; (d) polycrystalline lead. Lead layer prepared as indicated in caption to Figure 3.17 and the text. Electrolyte was  $0.5 \, \underline{\text{M}} \, \text{NaClO}_4$ , pH = 3.5; for (b) and (c) additionally contained  $0.6 \, \mu \underline{\text{M}} \, \text{Pb}^{2+}$ .

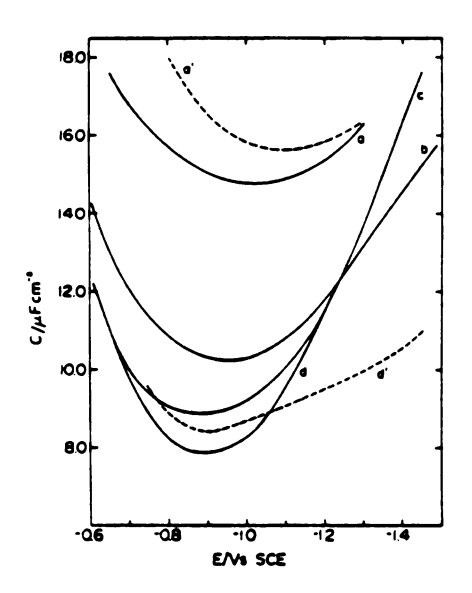


Figure 3.19. Differential electrode capacitance C versus electrode potential E for a monolayer of UPD lead on polycrystalline silver (curves a - d) and for polycrystalline bulk lead (curves a' - d') as a function of ionic strength of sodium perchlorate, adjusted to pH 3.5. Concentration NaClO<sub>4</sub>: (a,a') 0.5 M; (b) 0.1 M; (c) 0.05 M; (d,d') 0.01 M.

The double-layer capacitance was also measured in several sodium fluoride solutions. The values are slightly smaller than those obtained in NaClO<sub>4</sub> solutions. In dilute solutions (10 mm) the capacitance minimum occurs at about -0.80 V, compared with -0.9 V in NaClO<sub>4</sub>.

The capacitance data for silver are in reasonable agreement with earlier results. 140 The capacitance values for bulk lead are somewhat smaller than obtained earlier. 141 This discrepancy is probably due to differences in the electrode pretreatment methods employed. 136

The influence of submonolayer UPD lead on the C-E curves for a silver substrate in 0.5  $\underline{\text{M}}$  NaClO<sub>4</sub> is summarized in Figure 3.20. It is seen that capacitance values that are markedly closer to bulk lead than silver are obtained for UPD coverages as low as 35%.

# 4. Discussion

Taken together, the results presented in Figures 3.18 through 3.20 demonstrate that UPD lead having coverages in the vicinity of a monolayer and beyond exhibit double layer properties that are very similar to bulk lead, and very different from that obtained for the silver substrate. Admittedly, some differences are observed: the capacitances tend to be somewhat larger for the bulk lead electrode with a minimum at significantly (ca. 0.1 V) more negative potentials. However, the disparities are relatively minor and may well reflect differences in surface pretreatment rather than inherent structural dissimilarities.

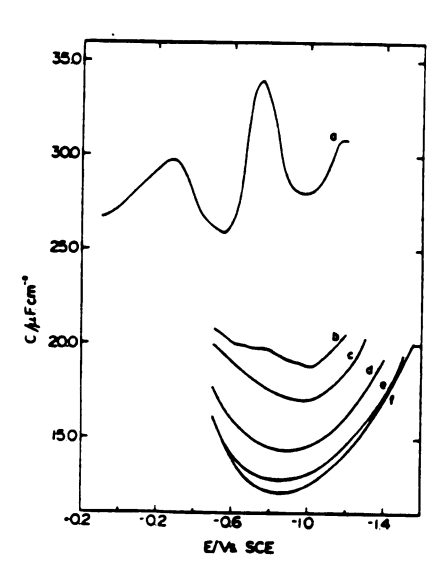


Figure 3.20. Differential electrode capacitance C versus electrode potential E for UPD lead layer on polycrystalline silver having various coverages of lead. Electrolyte was 0.5 M NaClO<sub>4</sub>, pH 3.5, with 0.6 µM Pb<sup>2+</sup>. Lead coverage (percentage of monolayer): (a) 0%; (b) 22%; (c) 35%; (d) 61%; (e) 93%; (f) 100%.

Assuming that fluoride specific adsorption is absent, the broad minimum at -0.80 V in dilute solutions can be identified as the effective potential of zero charge. This agrees essentially exactly with the findings for bulk lead, but represents a shift of about +0.13 V from that found for silver. These conclusions represent a slight correction to our previous assertion 101 that the minimum at -0.9 V in dilute sodium perchlorate solutions corresponds to the effective pzc. The 0.1 V difference between C-E curves in NaF compared to NaClO<sub>4</sub> solutions can now be taken as evidence of perchlorate anion specific adsorption. The slightly larger capacitance values at the most positive potentials in 0.5 M NaClO<sub>4</sub> compared with 0.5 M NaF are another indication of ClO<sub>6</sub> specific adsorption.

From these results, the structure of the double layer for these systems, as determined by the electrode capacitance and the potential of zero charge, seems to be determined primarily by the composition of the first atomic layer, and is surprisingly insensitive to the nature of the underlying metal substrate. This may occur because the double-layer properties arise chiefly from the interaction between the inner-layer water molecules and the surface metallic layer. Since the electrosorption valency for lead on silver has been found to be close to that expected for bulk lead, and the magnitude of the UPD effect for the Pb/Ag system is relatively small (0.16 V),  $^{134}$  it seems plausible that the nature of the water-surface interactions for UPD and bulk lead could be similar. It would be most interesting to gather corresponding data for UPD systems such as Ag/Au and Pb/Au for which the underpotential effect is larger than for Pb/Ag,  $^{134}$ 

Another facet of the present results is that they suggest that a useful way of obtaining comparative double-layer data at different surfaces would be to employ the most noble surface as a substrate upon which the other surfaces to be compared could be formed by electrodeposition. Such an approach avoids the uncertainties arising from differences in roughness factor, pretreatment, electrode geometry, etc., that are inevitable when double layer parameters for two different electrode materials are compared. Thus the data in Figure 3.18 clearly indicate that the double layer capacitances are at least a factor of two smaller at lead than at silver, at least in the potential region (-0.8 V to -1.0 V) where specific ionic adsorption is unlikely to provide a major influence. In concentrated, nonadsorbing electrolytes the differential double layer capacitance corresponds approximately to the capacitance of the inner layer of solvent molecules. On the basis of Trassatti's correlation 133c between the inner-layer capacitance at the pzc and the "degree of hydrophilicity" for different metals (i.e. the tendency to orient inner layer water molecules), we suggested 101 that the large capacitance of silver in comparison to UPD lead could be taken as evidence of the hydrophilic nature of the former. In a critical reassessment of Trasatti's work, Valette has shown rather convincingly that there is, in fact, no correlation between the magnitude of the inner layer capacitance and the degree of hydrophilicity. 142 The available evidence indicates that silver is probably one of the least hydrophilic surfaces, while lead is moderately hydrophilic. Although the capacitance data clearly indicate that a substantial change of the inner-layer structure accompanies lead underpotential deposition on silver, evidently they provide no clue to the nature of the restructuring.

One surprising result is the sharp decreases in C seen as the coverage of the UPD lead increases (Figure 3.20). The simplest model for the double-layer structure under such conditions is one where the regions covered by lead and silver contribute to the overall measured capacitance in proportion to the fraction of the structure occupied by each metal. Clearly, that model is not appropriate to the present system. For example, at only 35% coverage of lead, the measured capacitance had decreased roughly three-quarters of the way between the pure silver and lead monolayer values (Figure 3.20). One possible explanation is that the lead is preferentially depositing on one particular crystallographic plane of silver that is chiefly responsible for the larger values of C seen for pure silver, so that coverage of only a fraction of the silver surface by lead atoms would be sufficient to decrease C greatly. However, Valette and Hamelin44 have found that the capacitance of all three major crystallographic planes of silver exhibit similarly large values of C at high ionic strengths in the potential range of interest here (ca. -0.7 to -1.2 V vs. s.c.e.). Therefore some lead deposition on all three crystallographic planes of the polycrystalline silver surface would seem to be necessary in order to fully account for the observed decreases in C. A more likely explanation of the results in Figure 3.20 is that the deposition of individual lead atoms alters significantly the inner-layer structure for a number of surrounding silver atoms. Given the larger atomic radius of lead (1.75 Å) in comparison to silver (1.44Å) 143 it seems

certain that the initially deposited lead atoms must influence water adsorption at more than one, and possibly as many as four, silver atoms depending on the arrangement of the atoms at the surface.

On the basis of the present results, double-layer structural studies of UPD and related metal layers promise to provide a valuable and novel approach for probing the structural details of metal-electrolyte interfaces. Such surfaces can be formed in a highly controllable manner allowing subtle as well as major changes in the surface metallic composition to be made in situ, yielding surfaces of well-defined composition. It would be desirable to extend such measurements to other systems, including single crystal surfaces. In addition, such UPD layers provide a valuable way of systematically altering the properties of the metal surface for the purpose of examining the details of electrocatalytic phenomena. Further double-layer structural data for UPD layers, together with parallel kinetic measurements for simple electrode reactions following both inner-sphere and outer-sphere mechanisms are presented in the following sections.

# D. The Influence of Lead Underpotential Deposition on Anion Adsorption at the Silver-Aqueous Interface

#### 1. Introduction

To understand further the influence of the chemical composition of the metal electrode on the properties of the double layer it is useful to gather thermodynamic data in adsorbing electrolytes. Chiefly for this reason the specific adsorption of several anions has been

examined at silver electrodes which have been carefully modified by in situ underpotential deposition of a monolayer of lead atoms. An additional motivation for examining this problem relates to electron transfer kinetics studies of chromium complexes containing potential bridging ligands (Chapter IV). Direct characterization of the adsorption of such complexes via capacitance measurements is difficult due to their reduction at all but the most positive potentials. However, measures of the specific adsorption of the ligands themselves, in the form of free anions, may provide clues regarding complex adsorption. Finally, it has become evident in recent months that underpotential deposition is a useful means of probing and selectively "titrating" SERS-active sites on roughened silver electrodes. 125,126 Although the chemical state of the silver-aqueous interface is known in a variety of electrolytes from the work in Section III. A, similar information for UPD-modified surfaces is largely lacking.

The specific adsorption of Cl, Br, I, N<sub>3</sub>, NCS and ClO<sub>4</sub> from constant ionic strength NaX + NaF mixtures was examined at UPD Pb/Ag (electropolished) surfaces by measuring capacitance-potential curves and subjecting these to the Hurwitz-Parsons analysis <sup>35,36</sup> (cf. Sections III A and G). The experiments were initially carried out in NaX + NaClO<sub>4</sub> mixtures. However, it was discovered that perchlorate itself is significantly adsorbed. These initial experiments now represent an unintentional, but useful study of the influence of competitive adsorption of the base electrolyte on the specific adsorption of bromide and iodide ions, and are also reported here.

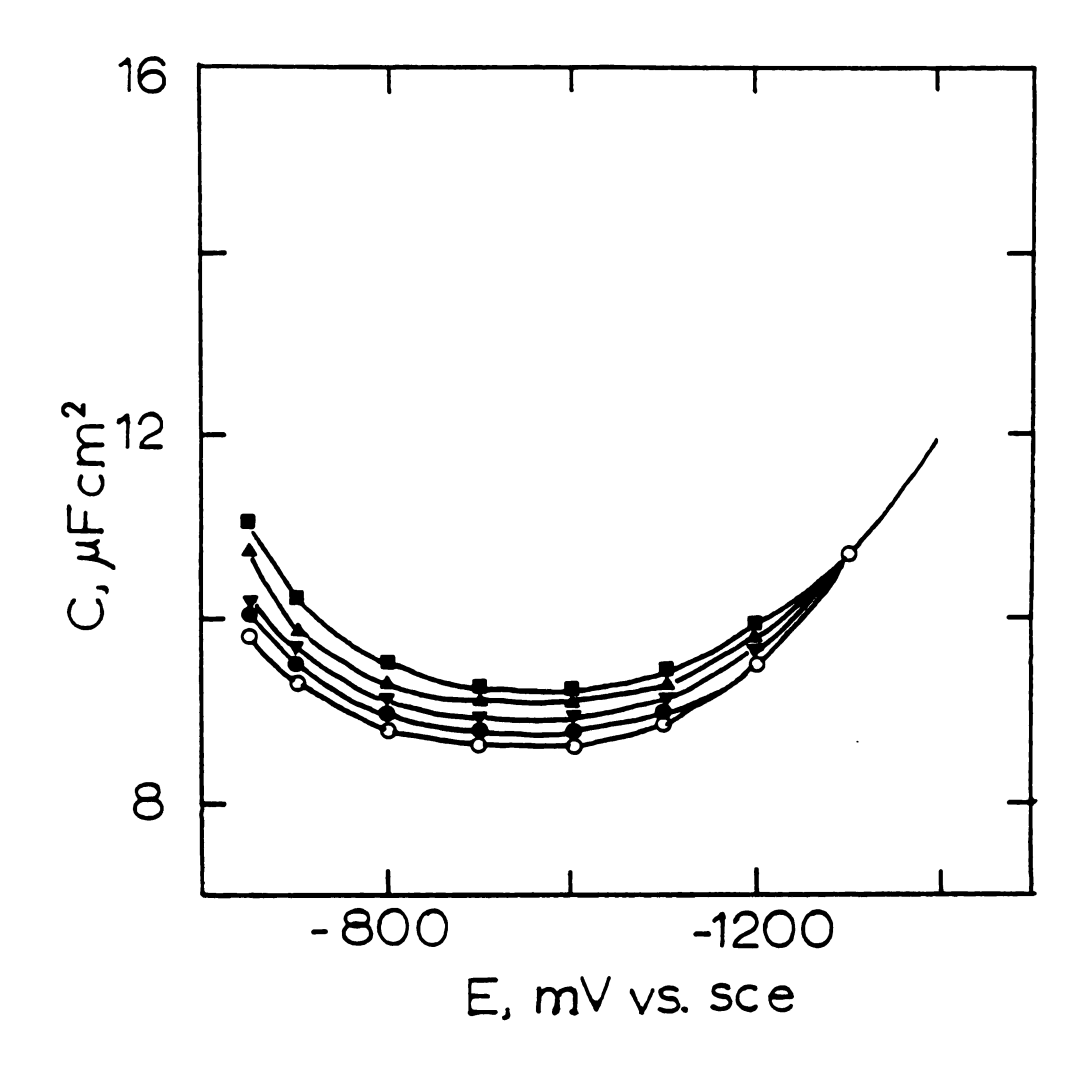


Figure 3.21. Differential capacitance vs. electrode potential for UPD lead/silver in NaCl + NaF mixed electrolytes at an ionic strength of 0.5 M. Key to chloride concentrations: (○) 0 mM; (●) 8 mM; (▼) 20 mM; (▲) 60 mM; (■) 200 mM.

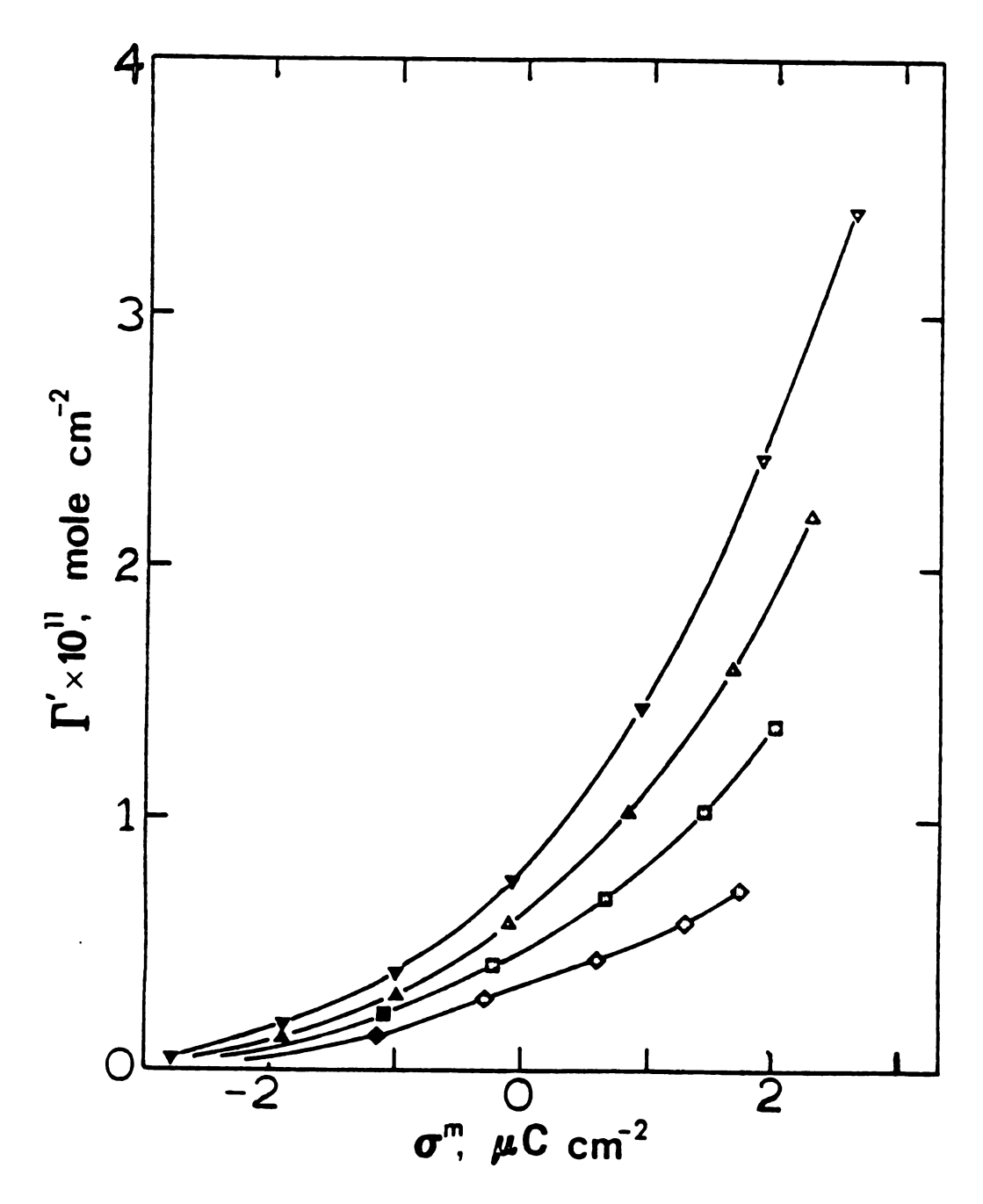


Figure 3.22. Differential capacitance vs. electrode potential for UPD lead/silver in NaBr + NaF mixed electrolytes at an ionic strength of 0.5 M. Key to bromide concentrations: (O) 0 mM; (\*) 3 mM; (\*) 10 mM; (\*) 30 mM.

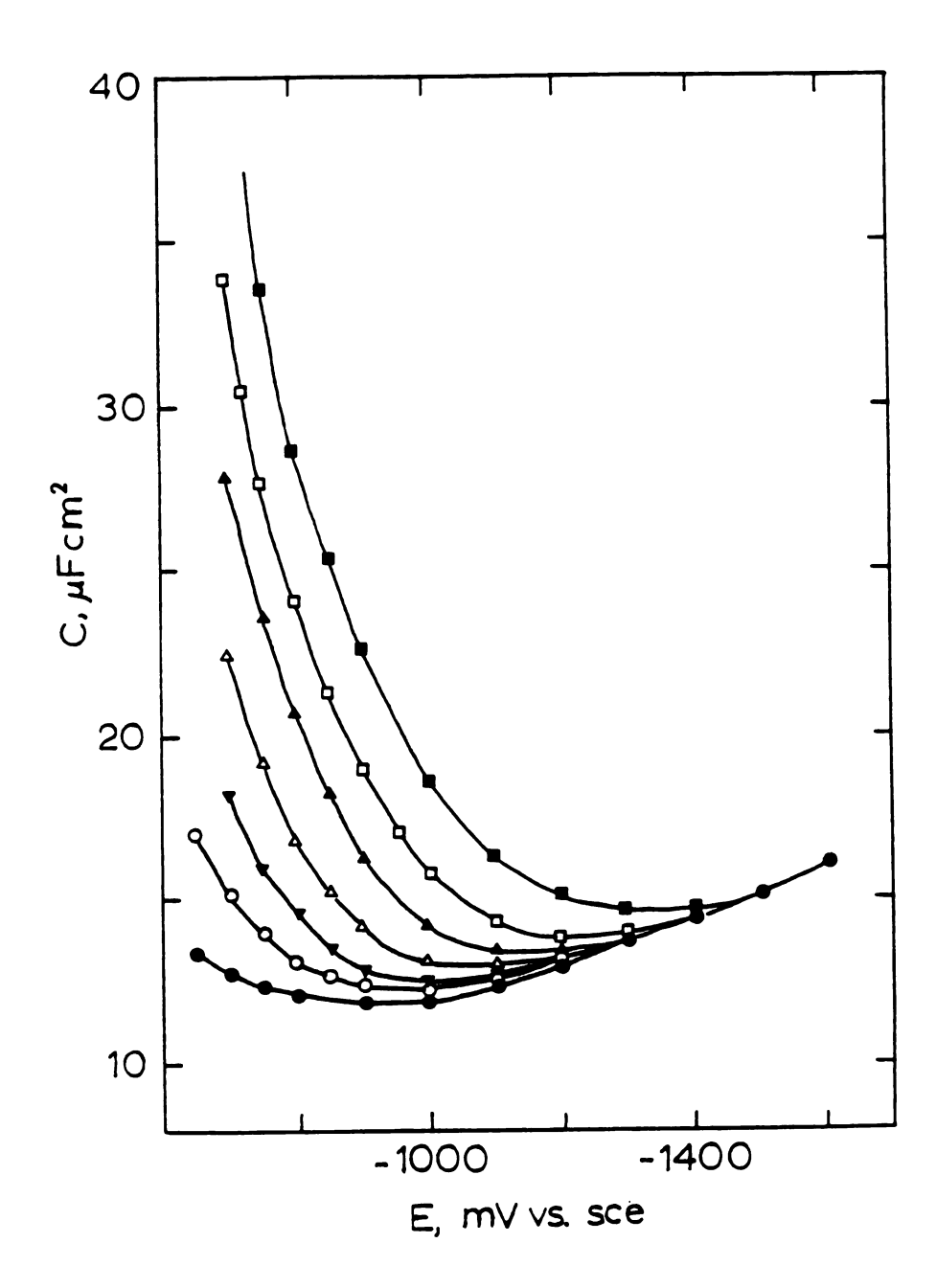


Figure 3.23. Differential capacitance vs. electrode potential for UPD lead/silver in NaI + NaF mixed electrolytes at an ionic strength of 0.5 M. Key to iodide concentrations: (●) 0 mM; (O) 0.3 mM; (▼) 1 mM; (△) 3 mM; (▲) 10 mM; (□) 30 mM; (■) 100 mM.

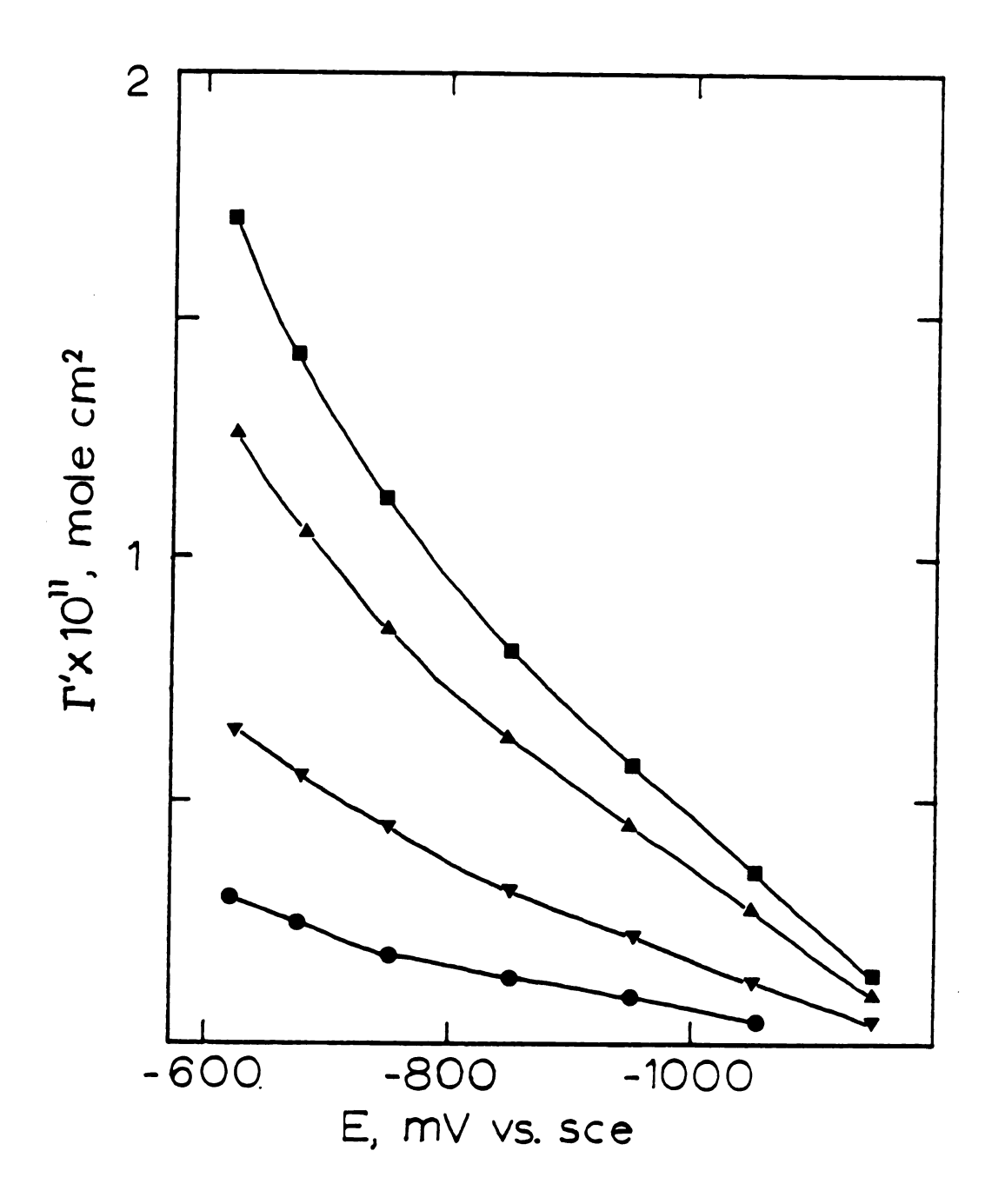


Figure 3.24. Surface concentration of chloride vs. electrode potential for UPD lead/silver. Conditions as in Figure 3.21.

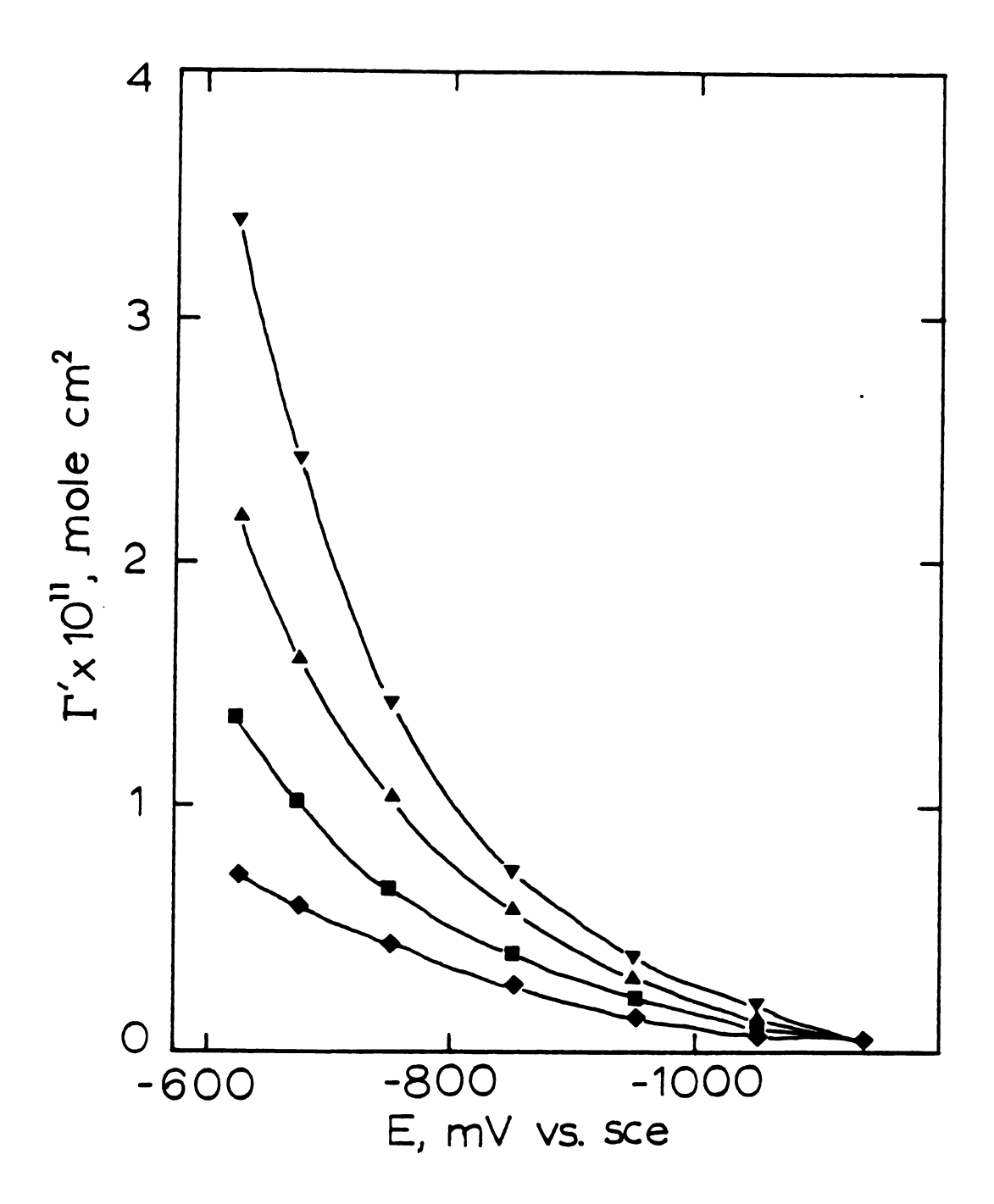


Figure 3.25. Surface concentration of bromide vs. slectrode potential for UPD lead/silver. Conditions as in Figure 3.22.

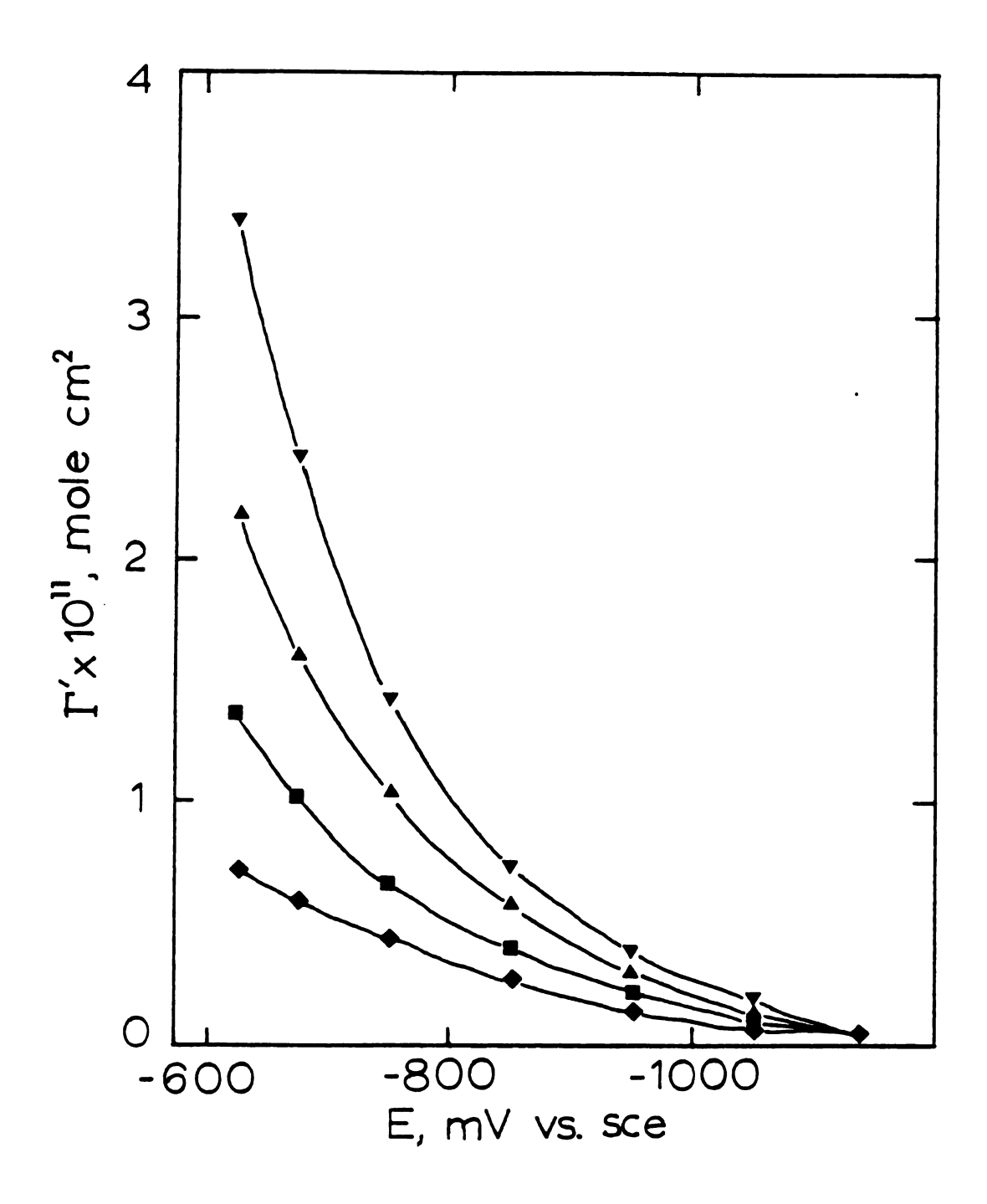


Figure 3.25. Surface concentration of bromide vs. slectrode potential for UPD lead/silver. Conditions as in Figure 3.22.

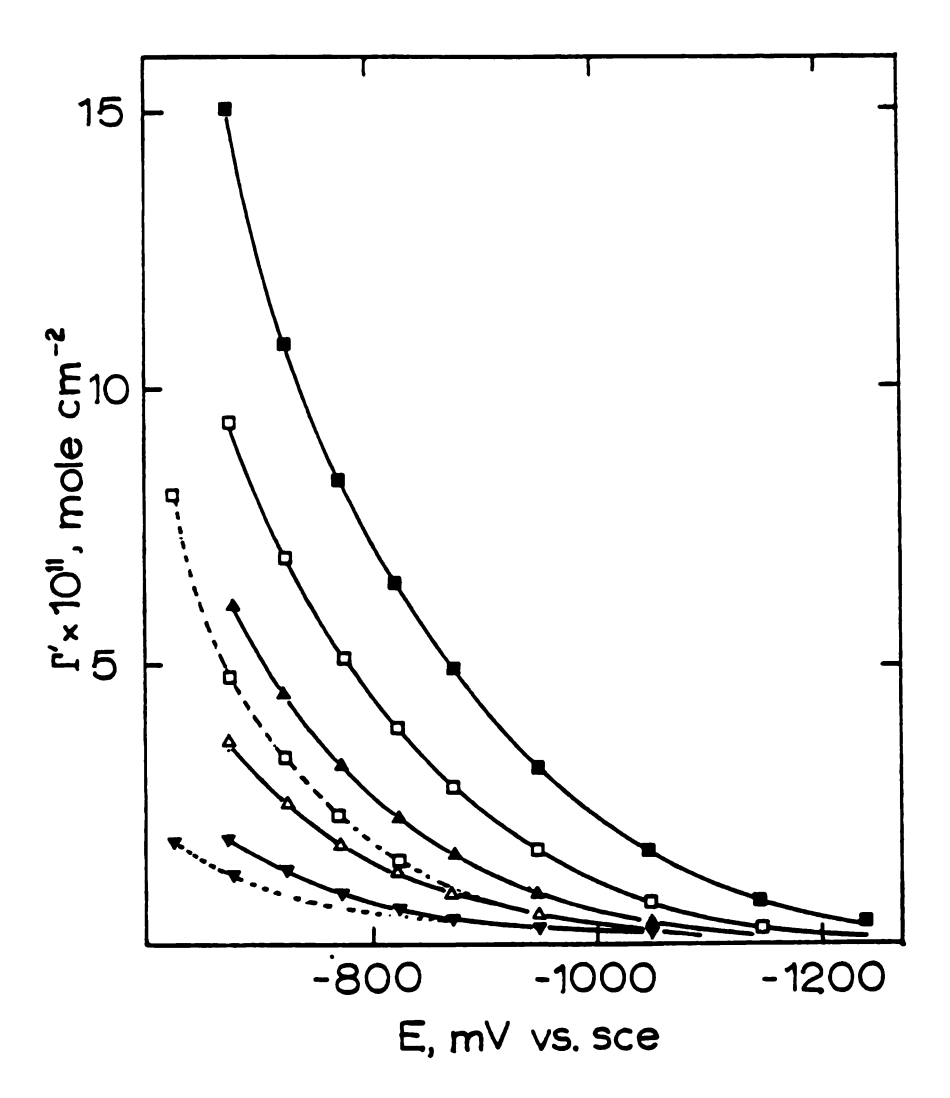


Figure 3.26. Surface concentration of iodide vs. electrode potential for UPD lead/silver. Solid line: NaI + NaF. Dashed line: NaI + NaClO<sub>4</sub>. Concentrations as in Figure 3.23.

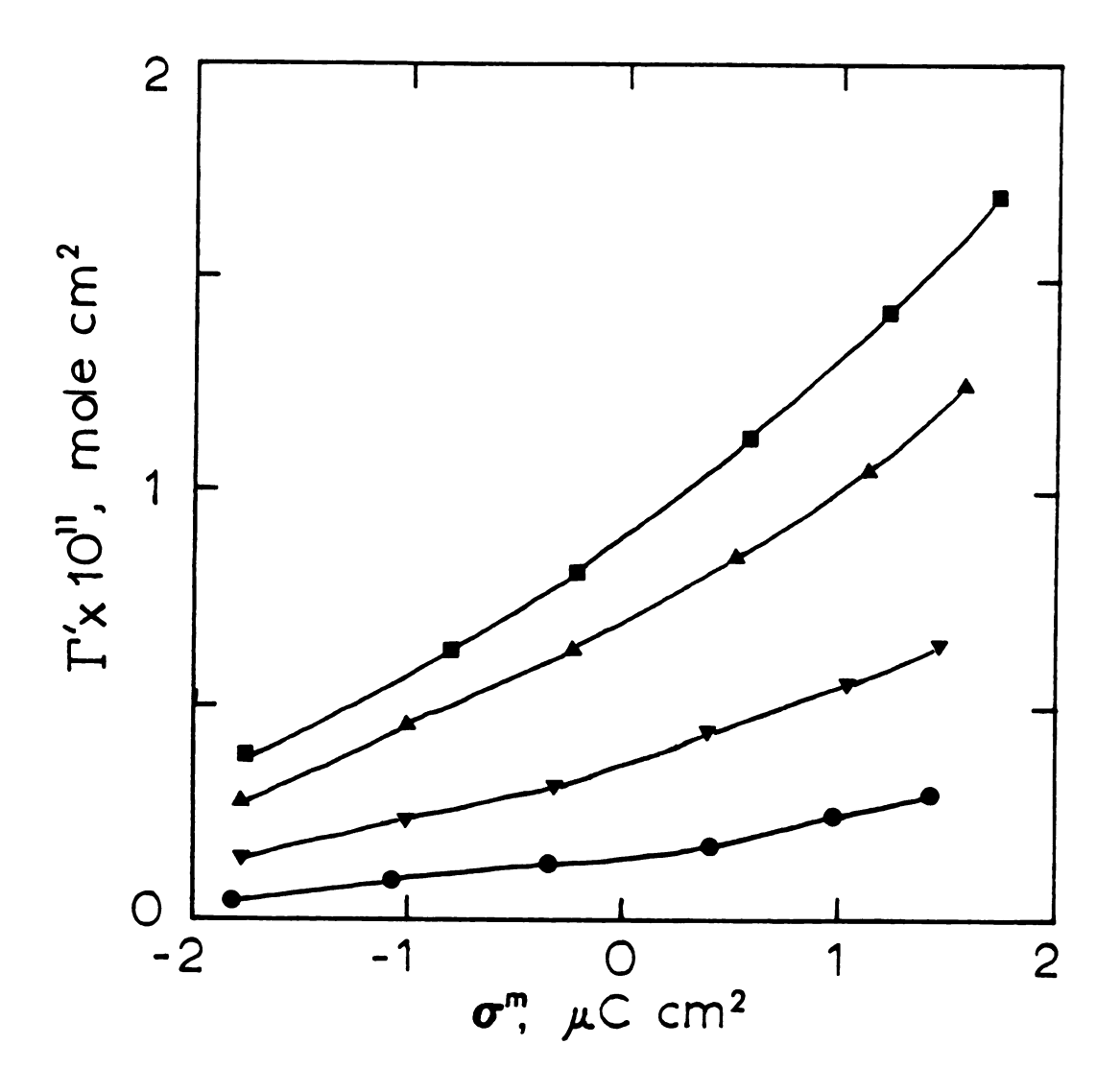


Figure 3.27. Surface concentration of chloride vs. electrode charge density for UPD lead/silver. Conditions as in Figure 3.21.

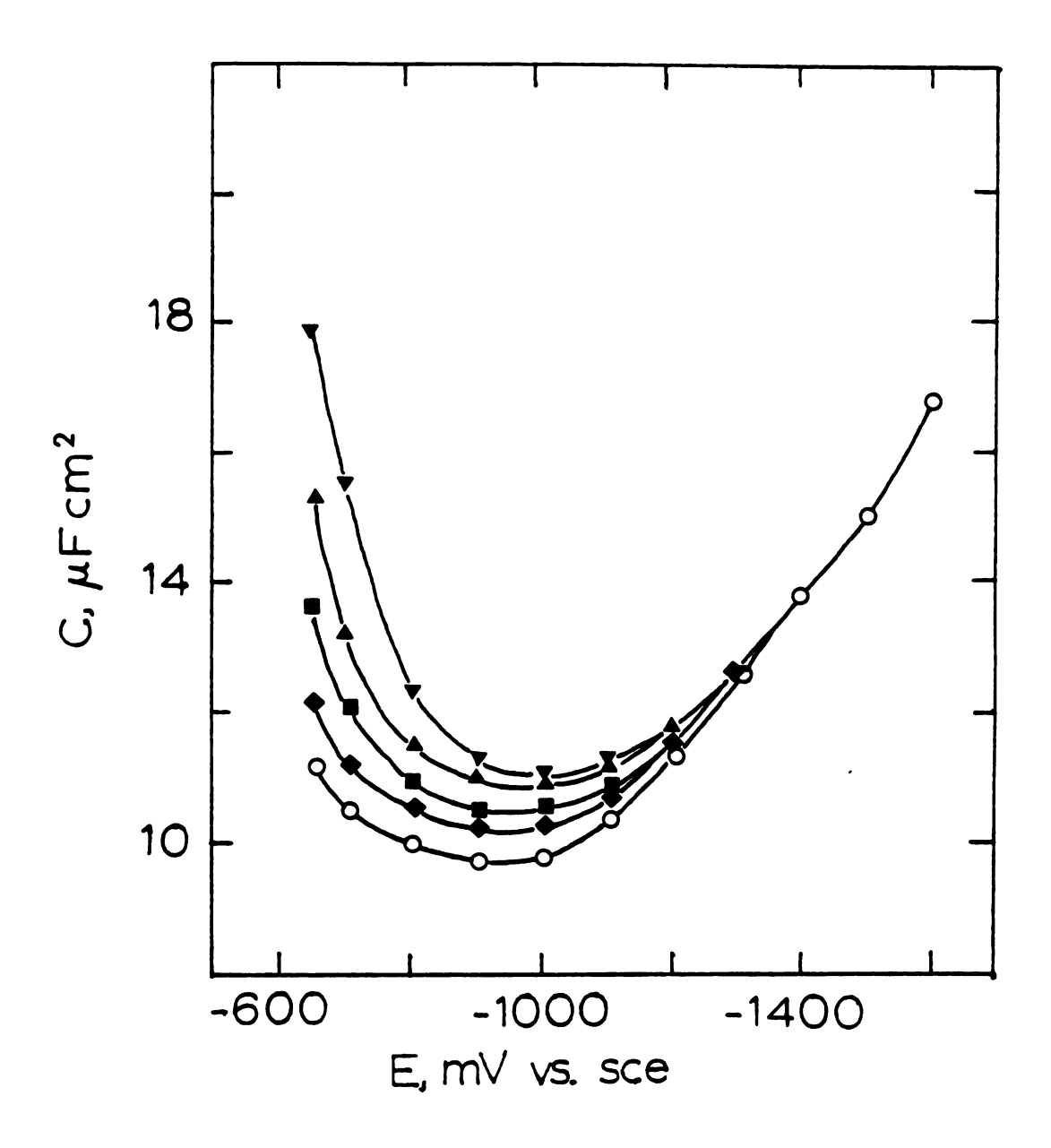


Figure 3.28. Surface concentration of bromide vs. electrode charge density for UPD lead/silver. Conditions as in Figure 3.22.

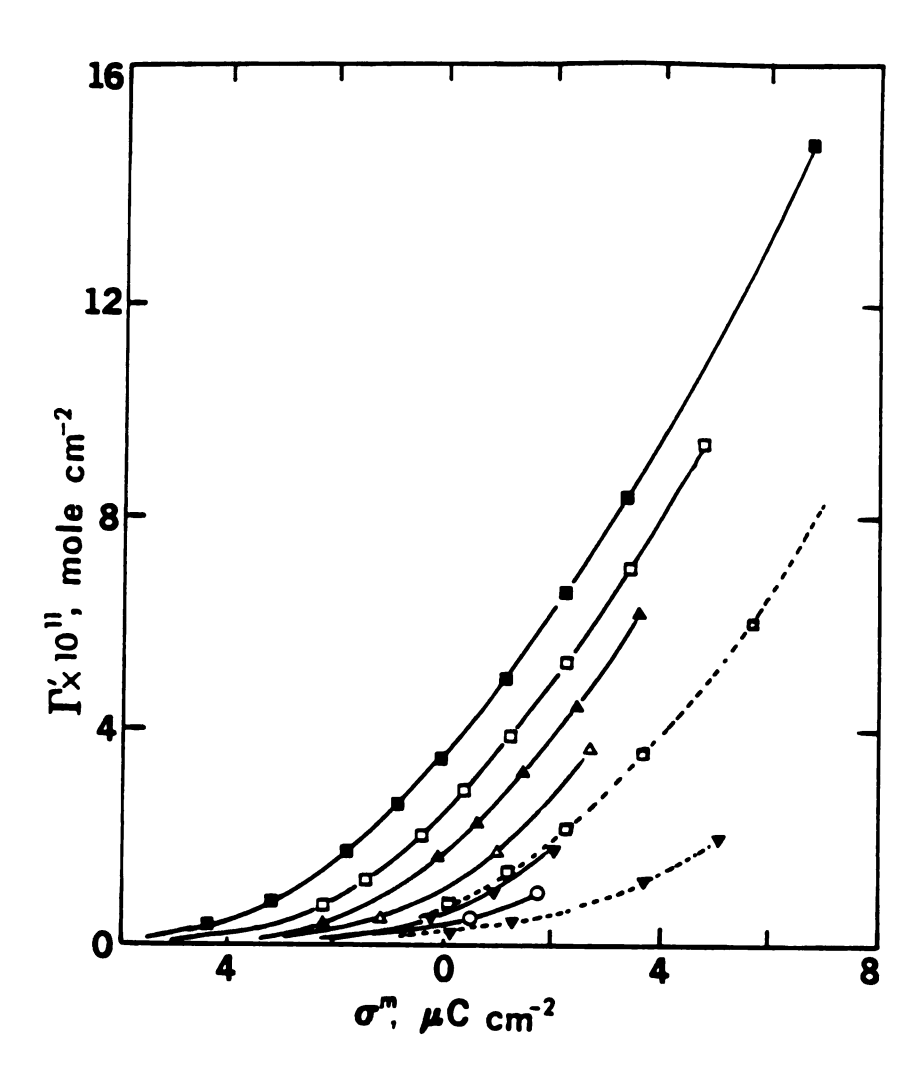


Figure 3.29. Surface concentration of iodide versus electrode charge density for UPD lead/silver. Conditions as in Figure 3.26.

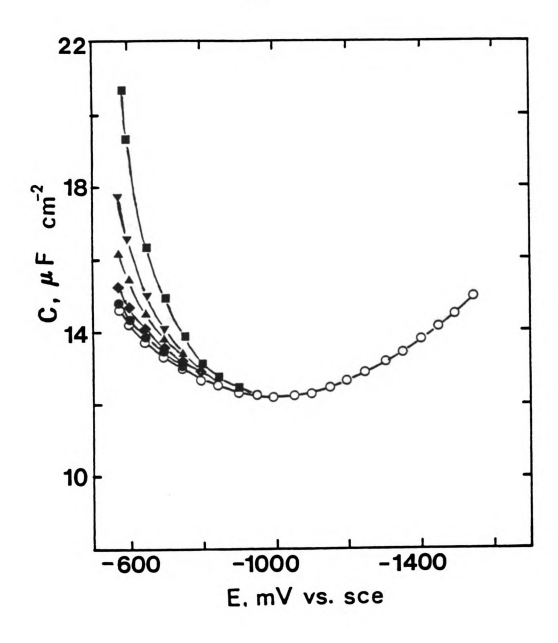


Figure 3.30. Differential capacitance vs. electrode potential for UPD lead/silver in NaBr + NaGlO<sub>4</sub> mixed electrolytes at an ionic strength of 0.5 M. Key to bromide concentrations: (O) 0 mM, (①) 1 mM, (①) 3 mM, (△) 10 mM, (→) 30 mM, (□) 100 mM.

## 2. Results

In several experiments, capacitance curves were observed to decrease slightly with consecutive measurements in the same solution. When this occurred all of the curves were "corrected" by up to a few percent by normalizing them at very negative potentials (circa. -1.6 V) where specific adsorption is absent. Therefore, surface excess concentrations derived from very small displacements of capacitance curves must be regarded as uncertain.

Shown in Figures 3.21 through 3.23 are capacitance-potential curves for chloride, bromide and iodide adsorption from fluoride based solutions of 0.5  $\underline{M}$  ionic strength. From these it is evident that the order of adsorption strength is I > Br > C1. This is confirmed by the  $\Gamma$  versus E curves shown in Figures 3.24 through 3.26 and the  $\Gamma$  versus  $\sigma^{\mathbf{m}}$  curves shown in Figures 3.27 through 3.29. (The surface concentrations are corrected in each case for the residual electrode roughness of 1.2, while the capacitance-potential curves are uncorrected.)

The effects of  ${\rm C10}_4^-$  co-adsorption can be gauged qualitatively, at least, by comparing the C-E curves in Figure 3.30 for NaBr + NaClO<sub>4</sub> with those in Figure 3.22. Particularly at more negative potentials perchlorate adsorption seems to diminish the adsorption of bromide. More quantitative comparisons are made in Figures 3.26 and 3.29 using I as an example. Here data obtained from NaI + NaClO<sub>4</sub> mixtures are shown as dashed lines. The  $\Gamma_1$  values are uncorrected for the error due to the extra term -[x/(1-x)]  $\Gamma_{C10_4}^-$  which is present when significant perchlorate adsorption occurs  $(\Gamma_{C10_4}^-)$ 0) (see Section III.G). However,

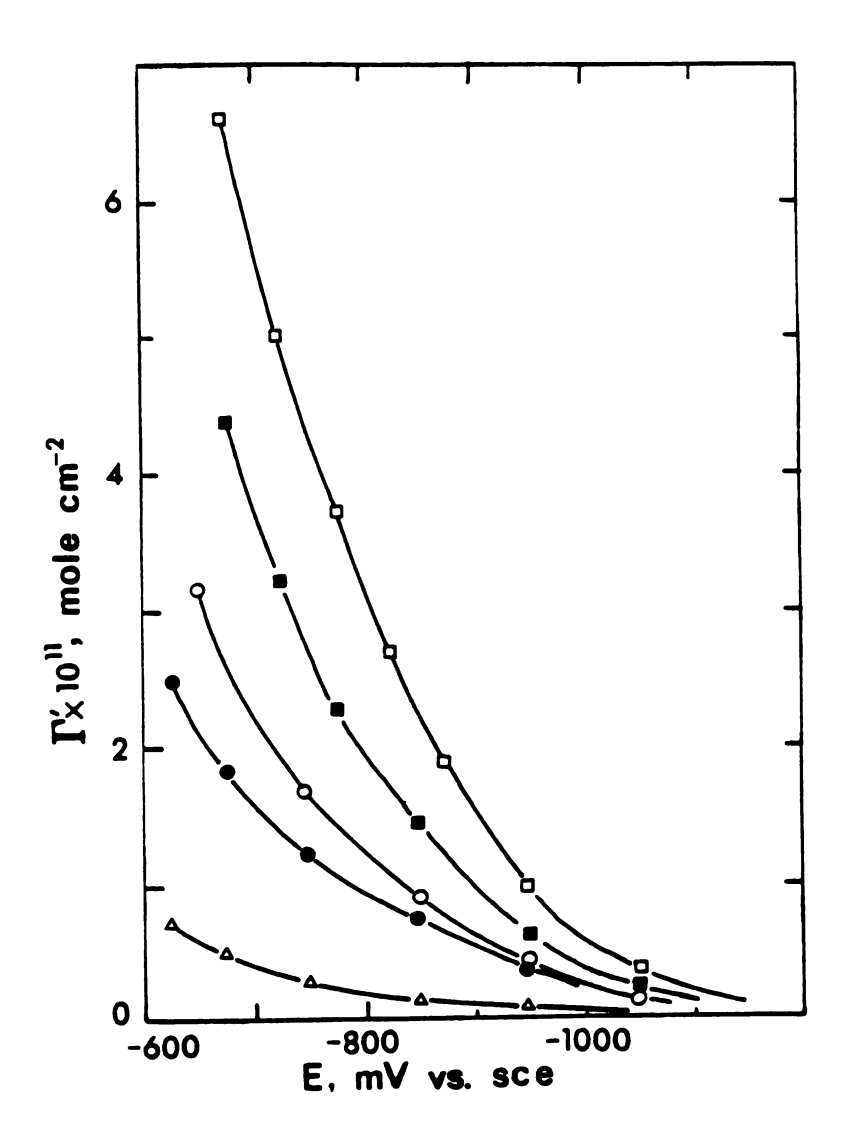


Figure 3.31. Surface concentration of thiocyanate vs. electrode potential for UPD lead/silver in NaNCS + NaF mixed electrolytes at an ionic strength of 0.5 <u>M</u>. Key to thiocyanate concentrations:

(Δ) 1 mM, (Θ) 3 mM, (Ο) 10 mM, (□) 30 mM, (□) 100 mM.

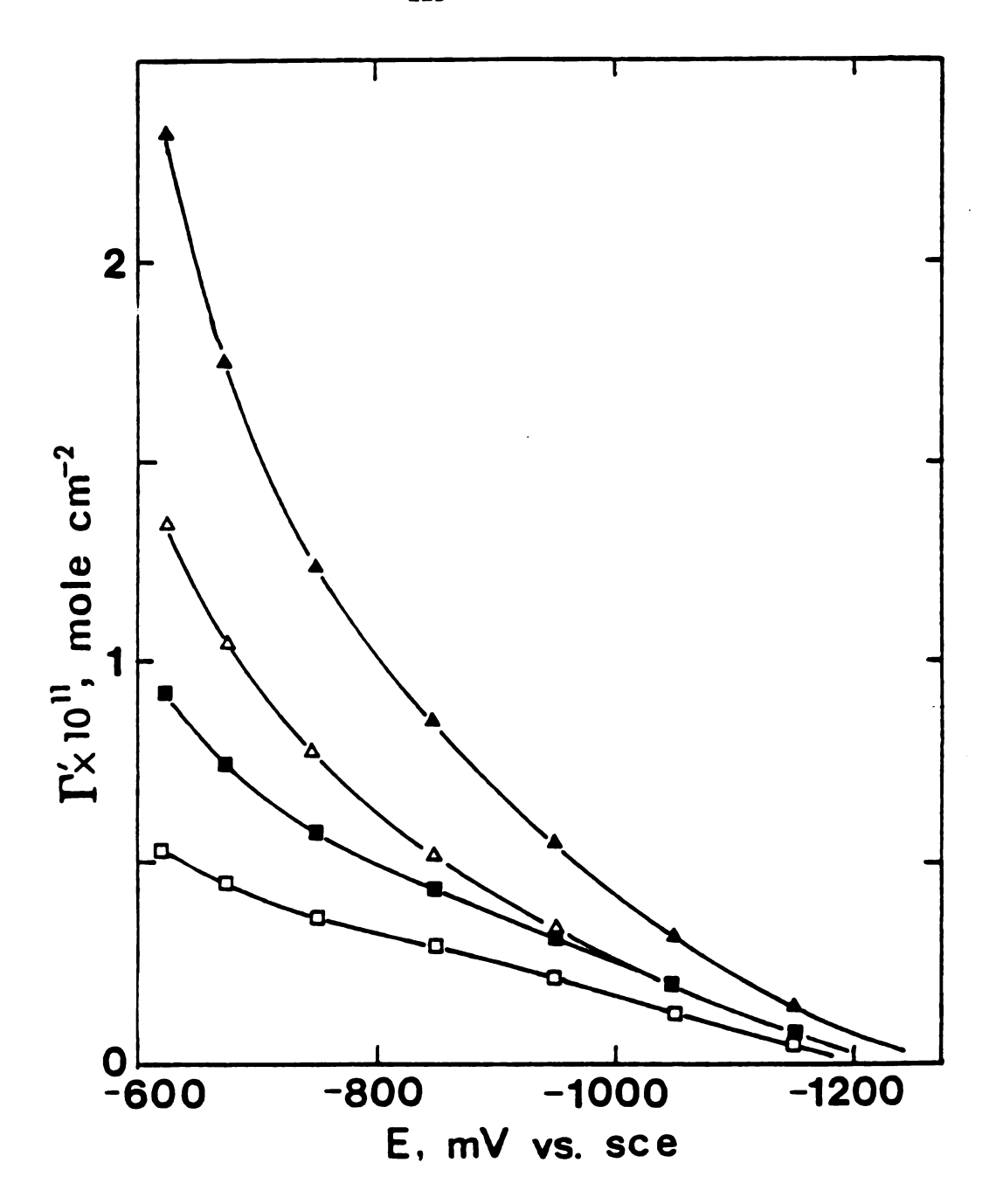


Figure 3.32. Surface concentration of azide vs. electrode potential for UPD lead/silver in NaN<sub>3</sub> + NaF mixed electrolytes at an ionic strength of 0.5  $\underline{\text{M}}$ . Key to azide concentrations: ( $\square$ ) 3  $\underline{\text{mM}}$ , ( $\blacksquare$ ) 10  $\underline{\text{mM}}$ , ( $\triangle$ ) 30  $\underline{\text{mM}}$ , ( $\triangle$ ) 121  $\underline{\text{mM}}$ .

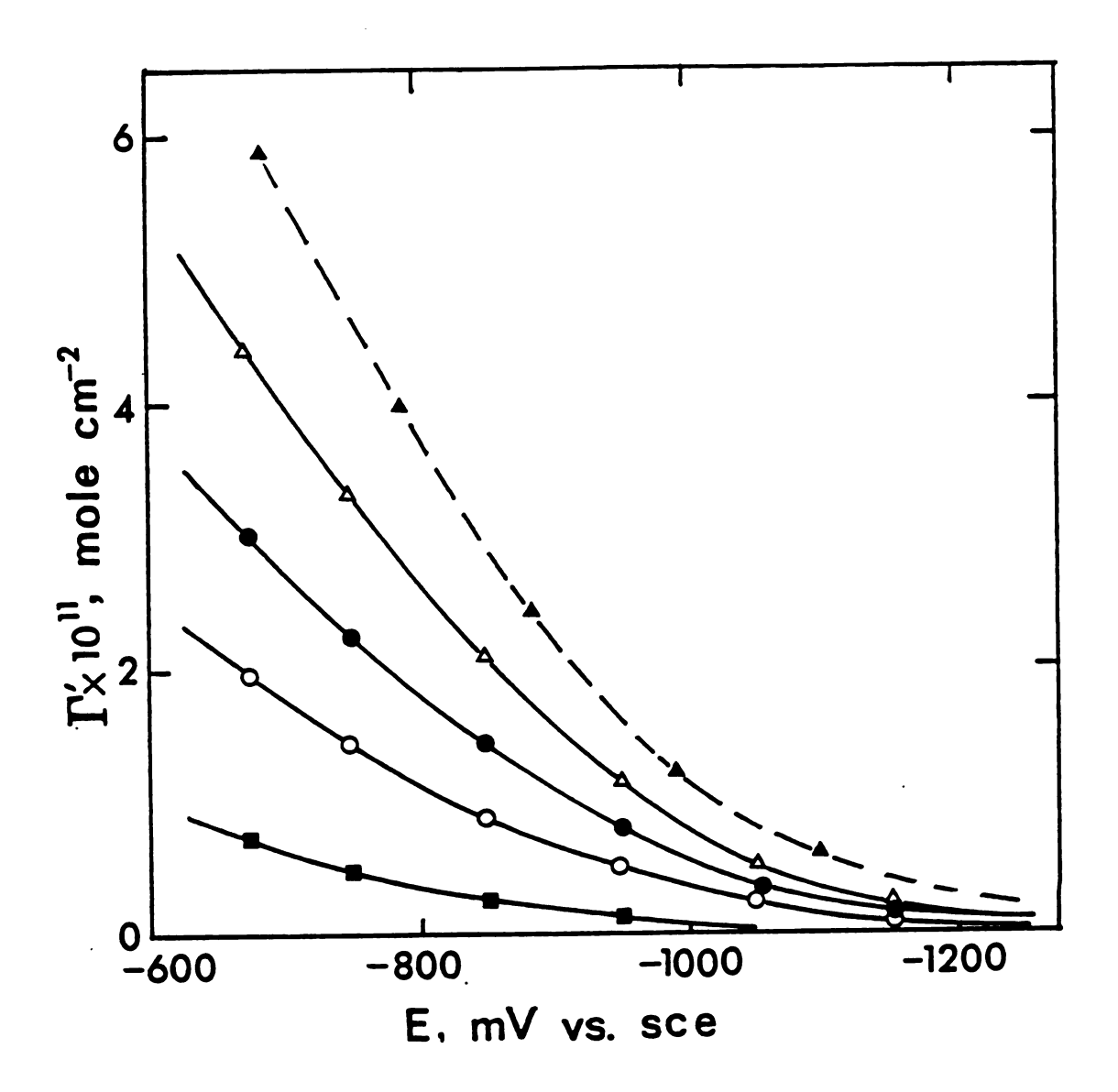


Figure 3.33. Surface concentration of perchlorate vs. electrode potential for UPD lead/silver in NaClO<sub>4</sub> + NaF at an ionic strength of 0.5 <u>M</u>. Key to perchlorate concentrations: (■) 10 mM, (O) 30 mM, (Φ) 80 mM, (Δ) 200 mM, (Δ) 500 mM (data at 500 mM were extrapolated).

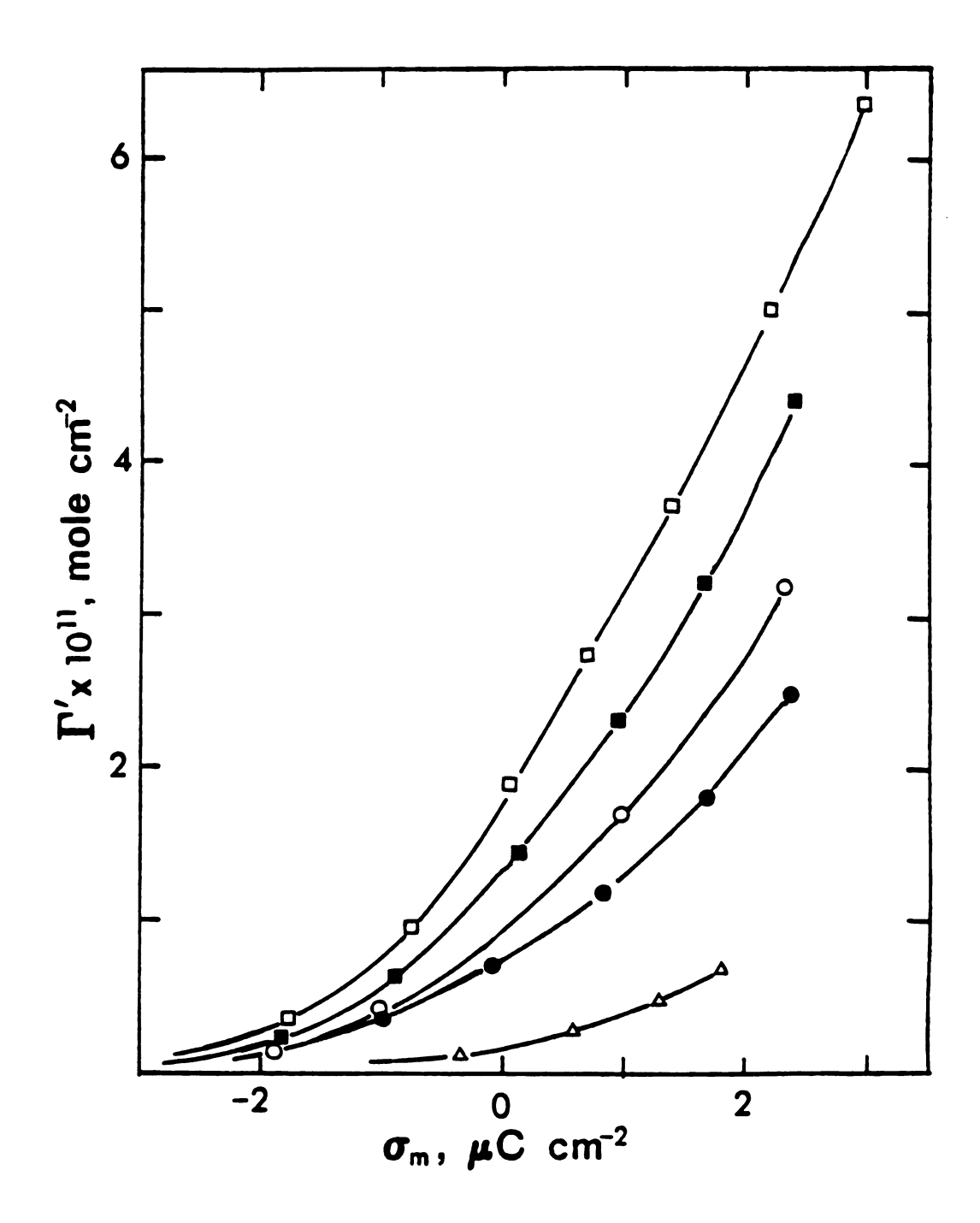


Figure 3.34. Surface concentration of thiocyanate vs. electrode charge density for UPD lead/silver. Conditions as in Figure 3.31.

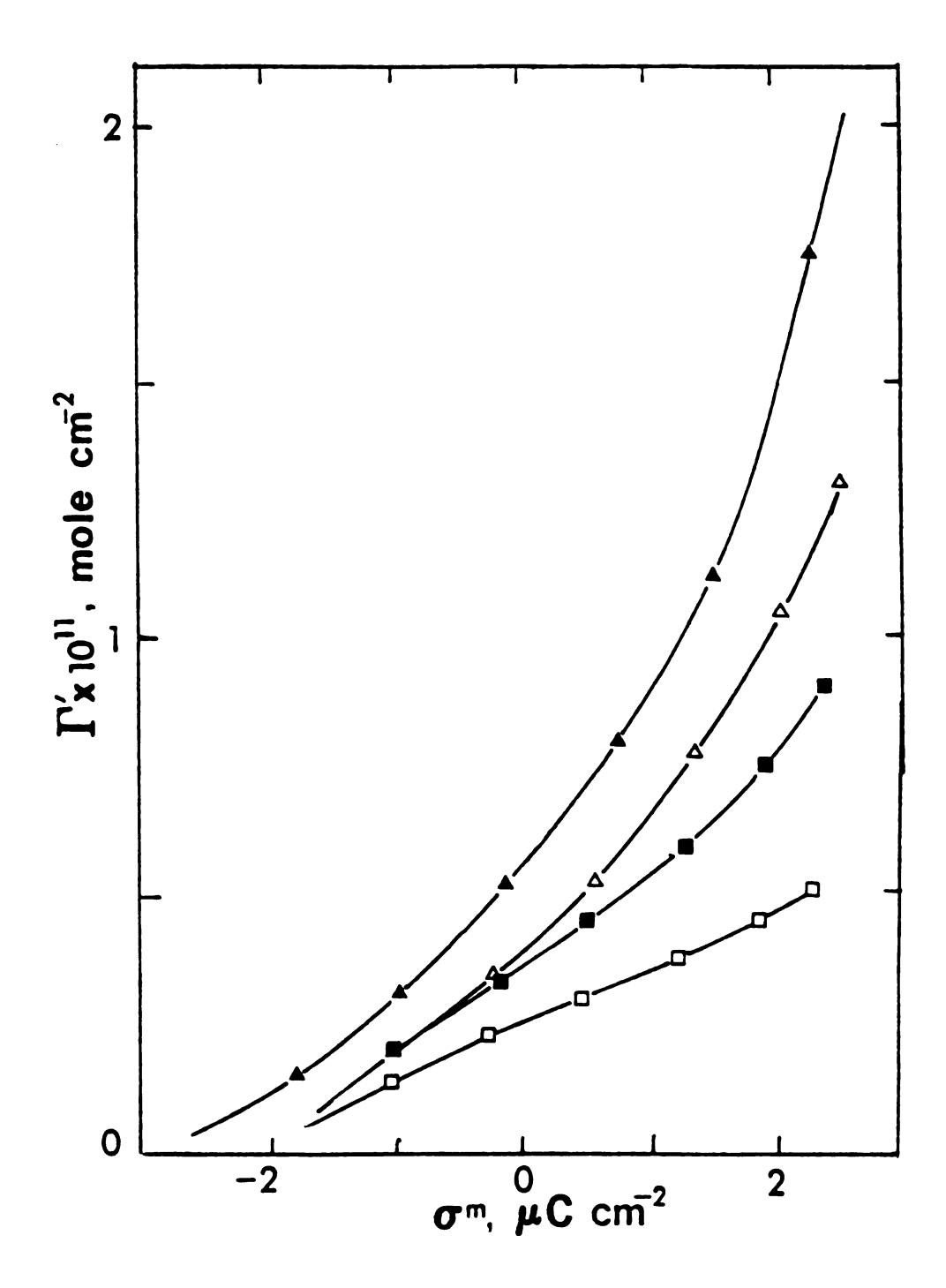


Figure 3.35. Surface concentration of azide vs. electrode charge density for UPD lead/silver. Conditions as in Figure 3.32.

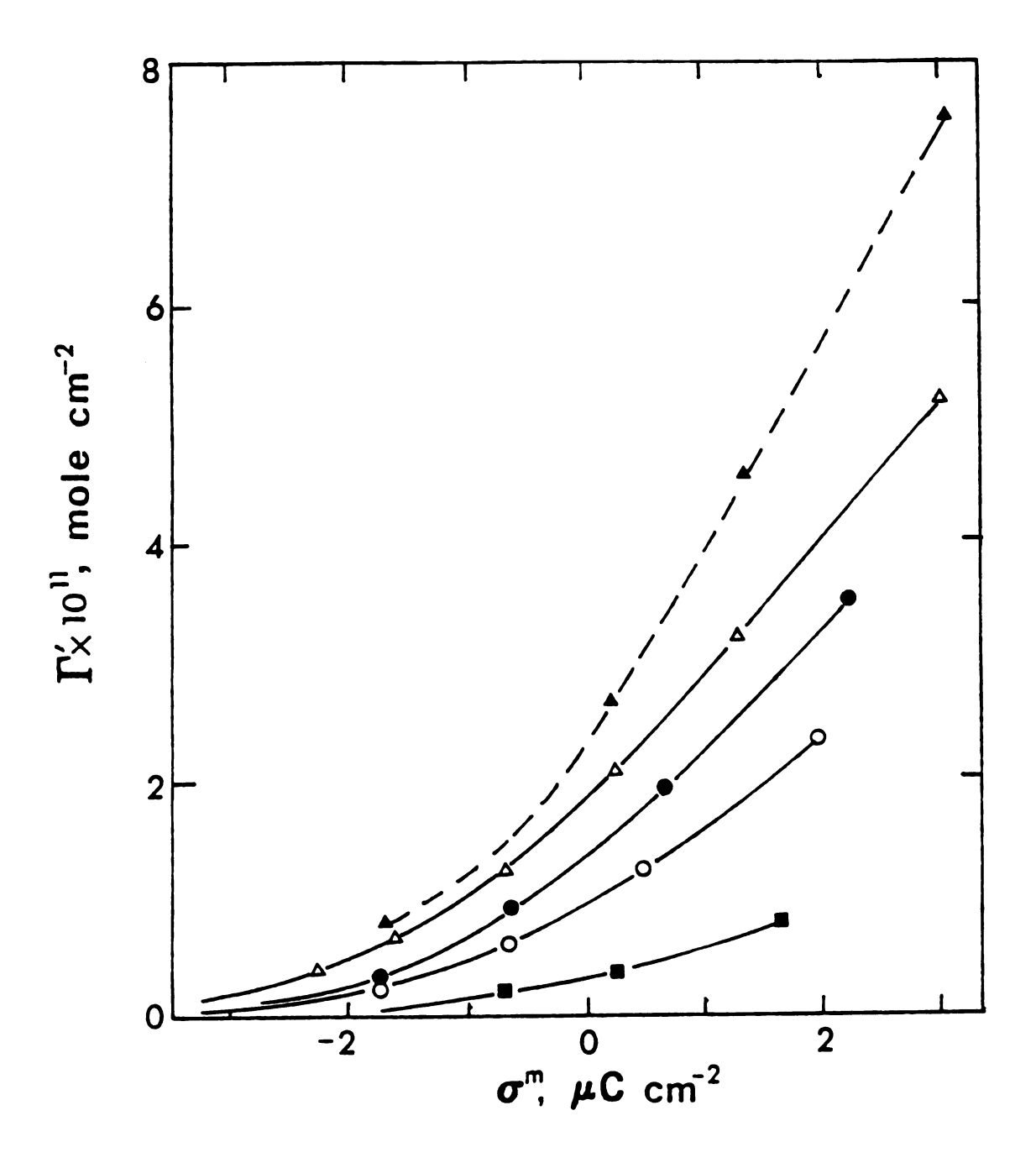


Figure 3.36. Surface concentration of perchlorate vs. electrode charge density for UPD lead/silver. Conditions as in Figure 3.33.

the  $\Gamma_{\rm I}^{'}$  -  $\sigma^{\rm m}$  curves do take account of the shift of the pzc from -800 mV in NaF solutions to -886 mV in 0.5 M NaClO<sub>4</sub>. (The latter value was calculated by back integrating capacitance-potential curves for various NaF-NaClO<sub>4</sub> mixtures).

Standard free energies of adsorption, as well as interaction coefficients, were calculated at various electrode charges by fitting the data in Figures 3.27 through 3.29 to the Frumkin isotherm (Equation 1.9). These parameters are listed in Table 3.3. Also included are  $\Delta G_a^0$  and g values for I adsorption from solutions of lower ionic strength. The values of  $\Gamma_s$  (the surface coverage at saturation) which were used in calculating  $\Delta G_a^0$  values are 1.6 x 10<sup>-9</sup>, 1.35 x 10<sup>-9</sup> and 1.07 x 10<sup>-9</sup> mole cm<sup>-2</sup> for chloride, bromide and iodide, respectively. 86

From capacitance-potential curves (not shown), plots of  $\Gamma$  versus E were constructed for NCS, N<sub>3</sub> and ClO<sub>4</sub> adsorption from NaF solutions (Figures 3.31, 3.32, and 3.33 respectively). The corresponding  $\Gamma$  -  $\Gamma$  curves are presented in Figures 3.34, 3.35 and 3.36. Values of  $\Gamma$  and  $\Gamma$  and  $\Gamma$  are less certain for these ions than for the small spherical ions. Based on a "radius" of 2.36  $\Gamma$  a value of 9.3 x 10<sup>-10</sup> mole cm<sup>-2</sup> was calculated for  $\Gamma$  clo<sub>4</sub>. Estimates of 1.65 x 10<sup>-9</sup> mole cm<sup>-2</sup> and 1.86 x 10<sup>-9</sup> mole cm<sup>-2</sup> were used for azide and thiocyanate anions, respectively. This assumes that a "vertical" orientation and hexagonal packing is preferred by each ion.

## 3. Discussion

By comparing the results presented here with those in Section III. A, it can be seen that anion adsorption (with the exception of perchlorate) is substantially diminished at silver when the surface is modified by underpotential deposition of lead. This is true even if the results are compared at a fixed electrode potential rather than charge, despite the 130 mV "advantage" for UPD lead due to the shift of the effective pzc. Similar observations concerning the inhibiting effects of lead UPD on halide adsorption were noted earlier by Stucki and Schmidt based on thin-layer electrochemistry experiments. 146

It may be instructive to compare the adsorption capabilities of UPD lead/silver with those of bulk lead.  $^{136}$  Listed in Table 3.4 are data obtained by H.Y. Liu for anion adsorption at polycrystalline lead at  $\sigma^{\rm m}=0.^{136}$  the values of  $\Delta \, {\rm G}_{\rm a}^{\rm O}$  generally are less negative for bulk lead indicating less adsorption at this surface, at least in the limit of infinite dilution. (The value in Table 3.4 for Br apparently was miscalculated and probably is actually more negative, judging from surface excess data also reported by Liu). A comparison of r versus  $\sigma^{\rm m}$  curves from Dr. Liu's dissertation with those presented here indicates that adsorption also is less at bulk lead compared with UPD Pb/Ag for finite bulk solution concentrations (10 mM) of adsorbing anions. Nevertheless, given the sensitivity of adsorption at bulk lead to the electrode pretreatment method,  $^{136,147}$  the differences between bulk and UPD surfaces may well represent artifacts rather than differences in chemistry. Overall, the adsorption capabilities of UPD lead/silver and

Standard Free Energies of Adsorption  $\Delta G^0$  (kJ mol<sup>-1</sup>) and Interaction Parameters g for Anions Table 3.3.

	F	,	E		F	E	-2
	σ = 1	Ţ.	0 <b>=</b> 0		<b>α</b>	σ=2 μC cm	c cm
Anion (base electrolyte)	ΔG <sup>O</sup>	<b>60</b>	ΔG <sup>o</sup>	60	ΔG <sup>O</sup> g	ΔG <sup>O</sup>	80
$I = (0.5\underline{M} \text{ NaF})$	-86	95	06-	110	-91.5 85	-95.5	85
$I^-$ (0.2 <u>M</u> NaF)			-89	185	-92 180	-95.5	150
$I^- (0.5\underline{M} \text{ NaClO}_4)$			~ -87	~430			
$NCS^{-}(0.5\underline{M} \text{ NaF})$	98-	870	-87	300	-90 200	-92	160
$Br^-$ (0.5 $\underline{M}$ NaF)	98-	1500	-88	720	-88.5 370	-89.5	190
$N_3 = (0.5\underline{M} \text{ NaF})$			-87	970		-87	320
$\text{ClO}_4^-(0.5\underline{\text{M}}\text{ NaF})$	-83	260	-84	120	-85.5 70	-86.5	50
C1 (0.5M NaF)	-79.	-79.5 200	-80.5	200	-82.5 220		

Table 3.4 Standard Free Energies of Adsorption  $\Delta G_a^{\ o}$  (kJ mol<sup>-1</sup>) of Anions at a Polycrystalline Lead Electrode.

Anion <sup>b</sup>	$\Delta oldsymbol{G}_{oldsymbol{a}}^{oldsymbol{o}}$
r <sup>-</sup>	-90
NCS	-86
Br <sup>-</sup>	-79
N <sub>3</sub>	-80
cı <sup>-</sup>	~-74

From H.Y. Liu, Ph.D. Dissertation, Michigan State University, 1982.

b Base electrolyte was 0.2  $\underline{M}$  NaF in each case.

bulk lead can be regarded as fairly similar. The central conclusion from this study is that the deposition of a single atomic layer of lead is sufficient to transform the silver surface into one resembling lead, at least with regard to adsorption properties.

It may be worthwhile to discuss briefly a few details of the results. One peculiar aspect of anion adsorption at UPD lead/ silver is the magnitude of the g values. These are greatest when adsorption is weak, when the electrode charge is zero or negative, and when perchlorate is used as the base electrolyte. The most extreme values (e.g., g = 1500 for Br ) are very unlikely to result from lateral interactions between adsorbed ions. Such large g values might be indicative of the existence of a limited number of active surface sites which are capable of adsorbing ions more strongly than are the majority of sites. Another idea is suggested by Payne's observation that the second virial coefficient (analogous to the g parameter) for chloride adsorption at mercury increases as much as ten-fold when water is replaced by a solvent which binds more strongly to the surface. 148 In changing from mercury to lead, solvent-metal interactions are likewise increased, as are the g values. One could speculate that metal-solvent and adsorbate-adsorbate interactions are somehow interrelated.

Another explanation is that these results are simply due to systematic analysis errors. When surface coverages by anions approach a few tenths of a percent or less the capacitance method has nearly reached its limit as a surface concentration measurement technique. Given the form of the Frumkin isotherm, errors in estimating very small

values of  $\Gamma$  can yield substantial errors in the value of the interaction parameter.

The difference in g values between fluoride and perchlorate electrolytes (see also reference 136) evidently reflects the complications due to  $\text{C10}_4^-$  co-adsorption. Perchlorate can influence the g parameter either by distorting the iodide adsorption isotherm via competition for surface sites or by introducing an extra term,  $-[x/(1-x)]_{\Gamma_{C10}}^-$ , which has been neglected.

It is evident from both the charge-based (Figure 3.26) and potential-based (Figure 3.29) comparisons that perchlorate coadsorption causes a substantial diminution of the extent of iodide adsorption. At higher iodide coverages at least, this diminution must be regarded as a real chemical effect rather than an artifact due to the term  $-[x/(1-x)]\Gamma_{C10_4}$ . The extent to which perchlorate coadsorption diminishes iodide adsorption is much larger than one would anticipate from a simple "blockage" of sites by a small amount of adsorbed  $C10_4$ . Evidently in addition to blocking a small portion of the electrode surface, adsorbed  $C10_4$  also exerts a repulsive force on surrounding ions thereby inhibiting I adsorption. Such an interpretation is consistent with observation of positive g values for both iodide and perchlorate adsorption from NaX-NaF mixtures.

E. The Influence of Thallium Underpotential Deposition on Anion

Adsorption and the Double Layer Structure at the Silver-Aqueous

Interface.

### 1. Introduction

We have found that lead underpotential deposition has a profound influence on the double layer structure and ionic adsorption capabilities of the silver-aqueous interface. Clearly it is desirable to investigate additional systems. Thallium underpotential deposition on silver is a logical choice, since this combination has already been employed in a number of studies aimed at characterizing 3,4 or applying the UPD phenomenon. 8,125,126 Nevertheless the interfacial properties of UPD as well as bulk thallium have scarcely been examined previously. An additional motivation for gathering data at this particular surface is the desire to understand more satisfactorily the results of electron-transfer kinetics at UPD thallium/silver.

#### 2. Electrode Preparation

The underpotentially desposited thallium surface was prepared in essentially the same manner as the UPD lead surface. To summarize briefly, a pretreated silver electrode was held at about -960 mV and rotated for several minutes in a dilute solution (~5 x 10<sup>-7</sup> M) of T1ClO<sub>4</sub> until a monolayer of thallium atoms had been deposited. According to Bewick and Thomas, two monolayers of thallium can be underpotentially deposited on carefully pretreated silver single crystals. Curves a and b of Figure 3.37 are linear-sweep voltam-

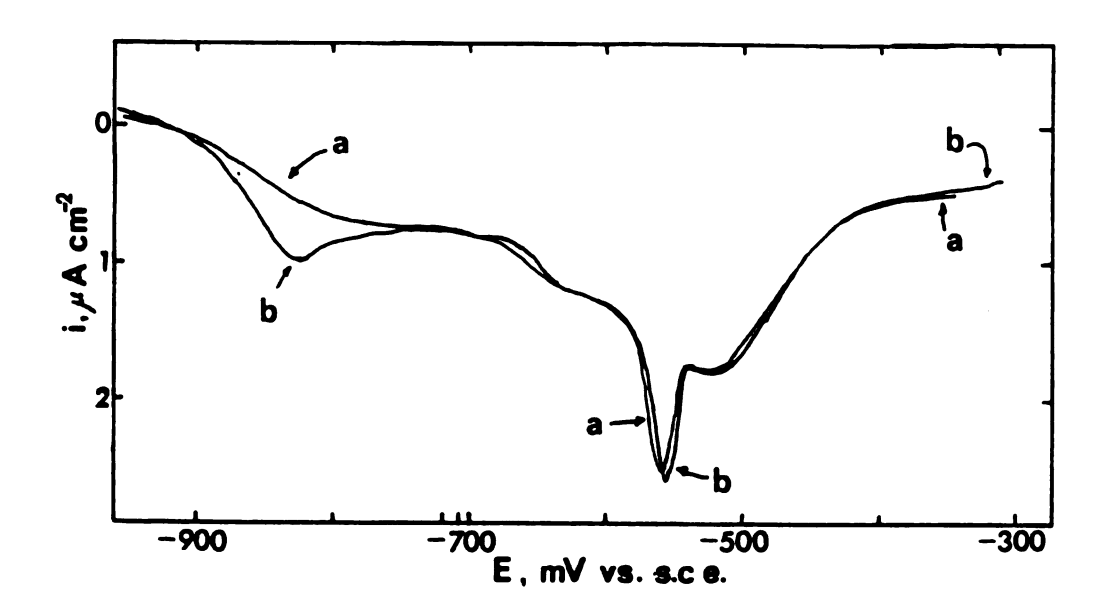


Figure 3.37 Linear sweep current-potential curves for anodic of thallium layer deposited on silver. Sweep rate was 20 mV/s. Electrolyte was 0.5 M NaF, convaining 0.8 M T1ClO<sub>4</sub>. Curve (a): electrode held at -960 mV for 12 minutes while rotating at 600 RPM; (b) electrode held at -960 mV for 12 minutes at 600 RPM and then held for 15 minutes at -1300 mV without rotation.

mograms showing the removal of UPD thallium from polycrystalline silver. The area under each curve is 200  $\mu$ C cm<sup>-2</sup> which is essentially exactly the amount expected for the removal of one atomic layer of thallium<sup>3</sup> from an electrode having a roughness factor of 1.2, given that the electrosorption valency for Tl<sup>+</sup>/Tl is unity.<sup>4</sup> If the potential is adjusted to a value negative of the UPD region and maintained for 15 minutes without rotating the electrode, only a small additional amount of thallium is deposited as evidenced by the additional peak on curve b of figure 3.37. Whether this represents the start of a second UPD layer or instead bulk deposition, is not clear since this was not investigated further.

#### 3. Results

# a. Capacitance Measurements in Single Electrolytes

Figure 3.38 summarizes the results obtained in sodium perchlorate electrolytes. The thallium-modified electrode is approximately ideally polarizable to about -1600 or -1700 mV versus sce, compared with -1300 mV for pure silver. As the potential is made more positive than about -900 mV, as in curve a, thallium is removed and the capacitance gradually increases until it attains values characteristic of silver. Curve b shows the effect of depositing the equivalent of about three atomic layers of thallium on silver. Curve c illustrates the effect on the capacitance of increasing the concentration of NaClO<sub>4</sub>. Difficulty was encountered in performing measurements with electrolyte concentrations below 50 mM. Nevertheless, capacitance-potential curves

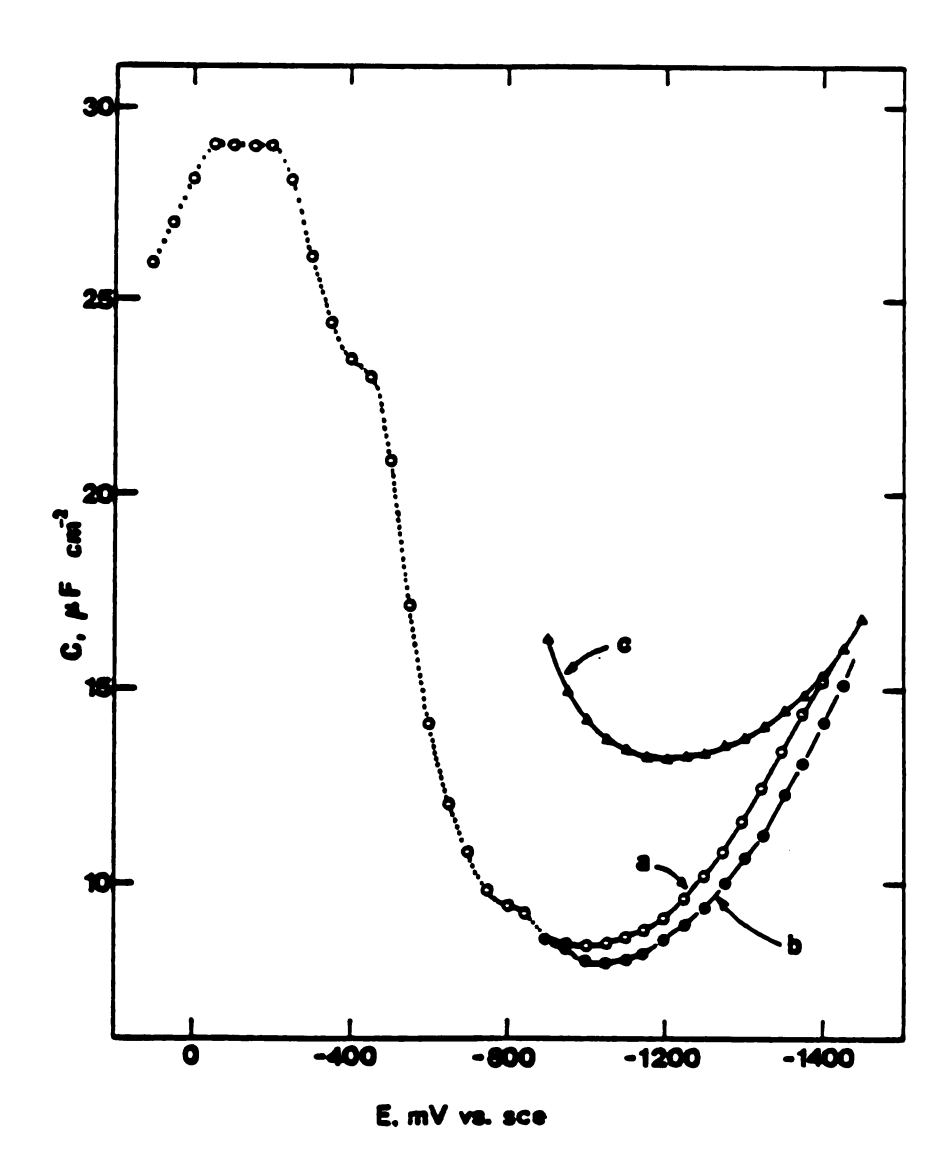


Figure 3.38. Differential capacitance versus electrode potential for: (a) a monolayer of underpotentially deposited thallium on polycrystalline silver in 0.05  $\underline{\text{M}}$  NaClO<sub>4</sub>; (b) the equivalent of circa. 3 monolayers of thallium on polycrystalline silver in 0.05  $\underline{\text{M}}$  NaClO<sub>4</sub>; (c) as in (a), except in 0.2  $\underline{\text{M}}$  NaClO<sub>4</sub>.

consistently exhibited minima at about -1020 mV in 10 mM NaClO<sub>4</sub> and -960 mV in 10 mM NaF. The latter value can be identified as the effective potential of zero charge if it is assumed that fluoride adsorption is negligible.

# b. <u>Capacitance Measurements and Anion Specific Adsorption in</u> <u>Mixed Electrolytes</u>

Capacitance-potential curves for chloride, bromide and iodide adsorption from constant ionic strength (0.5 M) NaX + NaF mixtures are shown in Figures 3.39, 3.40 and 3.41, respectively. Surface concentrations of specifically adsorbed anions were ascertained by applying the Hurwitz-Parsons analysis 35,36 to the C-E curves. The resulting surface concentration-potential data are plotted in Figures 3.42, 3.43 and 3.44 for Cl, Br and I, respectively. Surface concentration-charge curves are shown in Figures 3.45, 3.46 and 3.47.

Capacitance values for UPD thallium/silver were measured in perchlorate-containing and also in thiocyanate-containing mixed electrolytes. The  $\Gamma$  versus E and  $\Gamma$  versus  $\sigma$  data which were calculated from these measurements are shown in Figures 3.48 through 3.51. Capacitance measurements were also attempted in NaN<sub>3</sub> + NaF electrolytes, but the results were insufficiently reproducible to yield azide surface concentration data.

Free energies of adsorption were calculated for the five anions at  $\sigma^m=0$  by fitting  $\Gamma$  values to the Frumkin isotherm. The results are:

-90 kJ mol<sup>-1</sup> for  $\Gamma$ , -86.5 kJ mol<sup>-1</sup> for NCS, -82.5 kJ mol<sup>-1</sup> for Br,

-82.5 kJ mol<sup>-1</sup> for  $C10_4^-$ , and -77 kJ mol<sup>-1</sup> for  $C1^-$ .

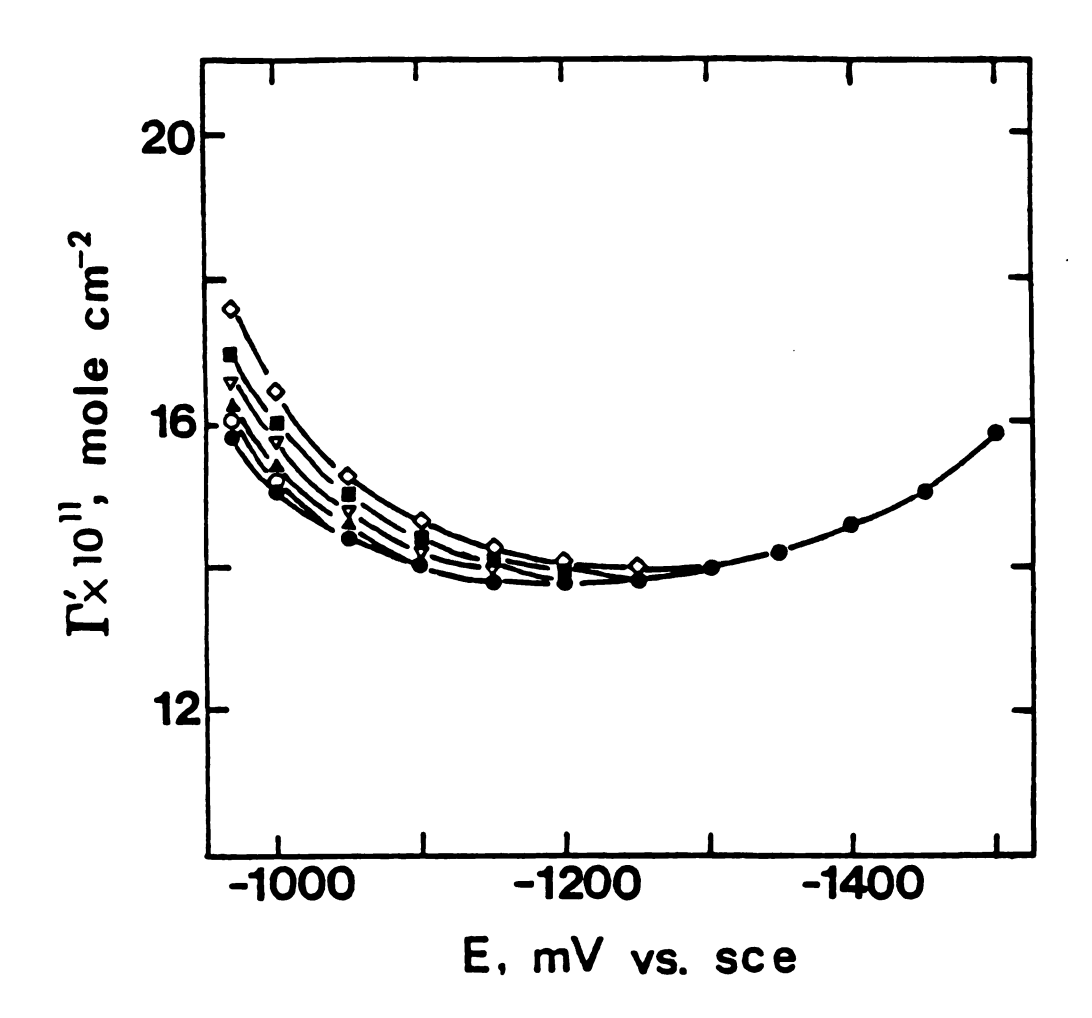


Figure 3.39. Differential capacitance vs. electrode potential for UPD thallium/silver in NaCl+NaF mixed electrolytes at an ionic strength of 0.5 M. Key to chloride concentrations: (•) 0 mM; (0) 1 mM; (•) 10 mM; (•) 50 mM; (•) 100 mM; (•) 200 mM.

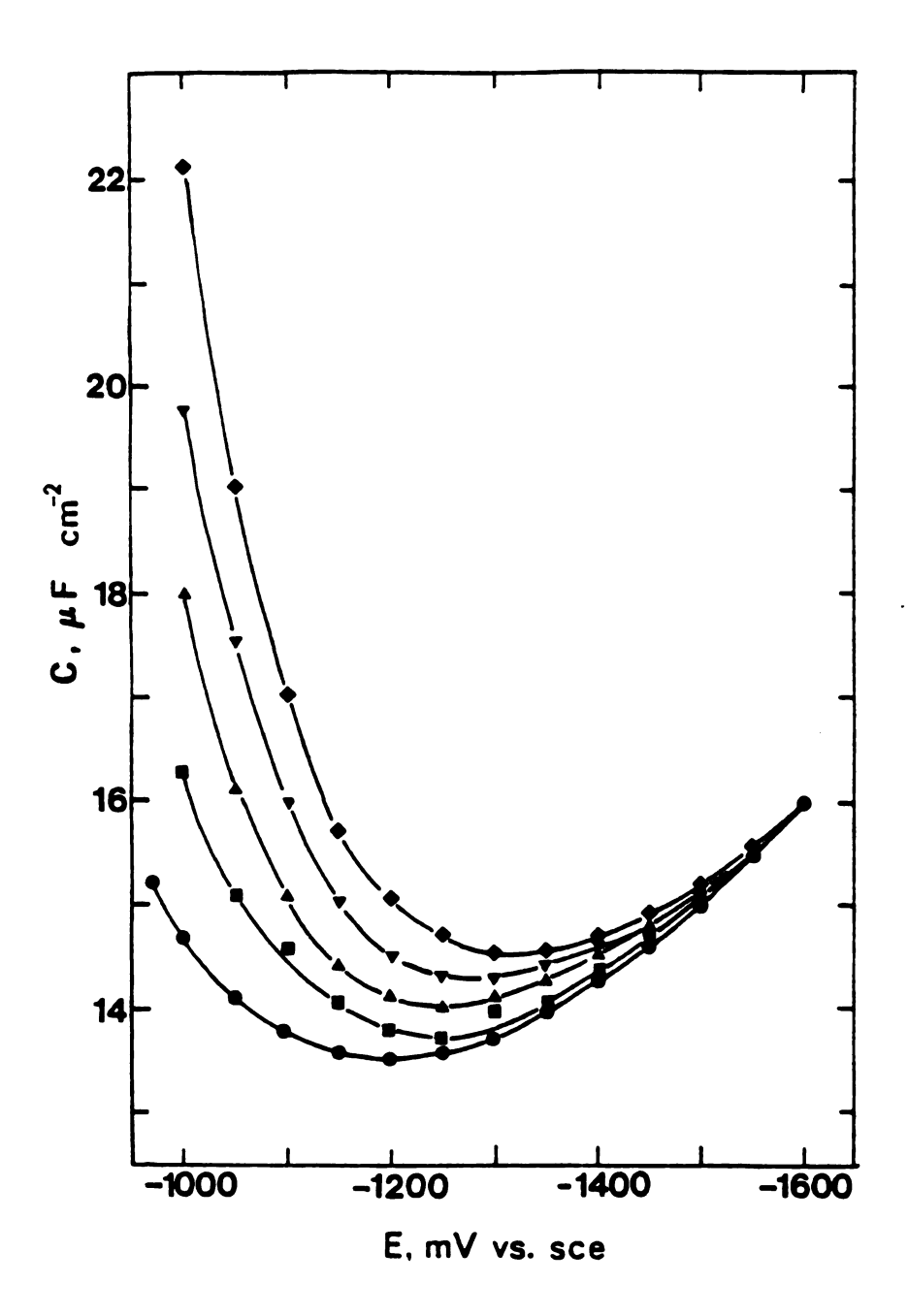


Figure 3.40. Differential capacitance vs. electrode potential for UPD thallium/silver in NaBr + NaF mixed electrolytes at an ionic strength of 0.5 M. Key to bromide concentrations: (●) 0 mM; (■) 20 mM; (▲) 50 mM; (▼) 100 mM; (◆) 200 mM.

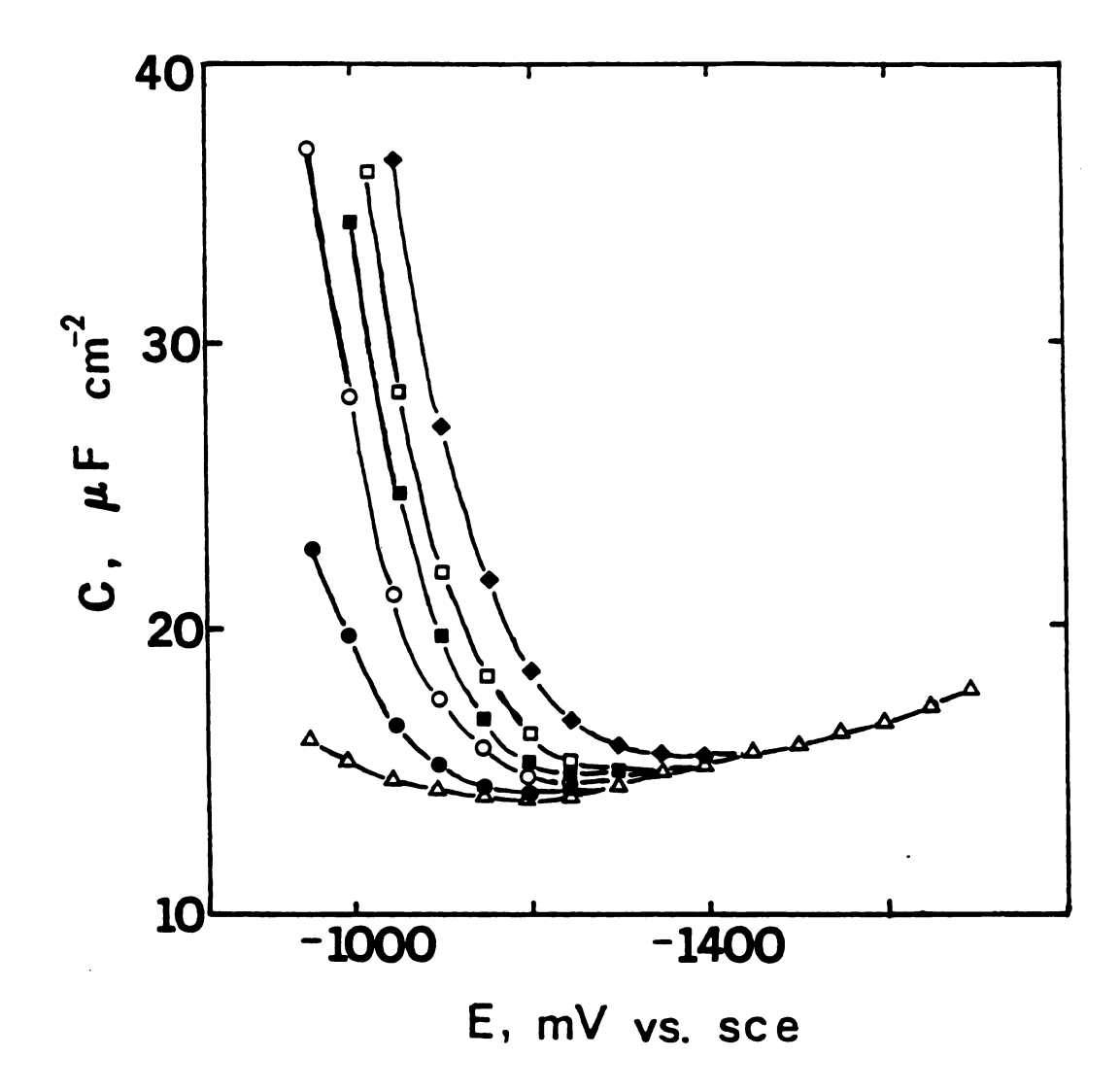


Figure 3.41. Differential capacitance vs. electrode potential for UPD thallium/silver in NaI + NaF mixed electrolytes at an ionic strength of 0.5 M. Key to iodide concentrations: (△) 0 mM; (●) 1 mM; (O) 5 mM; (■) 10 mM; (□) 20 mM; (◆) 50 mM.

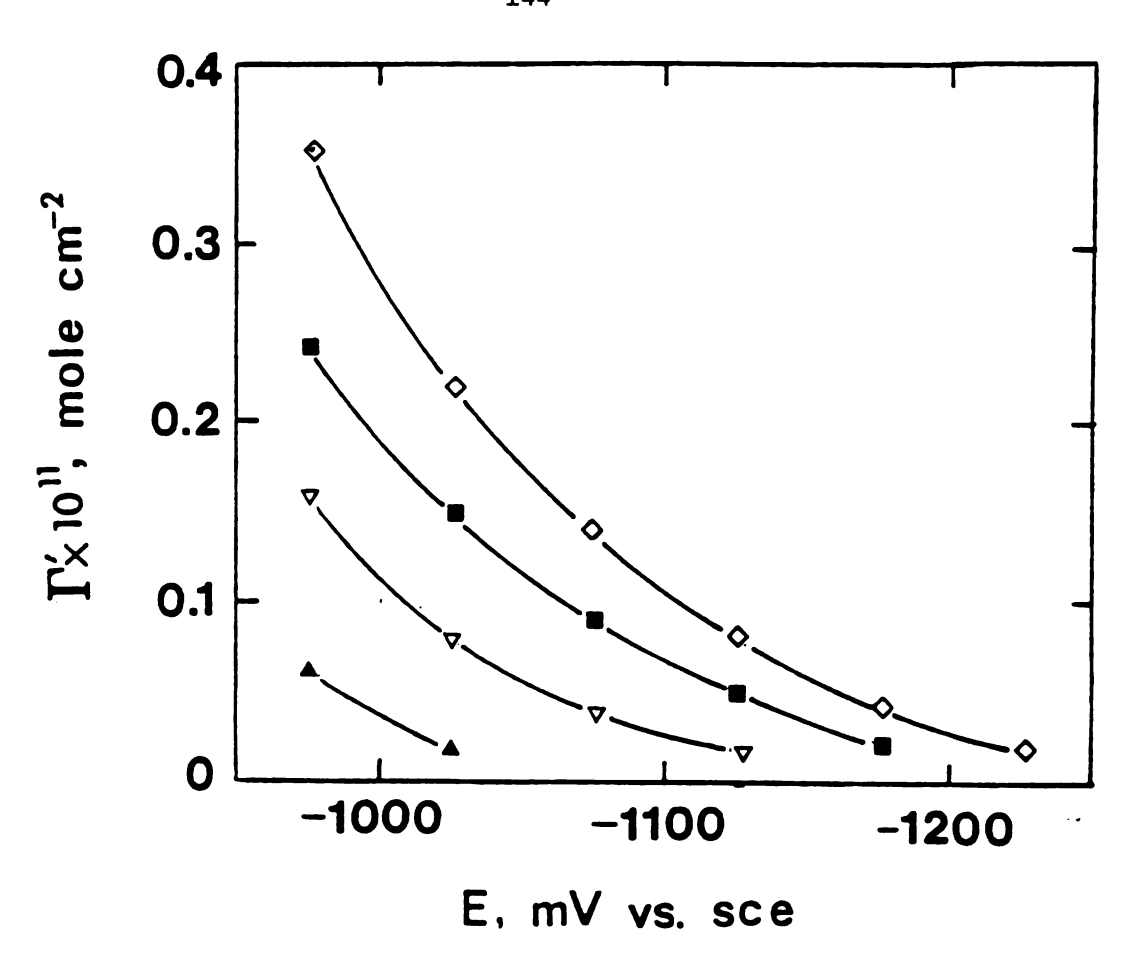


Figure 3.42. Surface concentration of chloride vs. electrode potential for UPD thallium/silver. Conditions as in Figure 3.39.

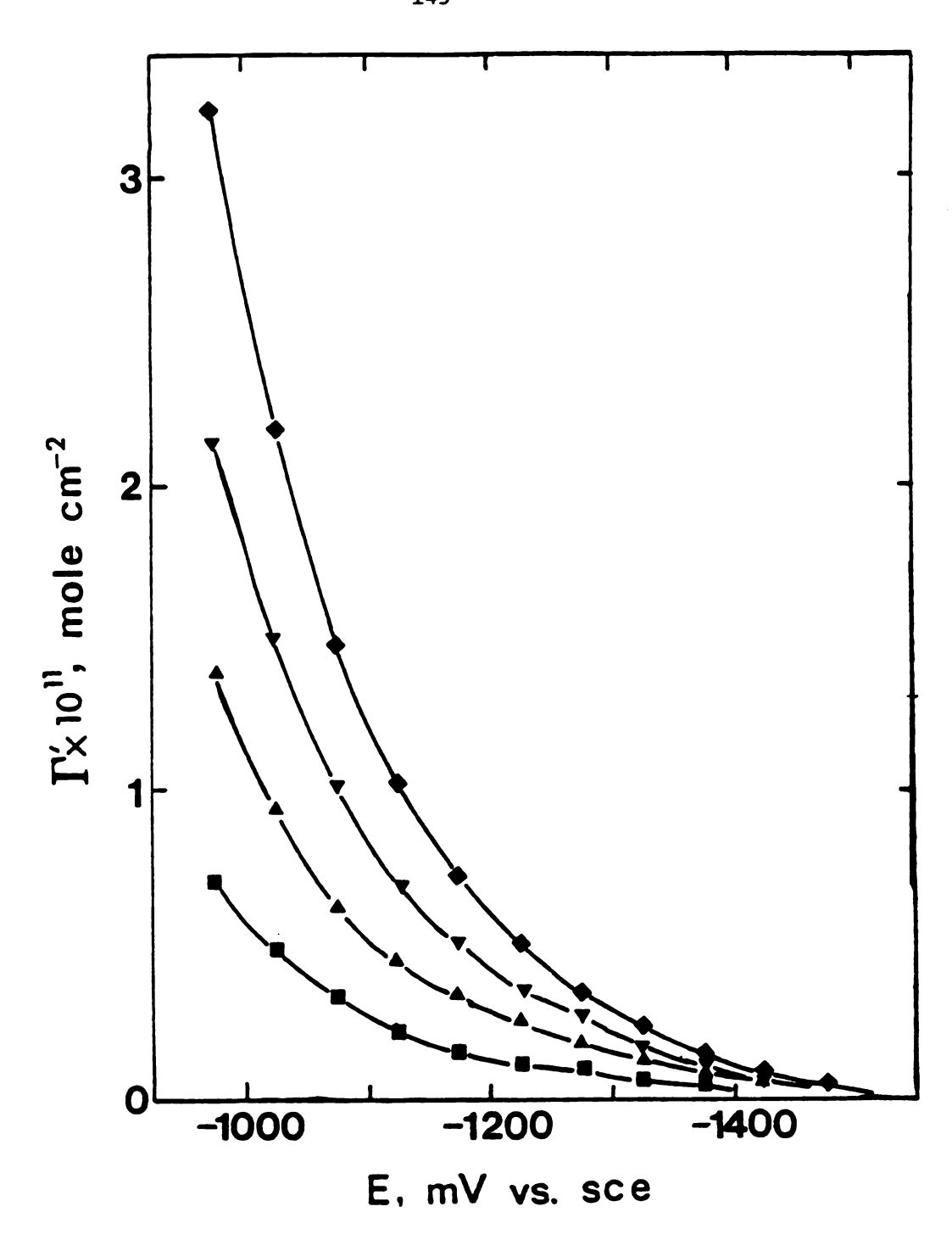


Figure 3.43. Surface concentration of bromide vs. electrode potential for UPD thallium/silver. Conditions as in Figure 3.40.

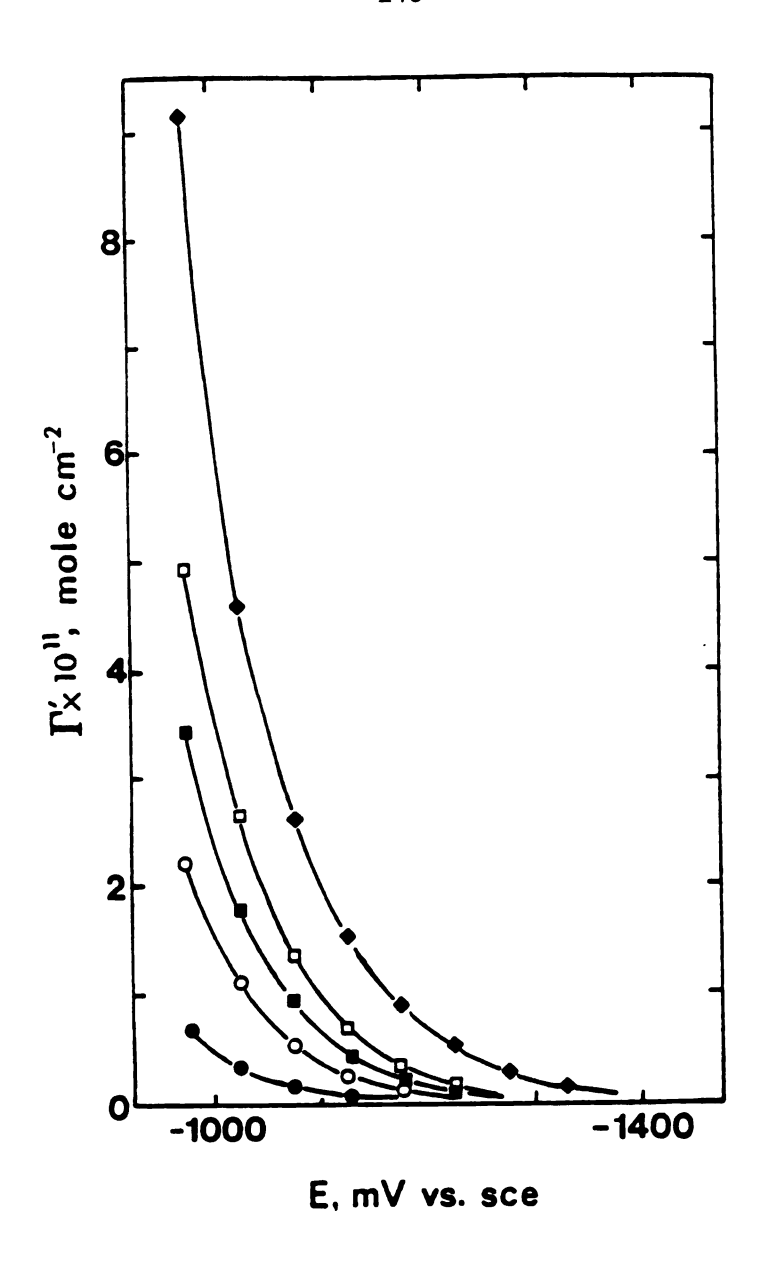


Figure 3.44. Surface concentration of iodide versus electrode potential for UPD thallium/silver. Conditions as in Figure 3.41.

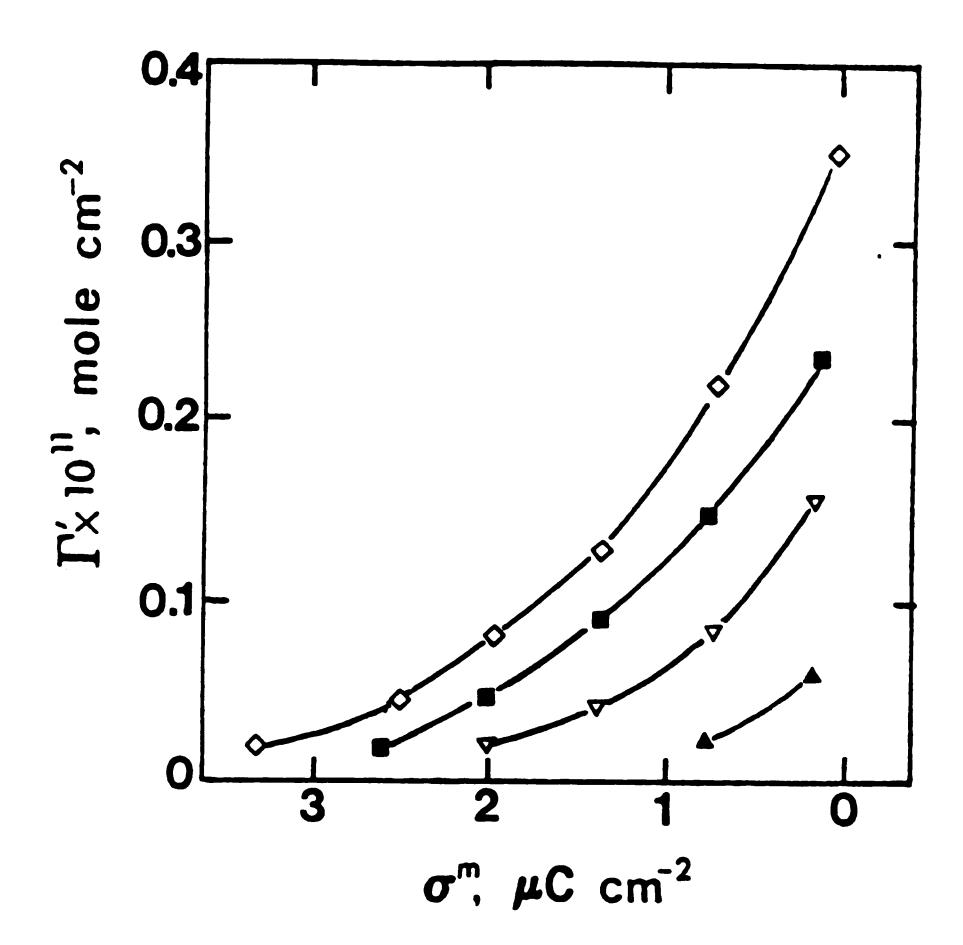


Figure 3.45. Surface concentration of chloride vs. electrode charge density for UPD thallium/silver. Conditions as in Figure 3.39.

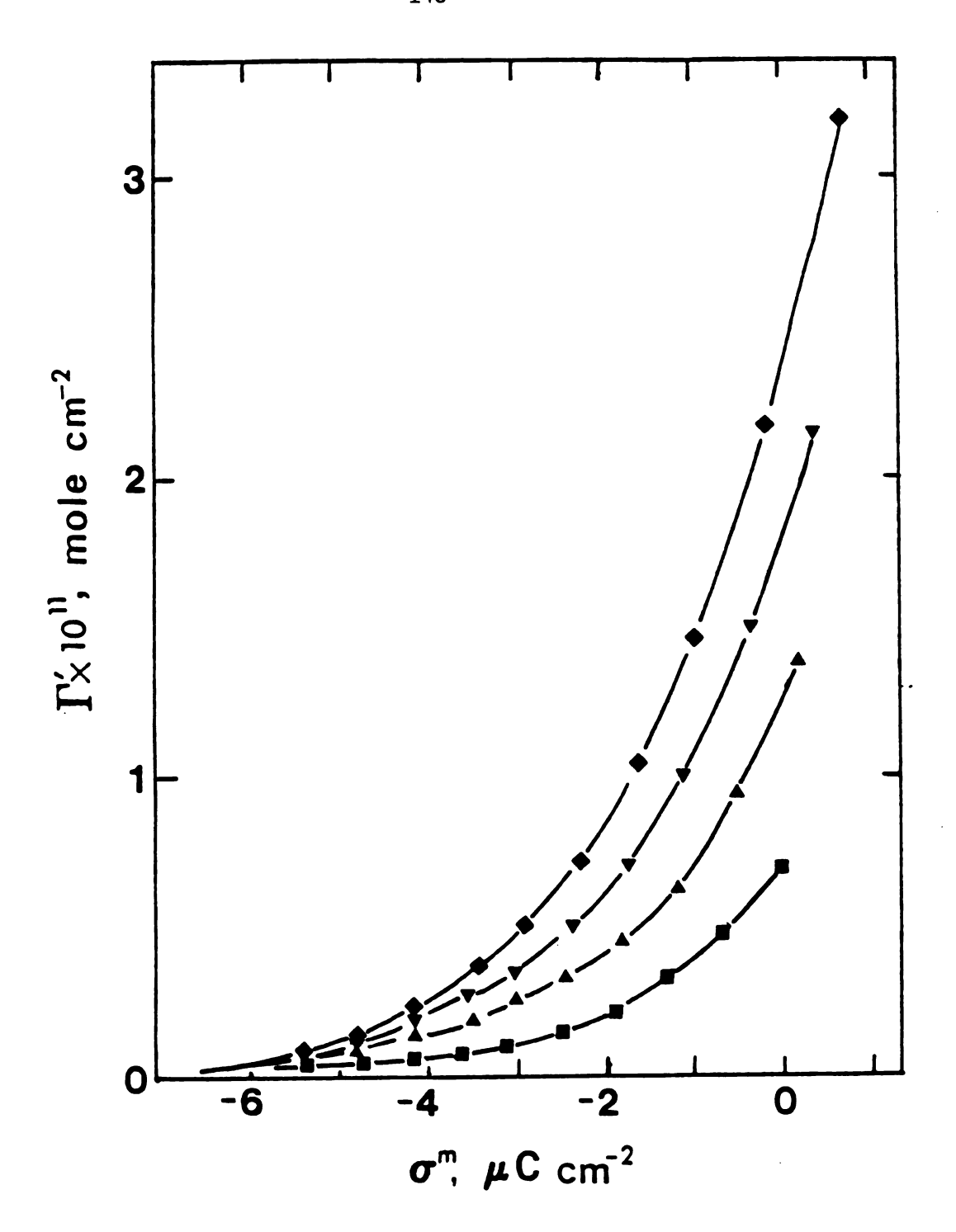


Figure 3.46. Surface concentration of bromide vs. electrode charge density for UPD thallium/silver. Conditions as in Figure 3.40.

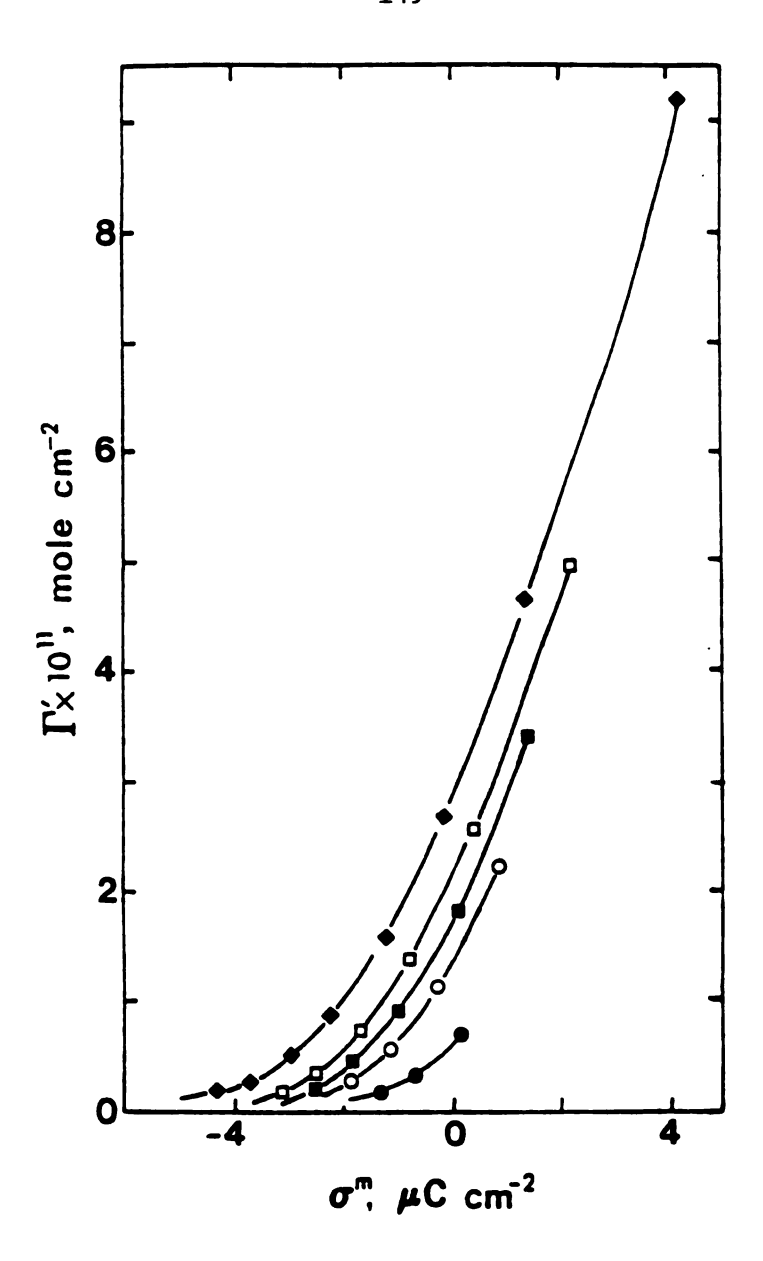


Figure 3.47. Surface concentration of iodide versus electrode charge density for UPD thallium/silver. Conditions as in Figure 3.41.

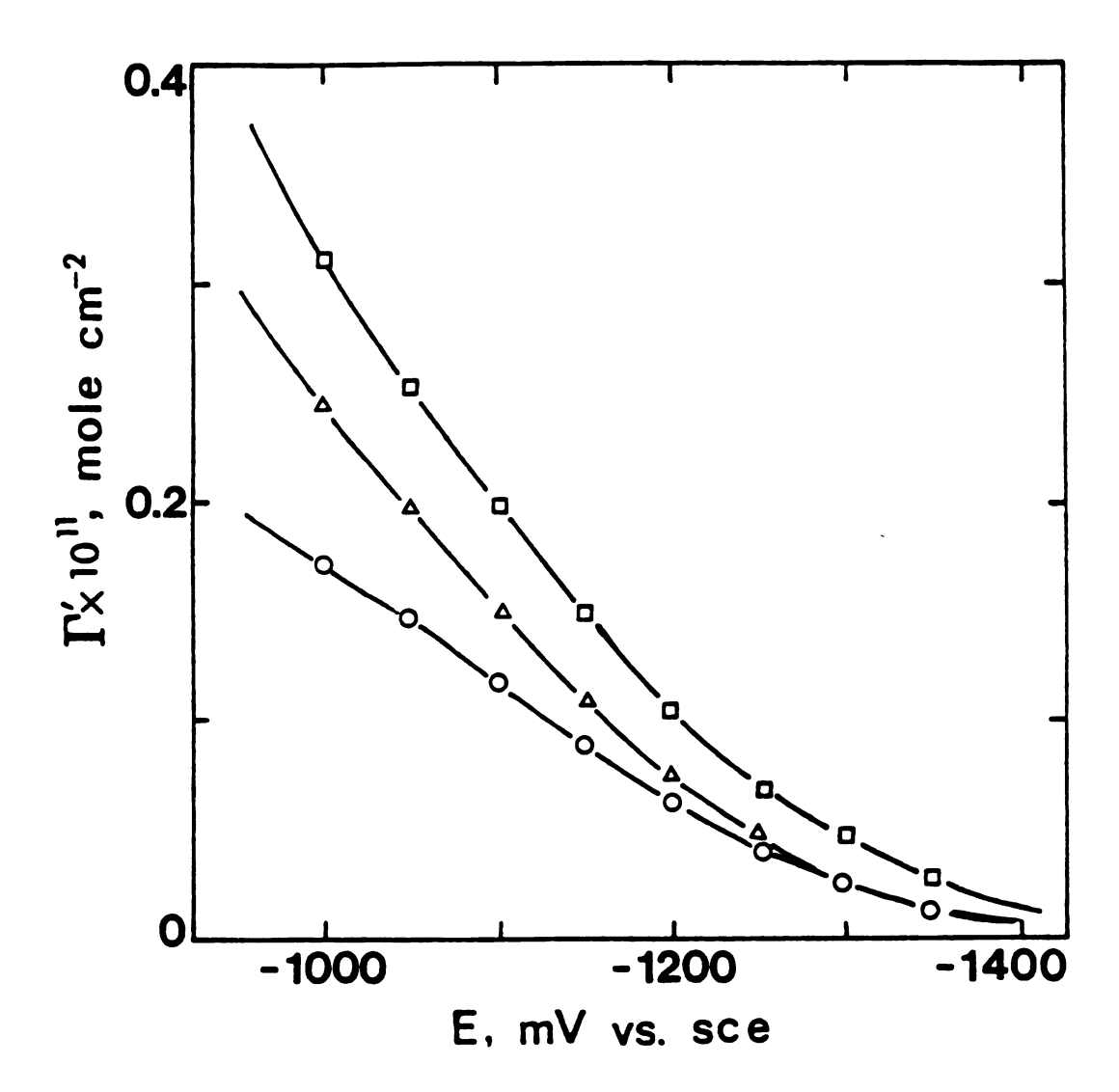


Figure 3.48. Surface concentration of perchlorate vs. electrode potential for UPD thallium/silver in NaClO<sub>4</sub> + NaF mixed electrolytes at an ionic strength of 0.5  $\underline{\text{M}}$ . Key to perchlorate concentrations: (O) 10 mM; ( $\Delta$ ) 60 mM; ( $\Box$ ) 200 mM.

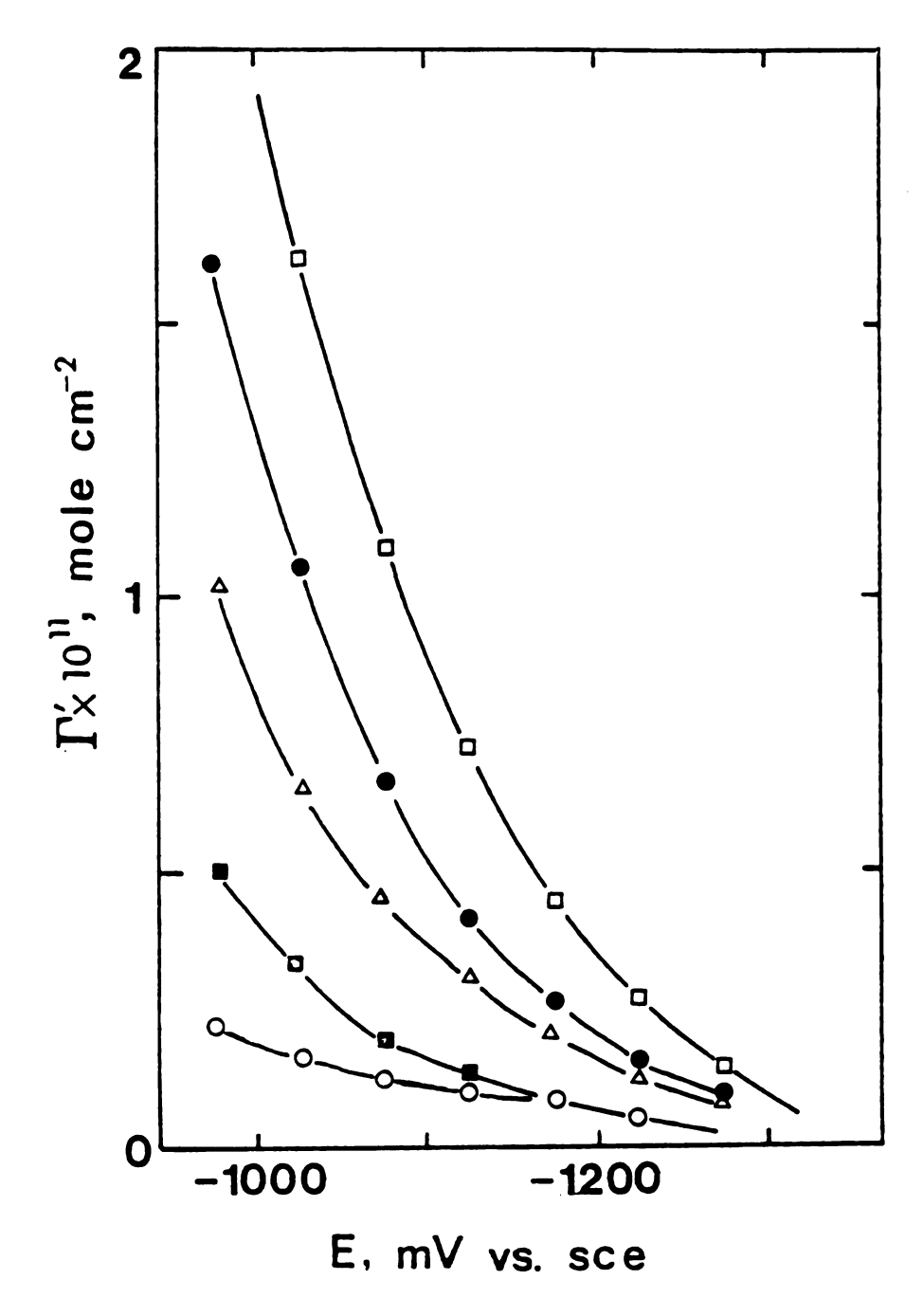


Figure 3.49. Surface concentration of thiocyanate vs. electrode potential for UPD thallium/silver in NaNCS + NaF mixed electrolytes at an ionic strength of  $0.5\underline{M}$ . Key to thiocyanate concentrations: (O)  $1 \ \underline{mM}$ , (B)  $5 \ \underline{mM}$ , (A)  $20 \ \underline{mM}$ , (B)  $50 \ \underline{mM}$ , (C)  $100 \ \underline{mM}$ .

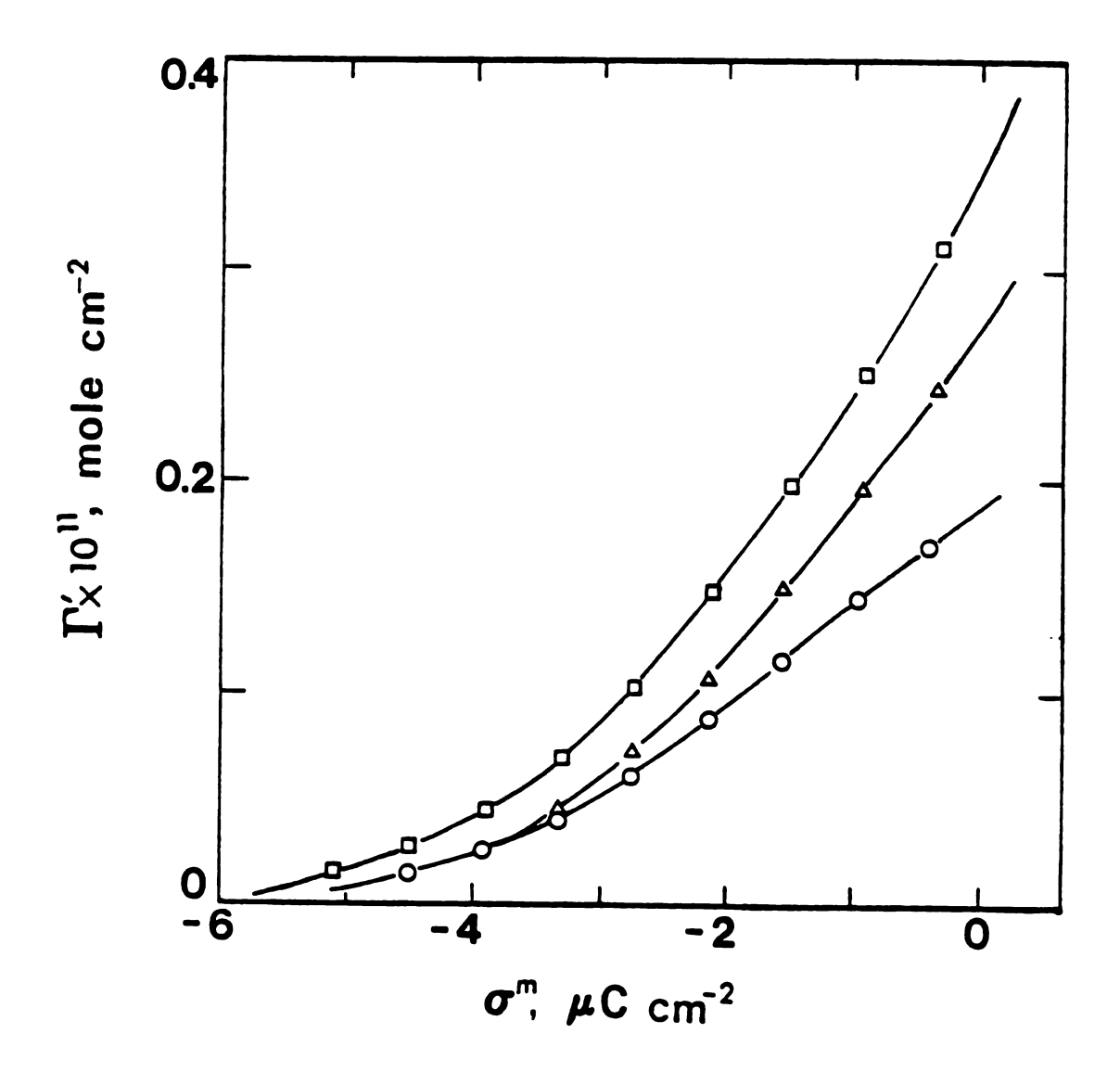


Figure 3.50. Surface concentration of perchlorate versus electrode charge density for UPD thallium/silver. Conditions as in Figure 3.48.

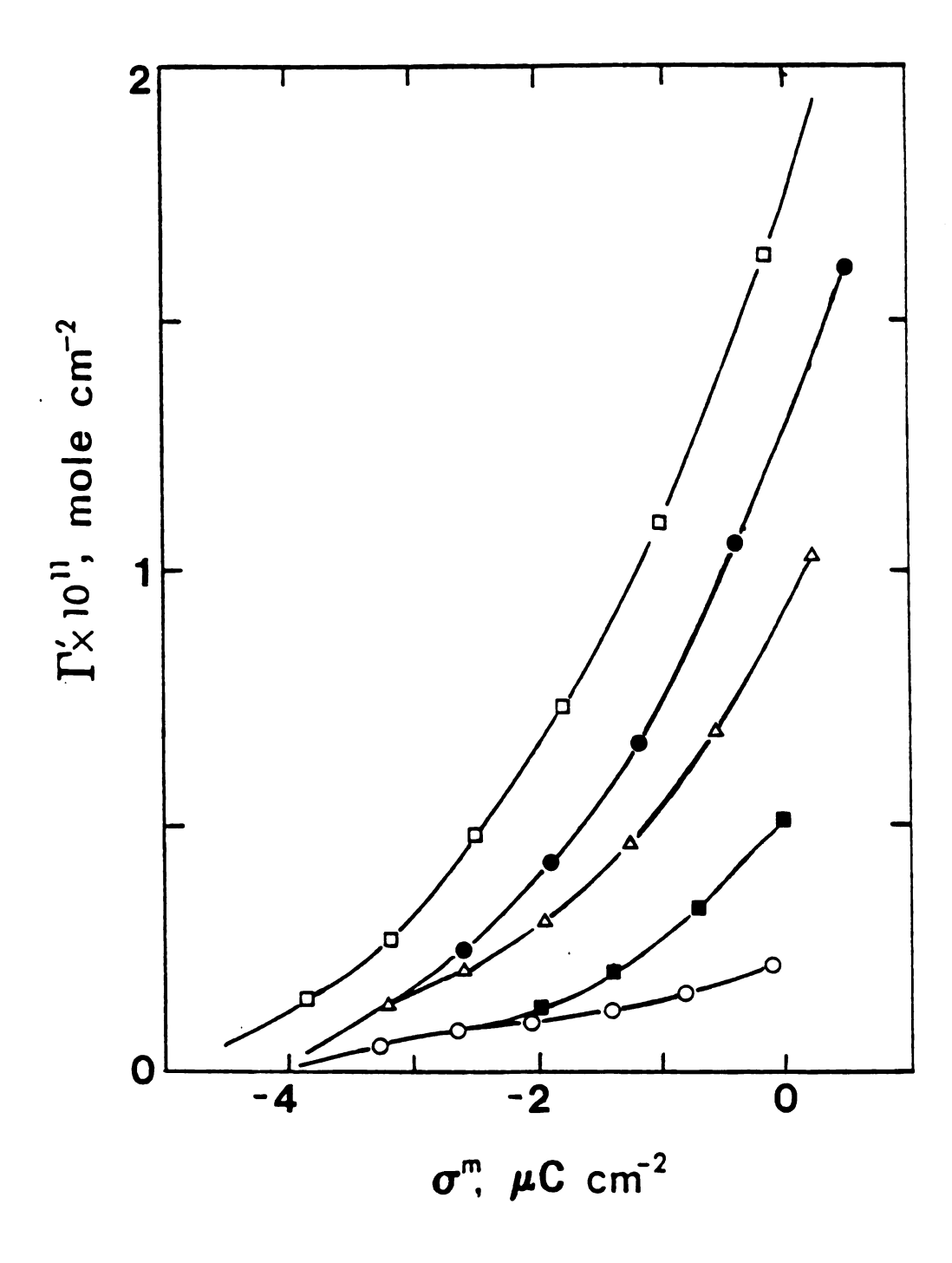


Figure 3.51. Surface concentration of thiocyanate versus electrode charge density for UPD thallium at silver. Conditions as in Figure 3.49.

## 4. Discussion

The pzc estimate of -960 mV for underpotentially deposited thallium is the same as the value reported by Leikis for bulk thallium. 149 This agreement, together with the observation that the capacitance for UPD Tl/Ag is influenced only marginally by further deposition of thallium, suggests that UPD Tl/Ag and bulk thallium surfaces possess similar chemical properties. The capacitance values obtained here are perhaps 25% lower than those found for bulk thallium. However, larger values are obtained if the silver electropolishing step is omitted in preparing the surfaces. This suggests that differences in surface roughness may well account for the differences in capacitance between bulk and UPD thallium.

The shift of the capacitance minimum potential in substituting fluoride by perchlorate is good evidence for specific adsorption of the latter. The ionic strength dependence of the capacitance points to the increasing influence of the diffuse layer as the electrolyte concentration is lowered.

Evidently no data exist regarding anion adsorption at bulk thallium. There is one report concerning the electrocapillary properties of a 0.02% thallium + 99.98% gallium alloy in contact with adsorbing electrolytes. Thallium apparently is the major component of the electrode surface, despite its small bulk concentration. The basic finding is that the alloy, in comparison to most other metals is able to adsorb halide ions only weakly. This is consistent with the findings for UPD thallium/silver.

## 5. Conclusions

Clearly, underpotential deposition of thallium alters the thermodynamic properties of the silver-aqueous interface. The differential double-layer capacitance is lowered and anion adsorption is diminished considerably. Such behavior is similar to that found with underpotential deposition of lead.

## F. The Role of the Surface Metal Composition in Determining Anion Adsorption

## 1. Introduction

In order to examine the question of how the thermodynamics of anion adsorption are influenced by the composition of the electrode surface, results for silver, UPD lead/silver, UPD thallium/silver and mercury electrodes will be compared. Since the same substrate electrode is used for each of the solid surfaces, differences ascribable to electrode pretreatment, surface roughness and so forth should be eliminated. Although not part of the same series as the three other surfaces, mercury is included since data gathered at this electrode generally are trustworthy.

### 2. Results and Discussion

Values of  $\Delta G_a^0$  and g at  $\sigma^m = 0$  are assembled in Table 3.5. the results for mercury were calculated in each case from data given in the literature.  $^{103}, ^{145}, ^{148}, ^{151-153}$  Parsons' surface concentration data for thiocyanate adsorption at mercury from single electrolytes  $^{145}$  could not

Standard Free Energies of Adsorption  $\Delta G_a^0$  (kJ mol $^{-1}$ ) and Interaction Parameters g for Anions at Several Confere. at Several Surfaces Table 3.5.

c	UPD T1/Ag	Ag	UPD Pb/Ag	/Ag	Mercury		Silver	
Adsorbate	ΔG	60	ΔG <sup>O</sup>	<b>50</b>	^G a	60	ΔG	60
	06-	115	06-	110	-102 <sup>b</sup> ,c	7 <sup>0</sup> p	1	!
	-86.5	320	-87	300	(-92) <sub>q</sub>	!	i	!
	-82.5	06	-88	720	-90e,f	40e,f	-101 <sup>8</sup>	~40 <sub>8</sub>
C10 <sub>4</sub>	-82.5	006	-84	120	-88 <sup>8</sup> ,h	408°h	;	!
	!	8 8 8	-87	970	-87 <sup>1</sup> , j	40 <sub>1</sub> ,j	- 95 <sup>8</sup>	100
	-77	200	-80.5	200	-81 <sup>e,k</sup>	~45e,k	- 95 <sup>8</sup>	~20¢~

 $^{a}$ 0.5 M NaF base electrolyte, unless otherwise noted.  $^{b}$  1 M NaClO $_{4}$  base electrolyte.  $^{c}$  Calculated from data given in reference 103.  $^{d}$  Estimated as outlined in text, from data for NaSCN given in reference 145.  $^{e}$  1 M NH $_{4}$ F base electrolyte.  $^{e}$  1 M NH $_{4}$ F base electrolyte.  $^{h}$  Calculated from data given in reference 151.  $^{f}$  0.95 M NaF base electrolyte.  $^{f}$  Calculated from data given in reference 148.  $^{f}$  0.5 M NaClO $_{4}$  base electrolyte.

be fitted to a Frumkin isotherm. The difficulty most likely can be traced to changes in diffuse layer (i.e.,  $\phi_2$ ) effects as the ionic strength varies. Since a good fit with a g value of about 40 was found for each of the other anions in constant ionic strength mixed electrolytes (Table 3.5), a  $\Delta G_a^0$  value for NCS adsorption at mercury was estimated from the surface concentration at  $\sigma^m = 0$  for 1 M NaNCS by assuming that in mixed electrolytes g=40 for NCS as well.

The  $G_a^0$  and g values in Table 3.5 indicate that at mercury and the two underpotentially deposited surfaces the extent of adsorption at  $\sigma^m$  = 0 varies with the nature of the anion as follows:  $I^-> NCS^{-}\ge Br^-> C10_4^{-}\ge N_3^{-}> C1^-> F^-\ge 0$ . At silver the order is  $I^-> NCS^-> Br^-> N_3^-> C1^-> F^-> C10_4^--\ge 0$ . For most ions, adsorption is greatest at silver, followed by mercury, UPD lead/silver and finally, UPD thallium/silver. In order to understand these trends it is useful to consider each of the factors controlling the energetics of adsorption. These are: the partial desolvation of the anion upon adsorption, desolvation of the electrode at the adsorption site, and the bonding interaction between the anion and the metal surface.  $^{154,155}$ 

For adsorption of different anions at the same surface only the first and third factors will vary. Table 3.6 lists values of "anion desolvation enthalpies" taken from Table 1 of reference 155. Interestingly, these follow the same order as the adsorption equilibria for anions at mercury, UPD thallium/silver and UPD lead/silver, suggesting that partial desolvation of anions is of central importance. Evidently, ion-metal bonding interactions at each of these electrodes are similar for different anions or else vary in exactly the same

Table 3.6
Enthalpies of Desolvation
for Anions in Water a

<u>Anion</u>	Δ <u><b>Η</b></u>
ı-	$-56 \text{ kJ mol}^{-1}$
Br <sup>-</sup>	-121
c10 <sub>4</sub>	-131
cı <sup>-</sup>	-168
F <sup>-</sup>	-329

a Taken from reference 155.

manner as the desolvation enthalpy. Since the ordering of adsorption strength is somewhat different at silver, variations in the anion-silver bond strength evidently must be significant, at least for perchlorate in comparison to the other anions.

Surprisingly, there is little consensus concerning the nature of the bond between an ion and an electrode surface. Levine has considered the adsorption bond to be little more than an image interaction between the ionic charge and the metal. 156 Vijh has tried to represent the anion adsorption process as the formation of surface compounds of the type  $M^+$   $X^-$ . However, this hardly seems reasonable when the electrode carries no charge. Barclay, 157, 158 as well as Conway, 159 claim that adsorption is analogous to metal complex formation. Barclay, in particular, has elaborated on this idea and attempted to apply the nebulous Hard-Soft Acid-Base approach 160 to adsorption. Although some success is claimed, one finds equally good agreement with experiment by ignoring completely the anion-electrode bond and focusing instead on ionic solvation. Trasatti dismisses both the Vijh and Barclay approaches on the grounds that they do not account for differences in the strength of adsorption as the electrode material is varied. 154 Unfortunately, the present results do not seem to provide many new clues concerning the merits of these different approaches to anion-electrode bonding.

Trassatti has popularized the idea that differences in metal-solvent interactions are the chief factor contributing to differences in the adsorption capabilities between various electrodes. <sup>154</sup> The most "hydrophilic" surfaces are expected to adsorb ions only weakly, while

the less hydrophilic surfaces should induce stronger adsorption. Unfortunately, Trassatti's attempts at testing these ideas are flawed because he chose as a quantitative measure of adsorption the shift of the pzc in nonadsorbing electrolytes following the addition of iodide. This measure is biased against the electrode-solution interfaces exhibiting large capacitance values since these will require large amounts of adsorbed charge in order to displace the pzc by a given amount. Similarly, the proposed correlation of the potential shift with the magnitude of the inner-layer capacitance  $^{154}$  or its reciprocal  $^{154}$  is hardly useful since a correspondence is expected in the absence of any sensitivity of adsorption strength to the electrode composition. A comparison of  $^{\Lambda}G_a^0$  and g values for anions at different metals should provide a more objective test than a comparison of shifts of zero-charge potentials.

An accurate knowledge of at least the relative strengths of interaction of the solvent with different metals is required in order to evaluate these ideas. A measure of such interactions is given by the difference between the work function of a metal and the potential of zero charge of the same metal in contact with a nonadsorbing electrolyte. 133b, 161 The two will differ on an absolute scale by the amount of the potential drop across the inner layer of solvent dipoles. This potential drop will be nonzero if the dipolar solvent molecules are preferentially oriented. A problem however is the lack of sufficiently accurate values of the work function for most metals.

A more approximate approach to evaluating hydrophilicity is based on the notion that water molecules, if preferentially oriented, will

Table 3.7

Heats of Formation of Metal Oxides

Reaction	$_{\Delta}\mathtt{H}_{\mathtt{f}}^{\mathtt{o}}$
$Pb(c) + 1/2 0_2 (g) + Pb0(c)$	-221 kJ mol <sup>-1</sup>
$2T1(c) + 1/2 0_2 (g) + T1_20(c)$	-184
$2Hg(1) + 1/2 0_2 (g) + Hg_2 0(c)$	<b>-</b> 93
$Hg(1) + 1/2 0_2 (g) + Hg0(c)$	<b>-91</b>
$2Ag(c) + 1/2 0_{2} (g) \rightarrow Ag_{2}0(c)$	-32

a Taken from reference 165, pp. D45-47.

bind to an electrode via the oxygen end 154,161 since metal surfaces should behave as Lewis acids. 158 If this is true (as seems to be the case) the enthalpy of metal oxide formation may provide an indication of the affinity of a surface for water. 161 A direct check of this hypothesis is possible by considering some recent work on the chemistry of oxygen-bound adducts of water with single metal atoms. 162-164 From matrix isolation spectroscopy, Margrave and co-workers 162 found that shifts of the  $v_2$  bending mode of water which accompany adduct formation with Group III A metal atoms are indeed paralleled by decreases in the heats of formation of HMOH compounds as well as the corresponding metal oxides. Also,  $v_2$  is shifted more for T1...OH<sub>2</sub> than for Pb...OH<sub>2</sub> indicating greater sigma bonding between water and thallium than between water and lead. 162,163 Silver and mercury have not been studied.

Table 3.7 lists  $\triangle H_f^o$  values for several metal oxides. <sup>165</sup> Although comparisons are hampered because the oxide stoichiometry is not the same in every case, the overall indication is that oxygen affinity increases in the order: Ag \(\mathref{Hg}\) \(\mathref{Tl}\)\(\mathref{Pb}\). In light of Margrave's findings a more correct sequence is: Ag \(\mathref{Hg}\)\(\mathref{Pb}\)\(\mathref{Tl}\). Recalling that anion adsorption capabilities change in the following order: UPD T1/Ag \(\mathref{UPD}\)\(\mathref{Pb}\)\(\mathref{Ag}\)\(\mathref{Hg}\)\(\mathref{Ag}\), these observations support Trassatti's basic suggestions.

## 3. Conclusions

Underpotential deposition provides an excellent means of varying the electrode surface composition in a controlled manner for the purposes of studying anion adsorption and double-layer properties.

Comparisons of free energies of adsorption for six anions at four

surfaces suggest that ionic solvation is a primary factor in determining relative degrees of adsorption of different anions at a given surface. Variations in anion-metal bonding interactions also contribute to the adsorption pattern found at silver. An inverse correlation is found between surface hydrophilicity and the extent of adsorption at different electrodes, in harmony with recent proposals by Trassatti. Thus, variations in the strength of metal-water interactions appear to be responsible, at least in part, for the differences in the abilities of various metal surfaces to adsorb anions.

G. A Method for Evaluating the Surface Concentrations of Two

Like-Charged Ions Simultaneously Adsorbed at an Electrode
Solution Interface

(Accepted for publication in J. Electroanal. Chem.)

A recent preliminary report by Gonzales and co-workers highlights the experimental difficulties in determining the amounts of specific adsorption of two types of ions simultaneously present at a mercury-aqueous interface. 166 The authors note that the elegant analysis of Lakshmanan and Rangarajan 167 requires such a large amount of data that the method has scarcely ever been employed. There are additional difficulties with this analysis. The Rangarajan approach relies on an evaluation of the ionic strength dependence of the interfacial tension at a constant electrode potential or charge. However, accurate absolute, or even relative, values of the interfacial tension at different

ionic strengths are largely inaccessible at solid surfaces.\* These difficulties vitiate the use of Rangarajan's method at polycrystalline solid electrodes and in many circumstances at single crystal solid electrodes. (For the same reasons, the single electrolyte adsorption analysis of Grahame and Soderberg<sup>34</sup> also is inapplicable to polycrystalline surfaces, despite statements to the contrary<sup>168</sup>). Additionally a knowledge of at least relative ionic activities in electrolyte mixtures over a range of ionic strengths is necessary. Clearly it would be desirable to find a method that could be applied at solid as well as liquid electrodes without requiring an inordinate amount of data and a detailed knowledge of electrolyte activity coefficients.

A suitable analysis method can be formulated via a simple extension of the well-known "Hurwitz-Parsons" approach. 35,36 Hurwitz and Parsons demonstrated independently that the amount of specific adsorption of, for example, an anion X can be assessed from differential capacitance-potential data for a series of mixed electrolytes containing varying proportions of the salts BX and BY at a constant total ionic strength, where Y is an anion that is not specifically adsorbed. The electrocapillary equation can be written in terms of salt chemical potentials:

$$-d\gamma = \sigma^{m} dE^{+} + \Gamma_{X} d\mu_{RX} + \Gamma_{V} d\mu_{RV}$$
 (3.7)

<sup>\*</sup>An exception is the case of a single crystal in contact with a dilute, nonspecifically adsorbed electrolyte. Here, capacitance-potential measurements can provide a route to the absolute electrode charge and therefore the relative interfacial tension.

where  $\gamma$  is the interfacial tension,  $\sigma^m$  is the electrode charge,  $E^+$  is the electrode potential with respect to a reference electrode reversible to the cation  $B^+$ ,  $\Gamma_i$  is the total surface excess of component i and  $\mu_j$  is the chemical potential of the salt j. Parsons showed that the required surface concentration of specifically adsorbed  $X^-$ ,  $X^-$ , could be obtained from these data using several differential relationships including

$$-(1/RT)(\partial Y_{rel}/\partial \ln m_{RK})_{E} = \Gamma_{X}$$
 (3.8)

where E is the potential with respect to a fixed reference electrode,  $m_{BX}$  is the mole fraction of X¯, and where  $Y_{rel}$  denotes the relative interfacial tension obtained by double integration of the capacitance-potential data. <sup>86,95</sup> However, if Y¯ is also specifically adsorbed all that can be obtained is a combination of the surface excesses of specifically adsorbed X¯ and Y¯, since <sup>36</sup>

$$-(1/RT)(\partial_{Y} = 1/\partial_{RX})_{E} = \Gamma_{X} - [m_{BX}/(1-m_{BX})]_{\Gamma_{Y}}$$
(3.9)

or

$$-(1/RT)(\partial \gamma_{rel}/\partial lnm_{BY})_{E} = \Gamma_{Y} - [m_{BY}/(1-m_{BY})] \Gamma_{X}$$
 (3.10)

(Note that Equations 3.9 and 3.10 are not independent since Equation 3.9 follows Equation 3.10 given that  $m_{RX} + m_{RY} = 1$ ).

If a third salt BZ is present in the solution the electrocapillary equation becomes

$$-d \Upsilon = \sigma^{\mathbf{m}} dE^{+} + \Gamma_{\mathbf{X}} d\mu_{\mathbf{B}\mathbf{X}} + \Gamma_{\mathbf{Y}} d\mu_{\mathbf{B}\mathbf{Y}} + \Gamma_{\mathbf{Z}} d\mu_{\mathbf{B}\mathbf{Z}}$$
(3.11)

If two of the anions, say X and Y , are specifically adsorbed while the third, Z , is not, it is possible to determine  $\Gamma_{X}$  independently of  $\Gamma_{Y}$  by obtaining relative surface tension versus potential data for a series of constant ionic strength solutions having the composition  $x_1$  BX +  $(1-x_1)$ BZ +  $y_1$ BY. The concentration variable  $x_1$  equals  $C_{BX}/(C_{BX} + C_{BZ})$ ;  $(C_{BX} + C_{BZ})$  is held constant as well as the solution concentration of co-adsorbed Y . For the salt BX (and similarly for the others) we can write:

$$d\mu_{MX} = RTdlna_{RX} RTdlnC_{RX}^{\tilde{z}}$$
 (3.12)

where  $a_{BX}$  is the activity of BX and  $C_{BX}$  is its molar concentration. Following Parson's derivation<sup>36</sup> and noting that  $dlnC_{BX} = dlnx_1$  and  $dlnC_{BY} = dlny_1$ , Equation 3.11 can be reformulated as

$$-d^{\gamma} = \sigma^{m} dE^{+} + \{ \Gamma_{X} - [x_{1}/(1-x_{1})] \Gamma_{Z} \} RTdlnx_{1} + \Gamma_{Y} RTdlny_{1}$$
 (3.13)

Provided that the components of  $\Gamma_X$ ,  $\Gamma_Y$  and  $\Gamma_Z$  in the diffuse layer are present in the same proportions as the concentrations of these anions in the bulk solution, then Equation 3.13 can be rewritten as

$$-dY = \sigma^{m} dE^{+} + \{\Gamma_{X} + [x_{1}/(1-x_{1})\Gamma_{Z}]\} RTdlnx_{1} + \Gamma_{Y} RTdlny_{1}$$
 (3.14)

If  $C_{BY}$  is invariant, then the term  $\Gamma_{Y}$  RTdlny<sub>1</sub> will disappear when the dependence of  $\Upsilon_{rel}$  upon  $\mathbf{x}_{l}$  is evaluated, <u>regardless</u> of whether specific adsorption of  $Y^{-}$  occurs. Similarly to the conventional analysis we obtain

$$-(1/RT)(\partial_{x_{el}}^{\gamma}/\partial_{x_{el}}^{\gamma}/\partial_{x_{el}}^{\gamma})_{E,C} = \Gamma_{X}^{\gamma} - [x_{1}/(1-x_{1})]\Gamma_{Z}^{\gamma}$$
 (3.15)

which enables  $\Gamma_{X}$  to be evaluated provided that  $[x_1/(1-x)]\Gamma_{Z}$  is small compared to  $\Gamma_{X}$ .

Similarly,  $\Gamma_{Y}$  can be determined from measurements in a series of solutions having the composition  $[y_2BY + (1-y_2)BZ + x_2BX]$ , where  $y_2 = C_{BY}/(C_{BY} + C_{BZ})$  and  $(C_{BY} + C_{BZ})$  is constant, as is  $x_2$ . The values of  $\Gamma_{Y}$  in the presence of co-adsorbing X can be obtained from

$$-(1/RT)(\partial \gamma_{rel}/\partial lnC_{BY})_{E,C} = \Gamma_{Y} - [y_{2}/(1-y_{2})] \Gamma_{Z}$$
 (3.16)

By performing two sets of experiments at the same total ionic strength,  $\Gamma_X$  can be obtained in mixed electrolytes having the same composition as in solutions used to determine  $\Gamma_Y$ . Thus values of both  $\Gamma_X$  and  $\Gamma_Y$  can be extracted using this analysis be employing electrolytes that also contain a third anion Z which is not specifically adsorbed, or at least is much less strongly adsorbed than either X or Y. Similarly to the usual Hurwitz-Parsons analysis, a major virtue of the present method is that it can be employed at solid, as well as liquid,

electrodes. This is because the required Y rel-E plots can be obtained by doubly integrating measured capacitance-E data provided that a potential region is accessible where the extent of anion specific adsorption is negligible. 86,95 (This constitutes the fundamental advantage of the constant ionic strength approach. Although absolute surface tension data can of course be obtained at liquid electrodes, even values of Y are unobtainable at solid electrodes for families of electrolytes at varying ionic strengths without making additional assumptions based on diffuse-layer theory). As an alternative to the use of Equations 3.15 and 3.16,  $\Gamma_{\chi}$  and  $\Gamma_{\chi}$  may be obtained from the displacement of relative electrode charge-potential curves obtained by singly integrating the capacitance-potential data. 86,103 although this latter procedure is often more sensitive to small amounts of specific adsorption 36,86 it is difficult to apply when the adsorption isotherms are highly noncongruent, as expected for the coadsorption of two like-charged ions. The evaluation of Y rel-E data via Equations 3.15 and 3.16 is therefore preferred as the route to  $\Gamma_{X}^{\bullet}$  and  $\Gamma_{\mathbf{v}}$  for most systems.

The total number of capacitance, charge or interfacial tension measurements required to evaluate  $\Gamma_{X}$  and  $\Gamma_{Y}$  via Equations 3.15 and 3.16 is perhaps no fewer than the number required for the Rangarajan analysis. However, the need for extensive auxillary information regarding ionic activities and absolute electrode charges is obviated. Also, in the present analysis the cumbersome  $E^{+}$  scale is replaced with potentials measured against a fixed reference electrode since the cation activity is anticipated to remain nearly constant for anion

mixtures at a constant ionic strength. If \(\Gamma\) values are needed for only one of two simultaneously adsorbed ions this analysis is more straightforward since considerably fewer data are required than in the Rangarajan approach. 167 It should be noted that \(\Gamma\) for the simultaneous adsorption of cations and anions can also be obtained individually by using the conventional Hurwitz-Parsons procedure 169 in a more straightforward manner than using the Rangarajan approach. In addition, the present analysis could be extended to treat the simultaneous adsorption of more than two like-charged ions, although the quantity of data required would become rapidly prohibitive as the number of coadsorbing ions increases.

The present analysis involves essentially the same assumptions as are required in the usual Hurwitz-Parsons approach. 35,36 Thus in addition to the assumption already made concerning diffuse-layer composition the activity coefficients of all three salts are presumed to remain constant in the various constant ionic strength solutions. This is perhaps more tenuous for mixtures of three salts than for two. In principle, it is possible to relax this assumption by reformulating the analysis in terms of activities. The chief disadvantage is one shared by the usual Hurwitz-Parsons analysis, namely, a relatively surface-inactive salt is needed or errors will be introduced into the results (Equations 3.9, 3.10, 3.15, 3.16). Nevertheless, this difficulty is anticipated to be less severe in the present case where a pair of like-charged ions are adsorbed since the repulsive interactions with the third, more weakly adsorbing, "reference" ion Z should maintain the adsorption of Z at sufficiently low levels to avoid

vitiating the analysis. It is hoped that the comparatively less extensive experimental effort required in order to utilize the present analysis coupled with its wider applicability will spur research on the topic of simultaneous ion adsorption. We intend to employ the analysis in our ongoing studies of ionic adsorption at metal interfaces that exhibit Surface-Enhanced Raman Scattering (SERS)<sup>86</sup>,87,97,102. In Raman studies of adsorbed anions, chloride supporting electrolytes which themselves are strongly adsorbed are routinely employed in order to facilitate the mild electrochemical surface roughening that is conducive to the observation of SERS. The extended Hurwitz-Parsons analysis should enable the surface concentrations of chloride and other anions to be assessed independently.

#### CHAPTER IV

#### ELECTROCHEMICAL KINETICS

# A. The Frequency Factor for Electrochemical Reactions [Originally published in J. Electroanal. Chem. 152, 1 (1983)]

## 1. Introduction

The observed rate constant,  $k_{ob}$  (cm sec<sup>-1</sup>), for heterogeneous outer-sphere electron transfer is usually related to the overall free energy barrier  $\Delta G$ , by <sup>13</sup>:

$$k_{ob} = \kappa_{el} A_{n} \exp(-\Delta G^{\dagger}/RT)$$
 (4.1)

where  $\kappa_{el}$  is the electronic transmission coefficient, and  $A_n$  is the nuclear frequency factor (cm s<sup>-1</sup>). The latter term equals the effective frequency at which the transition state is approached from the reacting species via rearrangement of the appropriate nuclear coordinates, whereas  $\kappa_{el}$  describes the probability with which electron transfer will occur once the transition state has been formed. For so-called adiabatic processes,  $\kappa_{el} \approx 1$ , whereas for nonadiabatic processes,  $\kappa_{el} <<1$ . Essentially equivalent approaches can be employed for both homogeneous and electrochemical electron-transfer processes. Knowledge

of  $A_n$  and  $k_{el}$  is required in order to extract estimates of  $\Delta G^{\neq}$  from experimental rate constants, thereby providing the link with theoretical treatments of electron transfer which are generally expressed in terms of Franck-Condon barriers. The value of the frequency factor is also closely related to questions concerning the theoretical upper limits to electrochemical rate constants.

Although A has conventionally been assumed to correspond to a collision frequency Z, there are good reasons to prefer a somewhat different formulation based on an "encounter preequilibrium" model whereby the frequency factor is determined by the vibrational activation of a binuclear "encounter (or precursor) complex" having a suitable geometric configuration for electron sfer. 10,17,18,23,28,30,31 Such a model has received a good deal of recent attention for homogeneous redox processes. 10,17,18,23,28 We have suggested that a similar preequilibrium, rather than a collisional, description is also appropriate for outer-sphere electrochemical reactions. 30,31 In this section, we critically compare such collisional and encounter preequilibrium formulations of the electrochemical frequency factor, and consider the consequences of employing the latter formalism upon some theoretical expressions for electrochemical kinetics and their relationship to those for homogeneous redox processes.

## 2. The Collisional Model

As already noted, the nuclear frequency factor for electrochemical reactions,  $A_n^e$ , has conventionally been assumed to equal the rate,  $A_e$ 

(cm s<sup>-1</sup>), at which unit bulk concentration of reactant molecules strike unit area of a two-dimensional "reaction plane" at (or suitably close to) the electrode surface, leading to reaction. This is usually taken to be equal to the collision number for gas-phase heterogeneous collisions involving hard spheres given by: 13

$$z_e = (k_B T / 2\pi m)^{1/2}$$
 (4.2)

where  $k_B$  is the Boltzmann constant and m is the mass of the reactant. The corresponding expression for the collision frequency,  $A_h(\underline{M}^{-1} s^{-1})$ , commonly used for electron-transfer reactions in homogeneous solution is  $^{13}$ 

$$A_{\rm h} = 10^{-3} Nr_{\rm h}^{2} (8\pi k_{\rm B} T/m_{\rm r})^{1/2}$$
 (4.3)

where N is Avogadro's number, and  $m_r$  and  $r_h$  are the effective reduced mass and the distance between the recting centers, respectively, for the collision complex.

Such expressions are not strictly applicable to condensed-phase reactions since collisions involving solute molecules are expected to occur within solvent cages ("encounters") having average lifetimes that are long compared to the collisions themselves. Expressions for the rate of diffusion-controlled encounter formation have been given for homogeneous reactions, 29,171 the best known being the Smoluchowski equation. An analogous expression for the rate of diffusion-

controlled encounters between a spherical reactant and a plane surface has been given as 172

$$Z_{p} = 3D/2\lambda \tag{4.4}$$

where D is the diffusion coefficient of the reactant and  $\lambda$  is the average distance over which the reactant is required to move between adjacent "lattice positions" in the solvent. Somewhat smaller estimates of Z<sub>e</sub> are obtained using Equation 4.4 than from Equation 4.2; thus inserting the typical values D =  $10^{-5}$  cm<sup>2</sup> sec<sup>-1</sup> and  $\lambda$  = 3 x  $10^{-8}$  cm into Equation 4.4 yields Z<sub>e</sub> = 5 x  $10^{2}$  cm sec<sup>-1</sup>, whereas Z<sub>e</sub> = 5 x  $10^{3}$  cm s<sup>-1</sup> from Equation 4.2 at ambient temperatureas taking Nm = 200. Similarly smaller estimates of Z<sub>h</sub> are obtained using the Smoluchowski equation in place of Equation 4.3. <sup>171</sup> A number of collisions are nevertheless expected to occur during each diffusive encounter, so that Equations 4.2 and 4.3 may predict roughly the correct order of magnitude of the collision frequencies in solution. Values of Z<sub>h</sub> that are somewhat larger than given by Equation 4.3 result from a detailed consideration of such "solvent cage" effects.<sup>29</sup>

However, there are two difficulties with such collisional formulations for electrochemical as well as homogeneous electron-transfer reactions. By extending the analogy with gas-phase reactions the model seems to imply that the collisions themselves are responsible for activating the reactant molecules; in other words, a portion of the translational momentum of the reactant is converted to an activation energy. In contrast, contemporary theories of electron transfer

maintain that reactants are activated through solvent polaron fluctuations (outer-shell modes) and by energy transfer from solvent phonons to inner-shell vibrational modes. This problem can be circumvented by noting that the collision model applied to electrochemical reactions requires only that suitably activated reactants strike the electrode at a certain frequency. Unlike gas-phase reactions, activation in solution need not occur simultaneously with the collisions. Thus the usual formulation of the collision model for electron-transfer processes in solution represents an anomalous situation in chemical kinetics, namely that the chosen frequency factor for the elementary reaction does not correspond to the frequency of passage across the barrier.

A more serious difficulty concerns the implication that charge transfer involves only those reactants striking the collision plane, presumably the outer Helmholtz plane for outer-sphere electrode reactions. Actually, since outer-sphere reactions involve only electron tunneling which in principle can occur between essentially isolated donor and acceptor orbitals, reactivity is not confined to the collision plane but instead can involve any reactant molecules located within a range of distances from the electrode surface. <sup>18</sup> The collisional model may therefore underestimate the number of molecules contributing to the observed reaction rate, yielding a falsely small value of the frequency factor A.

## 3. The Encounter Preequilibrium Model

These difficulties suggest that a more appropriate description of the frequency factor for outer-sphere electron-transfer is in terms of activation via solvent-resctant energy transfer of isolated reactant molecules that nevertheless are located so to allow electron transfer to occur with reasonable probability once the appropriate configuration of the nuclear coordinates has been achieved. The probability of electron tunneling,  $\kappa_{el}$ , between the reactant and electrode, as between a pair of reactants in homogeneous solution,  $^{17,18,23}$  will be sensitive to the degree of overlap between the donor and acceptor orbitals. It is therefore useful to conceive of a "reaction zone" of thickness  $\delta r_e$  that encompasses those molecules that lie sufficiently close to the surface to contribute importantly to the observed reaction rate. This enables the observed rate constant  $K_{ob}$  (cm s<sup>-1</sup>) to be related to a unimolecular rate constant,  $k_{et}$  (s<sup>-1</sup>), for electron transfer within this reaction zone ("precursor state"):

$$k_{\text{ob}} = K_{\text{p}}^{e} k_{\text{et}} \tag{4.5}$$

The effective "equilibrium constant" for forming the precursor state,  $K_{\rm D}^{\rm e}$  (cm), is given by  $^{30,31}$ 

$$K_{p}^{e} = \delta r_{e} \exp(-W_{p}^{e}/RT)$$
 (4.6)

where  $W_p^e$  is the average free energy required to transport the reactant from the bulk solution to the reaction zone. Approximate estimates of  $W_p^e$  may be obtained for outer-sphere reactions using the Gouy-Chapman or more sophisticated electrostatic models. This work term describes the modification to the effective "cross-sectional" reactant concentration

(mole cm<sup>-2</sup>) within the precursor state caused by differences in the environment around the reacting species in the reaction zone and that in the bulk solution.

The corresponding statistical model that describes the stability constant,  $K_p^h$  ( $\underline{M}^{-1}$ ), for formation of the precursor complex involving a pair of spherical reactants in homogeneous solution\* is  $^{10,57b,173,174}$  [cf. Equation 4.6]:

$$K_p = 10^{-3} 4\pi Nr_h^2 \delta r_h exp(-W_p^h/RT)$$
 (4.7)

where  $\delta r_h$  (cm) is the thickness of the reaction layer that lies beyond the distance,  $r_h$ , that separates the reactant pair when they are in contact, and  $\mathbf{W}_p^h$  is the average free energy work expended in forming this precursor complex. The quantities  $\delta r_e$  and  $\delta r_h$  are determined by the effective electron tunneling distances in heterogeneous and homogeneous environments, respectively. More precise treatments can be formulated for both electrochemical and homogeneous processes whereby the rate is expressed in terms of an integral of incremental reactant separations multiplied by the respective transition probabilities (vide infra). For nonsymmetrical reactants the necessary orbital overlap may only be achieved by attaining a particular molecular orientation at

<sup>\*</sup>Estimates of K for homogeneous reactions have also been obtained  $^{28}$  using the related expression  $K_p^h = (4 \text{ Nr}_h^{1/3} 3000) \exp(-W_p^h/RT)$ , which refers to the probability of forming contact pairs between two spherical species. However, Equation 4.7 or closely related expressions (reference 174) provide a more appropriate description of the probability that one reactant is present within a given inclusion volume surrounding the coreactant (references 17, 173 and 174).

the reaction site, requiring the inclusion of a fractional "steric factor" in Equations 4.5 and 4.6  $^{174}$ . Nevertheless, the simple treatment given here is adequate for the present purposes, especially in lieu of information on the dependence of  $\kappa_{el}$  upon  $\delta r_{e}$  and orbital symmetry for electrochemical reactions.

Equation 4.5 treats the overall reaction as a two-step process involving the unimolecular activation of reactant within the precursor state that is in quasi-equilibrium with respect to the bulk reactant state. A similar "encounter preequilibrium" model was advocated some time ago for bimolecular solution reactions in general. 173 It is expected that the rate-determining step commonly involves activation within an "encounter complex" formed with a solvent cage, although the effective frequency factor for ordinary chemical reactions, (e.g. atom, group transfers) refers to "vibrational collisions" between the reactants within this cage. 173 The unimolecular rate constant ket for an elementary electron-transfer step can be expressed as

$$k_{\text{et}} = \kappa_{\text{el}} \Gamma_{\text{n}} \gamma_{\text{n}} \exp(-\Delta G^{*}/RT) \qquad (1.21)$$

where  $\Gamma_{\rm n}$  is a nuclear tunneling factor,  $\nu_{\rm n}$  is a nuclear frequency factor (s<sup>-1</sup>), and  $\Delta G^*$  is the electrochemical free energy for activation from the precursor state. The nuclear tunneling term is a quantum-mechanical correction which adjusts the rate expression to account for the contribution from molecules which react without entirely surmounting the classical free energy barrier.<sup>23</sup> The nuclear frequency factor  $\nu_{\rm n}$  corresponds to the effective frequency with which the configuration

of the various nuclear coordinates appropriate for electron transfer is reached from the precursor state. Since such activation results from a combination of solvent reorientation, polarized solvent librations and inner-shell (reactant bond) vibrations  $^{18,23}$   $_{\rm n}$  can be taken as an appropriately weighted mean  $^{175}$  of the characteristic frequencies for these processes. The major contributions to these manifold motions arise from solvent reorientation and symmetric stretching vibrations of the reactant. Thus  $^{23}$ :

$$v = (\gamma_{os}^2 \Delta G_{os}^* + v_{is}^2 \Delta G_{is}^*)/(\Delta G_{os}^* + \Delta G_{is}^*)$$
 (4.8)

where  $v_{os}$  and  $\Delta G_{os}^{\star}$  are the characteristic frequency and free energy of activation associated with outer-shell (solvent) reorganization, and  $v_{is}$  and  $\Delta G_{is}^{\star}$  are the corresponding quantities associated with innershell bond vibrations. (There is some controversy concerning the correct formulation for  $v_{in}^{0.9,17}$ . The important point is that  $v_{in}$  is a frequency associated with some aspect of molecular activation, possibly energy transfer from the solvent "heat bath" to the metal-ligand bonds. In the nonadiabatic regime this is a moot point since "electron tunneling" is actually rate determing (vide infra)).

The preequilibrium formalism for electrode rections embodied in Equations 4.5, 4.6, 2.23 and 4.8 can be placed in the same format as Equation 4.1 by noting that the free-energy barrier for the overall reaction,  $\Delta G^{\neq}$ , and that for the elementary step within the precursor state,  $\Delta G^{\uparrow}$ , are related by  $\Delta G^{\neq} = \Delta G^{\uparrow} + W_p^e$ . Therefore from Equations 4.5, 46 and 2.23, the electrochemical frequency factor  $A_n^e$  is given by

$$\mathbf{A}_{\mathbf{n}}^{\mathbf{e}} = \delta \mathbf{r}_{\mathbf{e}} \Gamma_{\mathbf{n}} \mathbf{n} \tag{4.9}$$

Similarly, in view of Equation 4.7 the corresponding frequency factor  $\mathbf{A}_n^h$  for homogeneous rections is given by

$$A_n^h = 10^{-3} 4\pi N r_h^2 \delta r_h \Gamma_n v_n$$
 (4.10)

Although  $\Gamma_n$  is calculated to be substantially greater than unity at low temperatures for reactions having large iner-shell barriers  $\Delta G_{is}^*$ ,  $^{23}$  it typically approaches unity ( $\Gamma_n \approx 1$ -2) at ambient temperatures. Typical values of  $_n$  may be obtained from Equation 4.8 by noting that  $\nu_{os} \approx 10^{11-12} \text{ s}^{-1}$  in water and  $\nu_{is} \approx 10^{13} \text{ s}^{-1}$  for a typical metal-ligand stretching frequency. Although the numerical value of  $\nu_n$  also depends somewhat on the relative values of  $G_{os}^*$  for the common situation where  $\Delta G_{is}^* > 0.25 \Delta G_{os}^*$ ,  $\nu_n \approx 0.5$  to  $1 \times 10^{13} \text{ s}^{-1}$ . (For some organic compounds  $\nu_{is}$  may approach  $10^{14} \text{ s}^{-1}$ , yielding correspondingly larger values of  $\nu_n$ ).

There is some uncertainty regarding the magnitude of  $\delta$  r<sub>e</sub>. In an early discussion it was speculated that  $\delta$  r<sub>e</sub> ~  $1 \times 10^{-8}$  cm. <sup>52</sup> Weaver suggested that  $\delta$  r<sub>e</sub> could be set equal to the reactant radius, since reactants within this distance of the plane of closest approach might

<sup>\*\*</sup>The values of  $\Gamma$  for electrode reactions,  $\Gamma_n^e$ , will generally be smaller than those for homogeneous reactions,  $\Gamma_n^e$ , since only one reactant center is activated in the former processes. Thus for exchange reactions  $\Gamma_n^e = (\Gamma_n^e)^{1/2}$ . Also,  $\Gamma_n^e$  and hence  $\Gamma_n^e$  will gradually approach unity as the driving force is progressively increased (reference 176).

be expected to have a roughly equal chance of undergoing electron transfer.  $^{30}$  In order to deduce a more quantitative estimate of  $\delta r_e$  it is necessary to know how K el varies with the reactant-electrode separation distance. In the adiabatic limit there will be some range of distances beyond the plane of closest approach wherein  $\kappa_{a1} = 1$ , beyond which k el diminishes to negligibly small values. It has been suggested that electrode reactions at metal surfaces are much more likely to be adiabatic than are homogeneous redox processes. 177 (However, see Section IV C). Satisfactory calculations have yet to be performed. However, outer-sphere electrode reactions are believed to involve a plane of closest approach separated from the electrode surface by a layer of solvent molecules. 178 By analogy with the results of recent ab initio calculations for homogeneous outer-sphere reactions 14,15,17 one therefore might anticipate that outer-sphere electrode reactions are weakly adiabatic or even nonadiabatic. In this case K al is expected to vary with separation distance, r, according to:

$$\kappa_{e1}(\mathbf{r}) = \kappa_{o} \exp[-\alpha(\mathbf{r} - \sigma)] \tag{4.11}$$

where  $\kappa_0$  is the value of  $\kappa_{el}(r)$  at the plane of closest approach, and  $\sigma$  is the value of r at this point. The coefficient  $\alpha$  has been variously estimated to equal between 1.8 x  $10^8$  cm<sup>-1</sup> and 1.4 x  $10^8$  cm<sup>-1</sup> for reactions between metal ions.  $^{15,18,58,215}$  Taking  $\alpha$  = 1.6 x  $10^8$  cm<sup>-1</sup>, it is found that  $\kappa_{el}(r)$  drops to only 20% of  $\kappa_0$  at  $(r-\sigma)$  = 1 x  $10^{-8}$  cm. Comparable values of  $\alpha$  might be expected for related electrochemical

processes. Consequently, for electrode reactions that are either weakly adiabatic or nonadiabatic it is reasonable to assume that  $\delta r_e = 1 \times 10^{-8}$  cm. If the former is the case, then effectively  $_{e1}$  1 in Equation 2.22; for the latter, then  $_{e1}^{<1}$ , the magnitude of  $_{e1}^{<1}$  depending on the degree of overlap between the surface and reactant orbitals at the plane of closest approach. One factor that may diminish the effective value of  $\delta r_e$  is the expectation that the activation energy  $\Delta G^*$  will be somewhat smaller for transition states formed closer to the electrode as a result of stabilizing imaging interactions with the metal surface.  $^{13}$ ,  $^{179}$ 

Assuming then that  $\delta r_e = 1 \times 10^{-8}$  cm, along with  $v_n = 1 \times 10^{13}$  s<sup>-1</sup> and  $v_n = 1$  leads from Equation 4.9 to a "typical" value of  $A_n^e = 1 \times 10^5$  cm s<sup>-1</sup>, to be compared with the typical value  $5 \times 10^3$  cm s<sup>-1</sup> obtained using the collision formulation (Equation 4.2) that was noted above. It also appears likely that  $\delta r_h = 1 \times 10^{-8}$  cm. Inserting this estimate into Equation 4.10 along with the typical values  $r_h = 7 \times 10^{-8}$  cm,  $v_n = 1 \times 10^{13}$  s<sup>-1</sup>, and  $v_n = 1$  yields  $v_n = 1$  yields  $v_n = 1$  cm. As for the heterogeneous case, this estimate of  $v_n = 1$  is noticeably larger than the values of  $v_n = 1$  obtained from Equation 4.3; thus if  $v_n = 1$  and  $v_n = 1$  cm. As  $v_n$ 

### 4. Comparisons of Models

These different values of  $A_n$  predicted using the collisional and encounter preequilibrium formalisms reflect the disparate physical models upon which they are based. Comparison between these two models for electrochemical reactions is facilitated by noting that the col-

lision frequency can be viewed naively as the velocity with which reactants from bulk solution "pass through" the reaction zone. Taking a collision "velocity" to be 5 x  $10^3$  cm s<sup>-1</sup> along with an effective reaction zone thickness of 1 x  $10^{-8}$  cm, each reactant molecule is estimated to remain in the zone for about 2 x  $10^{-12}$  s. On the basis of the preequilibrium formulation, during this period reacting molecules would be activated about 20 times if  $v_n = 1 \times 10^{13}$  s<sup>-1</sup>. Therefore the encounter preequilibrium model yields an appropriately larger frequency factor accounting for the additional opportunities for a molecule to undergo electron transfer while within the reaction zone that is prescribed by the effective electron tunneling distance.

Under typical experimental conditions the encounter preequilibrium model therefore seems to provide a more appropriate description for electrochemical as well as homogeneous reactions. However, there may be circumstances in which the collisional model applies. Thus for small reactants  $A_e$  estimated from Equation 4.2 can be greater than  $10^4$  cm s<sup>-1</sup>, while  $v_n$  can be as small as ca.  $10^{11}$  s<sup>-1</sup> for reactions that require little or no innershell reorganization (i.e.  $\Delta G_{is}^* = 0$  in Equation 4.8). Characterizing  $Z_e$  again as a velocity, under these circumstances the reactant could pass through the prescribed ca. 1 x  $10^{-8}$  cm reaction zone in less than one tenth the time required for unimolecular activation, whereupon  $Z_e$  would provide the appropriate frequency at which the reaction could be consummated. Another situation where the preequilibrium model will clearly fail is when the rate of the elementary electron-transfer step becomes sufficiently large so that the preceding step involving precursor state formation is

no longer in quasi-equilibrium, ultimately becoming the rate-determining step. In this case the effective frequency factor will equal  $Z_{\rm e}$  given by Equation 4.4 since it refers to the transport-controlled formation of the precursor state.

Nevertheless, the onset of rate control by precursor state formation should only occur for outer-sphere electrochemical rections having rate constants approaching ca.  $10^2~{\rm cm~s}^{-1}$ , which are beyond the range of experimental accessibility using conventional methods. It should be noted that the onset of partial rate control by diffusion polarization that is commonly encountered in electrochemical kinetics will not vitiate the applicability of the preequilibrium formalism since quasi-equilibrium will normally be maintained throughout the diffusion-depletion layer. This allows the reactant concentration immediately outside the double layer that is required for the evaluation of  $k_{\rm ob}$  to be determined using Fick's Laws of diffusion.

The appearance of the precursor work terms  $W_p^e$  in Equation 4.6 suggests that the evaluation of  $k_{et}$  using the preequilibrium formulation also accounts for the influence of the double-layer structure upon  $k_{ob}$ . That this is only partly correct can be seen by recalling the general form of the double-layer effect upon  $k_{ob}$ .

$$\ln k_{corr} = \ln k_{ob} + (1/RT) [W_p^e + \alpha_I (W_s^e - W_p^e)]$$
 (4.12)

where  $W_s^e$  is the work of transporting the product from the bulk solution to the interfacial reaction site (the "sucessor state"), and  $\alpha_T$  is the

intrinsic transfer coefficient ("symmetry factor", 0.5). the "corrected" rate constant k<sub>corr</sub> is the value of k<sub>ob</sub> that would be observed at a given electrode potential in the absence of the double layer. By comparison, from Equations 4.5 and 4.6:

$$\ln k_{et} = \ln k_{ob} - \ln \delta r_{e} + (1/RT)W_{p}^{e}$$
 (4.13)

The difference between Equations 4.12 and 4.13 is that the latter corrects only for the effect of the double layer upon the stability of the precursor state, whereas the former, via the additional term  $\alpha_{\rm I}(W_8^{\rm e}-W_{\rm p}^{\rm e})$ , accounts also for the double-layer effect upon the elementary electron-transfer step. Nevertheless, a rate constant corresponding to  $k_{\rm corr}$ ,  $k_{\rm et}^{\rm corr}$ , may also be defined using the preequilibrium formulation, whereby:

$$k_{er}^{corr} = k_{corr}/\delta r_{e} \tag{4.14}$$

### 5. Relation Between Electrochemical and Homogeneous Rate Constants

According to the model of Marcus based on a weak adiabatic treatment, the (work-corrected) rate constant for electrochemical exchange of a given redox couple,  $k_{\rm ex}^{\rm e}$ , (i.e. the "standard" rate constant), is related to the (work-corrected) rate constant for the corresponding homogeneous self exchange reaction  $k_{\rm ex}^{\rm h}$ , by  $^{13,180}$ 

$$(k_{ex}^{e}/z_{e})^{2} < k_{ex}^{h}/z_{h}$$
 (4.15)

where  $Z_e$  and  $Z_h$  are given by Equations 4.2 and 4.3, respectively.

Equation 4.15 arises from the theoretically expected relationship between the corresponding intrinsic free energy barriers to electrochemical exchange and homogeneous self exchange,  $\Delta G_{\text{ex,e}}^{*}$  and  $\Delta G_{\text{ex,h}}^{*}$ , respectively. It is generally expected that

$$2\Delta G_{is,e}^{*} = \Delta G_{is,h}^{*} \tag{4.16}$$

where  $\Delta G_{is,e}^{\star}$  and  $\Delta G_{is,h}^{\star}$  are the components of these intrinsic barriers associated with inner-shell (usually metal-ligand) reorganization. The relation between the outer-shell (solvent reorganization) components of the intrinsic barriers,  $\Delta G_{os,e}^{\star}$  and  $\Delta G_{os,h}^{\star}$ , is more complicated (and tenuous), being dependent on the relative distances between the reacting centers for the homogeneous process and between the reactant and its image in the electrode for the electrochemical process,  $R_h$  and  $R_e$ , respectively. 13,180 From the Marcus treatment 13,180

$$2\Delta G_{os,e}^{*} = \Delta G_{os,h}^{*} + \frac{e^{2}(\frac{1}{R} - \frac{1}{R})(\frac{1}{\epsilon_{op}} - \frac{1}{\epsilon})}{(4.17a)}$$

$$= \Delta G_{os,h}^{\star} + C \qquad (4.17b)$$

where e is the electronic charge, and  $\epsilon_{\rm op}$  and  $\epsilon_{\rm s}$  are the optical and static dielectric constants, respectively. In view of Equations 4.1, 4.14 and 4.16 we can write

2 log 
$$(k_{ex}^e/\kappa_{e1}^e A_n^e) = log (k_{ex}^h/\kappa_{e1}^h A_n^h) - C/2.303RT$$
 (4.18)

where  $\kappa = \begin{pmatrix} e \\ e1 \end{pmatrix}$  and  $\kappa = \begin{pmatrix} h \\ e1 \end{pmatrix}$  are the effective transmission coefficients for the electrochemical and homogeneous exchange rections, respectively.

Equation 4.18 represents a more complete version of the conventional relation Equation 4.15. Since for outer-sphere rections it is generally expected that  $R_e > R_h$  then from Equations 4.17 C>0; this is responsible for the inequality sign in Equation 4.15. Commonly, however, an equality sign is employed in Equations 4.15 and the frequency factors are presumed to be given by Equations 4.2 and 4.3. In view of the above discussion, it is deemed more appropriate to employ Equation 4.18 with  $A_n^e$  and  $A_n^h$  estimated using the encounter preequilibrium formulation [Equations 4.9 and 4.10] rather than Equation 4.15.

Noticeably different numerical relationships between  $k_{ex}^e$  and  $k_{ex}^h$  are predicted by Equations 4.15 and 4.18. In the limiting case where C = 0 (i.e.  $2\Delta G_{ex,e}^* = \Delta G_{ex,h}^*$ ), using the typical numerical values Nm = 200, Nm<sub>r</sub> = 100, T = 298K,  $r_h = 7 \times 10^{-8}$  cm,  $\delta r_e = \delta r_h = 1 \times 10^{-8}$  cm,  $\epsilon_{el}^e$  =  $\epsilon_{el}^e$  = 1, yields from Equation 4.15

$$(k_{ex}^{e})^2 = 8.5 \times 10^{-5} k_{ex}^{h}$$
 (4.19)

whereas from Equation 4.18

$$(k_{ex}^e)^2 = 2.5 \times 10^{-3} k_{ex}^h$$
 (4.20)

with  $k_{\rm ex}^{\rm e}$  in cm s<sup>-1</sup> and  $k_{\rm ex}^{\rm h}$  in  $\underline{\rm M}^{-1}$  s<sup>-1</sup>. The common observation<sup>181</sup> that  $(k_{\rm ex}^{\rm e})^2 < 10^{-4}$   $k_{\rm ex}^{\rm h}$  therefore indicates that the inequality

 $\Delta G_{\mathrm{ex,e}}^{*} > \Delta 0.5 \; G_{\mathrm{ex,h}}^{*}$  is rather larger than previously suspected on the basis of the collisional formulation [Equation 4.19]. However, taking into account the likely magnitude of the inequality  $2\Delta G_{\mathrm{ex,e}}^{*} > \Delta G_{\mathrm{ex,h}}^{*}$  by estimating C as in Equation 4.17a leads to very good agreement between Equation 4.18 and experimental rate data for a number of transitionmetal couples.  $^{182}$ 

One recent discussion of the relationship between electrochemical and homogeneous rate constants also employs a preequilibrium model for the frequency factors. A relation was derived that is numerically the same as that conventionally obtained using the collisional treatment, resulting from an apparent identity of  $v_n$   $\delta r_e$  with  $Z_e$ . However, this numerical agreement is fortuitous, resulting from the assumptions  $\delta r_e = 10^{-7}$  cm and  $v_n = 10^{11}$  s<sup>-1</sup>.183 The latter choice was prompted by the presumption that  $v_n$  approximates the frequency of solvent reorientation when  $\Delta G_{os}^*$  provides the major part of  $\Delta G_{os}^*$ . As noted above, typically  $v_n \approx v_{is} = 10^{13}$  s<sup>-1</sup> even when  $\Delta G_{os}^* > \Delta G_{is}^*$ .

### 6. Comparison Between the Kinetics of Corresponding Inner- and Outer-Sphere Pathways

Besides the inherent virtues of the preequilibrium model, it is clearly also applicable to inner-sphere electrode reactions since these involve the formation of a specifically adsorbed intermediate of well-defined structure, analogous to the binuclear "precursor complexes" formed with homogeneous inner-sphere pathways, it can be measured directly for reactions for which the precursor intermediates are sufficiently stable to be analytically detected. Thus  $K_D^e = \Gamma_D/C_D$ ,

where  $\Gamma_{\rm p}$  is the concentration of the (adsorbed) precursor intermediate and  $C_{\rm b}$  is the bulk reactant concentration. Values of  $k_{\rm et}$  can therefore be determined from  $k_{\rm ob}$  and  $K_{\rm p}^{\rm e}$  using Equation 4.5, or directly from the current required to reduce or oxidize a known concentration of adsorbed reactant.  $^{107}$ 

Since Equation 2.23 is expected to apply equally well to precursor states involving surface-attached or unattached rectants, the comparison between corresponding values of  $k_{at}$  for a given electrode reaction proceeding via inner- and outer-sphere pathways provides fundamental information on the influence of reactant-surface binding upon the energetics of the elementary electron-transfer step. 30 We have made such a comparison for a number of reactions involving transitionmetal complexes at both mercury and solid electrodes; the results are described in detail elsewhere. 30,109,184 In particular, it appears that the overall catalyses (i.e. larger values of  $k_{\mbox{\scriptsize ob}}$ ) often observed for inner-sphere rections, especially at solid metal surfaces, are frequently influenced by larger values of K brought about by surface attachment. 109,184 In the context of the present discussion, it is important to note that  $\Delta G^*$  for outer- as well as inner-sphere electron transfer should be estimated using Equations 4.5, 4.6 and 2.23 rather than the conventional use of Equations 4.1 and 4.9 assuming that  $\mathbf{A}_{\mathbf{n}}$ equals Z [Equation 4.2].

### 7. The Apparent Frequency Factor from the Temperature Dependence of Electrochemical Kinetics

In principle, direct information on the magnitude of the frequency factor for electrochemical reactions can be obtained from measurements of the dependence of electrochemical rate constants upon temperature. Despite the early seminal work of Randles<sup>52,185</sup> relatively few measurements of electrochemical Arrhenius parameters have been reported, at least under well-defined conditions. This is due in part to a widespread doubt as to their theoretical significance arising from an apparent ambiguity in how to control the electrical variable as the temperature is altered. The matter has recently been discussed in detail for mechanistically simple electrode processes involving both solution-phase<sup>53-55</sup> and surface-attached reactants. <sup>186</sup> (following section).

Conventionally:

$$k_{COTT} = A^{\prime} \exp(-\Delta H^{\neq}/RT)$$
 (4.21)

where  $\Delta H^{\neq}$  and A' are the activation enthalpy and apparent frequency factor, respectively, obtained from an Arrhenius plot. Two different types of activation enthalpies should be distinguished. 53-55 The so-called "ideal" activation enthalpies  $\Delta H_{i}^{\neq}$ , are derived from the temperature dependence of the rate constant measured at a constant metalsolution (Galvani) potential difference. So-called "real" activation enthalpies,  $\Delta H_{r}^{\neq}$ , are obtained from the temperature dependence of the standard rate constant; i.e., of the rate constant measured at the

standard potential at each temperature. The former approximate the actual enthalpic barrier at the electrode potential at which it is measured, 53-55 whereas the latter equal the enthalpic barrier that remains in the absence of an enthalpic driving force, i.e. under "thermoneutral" conditions. 52,53

The frequency factor  $A_i$  obtained from  $\Delta H_i^{\neq}$  and  $k_{corr}$  will differ markedly from the "true" frequency factor  $A_n$  [Equation 4.1] since  $A_i$  will contain a contribution from the entropic driving force. 53-55 However, the frequency factor  $A_r$  extracted from  $\Delta H_r^{\neq}$  and  $k_{corr}$  is closely related to  $A_n$  since 53-55

$$k_{corr} = A_{r}^{'} \exp(-\Delta H_{r}^{\neq}/RT)$$

$$= \kappa e_{1} A_{r}^{e} \exp(\Delta S_{int}^{\neq}/R) \exp(-\Delta H_{r}^{\neq}/RT) \qquad (4.22)$$

where  $\Delta S_{int}^{\neq}$  is the "intrinsic" activation entropy, i.e. the activation entropy that remains after correction for the entropic driving force (see Section V.A). Providing that the outer-sphere transition state is formed in a similar solvent environment to that experienced by the bulk reactant and product, (see Section V C),  $\Delta S_{int}^{\neq}$  will be close to zero  $\binom{+}{-}10 \text{ J deg}^{-1} \text{ mol}^{-1}$ ),  $\binom{186}{-}$  so that  $A_r = A_r$  providing that k = 1 and the appropriate double-layer corrections upon the rate constants have been made.

Experimental values of  $A_r$  (or equivalently, apparent activation entropies obtained assuming a value of  $A_n$ ) are not abundant, especially for conditions where the electrostatic double-layer corrections are

known with confidence. At metal-aqueous interfaces, it appears that  $A_r < 10^3$  cm sec<sup>-1</sup> for most transition-metal redox couples. 53-55,185,187 Since these values are closer to that predicted from the collisional than from the encounter preequilibrium formulation (vide supra) it might be argued that the former model is more appropriate. However, it seems likely that these disparities arise in part from a breakdown in the assumption  $\Delta S_{int}^{\neq} = 0$  as a result of differences in the solvating environment at the electrode surface and in the bulk solution. Smaller (ca. 5- to 10-fold) values of  $A_r$  relative to  $A_n$  can also result for reactions having large inner-shell barriers since then  $\Gamma_n$  and therefore  $A_n$  will decrease significantly with increasing temperature. In addition, the observation  $A_r < A_n$  could result from  $\kappa_{el} < 1$  (Equation 4.22), i.e. from nonadiabaticity effects. However, values of  $A_r$  determined in aprotic solvents are typically close to those predicted by the encounter preequilibrium model, ca.  $10^5$  to  $10^6$  cm s<sup>-1</sup>. 188

#### 8. More Sophisticated Treatments

Although the treatment based on the simple encounter preequilibrium model that is described above represents a decided improvement over the conventional collisional approach, it is somewhat oversimplified. A more sophisticated treatment applicable to homogeneous reactions between metal complexes has recently been outlined. This considering the reacting ions as hard spheres the likelihood that the ligand envelopes may interpenetrate, leading to better overlap between the donor and acceptor orbitals, has been recognized. Rather than considering a uniform "reaction zone", the rate is treated in

terms of an integral of different reactant configurations averaged over spherical coordinates with a corresponding distribution of local values of  $\kappa_{el}$ ,  $\Delta H^*$ ,  $\Delta S^*$ , and hence rate constants to yield an integral value of  $k_{et}$ . In addition, the interaction between the reactants are treated using contemporary ion-ion pair correlation functions rather than the usual Debye-Hückel model. Although comparable values of  $K_p$  to the simplified treatment result from this approach, it does provide much better agreement with the experimental activation entropies as a function of ionic strength. 17

In principle, a similar treatment could be developed for electrochemical reactions. Recent statistical treatments of the diffuse double layer provide a more realistic picture of interfacial ionic distributions than given by the usual Gouy-Chapman model. Is In particular, these treatments demonstrate that the ionic surface excess (or deficiency) is contained within a noticeably smaller distance from the surface at high ionic strengths than deduced from the Gouy-Chapman model. Such approaches will therefore yield different local reactant concentrations and hence  $K_p^e$  (Equation 4.6). Another significant development is the inclusion of a (albeit crude) molecular model for the solvent. It is expected that the solvent ordering induced by hydrophilic surfaces, in particular, if will profoundly influence the local distribution of charged reactants.

Finally, although of no consequence numerically, the composite quantity  $\kappa_{\rm el}$   $\nu_{\rm n}$  in the semiclassical formulation is more properly written as  $\nu_{\rm el}$  for reactions in the nonadiabatic regime. The quantity

 $\nu_{\rm el}$  corresponds to the frequency of passage from reactants' to products' potential energy surfaces in the activated state (see Section 1.D).

#### Conclusions

Despite the approximations and numerical uncertainties in the parameters involved, the encounter preequilibrium formulation provides a description of the frequency factor for outer-sphere electrochemical reactions that is more appropriate than the collisional formulation which has usually been employed for this purpose. Most importantly, the former model describes the nuclear frequency factor for the elementary electron-transfer step in terms of an appropriate combination of unimolecular reorganization modes. The collisional model infers that the motion along the reactant coordinate arises from the translational motion of the reactant(s). In actuality, the ability of electrons to tunnel between the reacting centers and the unimolecular activation of the reactant via energy transfer with the surrounding solvent obviates the need for any such momentum transfer, in contrast to chemical reactions involving atom or group transfer. In addition, the electron tunneling probability appears as an integral part of the preequilibrium formalism by determining the appropriate size of the "reaction zone" within which the electronic transmission probability is sufficiently large for a given internuclear geometry to contribute significantly to the overall reaction rate. A similar electronic transmission coefficient is often contained in the collisional formulation, but as an arbitrary added component.

These considerations highlight the need for theoretical treatments of electron tunneling and associated molecular dynamics at electrode surfaces along similar lines to the important developments that are being made for electron transfer between metal ions in homogeneous solution. 14,15,17,215 The combination of such theoretical work with further detailed experimental studies, especially comparisons between apparent frequency factors as well as rate constants for corresponding electrochemical and homogeneous reactions, will provide a firm basis upon which to develop our understanding of the factors that influence electrochemical reactivity.

## B. The Significance of Electrochemical Activation Parameters for Surface-Attached Reactants

[Originally published in J. Electroanal. Chem., 145, 43 (1983)]

### 1. Introduction

In the past few years there has been considerable interest in electrochemical systems involving reactants attached directly to electrode surfaces. 192-194 Most research efforts have been directed towards the syntheses and structure elucidation of attached-molecule systems. However, some work is starting to appear on the redox reactivity of these molecules. 70,130,195-200 These studies should yield new insights concerning the dynamics of electron transfer at electrodes by providing critical tests of contemporary theories. 13,21,56 Comparisons of relative charge transfer rates for reactions of redox species in the attached state and in solution have

proved useful in understanding the influence of surface attachment on electron-transfer energetics. 197,198,200

Further information about particular factors such as Franck-Condon barriers and nonadiabatic effects may be gained by measuring activation parameters. Although the interpretation of activation parameters for electrochemical processes involving solution reactants has been discussed at length 53,54 there is some confusion in understanding their significance for reactions of surface-attached molecules. 197,198 It therefore seems timely to consider the interpretation of activation parameters for this special case.

There are two alternative formulations of electrochemical activation parameters that are especially useful.  $^{53}$ ,  $^{54}$ ,  $^{201}$  The socalled "ideal" parameters  $\Delta H_i^*$  and  $\Delta S_i^*$  are those derived from the temperature dependence of the rate constant measured at a constant metal-solution (Galvani) potential difference  $\phi_m$ .  $^{53}$ ,  $^{54}$  Although strictly speaking it is not possible to control  $\phi_m$  as the temperature is varied, in practice this can be achieved to a good approximation by using a nonisothermal cell arrangement where the reference electrode is held at a fixed temperature, allowing  $\Delta H_i^*$  and  $\Delta S_i^*$  to be reliably determined.  $^{54}$  These quantities are of fundamental interest since they equal the enthalpic and entropic barriers to electron transfer at the particular electrode potential at which they are evaluated. However, it is more common to determine so-called "real" activation parameters  $\Delta H_r^*$  and  $\Delta S_r^*$  which are obtained from the temperature dependence of the standard rate constant  $k^0$ , i.e., the rate constant measured at the

standard potential at each temperature\*. Despite earlier assertions to the contrary,  $\Delta H_{\mathbf{r}}^{\star}$  and  $\Delta S_{\mathbf{r}}^{\star}$  have been shown to have particular significance for simple electrode reactions since they represent the enthalpic and entropic barriers at the standard potential that remain after correction for the enthalpic and entropic driving forces,  $\Delta H_{\mathbf{rc}}^{\mathbf{O}}$  and  $\Delta S_{\mathbf{rc}}^{\mathbf{O}}$ , respectively, for the electrode reaction. Thus the corresponding "ideal" and "real" activation parameters measured for a given electrode reaction at the standard potential are related by 53

$$\Delta H_i^* = \Delta H_r^* + \alpha T S_{rc}^0$$
 (1.18)

and

$$\Delta S_{i}^{*} = \Delta S_{r}^{*} + \alpha \Delta S_{rc}^{0}$$
 (1.19)

where  $\alpha$  is the measured transfer coefficient (0.5) for the overall electrode reaction.

### 2. Relationship between Activation Parameters for Surface-Attached and Bulk Solution Reactants

According to the formalism originally due to Marcus  $^{202}$  the measured rate constant  $k_{sol}^E$  (cm s<sup>-1</sup>) for a one-electron reduction reaction involving a bulk solution reactant at an electrode potential E can be written as  $^{30,31,201}$ 

RT ln 
$$k_{sol}^{E}$$
 = RT lnA<sub>sol</sub> -  $\triangle G_{int}^{*}$  -

$$\left[\Delta G_{\mathbf{p}}^{\mathbf{o}} + \alpha_{\mathbf{i}} \left(\Delta G_{\mathbf{s}}^{\mathbf{o}} - \Delta G_{\mathbf{p}}^{\mathbf{o}}\right) - \left[\alpha_{\mathbf{i}} \mathbf{F} \left(\mathbf{E} - \mathbf{E}_{\mathbf{sol}}^{\mathbf{f}}\right)\right]$$
(4.23)

Most generally, "real" activation parameters are defined as those obtained at a fixed overpotential at each temperature (reference 15).

In Equation 4.23  $E_{sol}^f$  is the formal potential of the solution redox couple concerned,  $\Delta G_p^0$  and  $\Delta G_s^0$  represent the free energies required to form the precursor and successor states from the bulk reactant and product, respectively,  $\alpha_I$  is the "intrinsic" transfer coefficient (i.e. the symmetry factor for the elementary electron-transfer step),  $A_{sol}$  is a frequency factor (cm s<sup>-1</sup>), and  $\Delta G_{int}^*$  is the so-called "intrinsic barrier". This last term equals the activation free energy for the elementary step in the absence of a free energy driving force, i.e. when the work terms  $\Delta G_p^0$  and  $\Delta G_s^0$ , and the overall driving force  $F(E-E_{sol}^f)$ , each equal zero. The factor  $A_{sol}$  represents the frequency with which the reactant is able to surmount this activation barrier starting from the bulk solution state.

The determination of the frequency factor and intrinsic barrier contributions to  $k_{sol}$  is therefore of central fundamental interest. In principle, this may be achieved by measuring the temperature dependence of  $k_{sol}$  measured at  $E_{sol}^f$ ,  $k_{sol}^o$ , whereupon the last term in Equation 4.23 will vanish. The "real" activation enthalpy,  $H_{r,sol}^{\star}$  derived in this manner can therefore be expressed as

$$\Delta H_{r,sol}^{\star} = -R[dlnK_{sol}^{o}/d(1/T)] = \Delta H_{int}^{\star} + [\Delta H_{p}^{o} + \alpha_{I}(\Delta H_{s}^{o} - \Delta H_{p}^{o})] \qquad (4.24)$$

where  $\Delta H_p^O$  and  $\Delta H_s^O$  are enthalpic components of the work terms  $\Delta G_p^O$  and  $\Delta G_s^O$ , and  $\Delta H_{int}^*$  is the "intrinsic" activation enthalpy for the elementary electron-transfer step. This last quantity is the activation enthalpy that remains when the enthalpic driving force  $\Delta H_{et}^O$  for this step equals zero. The last term in brackets in Equation 4.24 accounts

for the contribution to  $\Delta H_{r,sol}^*$  arising from the steps involving precursor state formation and successor state decomposition that precede and follow the rate-determining electron-transfer step.

It is conventional to determine an accompanying "preexponential" factor  $A_{sol}$  by using the expression

$$k_{sol}^{o} = A_{sol}^{'} \exp(-\Delta H_{r,sol}^{'}/RT)$$
 (4.25)

However, in view of Equations 4.23 and 4.24 the desired "true" frequency factor  $A_{sol}$  differs from  $A_{sol}$  since the latter contains an activation entropy contribution:

$$A'_{sol} = A_{sol} \exp(\Delta S'_{r,sol}/R)$$
 (4.26)

Similarly to the "real" activation enthalpy,  $\Delta S_{r,sol}^*$  equals the activation entropy that remains after correction for the overall entropic driving force  $\Delta S_{rc}^0$ . This "real" activation entropy is closely related to the "intrinsic" activation entropy  $\Delta S_{int}^*$  that appears in electron transfer theory.  $^{53,54}$  However, strictly speaking  $\Delta S_{r,sol}^*$  will differ from  $\Delta S_{int}^*$  since the latter equals the activation entropy for the elementary step after correction for the entropic driving force,  $\Delta S_{et}^0$ , for this step. Given that  $\Delta S_{et}^0$  is related to  $\Delta S_{rc}^0$  by  $\Delta S_{et}^0 = \Delta S_{rc}^0 + \Delta S_{p}^0 - \Delta S_{s}^0$ , where  $\Delta S_{p}^0$  and  $\Delta S_{s}^0$  are the entropic components of the work terms  $\Delta G_{p}^0$  and  $\Delta G_{s}^0$ ,  $\Delta S_{r,sol}^*$  is related to  $\Delta S_{int}^*$  by (cf. Equation 4.24)

$$\Delta S_{r,sol}^{\star} = \Delta S_{int}^{\star} + [\Delta S_{p}^{o} + \alpha_{I}(\Delta S_{s}^{o} - \Delta S_{p}^{o})] \qquad (4.27)$$

For surface-attached (or adsorbed) reactants, a "unimolecular" rate constant  $k_a^E$  (s<sup>-1</sup>) can be determined that is related to  $k_{sol}^E$  by  $^{30,31}$ 

$$k_{sol}^{E} = K_{p}k_{a}^{E} = K_{o}k_{a}^{E} \exp(-\Delta G_{p}^{O}/RT)$$
 (4.28)

where  $K_p$  is the equilibrium constant (cm) for forming the precursor (surface-attached) state from the bulk reactant, and  $K_o$  is the value of  $K_p$  when  $\Delta G_p^0 = 0$ . Consequently, for the one-electron reduction of an adsorbed reactant we can write from Equation 4.23

RT ln 
$$k_a^E$$
 = RT ln  $A_a$  -  $\alpha(\Delta G_s^O - \Delta G_p^O)$  -  $F(E - E_{sol}^f)$  (4.29)

where  $A_a$  (= $A_{sol}/K_o$ ) is a frequency factor (s<sup>-1</sup>) for activation within the adsorbed state, i.e. the frequency with which the elementary barrier is surmounted. Equation 4.29 can be simplified by noting that the formal potential in the surface-attached state  $E_a^f$  will differ from  $E_{sol}^f$  according to

$$E_a^f = E_{sol}^f + RT(lnK_p - ln K_s)$$

$$= E_{sol}^f + (\Delta G_s^0 - \Delta G_p^0)/F \qquad (4.30)$$

where  $K_8$  is the equilibrium constant for forming the successor state from the bulk product. This allows Equation 4.29 to be written as

RT ln 
$$k_a^E$$
 = RT ln  $A_a$  -  $\Delta G_{int}^{\star}$  -  $\alpha F(E-E_a^f)$  (4.31)

Therefore the "real" activation enthalpy  $\Delta H_{r,a}^*$  obtained from the temperature dependence of  $k_a$  measured at  $E_a^f$  at each temperature,  $k_a^o$ , can be expressed simply as (cf. Equation 4.24):

$$\Delta H_{r,a}^{*} = -R[d \ln k_a^{\circ}/d(1/T)] = \Delta H_{int}^{*}$$
 (4.32)

The preexponential factor A obtained from

$$k_a^0 = A_a \exp(-\Delta H_{r,a}^*/RT)$$
 (4.33)

is related to the theoretically significant quantity A simply by (cf. Equations 4.26 and 4.27)

$$A_a = A_a \exp(\Delta S_{int}^*/R)$$
 (4.34)

Therefore in contrast to the activation parameters for solution reactants, the desired intrinsic enthalpic barrier and frequency factor can be obtained from the experimental quantities for adsorbed reactants without requiring additional information on the thermodynamic stabilities of the precursor and successor states. Moreover, the intrinsic entropic barrier AS in Equation 4.34 is predicted from electrontransfer theories to be small  $(0 \pm 10 \text{ J deg}^{-1} \text{ mol}^{-1})$ ; 54,203 i.e., the contributions to  $\Delta G_{int}^{\star}$  arising from solvent repolarization as well as inner-shell reorganization are almost independent of temperature. (However, see Section V. A). Indeed, this conclusion can be deduced on purely intuitive grounds since the degree of solvent polarization around the redox center within the transition state is expected to be appropriately intermediate between that for the precursor and successor This enables the frequency factor  $A_{\mathbf{g}}$  to be determined directly using Equation 4.30 from the experimental values of  $k_a^0$  and  $\Delta H_{r,a}^{*}$ . Also, since  $\Delta G_{int}^{*} = \Delta H_{int}^{*} - T\Delta S_{int}^{*}$ , in view of Equation 4.32  $\Delta H_{r,s}^{\pi}$  can be approximately identified with the intrinsic barrier  $\Delta G_{int}^{\pi}$ . This markedly closer relationship of the experimental activation enthalpy and preexponential factor to the desired intrinsic barrier and frequency factor for adsorbed reactants in comparison with the corresponding measured quantities for solution-phase reactants arises simply

because the former experimental quantities refer directly to the elementary electron-transfer step itself rather than to the multi-step process involved in the formation of bulk products from bulk reactants.

Values of  $k_a^0$  and  $\Delta H_{r,a}^*$  are clearly inaccessible for attached redox couples for which  $E_a^f$  cannot be determined, such as those for which the product is rapidly desorbed, irreversibly decomposes, or undergoes a multiple step reaction such as coupled electron and proton transfer. However, estimates of  $A_a$  may still be extracted from "ideal" activation enthalpies  $\Delta H_{i,a}^*$  obtained from an Arrhenius plot of  $\ln k_a$  versus (1/T) measured at a constant electrode potential using the nonisothermal cell configuration. The values of  $\Delta H_{i,a}^*$  and  $k_a$  at a given electrode potential are related to  $A_a$  by (cf. Equations 4.33 and 4.34):

$$k_a = A_a \exp(\Delta S_{i,a}^{*}/R) \exp(-\Delta H_{i,a}^{*}/RT)$$
 (4.35)

The "ideal" activation entropy  $\Delta S_{i,a}^*$  will generally differ from zero since in addition to the intrinsic entropic term  $\Delta S_{int}^*$  it contains a contribution from the entropic driving force for the electron-transfer step. Thus from Equations 1.19 and 4.27:

$$\Delta S_{i,a}^{*} = \Delta S_{int}^{*} + \alpha_{I}(\Delta S_{rc}^{o} + \Delta S_{s}^{o} - \Delta S_{p}^{o})$$
 (4.36a)

= 
$$\Delta S_{int}^{\star} + \alpha \Delta S_{et}^{o}$$
 (4.36b)

Providing that the entropic work terms  $\Delta S_8^o$  and  $\Delta S_p^o$  are approximately equal, the value of  $\Delta S_{1,8}^{\star}$  required in Equation 4.35 can therefore be estimated from experimental values of  $\Delta S_{rc}^o$  measured for structurally similar redox couples. The results of such an analysis for the irreversible reduction of adsorbed Cr(III) and Co(III) complexes at various metal surfaces has been reported elsewhere by Guyer, Barr and Weaver. 204

The relationship between the various activation enthalpies noted here,  $\Delta H_{r,sol}^{\star}$ ,  $\Delta H_{r,a}^{\star}$ , and  $\Delta H_{i,a}^{\star}$ , are shown schematically in Figure 4.1 in the form of potential-energy surfaces. The states Ox, P, A, S, and Red along the reaction coordinate refer to the bulk oxidized, precursor, activated, successor, and bulk reduced states, respectively. Curve 1 illustrates the actual potential-energy surface at a potential equal to E. The elementary step (PAS) is enthalpically "uphill" by an amount equal to  $T\Delta S_{et}^{o}$ , since  $\Delta H_{et}^{o} = T\Delta S_{et}^{o}$  at  $E_{a}^{f}$ . Thus the measured "ideal" activation enthalpy  $\Delta H_{1,a}^*$  will contain a contribution from the driving force TAS. Curve 2 shows the potential energy surface corresponding to the "real" activation enthalpy  $\Delta H_{r,a}^*$  also measured at  $E_a^f$ . Note that the driving force component  $T\Delta S_{et}^{0}$  is now absent. It is important to recognize that curve 1 and not curve 2 represents the actual potential energy surface at E<sub>a</sub>f. Curve 2 represents instead the surface corresponding to the electrode potential where  $\Delta H_{et}^{0} = 0$ , i.e. where the elementary step is "thermoneutral" so that  $\Delta H_{r,a}^* = \Delta H_{int}^*$  (Equation 4.32). Also shown in Fig. 4.1 is the surface corresponding to the "real" activation enthalpy  $\Delta H_{r,sol}^*$  measured for the solution reactant at E<sub>sol</sub> (curve 3). Note that now the states 0x and Red are isoener

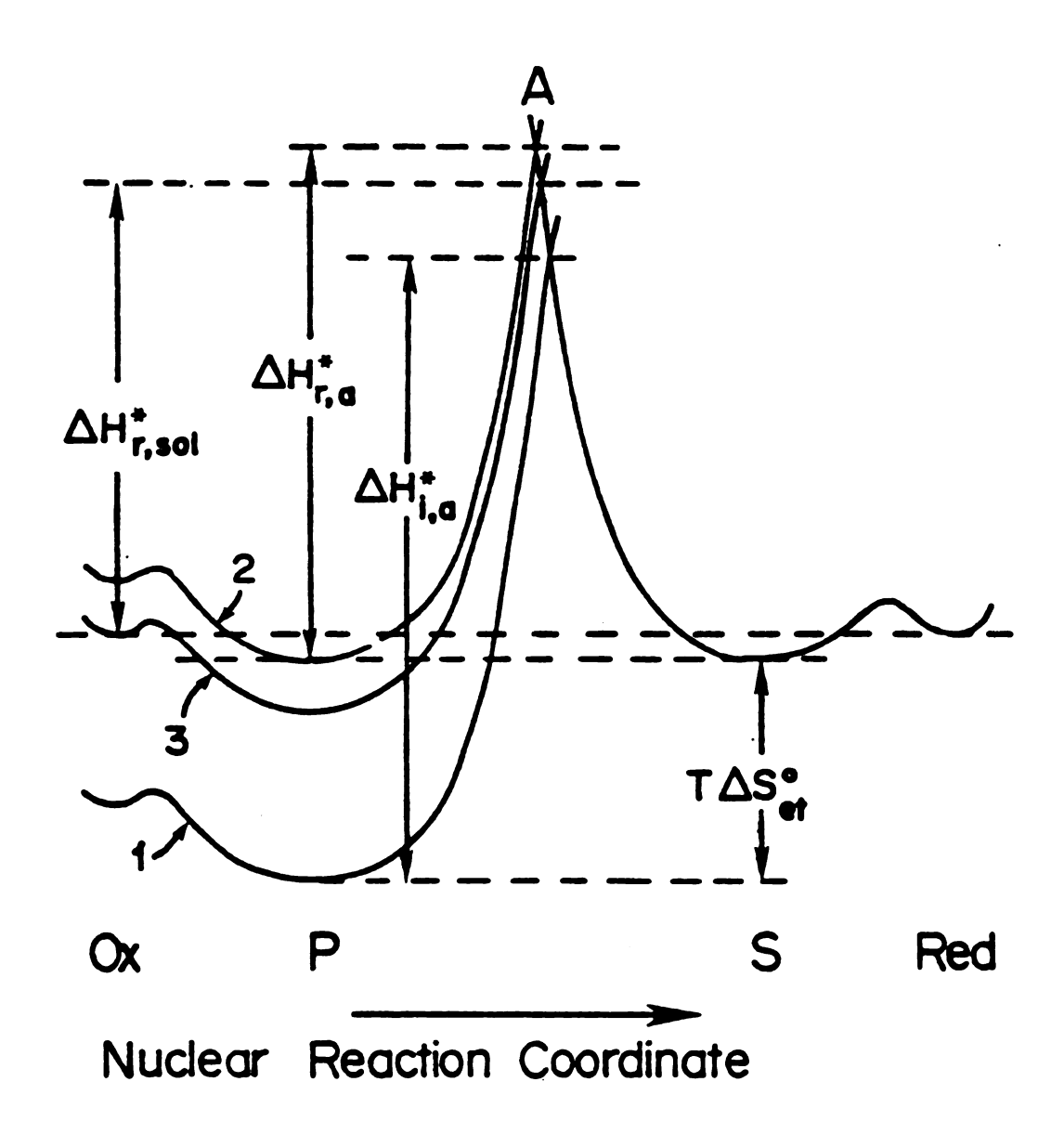


Figure 4.1. Schematic potential-energy surfaces for a single-step electrode reaction, illustrating the distinction between "real" and "ideal" activation enthalpies for attached reactants (see text for details).

getic rather than the states P and S as in curve 2. Consequently,  $\Delta H_{r,so1}^{\star} \text{ will differ from } \Delta H_{r,a}^{\star} \text{ not only by virtue of the precursor work term } \Delta H_p^0, \text{ but also because states P and S for curve 3 will differ in energy when } \Delta H_p^0 = \Delta H_s^0. \text{ These two factors are responsible for the two components, } \Delta H_p^0 \text{ and } \alpha_{\text{I}}(\Delta H_s^0 - \Delta H_p^0), \text{ by which } \Delta H_{r,so1}^{\star} \text{ differs from } \Delta H_{\text{int}}^{\star} \text{ (Equation 4.24).}$ 

### 3. Significance of the Frequency Factor for Attached Reactants

The determination of  $A_a$  is of particular interest since it provides a measure of the frequency with which electron transfer occurs once the configuration of the nuclear coordinates appropriate for electron transfer has been achieved. The usual collision frequency is clearly inappropriate for treating the reaction of an attached molecule. One suggestion has been to use instead the characteristic frequency of the electron in the metal electrode (ca.  $10^{15}$  s  $^{-1}$ ). 197 Although this frequency might be useful in calculating an electron tunneling probability or describing certain activationless reactions, it is an incorrect choice for adiabatic reactions because it ignores the slower nuclear processes involved in surmounting the Franck-Condon barrier. Nevertheless, it provides a useful starting point for estimating  $v_{el}(=\kappa_{el}v_n)$  for nonadiabatic reactions (i.e., reactions for which  $v_{el}(v_n)$ .

A recent "semi-classical" treatment of electron transfer 23 provides an enlightening description of the physical processes that influence such frequency factors. Although concerned with homogeneous electron transfer, the model described in reference 23 can also be

applied to electrochemical reactions. We can express  $A_a$  as  $^{23}$ 

$$\mathbf{A}_{\mathbf{a}} = \kappa \mathbf{e} \mathbf{1} \mathbf{n} \mathbf{n} \tag{4.37}$$

where el is an electronic transmission coefficient,  $\Gamma_n$  is a nuclear tunneling factor and  $\nu_n$  is a nuclear frequency factor. This last term is viewed as the frequency with which the transition state is approached from the precursor state. Since activation results from solvent reorganization and bond stretching (or compression),  $\nu_n$  is taken as an appropriately weighted average of the frequencies of these two processes. We can write:  $^{23}$ 

$$v_{n}^{2} = \left(v_{os}^{2} \Delta G_{os}^{*} + v_{is}^{2} \Delta G_{is}\right) / \left(\Delta G_{os}^{*} + \Delta G_{is}^{*}\right)$$
 (4.8)

where the parameters in Equation 4.8 have been defined in the previous section. (There is some controversy concerning the appropriateness of the particular expression for  $v_n^{24}$ ). Taking  $v_{os} \approx 10^{11} \text{ s}^{-1}$  in water  $^{23}$  and  $_{is}^{10^{13}} \text{ s}^{-1}$  as a typical bond stretching frequency yields  $v_n \approx 10^{12}$  to  $10^{13} \text{ s}^{-1}$ , if, as usual, bond reorganization is a significant contributor (>1%) to the overall reorganization energy. This result is numerically similar to the conventional frequency factor kT/h at ambient temperatures.

The nuclear tunneling factor  $\Gamma_n$  in Equation 4.37 is close to unity for small values of  $\Delta G_i^*$ . Although  $\Gamma_n > 1$ , it generally increases with decreasing temperature, thereby decreasing the measured values of  $\Delta H^*$  and hence yielding smaller apparent values of  $A_a$ . However, the

effect is calculated to be negligible at ambient temperatures for reactions where  $\Delta G_i^* < 40$  kJ mol<sup>-1</sup>.<sup>23</sup>

The only other contributor to  $A_a$  is the electron tunneling term  $\kappa_{el}$ , which is unity for an adiabatic reaction. Therefore any discrepancies between experimental values of  $A_a$  and the corresponding calculated values of  $\nu_n$  may normally be attributed to a small value of  $\kappa_{el}$ . Thus contrary to some recent statements,  $\mu_{el}^{197,198}$  the observation that  $\mu_{el}^{197,198}$  or, equivalently, of large negative activation entropies obtained from  $\mu_{r,a}^{197,198}$  by assuming that  $\mu_{el}^{197,198}$  (Equations 4.33 and 4.34) can be taken as evidence that  $\kappa_{el}^{197,198}$ 

Objections that the Marcus and other electron-transfer models based on "absolute reaction rate" theory do not apply to surfaceattached reactants 197 are incorrect; no extra assumptions are made in applying contemporary theories to these reactions besides the choice of an appropriate statistical formalism for the frequency factor. In fact, redox processes involving surface-attached reactants are in some respects better model reactions for testing electron-transfer theories than are outer-sphere electrochemical reactions. Since the surfaceattached reactant and product can be identified with the precursor and successor states, both the thermodynamics and kinetics of the elementary electron-transfer step are susceptible to direct experimental determination. As noted above, this is strictly not the case for outer-sphere reactions, so that the intrinsic barrier  $\Delta H_{int}^*$  and frequency factor A can only be obtained from the experimental kinetics parameters by estimating the enthalpic and entropic work terms (Equations 4.24-4.27).

In addition, for outer-sphere reactions there is a substantial uncertainty regarding the theoretical formulation of  $A_{sol}$  and its relation to the frequency factor for the elementary step. ventional collisional model predicts a typical value of  $A_{801}$  of ~5 x 10<sup>3</sup> cm s<sup>-1.54</sup> The alternative "preequilibrium" (Equation 4.27)<sup>54</sup> describes the frequency factor as a product of an equilibrium constant K for the formation of a precursor state from the bulk reactant, and a frequency  $\boldsymbol{\nu}_{\boldsymbol{n}}$  for solvent reorganization and bond vibrations as in Equation 4.8. Significantly larger values of  $A_{sol}$ , around 5 x  $10^5$  cm s<sup>-1</sup>, can be derived using this model. 31,200,210 However, there is a significant uncertainty in K and hence A sol, arising from the lack of information on the effective thickness of the precursor state "reaction zone" within which the reactant is required to reside so that electron tunneling can occur with sufficient probability to contribute to the reaction rate. 200,210 (However, see Section V. C). These uncertainties regarding the theoretically expected values of A lead to difficulties in separating out the various other contributions to the experimental frequency factors. Such difficulties are absent for reactions of surface-attached molecules.

It is interesting to note that the advantages that are expected in the study of attached molecule reactions as compared to solution electrochemical reactions have close parallels in studies of homogeneous electron transfer. Thus, rate data and activation parameters for intramolecular electron-transfer reactions in ridgid binuclear complexes are more easily interpreted than are the corresponding results for the usual second order outer-sphere reactions. The

problems associated with the choice of an appropriate theoretical formalism for the frequency factor, and the uncertainties in the work term corrections are absent for intramolecular reactions. The treatment of electron transfer between an attached reactant and an electrode surface contains closely analogous advantages and can usefully be perceived as a heterogeneous "intramolecular" reaction. 199,200

Studies of electron-transfer kinetics between surface-bound molecules and electrodes as a function of temperature are as yet uncommon. 196,197,198,204,211 Brown and Anson have determined that A = 10<sup>6</sup> s<sup>-1</sup> for the reduction of 9,10-phenanthrenequinone at graphite. 196 However, this reaction involves a proton-transfer step preceding electron transfer which precludes extraction of the true frequency factor A in the absence of thermodynamic data for the former equilibrium. Sharp and coworkers have obtained some interesting results for the ferrocene/ferricinium couple bound to a platinum electrode. 197,198 Values of k for this couple were reported as a function of temperature in acetonitrile and sulpholane. The frequency factor A was reported to be  $3\times10^8$  s<sup>-1</sup> in acetonitrile <sup>197</sup> and  $2\times10^8$  s<sup>-1</sup> in sulpholane. 198 Assuming that the inner-shell reorganization  $\Delta G_{i}^{*}$ comprises about 5% of the total reorganization energy,  $^{197}$  and  $v_{in}$  and  $v_{\rm out}$  are 10<sup>13</sup> s<sup>-1</sup> and -2x10<sup>11</sup> s<sup>-1</sup>, respectively,  $v_{\rm n}$  is estimated to be about 2x10<sup>12</sup> s<sup>-1</sup>. From the usual dielectric continuum expression neglecting the influence of the reactant-electrode image interactions 54 and using literature values of the optical and static dielectric constants and their temperature derivatives 207-209  $\Delta S_{int}^*$  is calculated

to be -12 J deg<sup>-1</sup> mol<sup>-1</sup> in acetonitrile and -7 J deg<sup>-1</sup> mol<sup>-1</sup> in sulpholane. From these values of  $A_a$  and  $v_n$  using Equations 4.34 and 4.37, estimates of  $k_{el}$  of about  $6 \times 10^{-4}$  in acetonitrile and  $2 \times 10^{-4}$  in sulpholane are obtained, indicating that the electron-transfer reaction is moderately nonadiabatic under these conditions.

# C. An Experimental Estimate of the Electron-Tunneling Distance for Some Outer-Sphere Electrochemical Reactions (Accepted for publication in J. Phys. Chem.)

### 1. Introduction

An important question in the treatment of electron-transfer reactions concerns the magnitude of the frequency factor, A, in the expression

$$k_{ob} = A \exp(-W_{D}/RT) \exp(-\Delta G_{et}^{*}/RT)$$
 (4.38)

where  $k_{ob}$  is the observed rate constant,  $W_p$  is the work required to bring the reactants together (or the reactant to the electrode surface), and  $\Delta G_{et}^*$  is the free-energy barrier for the elementary electron-transfer step. Although sophisticated theoretical methods have been developed for evaluating  $\Delta G_{et}^*$  from structural and thermodynamic information, there remains considerable uncertainty as to the numerical values of the frequency factor for outer-sphere pathways. 9,10,14,15,17,23,28,213

In the recent literature it has been emphasized that outer—as well as inner-sphere redox reactions in homogeneous solution and at electrode surfaces can usually be viewed as involving formation of a reactive precursor complex from initially separated reactants followed by the rate-determining transfer step. 9,10,14,15,17,18,23,28,30,31,213,214

Thus the observed rate constant can be formulated as

$$k_{ob} = K_{pet} \tag{4.5}$$

where K<sub>p</sub> is the equilibrium constant for forming the precursor state and k<sub>et</sub> is the rate constant describing the elementary electron-transfer step. When applied to outer-sphere pathways, this approach can be termed an "encounter preequilibrium" treatment. It views the reaction as taking place via the unimolecular activation of a weakly interacting reactant pair having a suitably close proximity and geometrical configuration to enable electron transfer to occur once the appropriate nonequilibrium nuclear configuration has been achieved. 17,23,211,213

According to the encounter-preequilibrium treatment, the frequency factor can be expressed as 23,211,213

$$\mathbf{A} = \mathbf{v}_{\mathbf{n}} \mathbf{r}_{\mathbf{n}} \mathbf{c}_{\mathbf{n}} \mathbf{K} \tag{4.39}$$

where  $v_n$  is the nuclear tunneling factor,  $\Gamma_n$  is the effective frequency for activating nuclear reorganization modes,  $\kappa \stackrel{o}{el}$  is the electronic

transmission coefficient at the distance of closest approach of the reactants and  $K_{_{\hbox{\scriptsize O}}}$  is the statistical part of the precursor stability constant  $K_{_{\hbox{\scriptsize D}}}$  where

$$K_{p} = K_{o} \exp(-W_{p}/RT) \tag{4.40}$$

For electrochemical reactions the statistical factor  $K_o^e$  can be expressed simply as  $211^{\circ}$ 

$$\mathbf{K}_{\mathbf{O}}^{\mathbf{e}} = \delta \mathbf{r}_{\mathbf{e}} \tag{4.41}$$

where  $\delta r_e$  is the thickness of a "reaction zone" beyond the plane of closest approach within which the reactant must reside in order to contribute significantly to the overall reaction rate. The value of  $\delta r_e$  is determined by the need for the reactant and surface to be in sufficiently close proximity to achieve significant overlap of donor and acceptor orbitals, and hence nonzero values of the transmission coefficient  $\kappa_{el}$  for a given reactant orientation (vide infra). The composite term  $\kappa_{el}^{0} R_{o}^{e} (\kappa_{el}^{0} \delta r_{e})$  appearing in Equation 4.39 for electrochemical reactions can therefore be considered to be an "effective reaction zone thickness". If  $\kappa_{el}^{0} < 1$ , the reaction is termed "nonadiabatic", whereas "adiabatic" processes are those for which  $\kappa_{el}^{0} \sim 1$ . Since the magnitude of  $\delta r_{el}$  is determined by the dependence of  $\kappa_{el}^{0}$  upon the donor-acceptor separation distance, markedly smaller values of  $\kappa_{el}^{0} \delta r_{el}^{0}$  are anticipated for the former compared to the latter processes as a result of smaller values of  $\delta r_{el}^{0}$  as well as  $\kappa_{el}^{0}$ .

The statistical factor for homogeneous reactions,  $K_0^h$ , is more complex than  $K_0^e$  yet entirely analogous, corresponding to the probability of finding one reactant within a reaction zone of thickness  $\delta r_h$  beyond the bimolecular contact distance. This term can be estimated approximately from  $^{9}$ ,  $^{15}$ ,  $^{17}$ ,  $^{213}$ 

$$K_o^h = 4\pi N r_h^2 \delta r_h / 10^3$$
 (4.42)

where N is the Avogadro number, and  $\mathbf{r}_{h}$  is the distance between the reacting centers when in contact.

Recent <u>ab initio</u> calculations for some homogeneous outer-sphere reactions <sup>14,15,17,215</sup> indicate that  $\kappa_{el}$  can be substantially below unity even at a relatively small internuclear separation  $r_h$ , decreasing sharply with increasing r. This corresponds to relatively small values of  $\kappa_{el}^0$   $\delta r_h$  (<1Å, <u>vide infra</u>). <sup>9,213</sup> It would be extremely desirable to obtain an experimental measure of such quantities. In the approach decribed here, estimates of  $\kappa_{el}^0$   $\delta r_e$  for several outer-sphere electrochemical processes are obtained by a relatively direct method involving the comparison of rate constants for these pathways with those for structurally related electrochemical reactions occurring via geometrically well-defined ligand-bridged transition states. The results provide evidence that heterogeneous, as well as homogeneous, electrontransfer processes can be significantly nonadiabatic.

#### 2. Data Analysis

The virtue of comparing rate parameters for corresponding electrochemical reactions occurring via outer- and inner-sphere (ligand-bridged) pathways can be seen by noting that in contrast to the former, unimolecular rate constants for the electron-transfer step involving a ligand-bridged precursor state,  $k_{\rm et}^{\rm is}({\rm s}^{-1})$ , can often be determined directly from the overall rate constant,  $k_{\rm ob}^{\rm is}$ , using Equation 4.5 since  $K_{\rm D}$  can be found from

$$K_{p} = \Gamma_{p}/C_{b} \tag{4.43}$$

where  $\Gamma_p$  is the precursor state concentration (mole cm<sup>-2</sup>) corresponding to a given bulk reactant concentration  $C_b$ . The values of  $k_{et}^{is}$  can be expressed as

$$k_{\text{et}}^{\text{is}} = \Gamma_{\text{n n el}}^{\text{kis}} \exp(-\Delta G_{\text{et}}^{\text{*}}/RT)$$
 (4.44)

where  $k_{el}^{is}$  is the electronic transmission coefficient for the ligand-bridged reaction pathway. In view of Equations 4.38-4.41 the work-corrected rate constant for the corresponding outer-sphere electrochemical pathway,  $k_{corr}^{OS}$ , can be expressed as

$$k_{\text{corr}}^{OS} = \Gamma_{\text{n L}} \kappa_{\text{el}}^{OS} \delta_{\text{re}} \exp(-\Delta G_{\text{et}}^{*}/RT)$$
 (4.45)

Provided that  $\Delta G_{et}^*$ ,  $\Gamma_n$ , and  $v_n$  are unaffected by surface attachment at a given electrode potential (<u>vide infra</u>), evaluation of the rate

ratios  $k_{\text{corr}}^{\text{OS}}/k_{\text{et}}^{\text{is}}$  enable estimates of  $k_{\text{el}}^{\text{O}}\delta r_{\text{e}}$ , at least relative to  $k_{\text{el}}^{\text{is}}$ , to be obtained. This procedure will now be utilized to estimate the effective electron-tunneling distances for some outer-sphere Cr(III) reductions at the mercury-aqueous interface.

Pertinent kinetic and thermodynamic data are assembled in Table 4.1 for the electroreduction of three  $\mathrm{Cr^{III}}(\mathrm{NH_3})_5\mathrm{X}$  complexes, where  $\mathrm{X}=\mathrm{NCS^-}$ ,  $\mathrm{N_3^-}$ , and  $\mathrm{Cl^-}$  and five  $\mathrm{Cr^{III}}(\mathrm{OH_2})_5\mathrm{X}$  complexes, where  $\mathrm{X}=\mathrm{OH_2}$ ,  $\mathrm{SO_4^{2-}}$ , F-, NCS-, and N<sub>3</sub>. The data were extracted from references 30, 73 and 215. These reactions were chosen because rate constants corresponding to both inner- and outer-sphere pathways,  $\mathrm{k_{et}^{is}}$  and  $\mathrm{k_{corr}^{os}}$  respectively, can be obtained directly or estimated from experimental data. 211 Several of these reactions have been examined previously in a related discussion of the relative energetics of inner- and outer-sphere pathways.  $^{30}$ 

The work-corrected rate constants,  $k_{corr}^{OS}$ , were determined from the corresponding observed rate constants,  $k_{ob}^{OS}$ , using the electrostatic double-layer corrections as outlined in reference 216. (See footnotes to Table 4.1). Of the three Cr(III) ammine reactants,  $Cr(NH_3)_5N_3^{2+}$  and  $Cr(NH_3)_5C1^{2+}$  exhibit mixed electroreduction kinetics which enable both  $k_{ob}^{OS}$  and  $k_{ob}^{iS}$  to be obtained. The latter values are combined with estimates of  $K_p$  obtained under the same conditions from kinetic probe measurements  $k_p^{OS}$ 0,217 to yield values of  $k_p^{iS}$ 1 by using Equation 4.8. The common electrode potential of -600 mV vs. the saturated calomel electrode (see) was chosen so to minimize the extent of data extrapolation that is involved. The estimate of  $k_p^{iS}$ 1 for  $Cr(NH_3)_5N_3^{2+}$ 1 reduction (1 s<sup>-1</sup>) is close to that observed for  $Cr(NH_3)_5NCS^{2+}$ 2 reduction (0.5 s<sup>-1</sup>);

Kinetic and Thermodynamic Data for the One-Electron Reduction of Cr(III) Complexes at the Mercury-Aqueous Interface at 25°C. Table 4.1.

	a		q	o	đ	w .	
Reactant	Pathway	-E mV. vs sce	$\frac{k}{cb_1}$	kos corr cm s-1	R p a	kis et s-1	k <sup>os</sup> /k <sup>18</sup> corr <sup>e</sup> et
Cr (NH <sub>3</sub> ) <sub>5</sub> NCS <sup>2+</sup>	is	009	1 x 10 <sup>-5</sup>		2 x 10 <sup>-5</sup>	0.5	
$Cr(NH_3)_5N_3^{2+}$	80	009	$6 \times 10^{-7}$	$1 \times 10^{-7}$			5-10
	1s	009	~5 x 10 <sup>-7</sup>		$5 \times 10^{-7}$	_1	
$cr(NH_3)_5c1^{2+}$	so	009	$3 \times 10^{-6}$	$6 \times 10^{-7}$			L.
	ıs	009	$1 \times 10^{-5}$		°1 x 10 <sup>-6</sup>	~10	0
${\rm Cr}(0{\rm H}_2)_6^{3+}$	80	655	$7.5 \times 10^{-6}$	$2.5 \times 10^{-6}$			
$Cr(OH_2)_5SO_4^+$	80	705	4.6 x 10 <sup>-6</sup>	$3.5 \times 10^{-6}$			
${ m Cr}({ m OH}_2)_5{ m F}^{2+}$	so	860	6 x 10 <sup>-6</sup>	$2 \times 10^{-6}$			~0.1-0.3
$Cr(0H_2)_5NCs^{2+}$	is	720	$4 \times 10^{-3}$		~4 x 10 <sup>-6</sup>	$1 \times 10^3$	
$Cr(OH_2)_5N_3^{2+}$	is	~720	1.2 x 10 <sup>-4</sup>		$^{2} \times 10^{-7}$	$2 \times 10^3$	

 $a_{18} = inner-sphere$  (ligand-bridged) pathway; os = outer-sphere pathway

 $<sup>^{</sup>b}$  Observed rate constant for overall electrode reaction following is or os pathway indicated at electrode potential, E, listed in adjacent column. Values of  $k_{ob}$  for Cr(III) aquo complexes determined at formal potential for Cr(III)/(II) couple Data taken from references 30, 70 and 216.

 $^{\mathcal{C}}$  Work-corrected rate constant for outer-sphere pathway. Determined from corresponding value of  $k_{\mathrm{ob}}$ using  $k^{OB} = k_{Ob} \exp[(Z-0.5)\phi_{Tp}]$ , where Z is the reactant charge number, and  $\phi_{Tp}$  is the average potential at the reaction plane (see 73 and 216 for details).

dStability constant for the inner-sphere precursor state, determined from Equation 4.43; taken from reference 30.  $^{ heta}$  Unimolecular rate constant for electron-transfer step involving ligand-bridged intermediate. Obtained from listed values of  $k_{ob}$  and  $K_{p}$  using Equation 4.5. this supports the validity of the former estimate in view of the closely similar coordination properties of  $-N_3^-$  and  $-NCS^-$ .

Each of the five Cr(III) aquo reactants in Table 4.1 undergoes electro-reduction via sufficiently rate-dominating outer- or inner-sphere pathways so that only  $k_{Ob}^{OS}$  or  $k_{et}^{is}$  can be evaluated for each reactant. Nevertheless, an approximate estimate of  $k_{corr}^{OS}/k_{et}^{is}$  for these structurally related rections can still be obtained as follows. As noted previously by Weaver. The values of  $k_{corr}^{OS}$  for  $Cr(OH_2)_{6}^{3+}$ ,  $Cr(OH_2)_{5}^{SO_4^+}$ , and  $Cr(OH_2)_{5}^{F^{2+}}$  reduction are closely similar when evaluated at their respective formal potentials. This indicates that the intrinsic electron-transfer barrier is approximately independent of the nature of the sixth ligand, even though the coordinating properties of  $OH_2$ ,  $SO_4^{2-}$  and  $F^-$  differ widely. These values of  $k_{corr}^{OS}$ , listed in Table 4.1, are therefore also likely to be close to those for  $Cr(OH_2)_{5}NCS^{2+/+}$  and  $Cr(OH_2)_{5}N_3^{2+/+}$  which cannot be measured but for which the corresponding values of  $k_{et}^{is}$  are known, enabling the desired estimate of  $k_{corr}^{OS}/k_{et}^{is}$  to be obtained (Table 4.1).

#### 3. Discussion

Inspection of Table 4.1 shows that the resulting values of  $k_{\rm corr}^{OS}/k_{\rm et}^{is}$  for Cr(III) aquo reduction, ca. 0.2 Å, are ca. 10-30 fold smaller than those for the Cr(III) ammine reductions, ca. 5 Å. Quantitative interpretation of these results can be made by referring to Equations 4.44 and 4.45. Of the various terms,  $\Gamma_{\rm n}$  and  $\nu_{\rm n}$  will almost certainly have the same values for the corresponding inner- and outersphere pathways. Thus  $\nu_{\rm n}$  is determined chiefly by the metal-ligand

stretching frequencies  $^{211}$  and  $\Gamma_n$  is usually close to unity, being dependent upon the magnitude of  $^{\Delta}G_{et}^*$  rather than the transition-state geometry. The reorganization energy  $^{\Delta}G_{et}^*$  may differ significantly for corresponding inner- and outer-sphere pathways, arising both from differences in the inner-shell (metal-ligand) and outer-shell (solvent) reorganization terms. Ligand bridging may yield some decreases in the inner-shell component of  $^{\Delta}G_{et}^*$  arising from the influence of surface attachment on the Cr(III)-ligand bonding. However, there is scant evidence for such catalyses with Cr(III)/(II) and Co(III)/(II) electrode rections, even at surfaces such as platinum and gold that bind inorganic ligand bridges much more strongly than does mercury.  $^{218}$ 

Surface attachment may yield an alteration in the outer-shell component of  $\Delta G_{\text{et}}^*$  since this is predicted to diminish as the distance between the redox center and the surface decreases, as a result of greater image stabilization of the transition state. 13 With the azido and isothiocyanato bridges, the redox center is estimated to lie about 5-6 % from the surfce. 219 Provided that the outer-sphere transition state is formed with the reactant in contact with a monolayer of inner-layer water molecules (vida infra), the redox center will be about 6.5 % from the surface, based on a reactant crystallographic radius of 3.5 % and a water molecule diameter of 3 %. 216 On the basis of the well-known relation for the outer-shell component of  $\Delta G_{\text{et}}^*$  due to Marcus,  $\Delta G_{\text{et}}^*$  due to increase by only ca. 50% upon decreasing the reactant-electrode separation from 7 to 6 %, and by only ca 3-fold from 7 to 5 %. It therefore appears likely that  $\Delta G_{\text{et}}^*$  only differs to a small extent between corresponding outer- and inner-sphere

pathways involving thiocyanate or azide bridges. The similar values of  $k_{\text{corr}}^{\text{OS}}/k_{\text{et}}^{\text{is}}$  seen for  $\text{Cr}(\text{NH}_3)_5\text{Cl}^{2+}$  and  $\text{Cr}(\text{NH}_3)_5\text{N}_3^{2+}$  reduction (Table 4.1), even though the Cr(III) - surface distance is expected to be ca. 2 Å smaller for the former reaction, lends support to this assertion.

To a first approximation, then, from Equations 4.44 and 4.45 the rate ratios  $k_{\rm corr}^{OS}/k_{\rm et}^{is}$  for the present system can be related to the effective reaction zone thickness for the outer-sphere pathways,  $k_{\rm cl}^{O} \delta r_{\rm c}$ , simply by

$$k_{corr}^{os}/k_{et}^{is} \approx \kappa_{el}^{o} \delta r_{e}/\kappa_{el}^{is}$$
 (4.46)

Since the ligand bridge should facilitate overlap between the surface donor and Cr(III) acceptor orbitals it is anticipated that the innersphere pathways are adiabatic, i.e.  $\kappa_{el}^{is}$ -1. If indeed  $\kappa_{el}^{is}$ -1, then the values of  $k_{corr}^{os}/k_{et}^{is}$ , ca 5 % and 0.2 %, can be identified directly with the effective reaction zone thickness  $\kappa_{el}^{o}$  for the ammine and aquo reactants, respectively. Even if  $k_{el}^{is}$ -1, it is likely to have essentially the same value for both pentamine—and pentasquo Cr(III) reductions bridged by azide and isothiocyanato ligands since the Cr(III)—surface distance and hence the degree of orbital overlap should be determined by the bridging ligand. It therefore appears certain that  $k_{el}^{os}$  is markedly larger for the ammine compared to the aquo reactants.

A persuasive explanation for this striking result is to be found in the differences in the location of the outer-sphere reaction sites that have been noted previously for these reactions.  $^{216,220,221}$  Thus the reduction rates of  $\text{Cr}(\text{OH}_2)_6^{3+}$  and other Cr(III) aquo complexes are

markedly less sensitive to variations in the double-layer potential profile than are the reduction rates of  $Cr(NH_3)_6^{3+}$  and related Cr(III)ammines. 216 These results provide evidence that the Cr(III) aquo reaction sites are constrained to lie significantly further from the electrode surface. This is consistent with the larger hydrated radii for aquo versus ammine reactants due to the more extensive ligand-solvent hydrogen bonding exhibited by the former complexes. 55,216,222 From an analysis of the observed double-layer effects, Weaver and Satterberg estimated that the reaction site for  $Cr(OH_2)_6^{3+}$  reduction lies 6-7 % from the surface, whereas that for  $Cr(NH_3)_6^{3+}$  reduction is about 1.5 Å closer. 216 (Although the absolute reactant-electrode distances are subject to as much as 1 - 1.5 A uncertainty, the relative distances for the aquo versus ammine reactants are rather more reliable). It is therefore to be expected that k = 0 will be larger for the ammine than for the aquo reactants unless the reactant-surface electronic coupling is sufficient to provide adiabatic pathways  $(\kappa_{el}^{0} = 1)$  in both cases.

In order to interpret the individual values of  $\kappa_{el}^{0}$   $\delta r_{e}$ , it is advantageous to consider the encounter preequilibrium treatment in a little more detail. Since  $\kappa_{el}$  will depend upon the donor-acceptor separation distance within the reaction zone of thickness  $\delta r_{e}$ , strictly speaking one should express the overall observed rate constant in terms of an integral of "local" values of  $k_{et}$ , each being associated with a particular spatial position and orientation of the reactant and hence individual values of  $\kappa_{el}$ ,  $W_{p}$  and  $\Delta G_{et}^{*}$ . The dependence of  $\kappa_{el}$  upon the separation distance,r, for nonadiabatic pathways can be approximated by  $^{28,213}$ 

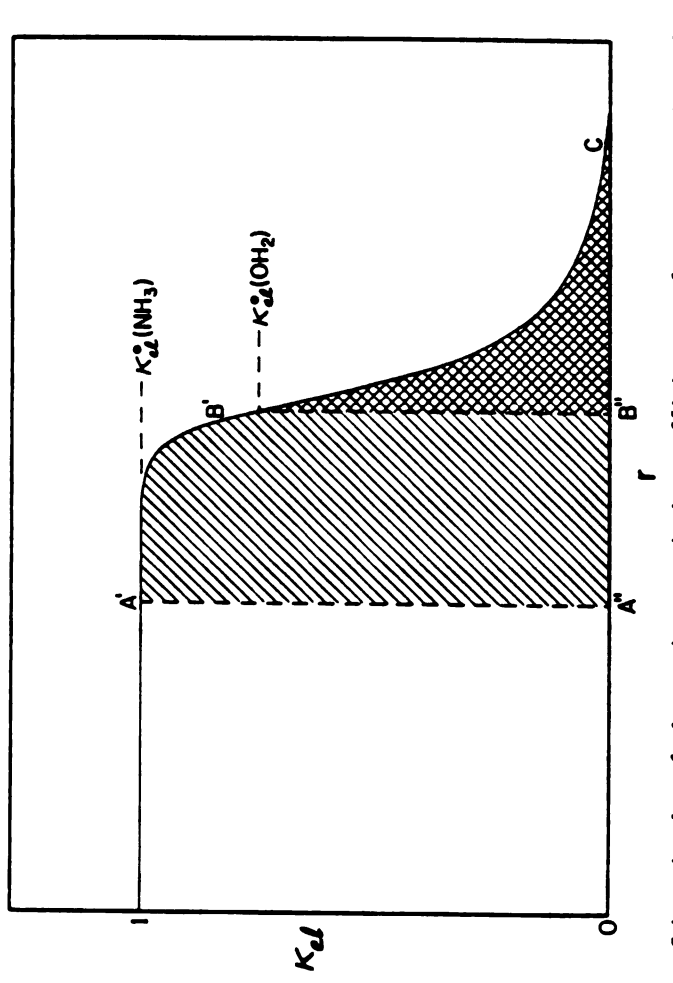
$$\kappa_{el}(\mathbf{r}) = \kappa_{el}^{0} \exp[-\alpha(\mathbf{r} - \sigma)] \tag{4.11}$$

where  $\sigma$  is the separation distance corresponding to closest approach, and  $\alpha$  is a constant which is typically estimated to lie in the range ca. 1.4 to 1.8 Å<sup>-1</sup>. <sup>15,58,213</sup> Consequently, if  $\kappa_{el}^{0}<1$  (i.e. the reaction is nonadiabatic at the plane of closest approach), the effective value of  $\delta r_{el}$  will equal  $\alpha^{-1}$ . On the other hand, if  $\sigma$  is sufficently small so that  $\kappa_{el}$  = 1 not only at the distance of closest approach but also for a significant distance,  $\chi$ , beyond it, we expect that roughly

$$\delta \mathbf{r}_{\mathbf{a}} = \chi + \alpha^{-1} \tag{4.47}$$

Equation 4.47 therefore provides a general relationship where  $\chi = 0$  if  $\kappa_{el}^{0} < 1$ , and  $\chi > 0$  if  $\kappa_{el}^{0} = 1$ .

Figure 4.2 is a schematic representation of the dependence of  $\kappa_{el}$  upon r. The magnitude of  $\kappa_{el}^{0} \delta r_{e}$  will equal the area under the curve bounded by the distance of closest approach, for example the shaded area A'A"C. Taking  $\alpha = 1.6 \text{ A}^{-1}$ , it follows that  $\kappa_{el}^{0} \delta r_{e} < 0.5 \text{ A}$  if  $\kappa_{el}^{0} < 1.05 \text{ A}$  therefore suggests that  $\kappa_{el}^{0} < 1.05 \text{ A}$  at the plane of closest approach for the aquo cations, so that  $\kappa_{el}^{0} < 1.05 \text{ A}$  is estimate of  $\kappa_{el}^{0} \delta r_{e}$  may be call.5 to 2-fold too small as a result of the likely differences in  $M_{el}^{\infty}$  between the inner—and outer—sphere pathways noted above, although it may be too large if  $\kappa_{el}^{1} \delta r_{e}$  is the Another factor which would decrease the apparent value of  $\kappa_{el}^{0} \delta r_{e}$  is the



anticipated planes of closest approach for Cr(III) amine and aquo, reactants, respectively. The shaded and cross-hatched areas represent the corresponding values of the "effective reaction zone thickness" Figure 4.2. Schematic plot of electronic transmission coefficient kel for an outer-sphere electrochemical reaction against the reactant-electrode separation distance r. A'A'' and B'B'' represent  $\kappa_{\rm el}^{0}$  for these reactants.

possibility that a specific reactant orientation is required either to enable the reactant to approach the electrode more closely or to provide more effective coupling of the surface donor and Cr(III) acceptor orbitals. Such factors have recently been considered in detail for  $Fe(OH_2)_6^{3+/2+}$  self exchange.  $^{14,15,17,215}$  In any case, we conclude that outer-sphere electron transfer involving the Cr(III) aquo reactants only approaches adiabaticity for electron-tunneling distances very close to the plane of closest approach of these cations (represented by B'B" in Figure 4.2), around 6-7 R from the electrode surface.

On the other hand, the estimate of  $\kappa_{el}^{0} \delta r_{el}$  for the Cr(III) ammines, ca 5 R, suggests that electron transfer to these reactants remains adiabatic even for reaction sites several Angstroms from the plane of closest approach (represented by A'A" in Figure 4.2). The exact value of  $\kappa e_{e1}^{0} \delta r_{e}$  for the ammine reactants is in one respect subject to greater uncertainty than for the aquo reactants in that the magnitude of the work-term ("double-layer") correction upon kob is somewhat greater for the former. 216 Moreover, the work-term correction employed assumes that the reaction occurs only at the outer Helmholtz plane (oHp), whereas the large value of  $\kappa_{el}^{0} \delta r_{e}$  suggests that the effective reaction zone is relatively thick. Given that the ammine reactants can probably penetrate inside the oHp, this work-term correction may well be an underestimate, so that  $k_{corr}^{O}$  and hence  $k_{el}^{O}$  are actually smaller than the present values. Given that the aquo reactants are marginally adiabatic at their plane of closest approach, from the reaction site differences noted above it would be expected that ~2 Å for the ammines, yielding  $\kappa_{el}^{0} \delta r_{e}^{-2-3} \hat{A}$ . One factor which may enhance

 $\kappa_{el}^{o}$  for the ammine versus the aquo complexes is the likely greater ligand character of the acceptor orbital on the former reactants,  $^{15,215}$  leading to greater electrode-reactant orbital overlap at a given electrode-reactant separation distance. The difference in the effective reaction zone thickness between the aquo and ammine reactants is therefore roughly compatible with the likely differences in the reaction sites if the dependence of  $\kappa_{el}$  upon the surface-reactant separation is similar for these reactants, with  $\kappa_{el}$  decreasing below unity for surface-reactant separations greater than ca. 6 Å.

Taking  $\Gamma_n=2.5$  and  $\nu_n=1.2\times 10^{13}~s^{-1}$  for the present reactions  $^{223}$  it is deduced from Equations 4.39 and 4.41 that the overall frequency factor A is ca.  $6\times 10^4$  and  $1.5\times 10^6$  cm s<sup>-1</sup> for the aquo and ammine reactants, respectively. Both these values are somewhat larger than the frequency factor, ca.  $5\times 10^3$  cm s<sup>-1</sup>, derived from the conventional collisional model assuming adiabatic behavior.  $^{54},^{211}$  It should be noted that the encounter preequilibrium treatment employed here represents a departure from the collisional model since the latter views the reaction as being consumated only by collisions between the reactant and the electrode surface (or a coreactant).  $^{211}$ 

It is of interest to compare the above estimate of A for the Cr(III) aquo reactants with that obtained for  $\text{Cr}(\text{OH}_2)_6^{3+}$  reduction under the same conditions from the temperature dependence of  $k_{\text{corr}}^{\text{OS}}$ . We can write  $^{54}$ 

$$k_{corr}^{os} = A \exp(\Delta S_{i}^{*}/R) \exp(-\Delta H_{i}^{*}/RT)$$
 (4.48)

where  $\Delta S_i^*$  and  $\Delta H_i^*$  are the work-corrected "ideal" entropies and enthalpies of activation which form the components of  $\Delta G_{et}^*$  at the particular electrode potential at which  $k_{corr}^{OS}$  is obtained. The activation enthalpy  $\Delta H_i^*$  can be obtained directly from the Arrhenius slope of  $\ln k_{corr}^{OS}$  versus (1/T), being measured at a constant electode potential using a nonisothermal cell arrangement. The value of  $\Delta S_i^*$  can be obtained from  $\Delta S_i^*$ 

$$\Delta S_{i}^{*} = \alpha_{corr}^{\Delta} S_{rc}^{o} + \Delta S_{int}^{*}$$
 (1.19)

where  $\alpha_{corr}$  is the work-corrected transfer coefficient,  $\Delta S_{rc}^{o}$  is the so-called reaction entropy of the redox couple concerned,  $^{55}$  and  $\Delta S_{int}^{*}$  is the intrinsic activation entropy.  $^{225}$  From the data given in reference 54. at -800 mV vs. sce,  $k_{corr}^{os} = 5.5 \times 10^{-5}$  cm s<sup>-1</sup> (25°C),  $\Delta H_{i}^{*} = 17.5$  kcal. mol<sup>-1</sup>,  $^{226}_{os}$   $^{corr}$  = 0.50.  $\Delta S_{rc}^{os} = 49$  cal. deg<sup>-1</sup> mol<sup>-1</sup>, and  $\Delta S_{int}^{*} = 3.5$  cal. deg<sup>-1</sup> mol<sup>-1</sup>. Inserting these data into Equations 4.49 and 1.19 yields  $\Delta = 9 \times 10^{3}$  cm s<sup>-1</sup>. (This calculation cannot be performed for Cr(III) ammine reductions since the  $\Delta S_{rc}^{os}$  values are not known with sufficient accuracy.)

The ca 7-fold discrepancy between this and the above estimate of A probably arises in part from the very approximate nature of Equation 1.19. This relation presumes that the transition-state entropy is unaffected by the proximity of the reacting ions to the electrode surface, whereas it is likely that  $\Delta S_{i}^{*}$  and  $\Delta H_{i}^{*}$  are much more sensitive than is the overall barrier  $\Delta G_{et}^{*}$  to the solvating environment at the interface and in the bulk solution. Indeed, it is found that the acti-

vation parameters for these and other reactions are rather more sensitive than is  $k_{\text{corr}}^{OS}$  to the nature of the electrode material, surprisingly small frequency factors being typically obtained at solid metal surfaces 136,187 (see section IV.D).

### 4. Conclusions

The foregoing treatment provides a relatively direct, albeit very approximate, experimental method for evaluating the effective electron-tunneling distances for outer-sphere electrochemical reactions. It exploits both the close relationship between the energetics of corresponding inner- and other-sphere electrode reactions and the information that can be derived 216,221 on the reactant-electrode separation distance from the magnitude of the double-layer effects in electrochemical kinetics. A strictly analogous approach cannot be employed for homogeneous processes due to the inevitable changes in reactant coordination between otherwise related inner- and other-sphere pathways and the lack of a means for subtly altering the electrostatic interactions between ionic reactants in solution.

Although it would not be surprising if similar differences in the internuclear distances and hence  $\kappa_{el}^0\delta r$  also arise between aquo and ammine complexes in homogeneous electron-transfer reactions, the solvating environments may be sufficiently different to that pertaining to the present electrochemical reactions  $^{227}$  to bring other factors to the fore. Indeed, the larger rate ratios for Co(III) ammine versus aquo reactants observed at mercury electrodes relative to that obtained with a given reductant in homogeneous solution  $^{220}$  suggest that these differ-

ences in  $k_{el}^0$  for may well be smaller in the latter environment. Nevertheless, the present finding that outer-sphere electrochemical reactions can be at least marginally non-adiabatic bears a close resemblance to the interpretation of some anion catalytic effects upon homogeneous outer-sphere reactions between cationic complexes 225 as well as to the results of the recent ab initio calculations noted above. 14,15,17,215 Similar calculations have yet to be performed for electron-transfer processes at metal surfaces. They would provide an invaluable guide to the further interpretation of the experimental data.

The present results therefore are at variance with a previous suggestion that the effective electron-tunneling probabilities should be much larger at metal surfaces due to the multitude of electronic energy states in the vicinity of the Fermi level that are available for coupling with the reactant orbitals. 231,232 Further support to the present findings is given by the observations of Weaver and Li that both the unimolecular rate constants and frequency factors for the electro-reduction of pentaamminecobalt(III) bound to a mercury surface via organic bridges are decreased markedly upon interruption of bond conjugation in the bridging ligand. 200,218,233 These observations serve to highlight the previously neglected role of nonadiabatic electron tunneling in influencing electron-transfer reactivity at electrode surfaces as well as in homogeneous solution.

## D. The Influence of the Electrode Surface Composition on Redox Reaction Pathways and Electrochemical Kinetics

#### 1. Introduction

A key question in the study of electron-transfer reactions at electrodes concerns the role of the metal surface composition in determining the kinetics of such processes. A useful method of varying the surface composition in order to address this question is to utilize the underpotential deposition phenomenon. Thus, redox reaction kinetics at UPD lead/silver and UPD thallium/silver electrode surfaces are examined here and are compared with the kinetics of corresponding reactions at silver and mercury surfaces. The purposes of this study are first to establish the reaction pathways, either inner- or outer-sphere, for the reduction of several metal complexes at different surfaces, and second, to uncover any "electrode-specific" factors controlling electron-transfer reactivity.

A number of previous studies have examined the influences of the electrode material on the kinetics of outer-sphere redox reactions. 109,111 For the most part, reactivity differences have been traced to differences in electrostatic double-layer effects 45,47,239 (i.e. "\$\phi\_2\$ effects") at various electrodes. Nevertheless, in several cases more complicated behavior has been uncovered. 110,136 This study is somewhat more general in that the reductions of a number of metal complexes potentially capable of following inner-sphere (ligand-bridged) pathways are also scrutinized. In order to compare the energetics of inner- and outer-sphere reactions on a common basis

considerable use is made of the encounter pre-equilibrium model proposed in Section IV. A. This model provides a means of separating environmental factors, defined here as any factors affecting the relative interfacial concentration of the reactant, from additional elements contributing to reactivity.

For a number of reasons one-electron reductions of chromium(III) ammine and aquo complexes were selected for study. First, these reactions occur over a suitably negative potential range. (The UPD T1/Ag surface is unstable at potentials positive of circa. -950 mV versus s.c.e.). Secondly, such complexes are substitutionally inert in the oxidized state. Therefore the ligand composition of each reactant in the transition state is known with certainty. Finally, such reactions have already been investigated extensively at silver 85.130.199,204 and mercury 30,54,216,240 electrodes.

#### 2. Results and Discussion

#### a. Rate Formulations

It is desired to separate environmental factors from other factors influencing reactivity. This is conveniently accomplished (in principle) by separating the observed electron-transfer rate constant k into a precursor formation constant K containing the terms relating to the relative interfacial concentration of the reactant, and a first-order rate constant k for the elementary step. For inner-sphere reactions K can be expressed as a formal equilibrium constant for reactant adsorption, such that:

$$K_{p} = \Gamma/C_{h} \tag{4.43}$$

where  $\Gamma$  and  $C_b$  are the surface and bulk concentrations of the reactant, respectively. For outer-sphere reactions we have written (cf. Equation 4.40):

$$K_{p} = \delta r \exp \left(-W_{p}/RT\right) \tag{4.50}$$

where  $\delta$ r is the reaction zone thickness and the work term  $W_p$  equals, in the simplest case,  $Z\phi_2$ . The magnitude of  $\delta$ r is determined by electron-tunneling considerations. We have been able to deduce from experimental data that the values of  $\delta$ r at the mercury-aqueous interface are approximately  $2 \times 10^{-9}$  cm for chromium aquo couples and  $5 \times 10^{-8}$  cm for chromium ammine couples (Section IV. C). In lieu of additional information, these values will be employed for other electrode-solution interfaces as well. It will be expedient in the discussion to follow, to consider outer-sphere reactions and innersphere (or potentially inner-sphere) reactions separately.

# b. Reduction Kinetics of Complexes Containing Potential Bridging Ligands

In order to minimize electrostatic work terms the apparent rate constants reported in this section and the next were obtained in weakly adsorbing electrolyte solutions of high ionic strength [either 0.5  $\underline{\text{M}}$  NaClO<sub>4</sub> or 0.04  $\underline{\text{M}}$  La(ClO<sub>4</sub>)<sub>3</sub>]. Reactant concentrations typically were 1  $\underline{\text{mM}}$ . In order to avoid decomposition of the aquo complexes and precip-

itation of Cr(II), the electrolyte solutions were made moderately acidic (pH ~ 2.5). At the UPD metal surfaces, rate constants were measured by using pulsed rotating disk voltammetry as outlined in Chapter II. Uncertainties in the rate constants amount to a factor of 2 to 3, which is typical of what can be achieved at solid metal electrodes. 85.92.109,136 (The reproducibility is considerably greater for consecutive rate measurements within a given experiment). Apparent rate constants for reactions at silver and mercury surfaces were extracted from previous reports from this laboratory. For a number of reactions at these two surfaces, Guyer and Weaver 199 have also reported directly measured values (fast cyclic voltammetry method) of kare.

For several reactions at silver, mercury, UPD lead/silver and UPD thallium/silver, apparent rate constants at -700 mV versus s.c.e. are assembled in Table 4.2. This potential was selected in order to minimize the extrapolations which are necessary in order to compare rate data obtained at different surfaces. Rate constants for Cr(NH<sub>3</sub>)<sub>5</sub>Cl<sup>2+</sup> reduction at silver <sup>85</sup> and at UPD lead/silver are plotted against electrode potential in Figure 4.3. Relative reactivities are compared for reactions at silver <sup>85</sup> versus the UPD metal surfaces (Figure 4.4) by plotting log k values (at -700 mV) at one surface against those obtained at another.

The results given in Table 4.2 as well as Figures 4.3 and 4.4 indicate that underpotential deposition of either thallium or lead causes a remarkable decrease in electron-transfer reactivity at the silver-aqueous interface. Rates at UPD Pb/Ag and UPD Tl/Ag are also lower than those found at mercury. All seven reactions are known to

Table 4.2. App Bri	Apparent Rate Constants for Bridging Ligands. $E = -700 \text{ mV}$ .	nts for the Reduct: -700 mV.	ton of Complexes	Apparent Rate Constants for the Reduction of Complexes Containing Potential Bridging Ligands. E = $-700  \text{mV}$ .
Reactant	Silver	Mercury	UPD lead	UPD thallium
$cr(NH_3)_5Ncs^{2+}$	2x10 <sup>-3</sup> cm s <sup>-1</sup>	6x10 <sup>-5</sup> cm s <sup>-1</sup>	5x10 <sup>-6</sup> cm s <sup>-1</sup>	4x10 <sup>-6</sup> cm s <sup>-1</sup>
$Cr(H_2^0)_5NCS^{2+}$	$7 \times 10^{-3}$	3.3×10 <sup>-3</sup>	2.5×10 <sup>-4</sup>	
$\operatorname{Cr}(\operatorname{NH}_3)_5 \operatorname{N}_3^{2+}$	~7×10 <sup>-5</sup>	4.8×10 <sup>-6</sup>	3×10 <sup>-6</sup>	3×10 <sup>-7</sup>
$Cr(H_2^0)_5^{1}_3$	5×10 <sup>-2</sup>	1.0x10 <sup>-4</sup>	2×10 <sup>-5</sup>	
$Cr(NH_3)_5C1^{2+}$	$2.2 \times 10^{-1}$	8.2×10 <sup>-5</sup>	9×10 <sup>-6</sup>	3×10 <sup>-5</sup>
$Cr(H_2^0)_5C1^{2+}$	. 3	$6.4 \times 10^{-3}$	$7 \times 10^{-4}$	
$\operatorname{cr}(\operatorname{NH}_3)_5\operatorname{Br}^{2+}$	-2.6	3×10 <sup>-2</sup>	1.4×10 <sup>-3</sup>	

<sup>a</sup>Data taken from reference 85.

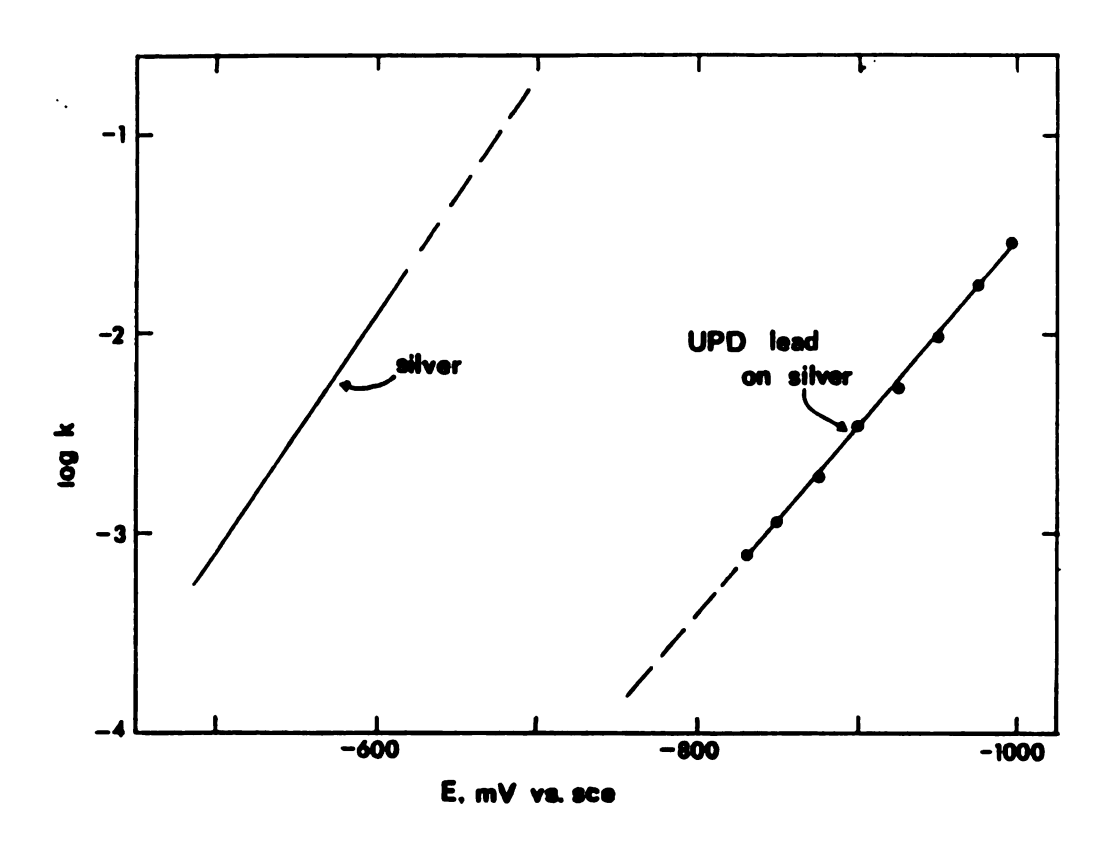


Figure 4.3. Log of apparent rate constant for  $Cr(NH_3)_5C1^{2+}$  versus electrode potential at UPD lead/silver and at silver.

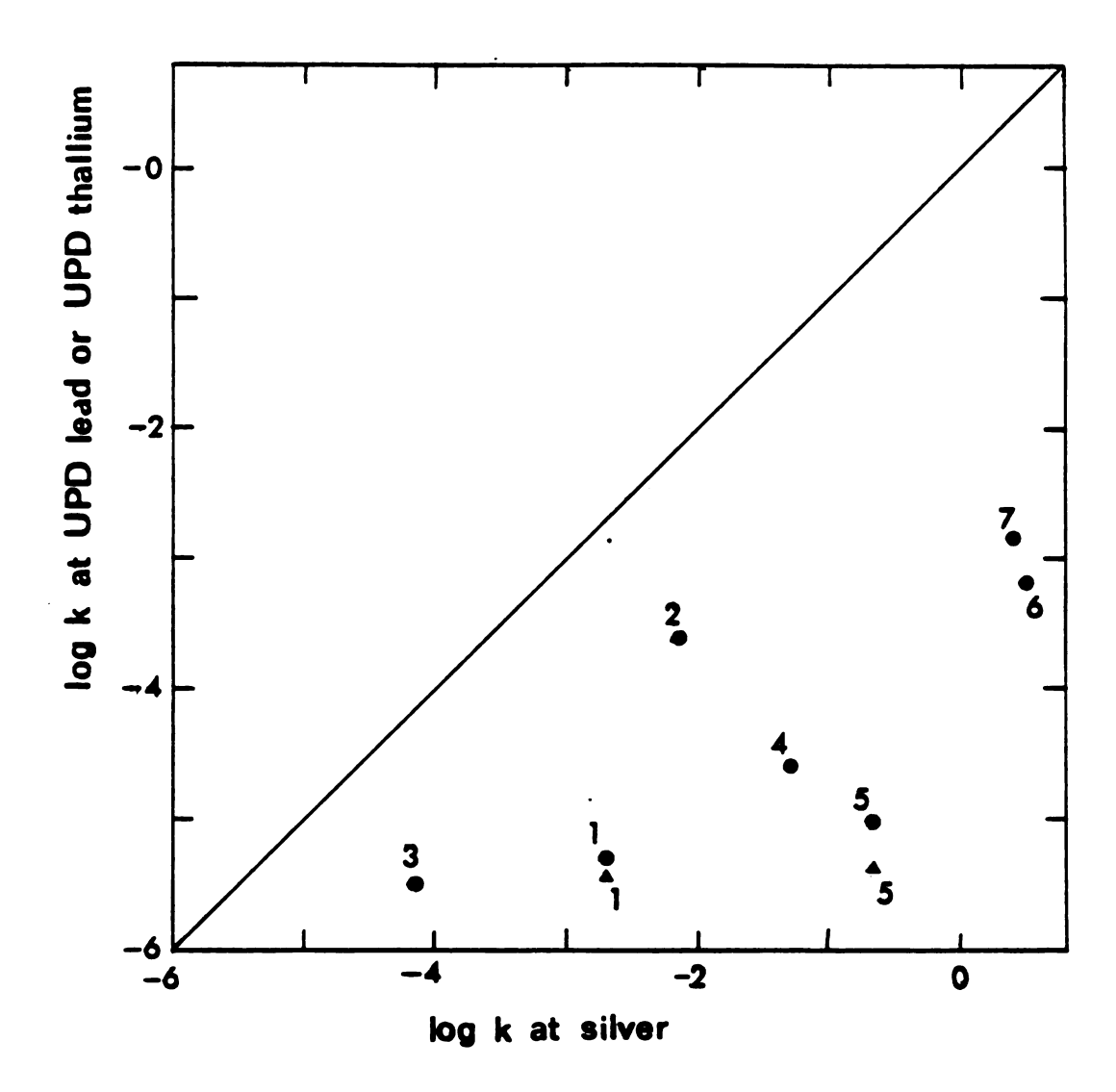


Figure 4.4 Log of apparent rate constant at UPD lead/silver or UPD thallium/silver versus log of apparent rate constant at silver. Key to reactants: (1)  $Cr(NH_3)_5NCS^{2+}$ ; (2)  $Cr(H_2O)_5NCS^{2+}$ ; (3)  $Cr(NH_3)_5N_3^{2+}$ ; (4)  $Cr(H_2O)_5N_3^{2+}$ ; (5)  $Cr(NH_3)_5C1^{2+}$ ; (6)  $Cr(H_2O)_5C1^{2+}$ ; (7)  $Cr(NH_3)_5Br^{2+}$ .

follow inner-sphere reduction pathways at mercury and silver. Generally inner-sphere pathways yield larger rate constants than the corresponding outer-sphere routes since K<sub>p</sub> values for the former are larger. It is reasonable to suppose that the relatively slow rates at the UPD metal surfaces might be due to a change of mechanism from inner- to outer-sphere or due to decreases in K<sub>p</sub> values for inner-sphere routes in comparison to those at mercury and silver.

A number of tactics were used in attempting to establish whether and to what extent adsorbed precursor complexes are involved in reactions at underpotentially deposited lead and thallium. The problem is made difficult because precursor adsorption, if it occurs at all, should be fairly weak at the UPD metal surfaces and therefore difficult to detect. A fairly indirect approach for detecting adsorbed reactants involves monitoring rate responses to systematic alterations in doublelayer structure caused by the adsorption of anions. 73,216,241,242 Rates of outer-sphere reactions involving cations are expected to be accelerated following the addition of iodide since the total charge at the electrode surface will be made more negative and work terms will become more favorable. On the other hand, inner-sphere reactions involving anionic bridging ligands are decelerated, at least at mercury and silver, evidently because of unfavorable Coulombic interactions between the incoming ligand and adsorbed anions. $^{73}$  Table 4.3 summarizes the rate responses at -800 mV for several reactions at UPD Pb/Ag following the addition of 30 mm I. Also included are semi-quantitative estimates of the rate increases expected for bona fide outer-sphere reactions. These estimates were

Table 4.3. Effects of Iodide Addition on Rate Constants at UPD Lead/Silver

Reactant	$\Delta \log k^{-800}$ (observed after adding iodide)	-800 (calculated assuming outer-sphere reactivity)
Cr(H <sub>2</sub> 0) <sub>5</sub> C1 <sup>2+a</sup>	0.69	0.31
$Cr(NH_3)_5Cl^{2+a}$	0.42	0.28
Cr(NH <sub>3</sub> ) <sub>5</sub> Br <sup>2+a</sup>	0.4	0.29
Cr(H <sub>2</sub> O) <sub>5</sub> N <sub>3</sub> <sup>2+b</sup>	0.43	0.24
$Cr(H_2^0)_5 NCS^{2+a}$	0.32	0.30
$Cr(NH_3)_5NCs^{2+c}$	0.50	
$Cr(NH_3)_5H_20^{3+a}$	0.47	0.45
Cr(H <sub>2</sub> 0) <sup>3+a</sup>	0.64	0.47

a. Initial electrolyte:  $0.5\underline{M}$  NaClO<sub>4</sub>; final electrolyte:  $0.47\underline{M}$  NaClO<sub>4</sub> +  $0.03\underline{M}$  NaI.

b. Initial electrolyte:  $0.5\underline{M}$  NaClO<sub>4</sub>; final electrolyte:  $0.49\underline{M}$  NaClO<sub>4</sub> + 0.01  $\underline{M}$  NaI.

c. Initial electrolyte: 0.2 $\underline{M}$  NaClO<sub>4</sub>; final electrolyte: 0.17 $\underline{M}$  NaClO<sub>4</sub> + 0.03  $\underline{M}$  NaI.

obtained by estimating the surface concentrations of specifically adsorbed iodide and perchlorate ions as well as the electrode charge from capacitance measurements, combining these to calculate the difference in  $\phi_2$  values (Equation 1.11) between perchlorate plus iodide and pure perchlorate electrolytes, and then inserting this difference into the Frumkin equation (1.16) together with the appropriate values of  $\alpha$  and Z. (Estimated values of  $\phi_2$  in various electrolytes are plotted against electrode potential in Figure 4.5). Table 4.3 indicates that the addition of iodide causes an increase in reduction rate for potentially inner-sphere reactants as well as for reactants such as Cr(NH<sub>3</sub>)<sub>5</sub>H<sub>2</sub>0<sup>3+</sup> which lack obvious bridging ligands. At UPD thallium/silver, rate constants for  $Cr(NH_3)_5NCS^{2+}$  and  $Cr(NH_3)_5C1^{2+}$ reduction are also increased by iodide. Such results suggest that each reaction listed in Table 4.3 follows an outer-sphere mechanism. Nevertheless, a certain ambiguity remains concerning this mechanism diagnosis since the overall rates of weakly inner-sphere reactions may still be accelerated by adsorbed anions if the competing outer-sphere route is sufficiently influenced by alterations to the double layer structure to become the predominant reaction pathway. 216 A safe conclusion would be that these reactions are at least not strongly inner-sphere processes.

A second approach, used previously for reactions at mercury, 30 employs free anions as models for ligand-induced complex ion adsorption. Values of K<sub>p</sub> for five anions at silver, UPD thallium/silver and UPD lead/silver are listed in Table 4.4. These were calculated from adsorption data given in Chapter III. On the basis of these results,

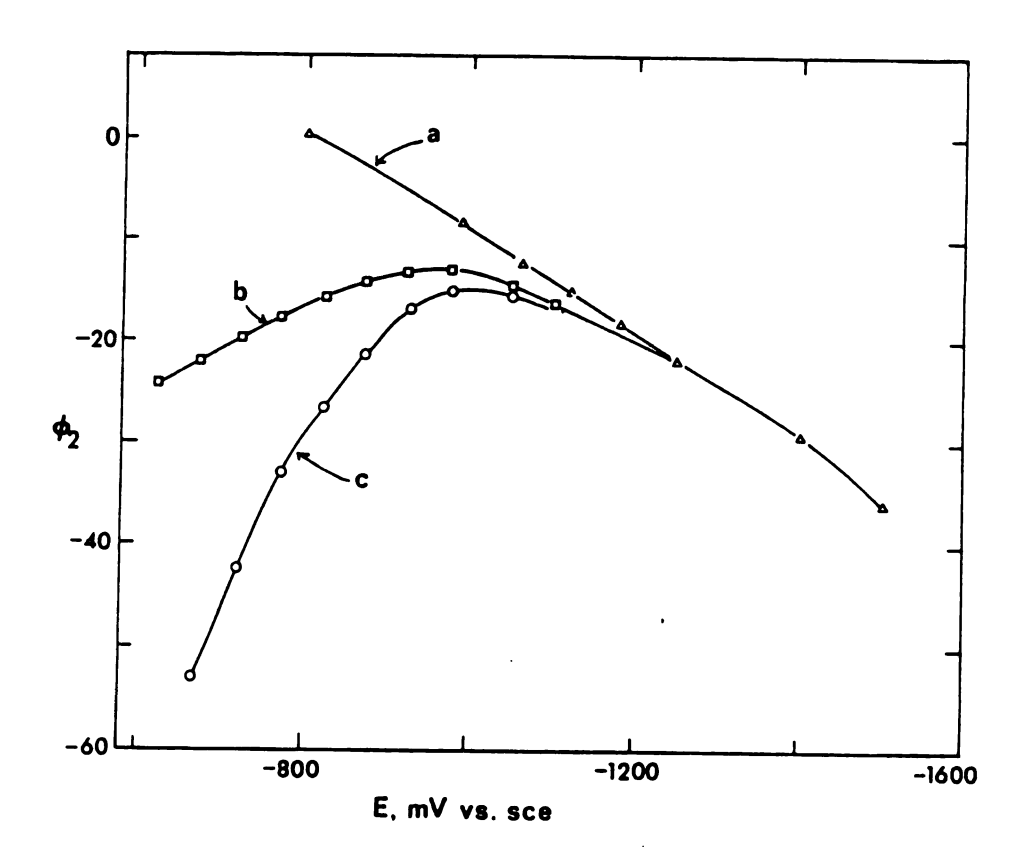


Figure 4.5. Diffuse layer potential  $\phi_2$  versus electrode potential at UPD lead/silver. Electrolytes: (a)  $0.5\underline{\text{M}}$  NaF; (b)  $0.5\underline{\text{M}}$  NaClO<sub>4</sub>; (c)  $0.47\underline{\text{M}}$  HaClO<sub>4</sub> +  $0.03\underline{\text{M}}$  NaI.

Formal Equilibrium Constants for Anion Adsorption at Solid Electrode/ Aqueous Interfaces Table 4.4.

<u>V</u> n	K <sub>p</sub> (silver) <sup>a</sup>	1.5 x 10 <sup>-5</sup> cm	7 x 10 <sup>-3</sup>	~1 x 10 <sup>-3</sup>	$>1 \times 10^{-3}$	$2.2 \times 10^{-5}$
-950 mV	K <sub>p</sub> (UPD thallium) <sup>b</sup>	5 x 10 <sup>-7</sup> cm	$2 \times 10^{-0}$	$2.6 \times 10^{-5}$	$6 \times 10^{-6}$	$1.4 \times 10^{-6}$
N m	K <sub>p</sub> (silver) <sup>a</sup>	1.5 x 10 <sup>-4</sup> cm	$3.5 \times 10^{-4}$	~1 x 10 <sup>-3</sup>	~1.8 x 10 <sup>-3</sup>	$1.4 \times 10^{-4}$
-700 mV	K <sub>p</sub> (UPD lead) <sup>a</sup>	-1 x 10 <sup>-7</sup> cm	$1.2 \times 10^{-0}$	$1.5 \times 10^{-5}$	$1.2 \times 10^{-5}$	2.3 x 10 <sup>-6 b</sup>
	Anion	c1 <sup>-</sup>	Br_	ı_I	NCS_	N 3 -

Unless\_noted otherwise, composition of electrolytes is  $0.499\underline{M}$  NaCl $0_4$  +  $0.001\underline{M}$  NaX. X = Cl\_, Br\_, I\_, NCS\_ or N\_3 . Composition of electrolytes is 0.499M NaF + 0.001M NaX. X = Cl<sup>-</sup>, Br<sup>-</sup>, I<sup>-</sup>, NCS<sup>-</sup>, or N<sup>-</sup><sub>3</sub>. ь.

a.

differences of circa. 102 would be expected between apparent rate constants at silver compared to UPD metal electrodes. Values of k were calculated for reactions at the latter surfaces by assuming that  $K_{p}$  (complex) equals  $K_{p}$  (anion). These  $k_{pt}$  values are listed in Table 4.5 together with values for reactions at mercury and silver. (Values of  $k_{at}$  at -700 mV at UPD thallium/silver were estimated by estimating  $K_{\rm p}$  (anion) and  $k_{\rm pt}$  at several potentials negative of -950 mV and extrapolating to -700 mV). It is clear that  $K_{_{\rm D}}$  values estimated in this manner can account partially for the disparities in apparent rate constants between various electrodes. Nevertheless, some differences remain. Evidently, there are additional factors beyond environmental effects or else the magnitudes of the  $K_{D}$  (complex) values have been systematically overestimated. The latter explanation is a distinct possibility, especially for the ammine complexes, in view of Weaver's findings at mercury. 30 Particularly at potentials as far negative as -700 mV values of  $K_{\rm p}$  (anion) probably represent, at best, only upper limits for K<sub>D</sub> (complex).30

An alternative assumption is that each complex reacts via an outer-sphere route at the UPD metal electrodes. Values of  $k_{\rm et}$  estimated according to this assumption are also listed in Table 4.5. For reactions at UPD lead/silver the estimated  $k_{\rm et}$  values agree quite closely (within a factor of five or less) with those found at mercury. The single exception is the reduction of  ${\rm Cr(H_20)}_5{\rm NCS}^{2+}$  for which the estimated  $k_{\rm et}$  value at UPD Pb/Ag exceeds that at mercury by a factor of twenty. In view of the close agreement for the others, this represents reasonable evidence for the existence of a mildly catalytic inner-

Estimated Values of Rate Constants for the Elementary Electron-Transfer Step of Several Reactions.  $\rm E = -700~mV.$ Table 4.5.

	Silver	Mercury	UPD1ead <sup>b</sup>	UPD1ead <sup>C</sup>	UPD thallium <sup>b</sup>	UPD thallium <sup>C</sup>
Cr(NH <sub>3</sub> ) <sub>s</sub> NCS <sup>2+</sup>	50 s <sup>-1</sup>	4 8 -1	0.4 s-1	19 5-1	0.7 5-1	4 , 1021
cr(H <sub>2</sub> 0) <sub>5</sub> Ncs <sup>2+</sup>	7.5	1.3x10 <sup>3</sup>	2.2	2×10 <sup>4</sup>	n	0 1 4
$\operatorname{Cr}(\operatorname{NH}_3)_5\operatorname{N}_3^2$	0.7	6	0.3	12	0.1	30
$Cr(H_20)_5N_3^2+$	7.0	9×10 <sup>2</sup>	3	2×10 <sup>3</sup>		
$\operatorname{Cr}(\operatorname{NH}_3)_5\operatorname{Cl}^{2+}$	3.3×10 <sup>2</sup>	06	06	40	50	2.6x10 <sup>3</sup>
Cr(H <sub>2</sub> 0) <sub>5</sub> C1 <sup>2+</sup>	~5×10 <sup>4</sup>	1.3×10 <sup>4</sup>	7×10 <sup>3</sup>	6×10 <sup>4</sup>		
$\operatorname{Cr}(\operatorname{NH}_3)_5\operatorname{Br}^{2+}$	1×10 <sup>4</sup>	2×10 <sup>3</sup>	1.2×10 <sup>3</sup>	5x10 <sup>3</sup>		

Assumed  $k_{et} = k/K_{p}$  (anion) Ą a Data from reference 85.

c Assumed  $k_{et} = k/[\delta r exp(-W_p/RT)]$ 

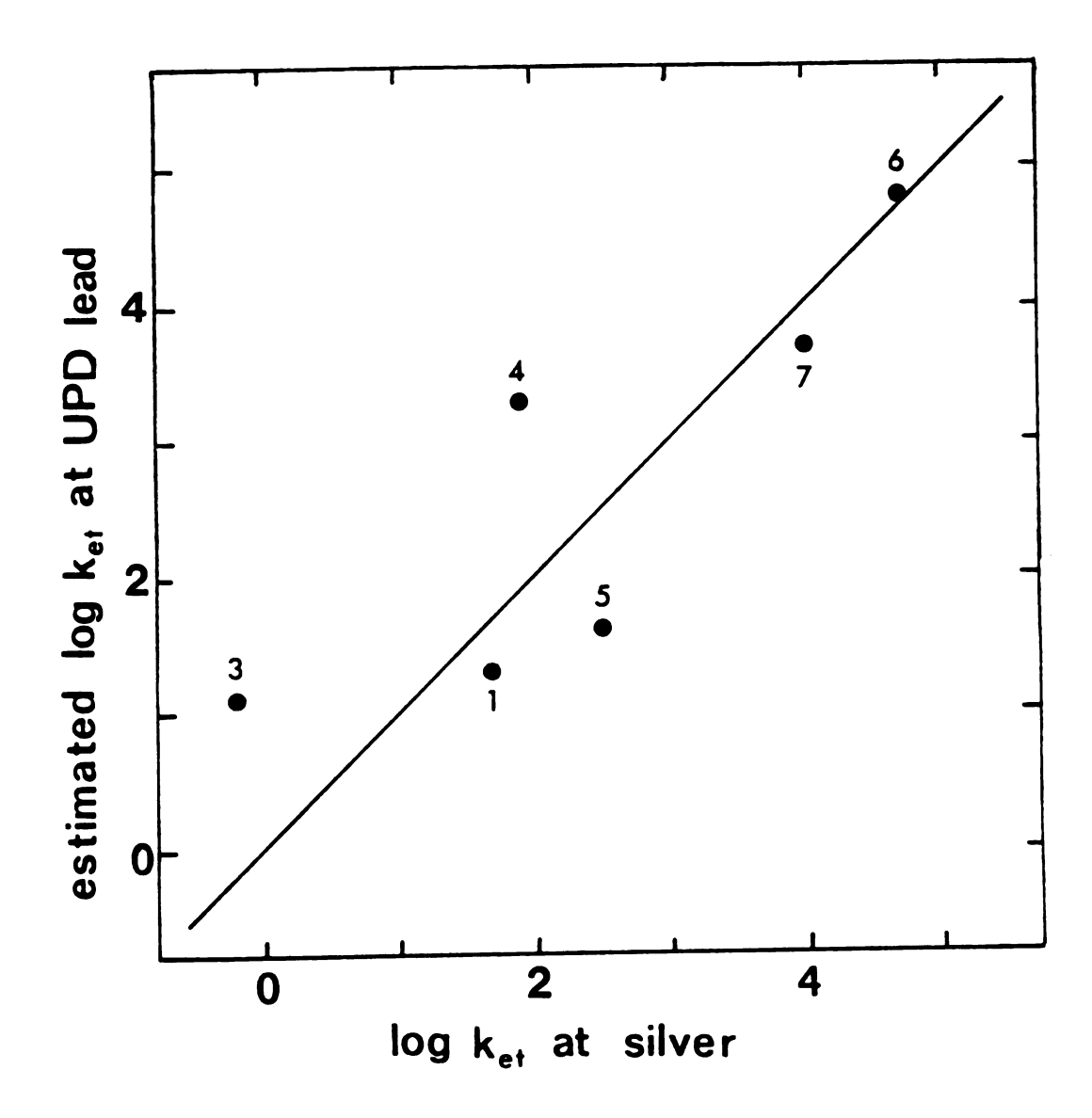


Figure 4.6. Estimated value (outer-sphere assumption) for  $\log k_{\mbox{et}}$  at UPD lead/silver versus  $\log k_{\mbox{et}}$  at silver. Reactants as in Figure 4.4.

sphere pathway for  $Cr(H_2O)_5NCS^{2+}$  reduction at UPD lead/silver. Of the seven complexes,  $Cr(H_2O)_5NCS^{2+}$  would be the most likely to react via an adsorbed precursor state since aquo chromium complexes are more strongly adsorbed than the corresponding ammine complexes at other surfaces  $^{30,85}$  and since free thiocyanate adsorbs more extensively than either chloride or bromide (cf. Section III. D).

Estimates of  $\log k_{et}$  at UPD lead/silver are compared with values  $\log k_{et}$  at silver in Figure 4.6. In contrast to the findings with apparent k values (Figure 4.4), the rate constants for the elementary step correlate fairly well, although there is a fair amount of scatter.

Rate constants gathered at UPD thallium/silver are difficult to compare quantitatively with those gathered at mercury since the required extrapolations for either data set are uncertain. In view of these difficulties the k values which are estimated for reactions at UPD thallium/silver based on outer-sphere reactivity are compared in the form of rate ratios with those at mercury at both -700 and -1000 mV (Table 4.6). At -1000 mV the work corrections for rates at UPD T1/Ag can be made with certainty and turn out to be small since  $\phi_2 \approx 0$ . The  $k_{at}$  estimate for  $Cr(NH_3)_5NCS^{2+}$  reduction at mercury is probably also trustworthy. 30 However the azido- and chloro- complexes are sufficiently weakly bound at mercury that the potential dependence of K cannot be assessed. 30 Nevertheless for the thiocyanato complex the value of  $log K_D$  evidently diminishes by 0.6 in changing the potential from -700 mV to -1000 mV. $^{30}$  In order to estimate  $k_{et}$  at -1000 mV for the azido and chloro complexes similar decreases of  $K_{\overline{D}}$  between -700 and -1000 mV were assumed to occur. The  $k_{et}$  values estimated in this

manner were used to calculate the rate ratios at -1000 mV that are listed in Table 4.6. The rate ratios at -700 mV also are uncertain because of difficulties in establishing accurately the degree of perchlorate adsorption at UPD T1/Ag and therefore the value of  $d\phi_2/dE$  which is required in order to extrapolate the work corrections. Nevertheless, the ratios at either potential suggest that  $Cr(NH_3)_5NCS^{2+}$  may well be adsorbed at UPD thallium/silver while the other complexes probably are not. In particular the ratios of 0.3 for the azido and chloro complex reductions are consistent with those found for bona fide outer-sphere reactions (cf. following subsection).

Taken in toto, the various analyses and observations suggest that the best interpretation of the rate data is that reactions which ordinarily follow inner-sphere reduction pathways instead follow outersphere routes at the UPD metal surfaces. The exceptions are the reductions of  $Cr(H_20)_5 NCS^{2+}$  at UPD lead/silver and  $Cr(NH_3)_5 NCS^{2+}$  at UPD thallium/silver. Apparently both proceed via weakly adsorbed precursor complexes. Given these interpretations it appears that differences in electron-transfer reactivity for inner-sphere (or potentially innersphere) reactions between different electrodes can be accounted for completely by considering the likely differences in precursor stabilities. This behavior is markedly different to that observed for the corresponding homogeneous inner-sphere reactions. Thus the chlorobridged exchange reaction between Cr(II) and Cr(III) aquo complexes is perhaps 10<sup>8</sup> faster than the corresponding outer-sphere exchange. 243 Enhanced precursor stability for the inner-sphere mechanism can account for only about a factor of 10<sup>3</sup> at most. 30 The remaining five orders of

Table 4.6. Ratios of Estimated  $k_{\mbox{et}}$  Values for Reactions at UPD Thallium/Silver and Mercury.

Reactant	$(k_{et}^{T1}/k_{et}^{Hg})^{-700}$	$(k_{et}^{T1}/k_{et}^{Hg})^{-1000}$
Cr(NH <sub>3</sub> ) <sub>5</sub> NCs <sup>2+</sup>	1 x 10 <sup>2</sup>	10
Cr(NH <sub>3</sub> ) <sub>5</sub> N <sub>3</sub> <sup>2+</sup>	2.5	0.3
Cr(NH <sub>3</sub> ) <sub>5</sub> C1 <sup>2+</sup>	30	0.3

magnitude must be attributed to a lowering of the Franck-Condon barrier and improved electronic coupling for the elementary step. Evidently when two metal centers are simultaneously activated as in homogeneous reactions, there exist opportunities for synergistic and cooperative behavior which are unavailable in unimolecular electrochemical reactions.

#### c. Reduction Kinetics for Complexes Lacking Bridging Ligands

The second group of reactants for which electron-transfer reduction kinetics were scrutinized consists of complexes lacking obvious bridging ligands. These reactants or their cobalt analogs appear to be reduced via outer-sphere mechanisms at gold, platinum. silver and mercury surfaces. 85,92.109,110,241,242 Thus, it is reasonable to suppose that such reactants follow outer-sphere reaction pathways at underpotentially deposited lead and thallium surfaces as well. Indeed, for most of the complexes it would be difficult to envisage transition-state geometries corresponding to alternative inner-sphere routes.

Apparent rate constants and transfer coefficients at -1000 mV for the reduction of outer-sphere reactants at mercury and the two UPD metal surfaces are listed in Table 4.7. Unfortunately the reactions are too slow to be monitored at silver. Also listed in Table 4.7 are work-corrected rate constants  $k_{\rm corr}$ , which were calculated from the Frumkin equation:  $^{45,47,239}$ 

$$lnk_{corr} = lnk + (1/RT)[(z-n_{\alpha_{corr}})F_{\phi_r}]$$
 (1.16)

Table 4.7. Rate Constants for Outer-Sphere Reactions. E = -1000~mV.

Reactant	Surface	8	k	kcorr
Cr(en)3+	mercury a, b	06.0	6 x 10 <sup>-2</sup> cm s <sup>-1</sup>	$1.7 \times 10^{-3} \text{cm s}^{-1}$
,	UPD Pb/A8 <sup>c</sup>	0.91	$1 \times 10^{-3}$	4 × 10 <sup>-4</sup>
Cr (NH <sub>2</sub> ) 3+	mercury b, d	0.84	$2.7 \times 10^{-2}$	9 x 10 <sup>-4</sup>
5 n	UPD Pb/Ag <sup>d</sup>	0.78	$2.5 \times 10^{-4}$	8 x 10 <sup>-5</sup>
	UPD T1/Ag <sup>d</sup>	0.70	8 x 10 <sup>-5</sup>	8 x 10 <sup>-5</sup>
$cr(NH_3)_5H_2^{03+}$	mercury a, b	0.73	$3.2 \times 10^{-2}$	$4 \times 10^{-3}$
	UPD Pb/Ag <sup>c</sup>	0.80	$1 \times 10^{-3}$	3 x 10 <sup>-4</sup>
	UPD T1/A8 <sup>C</sup>	97.0	$9 \times 10^{-5}$	9 x 10 <sup>-5</sup> .
Cr(H,0),	mercury <sup>a, b</sup>	0.58	$2.4 \times 10^{-2}$	3 x 10 <sup>-3</sup>
0 7	UPD Pb/Ag <sup>c</sup>	0.55	$3 \times 10^{-3}$	9 x 10 <sup>-4</sup>
	UPD T1/A8 <sup>c</sup>	0.50	$3 \times 10^{-4}$	3 x 10 <sup>-4</sup>
Cr(H <sub>2</sub> 0) <sub>5</sub> F <sup>2+</sup>	mercury a, b	0.59	1.3 x 10 <sup>-4</sup>	3.8 x 10 <sup>-5</sup>
,	UPD Pb/Ag <sup>c</sup>	-0.5	$-6 \times 10^{-5}$	3 x 10 <sup>-5</sup>
	UPD T1/A8 <sup>c</sup>	0.64	1.3 x 10 <sup>-6</sup>	1 x 10 <sup>-6</sup>
Cr(H,0), SO,	mercury c, e	67.0	$2.8 \times 10^{-3}$	$1.6 \times 10^{-3}$
r 1	UPD Pb/Ag <sup>d</sup>	0.41	$1 \times 10^{-4}$	$1 \times 10^{-4}$
Eu(H <sub>2</sub> 0) <sup>3+</sup>	mercury d,f	0.58	2.1	$3.2 \times 10^{-2}$
	UPD Pb/Ag <sup>d</sup>	0.41	$2 \times 10^{-2}$	$6 \times 10^{-3}$
a 1 <u>M</u> NaClO <sub>4</sub> ; b	reference 178;	c 0.5 <u>M</u>	NaC104; d 0.04 H.	c $0.5\underline{M}$ NaCl $0_4$ ; d $0.04\underline{M}$ La(Cl $0_4$ ) $_3$ ; e reference 136;

f reference 54.

The potential,  $\phi_r$ , at the reaction plane was assumed to equal  $\phi_2$  except for reductions of aquo complexes at mercury. For these reactions there is a good evidence that  $\phi_r$  more nearly equals 0.5  $2^{216}$ 

Before correcting for double-layer effects, the rate constants are 2- to 500- fold greater at mercury than at the other electrodes. Electrostatic double-layer effects appear to account for the largest portions of the rate disparities for each reaction. However, the corrected rate constant are still somewhat smaller at UPD lead/silver and especially at UPD thallium/silver, in comparison to mercury. It might be argued that these residual differences are due to errors in the double-layer corrections, especially in light of the well-known difficulties in accurately determining the potential of zero charge at polycrystalline metal electrodes. 41-44 However, the variation of electrode charge with potential is sufficiently weak at both UPD metal electrodes that errors of as much as 100 mV in estimating pzc values would yield errors of less than 7mV in  $\phi_2$  potentials. Rather than representing errors in electrostatic work corrections, the remaining differences may be vestiges of more complicated electrode-specific effects. Indeed, the results from activation parameter measurements (see below) as well as unpublished studies by H. Y. Liu with gallium electrodes 136 support this notion.

## d. <u>Activation Parameters for Outer-Sphere Reductions at UPD</u> <u>Lead/Silver</u>

The temperature coefficients of apparent rate constants were measured for several reactions which appear to follow outer-sphere

reduction pathways at UPD lead/silver. Experiments were performed also using UPD thallium/silver electrodes but the results were insufficiently reproducible to report. Measurements at UPD lead/silver were confined to the temperature region between 0 and 30°C since at higher temperatures leaks developed between the silver disk electrode and the surrounding Kel-F casing. Since rates were monitored at only three or four temperatures rather large uncertainties were obtained for the resulting activation parameters.

Table 4.8 lists the ideal activation enthalpies at -1000 mV which are derived from nonisothermal measurements<sup>55</sup> of rates at UPD lead/silver. The ideal activation enthalpy is defined<sup>54</sup> by Equation 4.51:

$$\Delta H_{ideal}^{*} = -R[dlnk/d(1/T)]\phi_{m}$$
 (4.51)

For comparison, results obtained by other workers using lead  $^{136}$  or mercury electrodes are listed also. The corresponding ideal activation entropies are listed in Table 4.9. These were determined by assuming that  $\nu_n$  equals  $1\times 10^{13}~\text{s}^{-1}$  and that  $K_p$  equals  $2\times 10^{-9}~\text{cm}$  for aquo rreactants and  $5\times 10^{-8}~\text{cm}$  for ammine reactants (see Section IV. C). Also listed in Table 4.9 are work-corrected  $\Delta S^*$  values. Because the double-layer capacitance at lead (and presumably UPD lead/silver) is virtually unchanged between 0 and  $40^{\circ}\mathrm{C}$ , diffuse-layer potentials will remain essentially unchanged over this temperature region (provided that the temperature coefficient of the pzc is small). As a result double-layer corrections will be needed for  $\Delta S^*_{ideal}$  but not for  $\Delta R^*_{ideal}$ . However, at mercury the double-layer capacitance, and neces-

sarily the charge, exhibit significant temperature variations. Therefore small work-corrections (circa. -1-3 kJ mol $^{-1}$ ) must be applied to  $^{\pm}$  as well. Such corrections are incorporated into the results quoted in Table 4.8.

On the basis of the activation enthalpies one would expect reduction rates to be much faster at UPD lead/silver and bulk lead electrodes than at mercury. However, the favorable enthalpic effects at the two lead surfaces are outweighed by unfavorable entropic effects. One way of determining which sets of data (mercury or lead) correspond more closely to "normal" behavior is to compare the experimental  $\Delta S^*$  values with those expected from theory. To a first approximation  $\Delta S^*_{corr}$  should be given by (cf. Equation 1.20):

$$\Delta S_{corr}^{\dagger} \simeq C_{corr}^{\Delta} \Delta S_{rc}^{O}$$
 (4.52)

Unfortunately the required thermodynamic reaction entropies are available only for the  $\mathrm{Cr}(\mathrm{H_20})_6^{3+/2+}$  and  $\mathrm{Eu}_{\mathrm{aq}}^{3+/2+}$  couples. However, in view of the empirical correlations of reaction entropies in Section V. B which indicate that such parameters are determined largely by reactant charge and size, ruthenium analogs of the chromium ammine couples may be expected to provide suitable estimates of  $\Delta \mathrm{S}_{\mathrm{rc}}^{0}$  for the latter. The values of  $\alpha_{\mathrm{corr}}^{-\Delta} \mathrm{S}_{\mathrm{rc}}^{0}$  which are calculated on this basis are listed in Table 4.9.

It is evident that the  $^{\Delta}S_{corr}^{\star}$  values obtained at mercury correspond more closely than those found at the lead surfaces to the values anticipated from Equation 4.52. One explanation for the less positive

values at the lead and UPD lead/silver surfaces is that reactions at these surfaces are strongly nonadiabatic. If nonadiabaticity is important the experimental  $\Delta S_{\text{corr}}^*$  values will differ from the true values by  $Rln_{el}$ . However, the observed enthalpy compensation effects argue against this interpretation.

Compensation effects are usually indicative of either solvent-related work terms or artifacts. 244 The latter possibility can probably be discounted for two reasons. First, the enthalpy-entropy compensation is large for most of the reactions. Second, care was taken in performing and repeating the measurements to vary the temperature in a random manner. Furthermore, the electrode was freshly pretreated prior to obtaining rate data contributing significantly to the scatter in the experimental results, such precautions insure that "time effects" which are notorious in kinetics work with solid electrodes, will not significantly influence the results.

The notion of solvent-related work contributions to activation parameters at UPD lead/silver and bulk lead electrodes (but not mercury electrodes) seems reasonable in view of the differences in inner-layer structure for lead-aqueous versus mercury-aqueous interfaces. At the former, water moelcules are probably oriented "oxygen down". 161 At the latter at -1000 mV the solvent molecules are likely to be either randomly oriented or possibly arranged with the hydrogens towards the surface given the appreciable negative charge on mercury at this potential. The mercury-aqueous interface may present an environment that is conducive to hydrogen bonding between incoming ammine or aquo reactants and inner-layer solvent molecules. On the other hand, the probable

Table 4.8. Ideal Activation Enthalpies (kJ mol<sup>-1</sup>) for Reductions of Metal Complexes at UPD Lead/Silver, Mercury and Lead Surfaces.

Reactant	UPD Lead/Silver ΔH <sup>*</sup> -1000 ideal	Lead <sup>a</sup> *-1000 <sup>ΔH</sup> ideal	Mercury <sup>b</sup> *-1000 ΔH ideal
Cr(NH <sub>3</sub> ) <sub>5</sub> C1 <sup>2+</sup>	19 ± 9		68 <sup>c</sup>
Cr(NH <sub>3</sub> ) <sub>5</sub> Br <sup>2+</sup>	50 ± 5		
Cr(NH <sub>3</sub> ) <sub>6</sub> <sup>3+</sup>	45 ±15	44	58
Cr(NH <sub>3</sub> ) <sub>5</sub> H <sub>2</sub> 0 <sup>3+</sup>	58±10	31	57
Cr(H <sub>2</sub> 0) <sup>3+</sup> 6	30 ± 5	48	62
Cr(en)3+	55 ± 5		94
Eu(H <sub>2</sub> 0) <sup>3+</sup>	24 ± 5	31	48

a. from reference 136. b. from reference 54 c. inner-sphere reaction

Table 4.9. Ideal Activation Entropies (J deg 1 mol 1) for Reduction of Metal Complexes at UPD Lead/Silver, Mercury and Lead Surfaces.

	UPD lea	d/silver	<u>lead</u>	mercury	
Reactant	ΔS <sup>*</sup> ideal	ΔS <sup>*</sup> corr	ΔS <sup>*</sup> corr	ΔS <sup>*</sup> corr	α <sub>corr</sub> ΔS <sup>o</sup> rc
Cr (NH <sub>3</sub> ) <sub>5</sub> C1 <sup>2+</sup>	-48	-41 <u>+3</u> 0			20
$Cr(NH_3)_5Br^{2+}$	-63	-56±15			
$Cr(NH_3)_6^{3+}$	-27	-37 <u>±</u> 50	-76	27	62
$Cr(NH_3)_5H_20^{3+}$	55	45 <u>+</u> 30	-78	63	80
$Cr(H_2^{0})_6^{3+}$	-30	-40 <u>+</u> 15	17	77	105
Cr(en)3+	- 2	-10 <u>+</u> 15		94	48
Eu(H <sub>2</sub> 0) <sup>3+</sup> n	-34	-44 <u>+1</u> 5	-30	52	82 <sup>c</sup> 105 <sup>d</sup>

a. data from reference 136. b. data from reference 54.

c. at UPD lead/silver and lead. d. at mercury.

inner-layer orientation at UPD lead/silver and bulk lead would not favor such interactions. Such interactions still might be possible at considerable entropic expense if the enthalpic stabilization accompanying hydrogen bonding were sufficient to force the inner-layer solvent to reorientate. Although such an explanation accounts qualitatively for the reactivity differences at lead and UPD lead/silver versus mercury, obviously it must be regarded as speculative.

#### 4. Conclusions

Wide variations in electron-transfer reactivity are observed for inner- as well as outer-sphere reactions as the composition of the electrode surface is varied. The encounter pre-equilibrium treatment of electrochemical kinetics can be used to disentangle the various effects influencing apparent rate constants. Reactions which proceed via adsorbed precursor complexes at silver and mercury are considerably slower at UPD Pb/Ag and UPD Tl/Ag electrodes apparently because of a change of mechanism from inner- to outer-sphere (and accompanying decrease of K<sub>p</sub>) at the UPD metal surfaces. Two reactants,  $Cr(H_2O)_5$ -NCS<sup>2+</sup> and  $Cr(NH_3)_5$  NCS<sup>2+</sup>, appear to follow weakly inner-sphere reaction pathways at UPD lead/silver and UPD thallium/silver surfaces, respectively. Despite the wide differences in apparent reactivity and probable differences in overall reaction mechanism, rate constants for the elementary electron-transfer step of several reactions appear to be closely similar at four different electrode surfaces.

Outer-sphere reactions are typically 3 to 10-fold slower at UPD lead and thalliums surfaces in comparison to mercury after accounting

for conventional electrostatic effects. However, the activation parameters observed at UPD lead/silver are very different to those at mercury. It is speculated that such differences are indicative of solvent-related work terms associated with hydrogen bonding between the reactant and inner-layer water molecules for the reactions at the UPD lead/silver electrode.